Efficient optimization of turning processes for powertrain components using multi model-based simulation

Dissertation (monograph) approved by the
Doctoral Degree Committee of
Hamburg University of Technology
in pursuit of the academic degree of

Doktor-Ingenieur (Dr.- Ing.)

written by

Pulkit Rana, M.Sc.

from

New-Delhi, India

2026

1. Reviewer: Prof. Dr.-Ing. Wolfgang Hintze

2. Reviewer: Prof. Dr.-Ing. Thomas Bergs

Date of Oral Examination: 16.10.2025

Wissen schafft Innovation

Herausgeber:
Prof. Dr.-Ing. Wolfgang Hintze
Prof. Dr.-Ing. habil. Hermann Lödding
Prof. Dr.-Ing. Jan Hendrik Dege
Prof. Dr.-Ing. Dr. h. c. Christian Nedeß

Anschrift:
Technische Universität Hamburg
Institut für Produktionsmanagement und -technik
Denickestraße 17
21073 Hamburg

Band 58:
Pulkit Rana
Efficient optimization of turning processes for powertrain components using multi model-based simulation
1. Auflage
Hamburg 2026

ISSN der Schriftenreihe: 1613-8244
DOI dieser Arbeit: https://doi.org/10.15480/882.16917

Abstract

In this thesis, various simulation methods for the analysis and optimization of turning processes in mass-scale production are developed and presented. The dry turning process was optimized by conducting simulations of different coating tools, coating thicknesses and tool cutting edge radii in commercial FEM software AdvantEdge. All simulations were experimentally validated. Two new simulation approaches were developed for flood lubricated turning process which significantly expanded the application of simulations. In the first approach, a coupling between two different software tools was developed and implemented. This solution coupled a commercial FEM tool (AdvantEdge) with a commercial CFD tool (Star-CCM+). In the second approach, a single software, LS-DYNA, was used to simulate flood lubricated orthogonal turning simulations. These simulations were additionally validated with literature and were compared to dry orthogonal turning simulations. Lastly, mechanistic modelling method was used in the MACHpro software to optimize the NC-program of inner contour turning process in mass production of turbine housing. For this purpose, a digital force model using FEM simulations was developed in order to optimize the NC program by means of feed-rate adjustments. By implementing these simulation results in mass-production, the tool life could be increased by 46%. Additionally, the best performing coating and coating thickness from the dry machining simulation was simulated with the mass production cutting insert geometry. In production tests, the optimized coating achieved a further increase of almost 75% in tool life and a reduction of 64% in the scrap costs.

Kurzreferat

In dieser Thesis werden verschiedene Simulationsmethoden zum Analysieren und Optimieren von Drehprozessen in der Massenproduktion entwickelt und vorgestellt. Methodisch wird dafür „design of experiment“ (DoE) angewendet. Die Optimierung beginnt mit FEM-Simulationen von trockenen Drehprozessen (AdvantEdge Software) für verschiedene Werkzeuge, Beschichtungen, Schichtdicken und Werkzeugkantenverrundungen. Alle Simulationen werden experimentell validiert. Zusätzlich werden Nassbearbeitungsdrehprozesse mit den zwei vorgestellten neuen Ansätzen simuliert. Im ersten Ansatz wird eine Kopplung zwischen zwei verschiedenen Softwares entwickelt und die Simulation eines Innendrehprozesses mit Nassbearbeitung wird in einer Software namens Star-CCM+ realisiert. Auch hier werden alle Simulationsergebnisse mit den experimentell ermittelten Ergebnissen validiert. Im zweiten Ansatz werden Orthogonaldrehprozesse mit Nassbearbeitung in einer Software namens LS-DYNA simuliert. Diese Simulationen werden mithilfe von Literaturdaten validiert und mit Simulationen von Orthogonaldrehprozessen mit Trockenbearbeitung verglichen. Zuletzt werden mechanistische Methoden zur Optimierung des NC-Programmes eines Innenkonturdrehprozesses der Massenproduktion von Turbinengehäusen in der Software MACHPro genutzt. Um das zu realisieren, wird ein digitales Kraftmodell mittels FEM-Simulationen entwickelt und das NC-Programm wird mittels Vorschubanpassungen optimiert. Bei einer Implementierung der Simulationsergebnisse in der Massenproduktion kann man einen Anstieg der Standzeit von 46% beobachten. Zusätzlich werden die beste Beschichtung und Schichtdicke von der Simulation der Trockenbearbeitungs-DoE auf der Schneidgeometrie der Massenproduktion simuliert. Dieses neue Werkzeug performt deutlich besser als das alte Schneidwerkzeug der Massenproduktion. Beim Testen dieses neuen Werkzeugs in der Massenproduktion ist ein Anstieg von 74% in der Standzeit und eine Reduktion von 64% in den Ausschusskosten zu beobachten.

Acknowledgement

Foremost I would like to express very special thanks to my doctoral supervisor Prof. Dr.-Ing. Wolfgang Hintze for supervising this thesis and for the trust he has placed in me. I would also like to thank Dr. Carsten Möller for his support in many organizational matters over the course of my doctoral thesis. I would also like to thank my 2nd doctoral supervisor Prof. Dr.-Ing. Thomas Bergs from RWTH Aachen University. A special thanks to Mr. Marco Hinrichs from Institute for Production Management and Technology in helping me with temperature measurements.

I would also like to thank my process development department colleagues at Mercedes Benz AG in Stuttgart, Untertürkheim, who made it possible for me to write this thesis in the first place. In particular, I would like to thank Dr. Wilfrid Polley, Dr. Waldemar Zielasko, Mr. Thomas Schall and Dr. Ulrich Mayer. I would also like to thank my former colleagues Mr. Matthias Dzeik, Mr. Eckhard Piroddi and Dr. Miguel Ávila for their excellent cooperation during this thesis work.

Furthermore, I would like to thank Dr. Christoph Czettl from Ceratizit group for providing experimental tools and other resources. A special thanks to software support teams of AdvantEdge, Star-CCM+, LS-DYNA and MACHPro.

I would also like to thank all my internship and thesis students for their commitment and support. I would like to take this opportunity to express my special thanks to Mr. Maximilian Müller and Mr. Gurpreet Singh Luthra for their outstanding performance.

Finally, I would like to dedicate this work to my parents and my family. A special thanks to my wife to constantly motivate and support me during this thesis work.

Table of Contents

Formula symbols, indices and abbreviations

Formula symbols

Symbol	Unit	Description
A	-	Elongation at break
C	m/s	Sonic velocity
[C]	kg/s	Damping matrix
E	J	Energy
F/f	N	Force
F_a	N	Active force
F^{body}	N	Body force
F_c	N	Cutting force
F_f	N	Feed force
F^{inert}	N	Inertia force
F_n	N	Normal force
F^{out}	N	Equivalent external force
F_p	N	Passive force
F_r	N	Radial process forces
F_t	N	Tangential force
F_{ext}	N	External force vector
F_{int}	N	Internal force vector
F_{stab}	N	Non-residual force stabilization vector
F_{fr}	N	Force resulting due to friction
K	J	Kinetic energy
[K]	kg/s^2	Stiffness matrix
M^{lump}		Lumped mass matrix
[M]	kg	Mass matrix
P/p	Pa	Pressure
P_b		Production term due to buoyancy
P_k		Production term for kinetic energy
R	J/K*mole	Universal gas constant
R_m	MPa	Tensile strength
R_{th}	µm	Theoretical roughness depth
Rz	µm	Averaged surface roughness
R'	K/W	Interface thermal resistance
S_E	J/m^3	Energy source per unit volume

Symbol	Unit	Description
S_u		User defined heat source placed at the interface
ΔT	K	Temperature difference
T	K	Temperature
T_{cut}	K	Cut off temperature
T_{melt} /T_m	K	Melting temperature
T_r	K	Reference temperature
T_{RANS}	MPa	Stress tensor
T_{w0} and T_{w1}	K	Interface temperatures on the solid and fluid side respectively
$\overline{U}$	m/s	Mean component from Navier-Stokes (NS) equation
U'	m/s	Fluctuation about the mean component from NS equation
U	m/s	Primary variable from Navier-Stokes equation
$\ddot{U}$	m/s^2	Particle acceleration vector
V	V	Voltage
VB	µm	Width of flank wear land
W	-	Smoothing function
$\dot{W}^p$	W	Plastic power per unit deformed value
Y	MPa	Elastic/Young's modulus
Y_m	MPa	Yield strength
Z	-	Fracture necking
a_p	mm	Depth of cut
b	mm	Width of undeformed chip
c_α	J/K	Heat capacity
c'	-	Decay constant
d	-	Number of space dimensions
f	mm	Feed rate
f_b	N	Body force resultant
f_β		Vortex-stretching modification factor
$f_{\beta*}$		Free-shear modification factor
$g(\varepsilon^p)$	MPa	Strain hardening
h	mm	Undeformed chip thickness
h_1	J	Heat supply to chip
h_2	J	Heat supply to tool
h'	mm	Chip thickness
k_α	W/mK	Thermal conductivity
l_{ch}	mm	Chip length
m	kg	Mass

Symbol	Unit	Description
m_1	-	Low strain rate sensitivity coefficient
m_2	-	High strain rate sensitivity coefficient
1/n	-	Strain hardening exponent
q	W/m^2	Heat flux
$\dot{q}_0$	W/m^2	Heat flux from fluid
$\dot{q}_1$	W/m^2	Heat flux leaving the solid
r	mm	Radius
r_β	µm	Cutting edge radius
r_ϵ	mm	Corner radius
s	-	Plastic deformation
Δt	s	Time step
t	s	Time
t'	Pa	contact traction
u	mm	Displacement
u+	mm/s	Time averaged velocity parallel to wall
$\dot{u}$	m/s	Velocity vector
$\ddot{u}$	m/s^2	Acceleration vector
v	m/s	Velocity
v	m/s	Relative velocity between slave node and master segment
v_c	m/min	Cutting speed
v_e	m/min	Effective speed
$v_{f.}$	m/min	Feed velocity
$[\![v]\!]$	m/s	Jump in velocity across contact
w	-	Weight function
y+	-	Non-dimensional normal distance from wall
$\otimes$	-	Product of vector quantities
α_o	°	Clearance angle
β_o	°	Wedge angle
β	-	Taylor-Quinney coefficient
γ_o	°	Rake angle
$\Gamma(\dot{\varepsilon})$	-	Strain rate sensitivity
ε_0^p	-	Reference plastic strain
ε_{cut}^p	-	Cut off strain
$\dot{\varepsilon}_o$	-	Reference strain rate
$\dot{\varepsilon}_t$	s^{-1}	Strain rate where the transition between low and high strain rate sensitivity occurs
ε	-	Strain (in FEM)

Symbol	Unit	Description
ε	m^2s^{-3}	Dissipation rate (in CFD)
ε^p	-	Plastic strain
$\dot{\varepsilon}$	s^{-1}	Strain rate
ζ	MPa	Viscous stress tensor
$\Theta(T)$		Thermal softening
I	-	Identity matrix
κ_r	°	Cutting edge angle
κh	m	Smoothing length
λ_{ch}	-	Chip thickness ratio
λ_s	°	Tool inclination angle
μ'	-	volumetric parameter
μ	-	Coefficient of friction
μ_d	-	Dynamic coefficient of friction
μ_s	-	Static coefficient of friction
μ	Ns/m^2	Dynamic viscosity
Π	-	Particle approximation function
ρ	kg/m^3	Density of material
ρ'	°	Friction angle
σ	MPa	Flow stress
σ_y	MPa	Yield stress
σ'	MPa	Stress tensor
σ_o	MPa	Initial yield stress
τ_S	MPa	Shear stress
τ_{max}	N/m^2	Maximum shear stress
υ	-	Poisson's ratio
ϕ	°	Shear angle
ω	s^{-1}	Turbulence frequency

Indices

Symbol	Description
C	Carbon
Co	Cobalt
Cr	Chromium
i, j	SPH Particle
Mn	Manganese
N	Nitrogen

Symbol	Description
Nb	Niobium
Ni	Nickel
Si	Silicon
Ta	Tantalum
Ti	Titanium
W	Tungsten
X, Y, Z	Coordinates
θ	Mathematical function

Abbreviations

Short form	Description
AMG	Algebraic Multigrid
ALE	Arbitrary Lagrange-Euler
BEM	Beam Element Method
CVD	Chemical Vapour Deposition
CFD	Computational Fluid Dynamics
CAD	Computer Aided Design
CAM	Computer Aided Manufacturing
CNC	Computer Numerical Control
CHT	Conjugate Heat Transfer
CEL	Coupled-Eulerian Lagrangian
CLS	Cutter Location Source File
COF	Coefficient of Friction
CT	Coating thickness
CGNS	CFD General Notation System
CSV	Comma Separated Value
DEM	Discrete Element Method
DoE	Design of Experiments
DNS	Direct Numerical Simulation
EFG	Element Free Galerkin
EOS	Equation of State
ER	Cutting edge radius
FDM	Finite Difference Method
FEA	Finite Element Analysis
FEM	Finite Element Method

Short form	Description
FVM	Finite Volume Method
HPC	High Performance Cluster
HTC	Heat Transfer Coefficient
HT-CVD	High Temperature CVD
JC	Johnson-Cook
LES	Large Eddy Simulation
MT-CVD	Medium Temperature CVD
MC-SPG	Momentum-Consistent SPG
MBD	Multi Body Dynamics
NC	Numerical Control
ODE	Ordinary Differential Equation
O-to-O	Orthogonal-To-Oblique
PDE	Partial Differential Equations
PVD	Physical Vapour Deposition
PA-CVD	Plasma Activated CVD
RANS	Reynolds-Averaged Navier Stokes
SHPB	Split-Hopkinson Pressure Bar
SPG	Smooth Particle Galerkin
SPH	Smooth Particle Hydrodanamics
STL	Stereolithography
TP	Trim Points

1 Introduction

The constant change in industrial environment is a testament to time. A large variety in product portfolio to capture more markets internationally has been a trend in industry. New product ideas are required continuously to achieve this product variety. At many instances, these new product ideas require further development in materials and manufacturing processes. Due to ever changing products and a desire to use novel materials, the competitiveness within the industry depends increasingly on cost-effective and short planning cycles for manufacturing operations. This is particularly true for automotive industry. In addition to these technological and economical demands, automotive industries are increasingly facing political and global challenges in the area of energy, environment and mobility. In the past few years, automotive industry is going through a constant transformation, which has broadened the product portfolio of powertrain components and has reduced the product development cycle to the shortest timespan that ever existed in the powertrain area. Petrol and diesel engines have undergone downsizing in the past decade to cut down emissions. The idea behind this is to replace large engines with small engines, which have fewer cylinders with lower friction and heat losses, at the same time keeping the engine output constant. To accomplish this, engine combustion process has to be optimized and cylinders must be filled at higher level, which can be achieved through turbocharging of engine [1,2]. Since temperature of exhaust gases can be as high as 1050°C, very high demands are placed on thermo-mechanical properties of turbine housings [1,2,3]. To withstand such high exhaust gas temperatures, a novel material, 1.4837D, was developed by Mercedes-Benz AG. However, it brought its own challenges during the machining process. Low tool-life and high scrap rate were two of the major challenges in using the 1.4837D material in mass production. Thus, in this thesis work, one of the critical processes, namely inner contour turning process from turbine housing was selected for optimization. This process accounted for high scrap rate and tool costs.

The variety of products not only exist in the automotive industry but also in the tool manufacturing companies. Therefore, conventional optimization method of experimental trials could not be utilized in mass-production of turbine housing. Additionally, an optimization strategy was required that would not only be implemented for turbine housing but will also serve as a base for future components of automobiles, such as for electric vehicles. Thus, simulation methods were developed in this thesis work that can be used for any machining process regardless of whether a component is from conventional engine or electric vehicle.

Though simulation methods have been widely used in the past two decades for forming technology at mass production level in development, design and process optimization, it is not the case for machining technology. This is because of significantly more complex geometric and physical interactions during machining process as compared to forming process. Different simulation tools were developed and coupled in this thesis work to provide a digital strategy for machining process, which can also be implemented at mass production level. Initially, simulation results were compared to experimental results for simple workpiece geometry. Later, simulation tools were used to optimize the inner contour turning process from turbine housing with an aim to reduce the scrap rate and increase the tool-life.

2 State of the Art

This chapter describes the basics and state of the art relevant for this thesis. The three major topics of this thesis are explained below in detail to provide a better and deeper understanding.

2.1 Basics of machining process

According to DIN 8580 [4], manufacturing processes are divided into six main groups. Machining belongs to the third main group, cutting. During machining, layers of a material are mechanically separated from a workpiece in the form of chips by one or more cutting edges of a tool to achieve the desired shape and surface of the workpiece [4,5]. Machining is further subdivided in DIN 8589-0 into processes with geometrically defined and undefined cutting edges. Due to the defined number and position of cutting edges, turning, drilling, and milling are a part of machining with defined cutting edges. On the other hand, grinding, lapping and honing are the examples of undefined cutting edges [5]. Since this research work is on turning process, it will be further discussed in section 2.1.1.

2.1.1 Turning

Turning process is defined in DIN 8589-1 [6] as a machining process with geometrically defined cutting edges. In turning, a rotational cutting movement and an arbitrary transverse translational feed movement is realized through a relative movement between the workpiece and the tool. Turning can be further subdivided into large number of process variants whose respective definitions can be found in DIN 8589-1. Since an explanation of all the turning processes would go beyond the scope of this research work, only the longitudinal cylindrical turning and internal turning process are defined here.

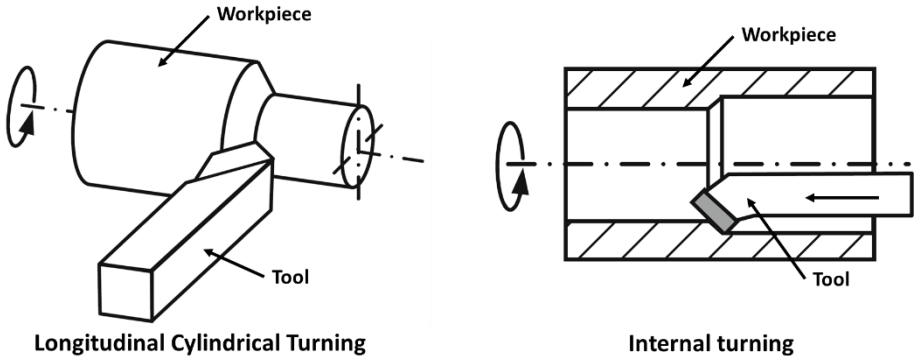

Figure 2-1: DIN-8589-1 reference [7]

To build a coaxial cylindrical surface to the axis of rotation of the workpiece, longitudinal cylindrical turning is utilized where the tool is provided a parallel feed to the axis of rotation as shown in Figure 2.1 (left side). It is one of the most common forms of turning processes that is used from finishing very small parts to roughing casted turbochargers [6, 7]. This process is basically an external machining process but can also be used as an internal machining process called internal turning, as shown in Figure 2.1 (right side), to produce deep contours or to increase the internal diameter of hole [6, 7].

2.1.2 Geometry of cutting part

The terms and designations to define the geometry of a cutting part are mentioned in DIN 6581 [8]. A cutting part is the active part of the tool where cutting wedges and cutting edges are located. The main components of cutting wedge, rake face and flank face, meet at a common point named cutting edge. The chip created on the cutting-edge slides over the rake face, while the flank face faces the new workpiece surface. Additionally, the cutting wedge is described by three angles: Clearance angle α_o , the angle between the flank face of the cutting wedge and the newly created workpiece surface; Wedge angle β_o, the angle between the flank face and the rake face; Rake angle γ_o, the angle between the plane perpendicular to the workpiece surface and the rake face. Figure 2.2 shows an ideal cutting wedge. In practice, however, tools are ideally not that sharp. Therefore, there is usually a curved transition between the rake and flank face, and this curvature is called the cutting edge radius r_β [7]. For the sake of simplicity, process kinematics are summarized at cutting point in vector form. The effective speed v_e can be decomposed into cutting speed v_c and feed velocity v_f.

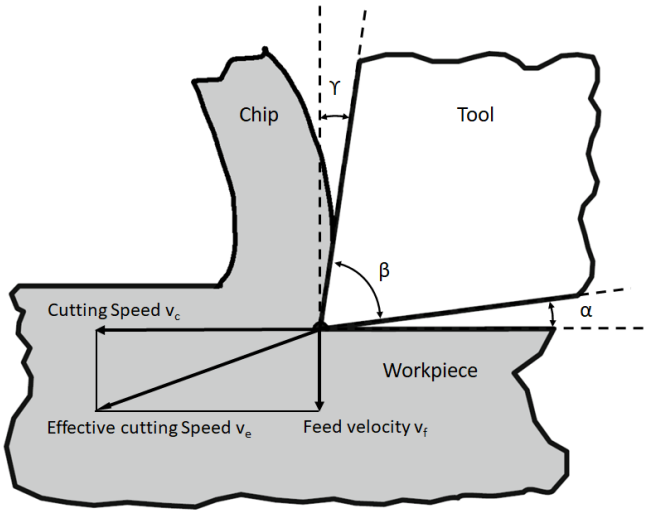

Figure 2-2: Idealized Cutting wedge [7]

2.1.3 Chip formation and chip form

Due to a relative motion between the tool and workpiece, the cutting edge of the tool penetrates the workpiece material, causing an elastic deformation, which results in plastic deformation. If the material-dependent shear stress exceeds the maximum limit, the workpiece material starts to slide over the rake face of the tool, hence creating a chip [7]. The chip form depends on various factors like workpiece material, cutting parameters, tool geometry etc. Based on these factors, four types of chip forms can be observed: continuous chip, lamellar chip, segmented chip, and discontinuous chip, as shown in Figure 2.3.

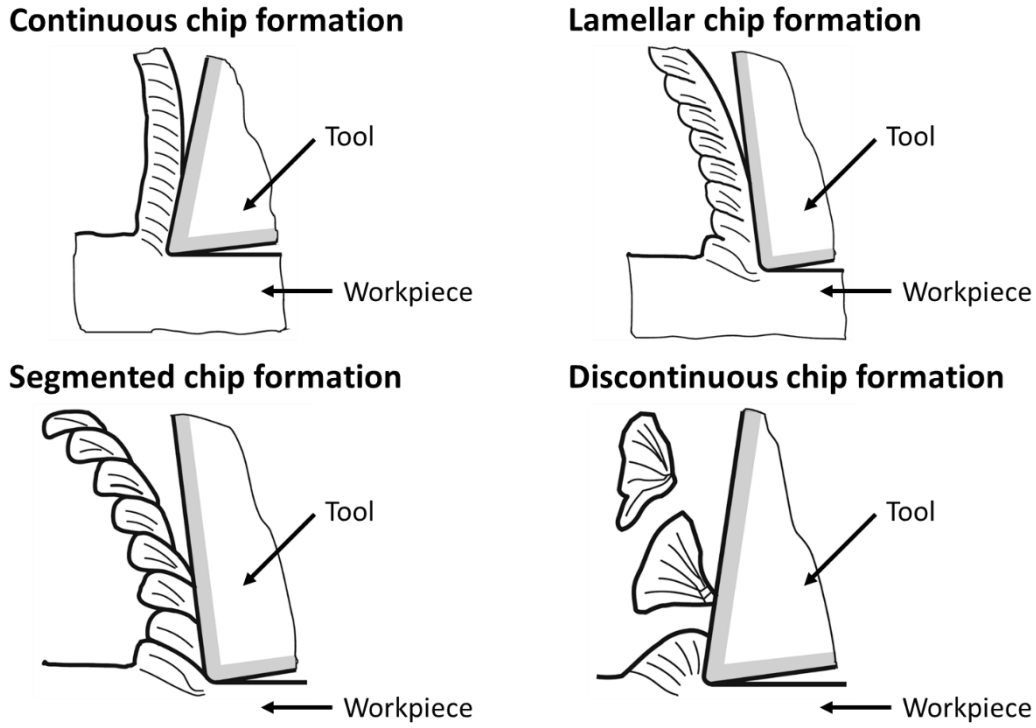

Figure 2-3: Types of chip formation [9]

It can be noted in Figure 2.4 that the major plastic deformation of the workpiece material happens in the primary shear zone around the shear plane due to the maximum specific shear stress τ_{max}. The angle between the shear plane and workpiece material surface is called the shear angle ϕ. In the secondary shear zone along flank and rake face, the material deforms due to friction, area 2 and 4 in Figure 2.4. In front of the cutting edge, a stagnation zone is formed because of a high pressure from all the sides, marked as area 3 in Figure 2.4. In the preliminary deformation zone, plastic deformation is minimal, and it has an influence on penetration depth of the workpiece [9, 10].

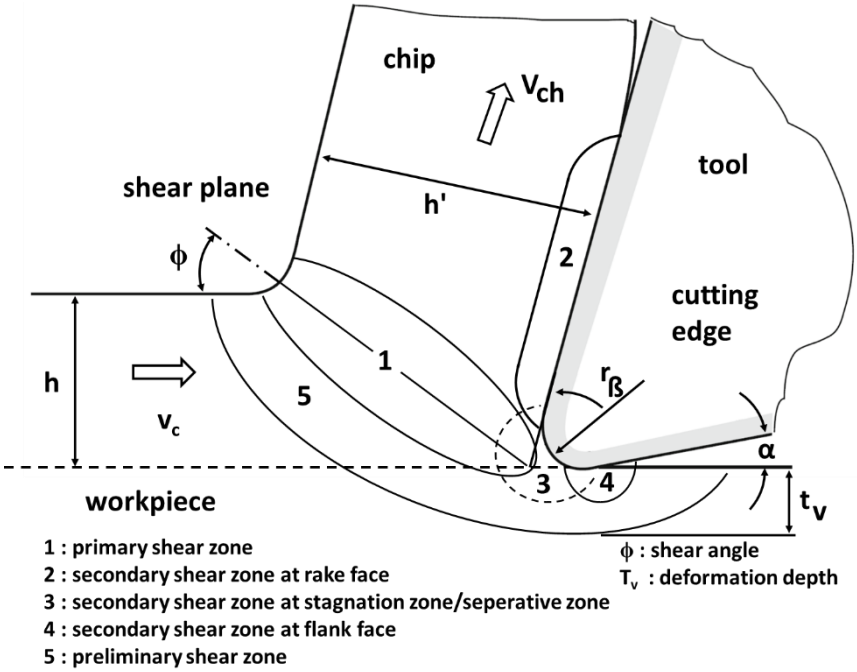

Figure 2-4: Zones in Chip formation according to Warnecke [9]

2.1.4 Cutting forces and temperature development

Cutting forces generated in the machining process are defined in DIN 6584. The resultant force F, as shown in Figure 2.5, can be decomposed into two components, active force F_a and passive force F_p. The active force is in the working plane and can be further divided into two force components, cutting force F_c and feed force F_f [11]. Generally, piezoelectric force sensors are used to measure passive, feed and cutting forces.

During machining, most of the mechanical work is converted into thermal energy. The chip generated due to the plastic deformation of the workpiece material slides over the rake face of tool, as shown in Figure 2.4, thus converting the frictional energy into heat. Due to this reason, the highest temperature during machining is observed at the contact zone, i.e., between the tool rake face and chip. Possible temperature fields during machining are shown in Figure 2.6 [7]. Determining the temperature generated during machining process has been a subject of research since many years. In the past, researchers have employed a variety of techniques, including radiation pyrometers, thermocouples, and many other for temperature measurement during machining process.

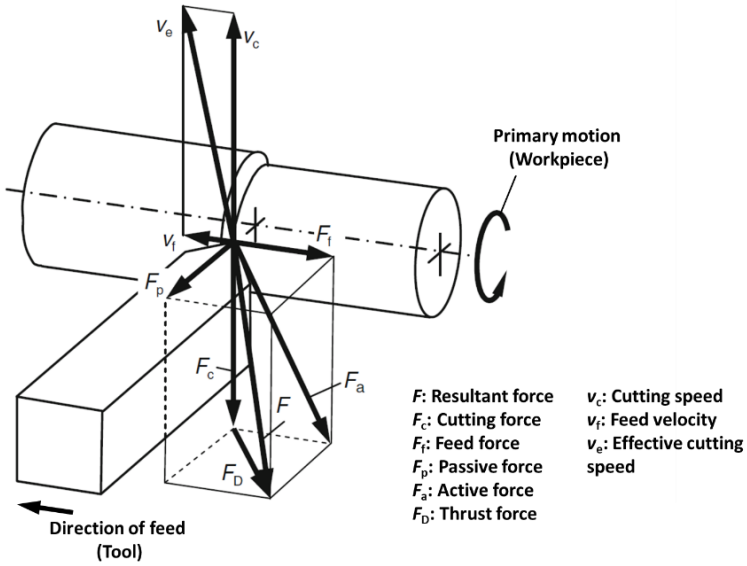

Figure 2-5: Resultant Force and its components according to DIN 6584 [11]

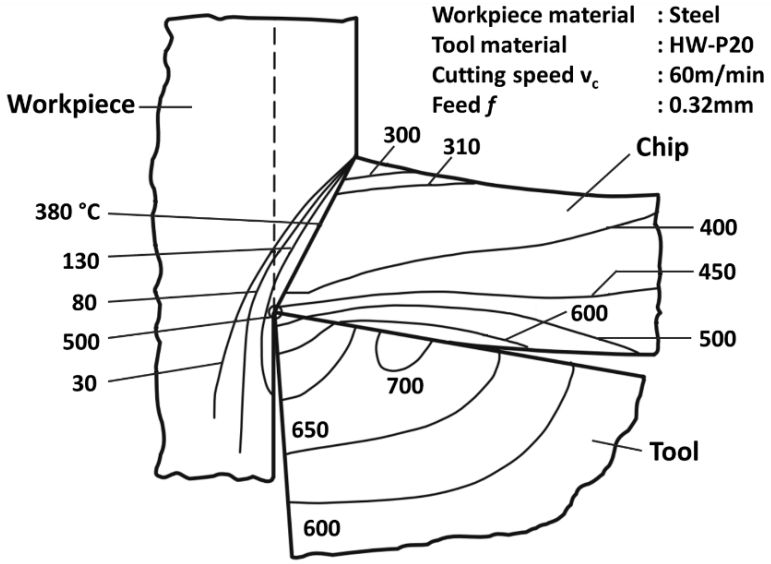

Figure 2-6: Temperature distribution in tool, workpiece and chip [7]

Despite numerous studies, temperature measurement during machining processes has been a constant area of investigation among the researchers over the years. According to Kronenberg, as shown in figure 2.7, tool temperature is about twice the mean chip temperature, depending on the cutting speed of tool [12]. This is because cutting tool is exposed to heat in a stationary manner [13].

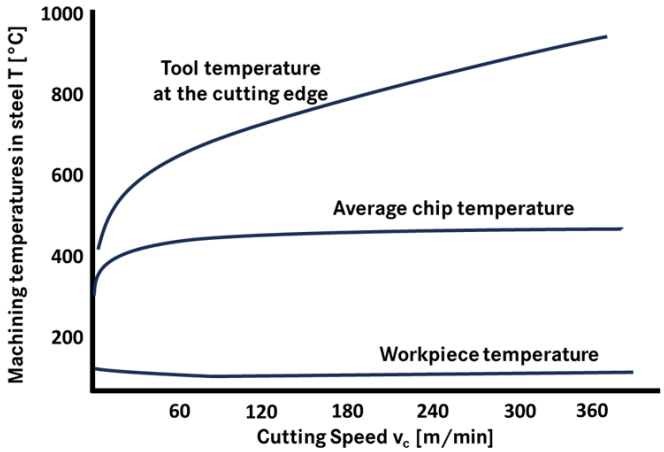

Figure 2-7: Temperature distribution during machining [12]

Thus, various measurement techniques like thermocouples, infrared camera, thermography and pyrometer have been used in the past by researchers for measuring temperatures of a tool. For different cutting velocities, Küsters [14] measured temperature inside the turning tool using thermocouples. It was concluded that the temperature distribution changes with change in rake angles due to a difference in contact conditions. Additionally, it was found that temperature during machining process also depends on the cutting speed. Arrazola et al. [15] analyzed the temperature distribution on chip, rake face and clearance face of tool using an infrared camera. During experiments, workpiece was prepared in a way that chip breaks off during the orthogonal turning. This exposed the chip surface, and the temperatures were measured by the infrared camera. They concluded that the maximum temperature in machining process occurs at the rake surface at some distance from the tool tip. Thakre and Nordgren [16] also used an infrared camera to measure the temperature in an orthogonal turning process and found that with an increase in cutting speed and wear, temperature also increases. Habermeier [17] in his research work used both, pyrometers and thermocouples, inside coated turning insert to measure temperature for 1.4837D material. It was found that with an increase in cutting speed and feed-rate, there was also an increase in temperature. While doing a direct comparison between thermocouple and pyrometer, it was deduced that thermocouple reacts much slower to changing temperatures, and contrastingly, pyrometer had a better reproducibility and response to change in temperature during machining. Müller [18] used a two-color pyrometer FIRE-1 in measuring temperature in orthogonal turning process. Pyrometer cable was placed inside the tool during the measurements. High temperature accuracy with an error below 5% was found in the measurements. Finally, it was concluded that a two-color pyrometer is well suited for temperature measurements due to its high time resolution and good repeatability.

2.1.5 Wear

During machining process, a tool is subjected to complex loads due to high compressive stresses and high temperatures generated at the tool-chip interface. These high stresses and temperatures are caused by plastic deformation of the material and friction between the tool and workpiece. Tools come to an end of their service lives due to an increase in wear on flank and rake face. Wear is basically the progressive loss of tool material due to the continuous contact and relative motion between the tool and workpiece. The major mechanisms that cause wear in machining process are abrasion, adhesion, surface disruption and tribochemical reactions [7]. Different wear mechanisms lead to different wear forms on the tool, for example flank wear, crater wear etc. Most important wear forms are shown in Figure 2.8 [9]. Flank wear is one of the most important wear forms and is used over time by various researchers to find a tool life.

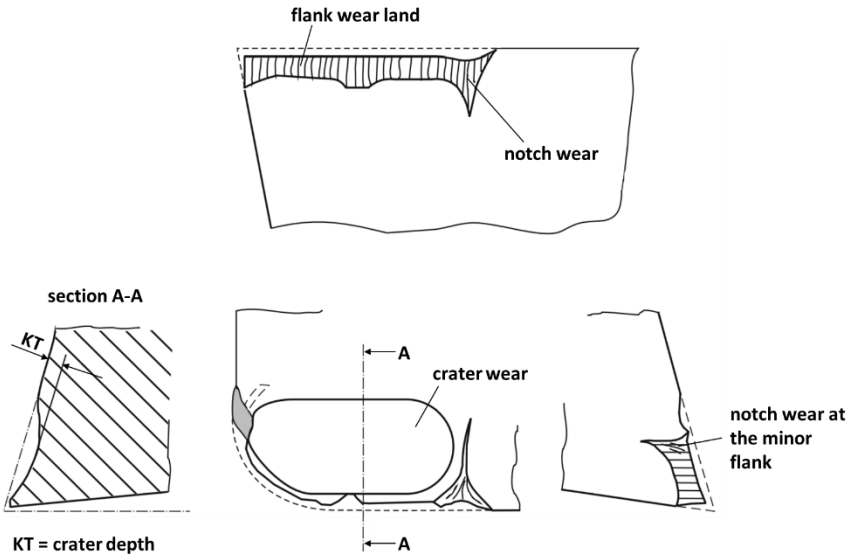

Figure 2-8: Wear forms in turning according to ISO 3685 [9]

2.2 Modelling techniques in machining process

A lot of research has been carried out in the field of metal cutting in the past 100 years to improve tools and tools' life. The traditional way of research in machining was based on an experimental approach. However, with the increase of computational power in the past decade, the focus has shifted towards digitalization. The reason for this shift is not only the advancement in computational power, but also the huge amount of time and resources required in the traditional approach for the optimization of machining process. For example, every year United States spends $300 billion in machining process research, which only includes the labor cost

and overhead cost [19]. In 1907, Taylor published his seminal work "On the Art of Cutting Metals" [20], where tool wear, and relation between cutting speed and tool life were summarized. Though earlier it was assumed that these experiments will last only 6 months, Taylor and his colleagues conducted around 30,000-50,000 recorded and many unrecorded experiments over a span of 26 years. They used more than 363,000 kg of work materials during this time [19]. To overcome the shortcomings of the traditional approach, researchers have used various modelling techniques which are briefly discussed below:

- **Empirical modelling:** In contrast to the theory where knowledge is acquired on the basis of physically justifiable laws, empirical research relies on the experience that is gained via acquisition of large amount of experimental data [21, 22, 23]. Taylor in his seminal work, "On the Art of Cutting Metals" [20], gave the first empirical cutting force model. Some other notable empirical models for the force calculation in machining are provided by Kienzle & Viktor [24, 25] and Kronenberg [26].
- **Analytical modelling:** This modelling approach is based on mathematical expressions which are usually derived from geometrical, mechanical, kinetic, and dynamic considerations [27]. Analytical models can be divided into two groups: shear plane models and shear zone models, as shown in Figure 2.9. In a shear plane model, the entire deformation during machining process happens in an infinitesimally narrow plane (shear plane) and the direction of material changes, which in turn forms a chip. On the other hand, in shear zone model, the deformation happens in an area or a relatively thick layer [27, 28]. Some of the notable analytical models are Merchant theory based on shear plane model [29, 30] and Oxley theory based on shear zone model [31].

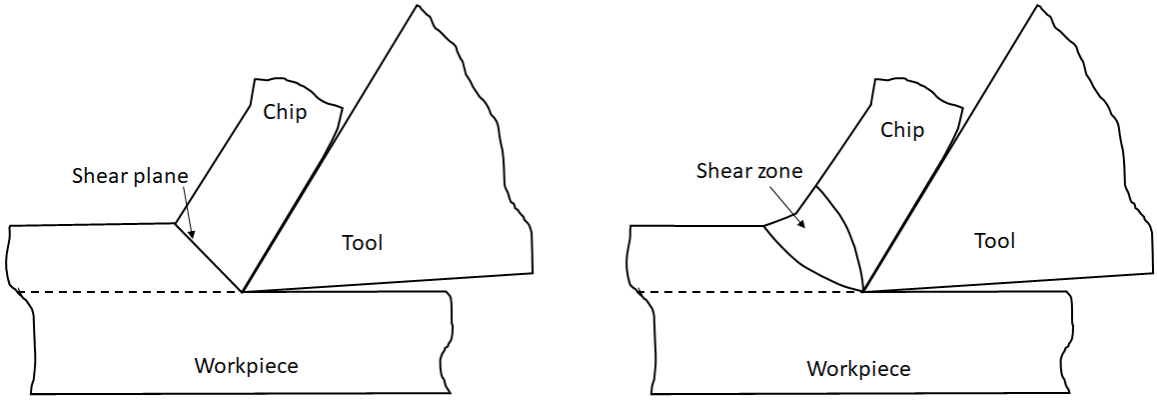

Figure 2-9: Analytical Modelling approach: Shear plane model (left) & Shear zone model (right)

- **Mechanistic modelling:** Machining process has many input variables like tool material, workpiece material, cutting parameters etc. Analytical models define machining process with mathematical formulas that are based on physical laws. One of the major advantages of these equations is that they are simple to solve. However, analytical models cannot represent various input variables and mechanisms with sufficient accuracy because of their complexity. Due to this reason, empirical models are still used by many researchers. The mechanistic modelling approach fundamentally combines the earlier mentioned modelling techniques, empirical and analytical. According to Altintas [10], the mechanistic approach describes the complete system, which includes tools, workpieces, and important machine components, using equations that characterize the machining process based on physical relationships and are expanded through empirical experiments.
- **Numerical modelling:** A few examples of numerical modelling techniques are Finite Element Method (FEM), Beam Element Method (BEM), and Computational Fluid Dynamics (CFD). The FEM method is primarily used to numerically model machining processes. Representation of non-linearities like tribological behavior in machining processes gives FEM an edge over other modelling techniques. Other modeling methods, on the other hand, are unable to model such non-linearity [28].
- **Artificial Intelligence:** Owing to the advancement in computational power, researchers have also studied the use of artificial intelligence in modelling various manufacturing processes. Artificial neural networks are one of the most powerful tools used for the same. These neural networks are similar to the biological neural networks. An artificial neuron receives a signal (input) in form of a numerical value, which is multiplied by a suitable weight w, and then an activation (threshold) function is applied to the weighted sum of the input value to get its output [32].

In the next three sub-sections, FEM, CFD and mechanistic modelling techniques will be discussed in detail as they are used in this thesis work.

2.2.1 Finite element method

FEM is the most common numerical modelling technique used in simulating machining process. In FEM, a large continuum is discretized into small finite elements that form a mesh. These elements are simple in geometry and could be easily analyzed as compared to the whole

structure. The elements are connected to each other via nodes, where the initial and boundary conditions are applied, and the degree of freedom is calculated. Between these nodes, problem variables are solved by interpolation. The problem variables and the properties applied to each element's nodes are assembled, and global relations are formatted. The discretization of the continuum can be done either with similar element types or by combining various element types, for example a three-node triangular element can be used along a four node quadrilateral element, if adjacent elements share nodes and no node is left unused, as shown in Figure 2.10 [33].

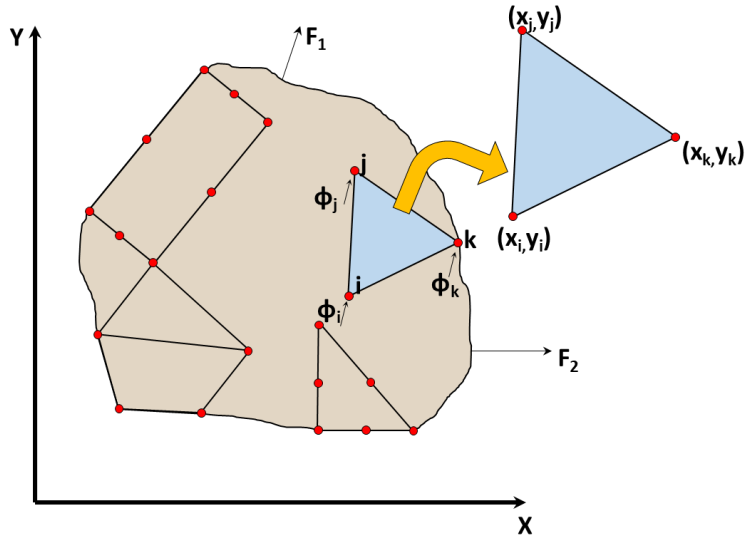

Figure 2-10: Discretization of a Continuum [33]

The discretization (also called as generation of mesh) of a continuum happens in the preprocessor of FEM software. The software preprocessor enables the users to create input files, which include material properties, boundary conditions, contact etc. and then this input file is submitted to the FEM-solver. The solver calculates the solution for the problem and results are stored in the form of output files. These output files are then analyzed by researchers in the postprocessor of FEM software. In the early 1970s, various researchers started creating their own FEM models for the simulation of machining process [33]. Initially most of the models were created by FEM codes that were made in house by the researchers. The growth in the usage of FEM in machining process is depicted in bibliography published by Mackerle [34, 35], where he cited all the 1047 papers from journals, conferences, and theses from 1976 to 2002, as shown in Figure 2.11. Ever since the advancements in the FEM saw a rise, many commercial Finite Element Analysis (FEA) software packages are available in the market, for example: ABAQUS, LS-DYNA, AdvantEdge, Deform etc. Some of these software packages serve

general purpose, such as ABAQUS and LS-DYNA, whereas others are purpose-specific software packages, like AdvantEdge for machining simulations.

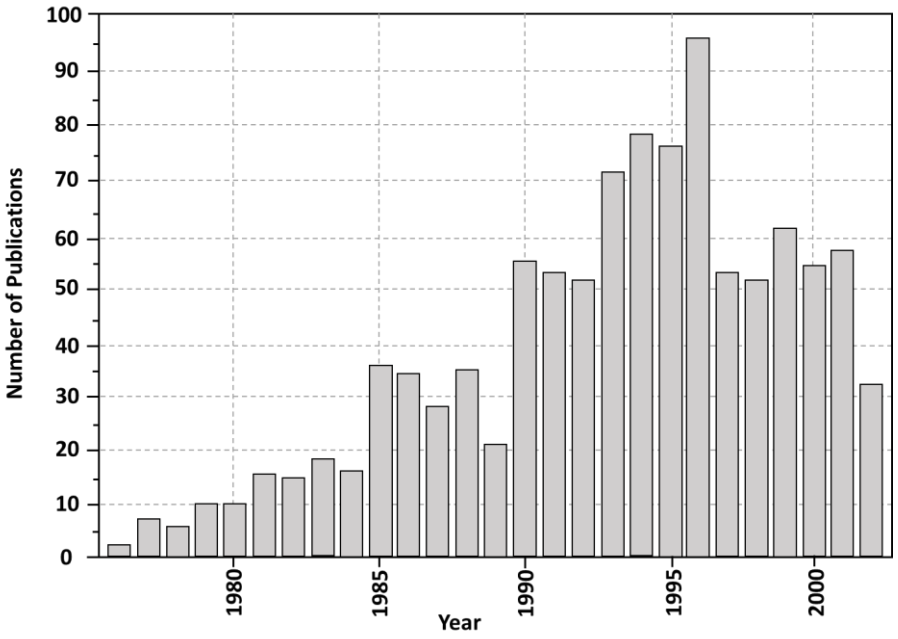

Figure 2-11: Number of publications per year on machining FEM models from 1976 to 2002 [33, 34, 35]

2.2.1.1 Time Integration

FEM is a method that uses a simple piecewise function valid within a small finite element to approximate complicated functions of spatial dimensions. In case of a perfect plastic material for a quasi-static loading, stiffness force is dominating, and the system equation can be written as [36]

$$[K]\{u\} = \{f\} \qquad 2.1$$

Where [K] is the stiffness matrix, u is the displacement of nodes and f is forces on those nodes.

The two main methods for solving the basic equation 2.1 are:

- Implicit Time Integration Method
- Explicit Time Integration Method

Implicit Method: It is an iterative method and, in this method, the desired output variable on a grid point (node) at time t+1 depends not only on time t but also on t+1 [7]. The equation of system can be written as

$$[K]\{u\} = \{F^{out}\} + \{F^{body}\} + \{F^{inert}\} \quad 2.2$$

Where [K] is the stiffness matrix, u is the displacement, F^{out} is equivalent external forces, F^{body} represents body forces and F^{inert} is the interia force.

The major advantage of implicit method is that large time steps can be made while calculating the solution. However, this is only possible if the problem is linear. In case of a non-linear behavior of system, due to elastic-plastic material behavior or contact between the bodies, larger time steps are not possible [37].

Explicit Method: In this method, the desired output variable on a grid point at time t+1 is determined solely from the values available at time t, with the help of center difference scheme [7]. The equation of motion for linear behavior leads to following linear ordinary differential equation (ODE) [37, 38]:

$$[M]\{\ddot{u}\} + [C]\{\dot{u}\} + [K]\{u\} = \{F\} \quad 2.3$$

Where [M] is the mass matrix, [C] is the damping matrix, [K] is the stiffness matrix, F are forces, u is the displacement, $\dot{u}$ is the velocity vector and $\ddot{u}$ is the acceleration vector.

For the convergence of solution, the time step size is bounded in an explicit method, i.e., the method is stable if the time step Δt is smaller than the time taken by an elastic wave to travel through the shortest element edge. In other words, the possible length of time step is a function of sonic velocity C existing in material [7, 36, 37]. For solid materials it can be written as in equation 2.4 below:

$$C = \sqrt{\frac{Y}{\rho}} \quad 2.4$$

Where Y is the elastic modulus and ρ is the density of material.

2.2.1.2 Element Formulation

In FEM, the spatial discretization of continuum is carried out by breaking it down into several small elements and solving the partial differential equations. The solution is then approximated with locally limited approach functions. In many formulations, the displacement of a point in space is taken to be primary unknown. [39]. Several element formulations are available in various FEM-software. These formulations can be divided into two types: Mesh based and Mesh-free formulations. Some of the commonly used mesh-based formulations like lagrangian and mesh free formulations like smooth particle hydrodynamics are defined in detail below.

Lagrangian formulation: This formulation is the most common numerical simulation method and is widely used in many engineering applications. In this formulation, mesh is attached to the workpiece, or in other words, nodes and elements deform with the workpiece as shown below in Figure 2.12 [39].

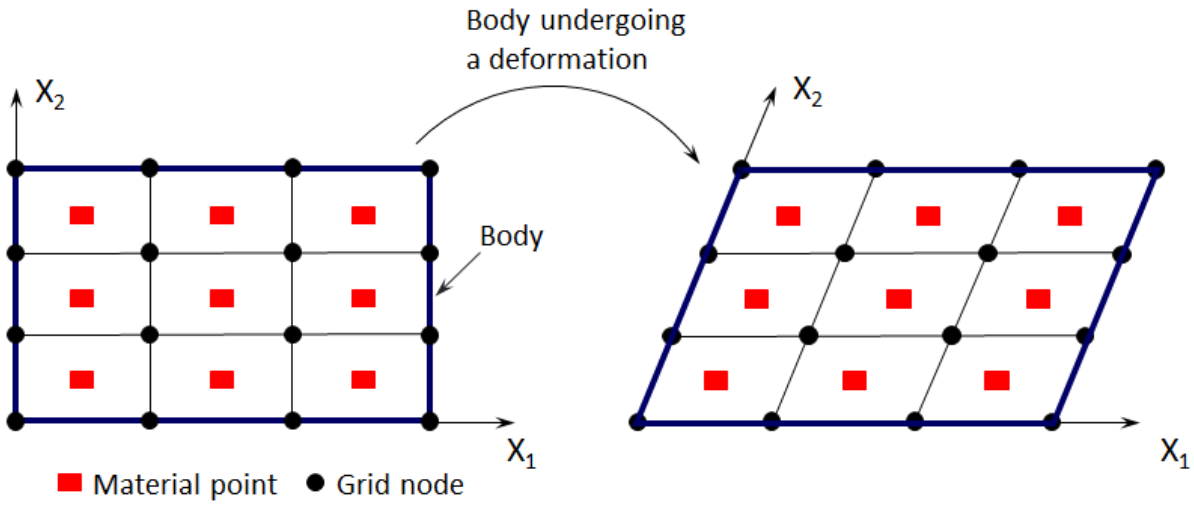

Figure 2-12: Lagrangian Formulation [39]

One of the major advantages of this formulation is that the history of state of material at each element is completely known and small deformations can be described with high accuracy [39]. However, a major disadvantage of this formulation is visible in case of severe mesh distortion problems, for example in case of chip formation during machining. Severe mesh distortions can cause the mesh to be ill-conditioned, leading to mesh entanglement, which further leads to decreasing stable time steps. In such scenarios, remeshing criterion or erosion mechanism is necessary to further continue with solution [39]. The remeshing criterion is discussed in detail in section 2.2.1.3. This formulation has been used in this research work for FEM-simulations with the AdvantEdge software.

Eulerian formulation: This formulation is mostly used for fluid dynamics problems. In Eulerian formulation, the grid point (nodes) and elements are spatially fixed, i.e., material flows through stationary mesh as shown in Figure 2.13. The major advantage of this formulation is that the mesh is spatially stationary, thus eliminating the probable numerical difficulties due to mesh distortions. Remeshing is, hence, not required in case of a problem with large distortions. One must keep in mind, though, that in Eulerian formulation, a larger mesh region is needed to model existing areas, as well as any areas where material might flow in future, causing the numerical simulation to take more computational time. Another disadvantage of Eulerian

formulation is that the user must know prior to simulation where the material may/could flow [39].

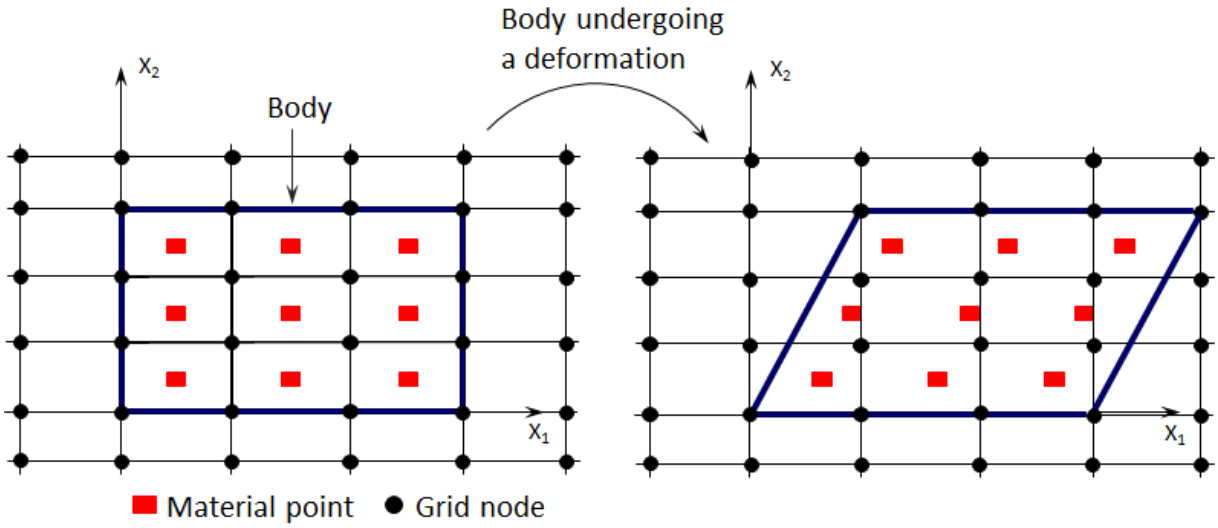

Figure 2-13: Eulerian Formulation [39]

Arbitrary Lagrange-Euler (ALE) formulation: As discussed above, both Lagrangian and Eulerian formulations have their own advantages and disadvantages. As the name suggests, ALE uses positives of both the formulations. The Lagrangian time step in this formulation is followed by an "advection" or "remap" step. The advection step executes an incremental rezone, where "incremental" could be explained as movement of the nodes' positions by only a small characteristic length of the nearby elements. However, like Lagrangian formulation, a manual rezoning is also possible in ALE [38].

Smooth particle Hydrodynamics (SPH) formulation: SPH formulation is an N-body integration scheme developed in 1977 [40, 41] with an aim to study astrophysical phenomena. It is a particle based, i.e., meshless langrangian method which has been in practice for years for simulating multiple problems in fluid flows, solid deformation, fluid-structure interaction, and heat transfer. While the mesh-based FEM needs connected nodes to construct spatial derivatives, SPH consists of a set of individual particles which poses individual material properties and move according to governing conservation equations [42, 43, 44]. The following literature [42, 43, 44] gives a mathematical overview of SPH method. The property that the particles are disconnected in SPH method affects the stability of a numerical solution. Figure 2.14 illustrates a set of particles interacting with each other.

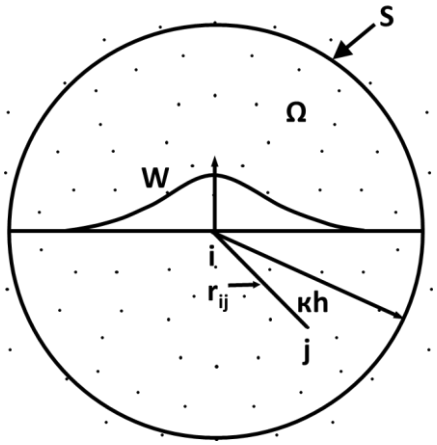

Figure 2-14: SPH Formulation- Illustration of a particle approximation [43]

Each of the two particles, *i* and *j*, interact with each other at a distance κh, called smoothening length. W, the smoothening function, weighs interaction and determines approximation scheme of the function. It also depicts accuracy of the kernel and particle approximation. This principle implies that if the values of surrounding particles are known, the value or derivative of a continuous function can be approximated for each particle. This formulation has been used in this research work for coupled FEM-CFD-simulations of flood lubrication with the LS-DYNA software. The particle approximation in LS-DYNA software is given by the following equation [38]:

$$\Pi^{\kappa h} f(x) = \int f(y)\, \mathrm{W}(x - y, \kappa h) dy \qquad 2.5$$

Where W is the smoothening function, and this function is defined using the function θ by the following equation:

$$\mathrm{W}(x, \kappa h) = \frac{1}{\kappa h(x)^d}\, \theta(x) \qquad 2.6$$

Where d is the number of space dimensions.

Smooth Particle Galerkin (SPG) formulation: SPG is a mesh free method (similar to SPH) which was developed by Wu et al. [45] to analyse deformation and failure in solid-state mechanics. Currently, this formulation can be only implemented in LS-DYNA software. According to Wu et al. [46], this method is useful for impact and penetration simulations with material failure. Partial differential equations of a linear elastic problem could be solved with this method, which is based on mesh-free Galerkin approach. Equation 2.7 depicts how SPG uses a direct node integration method to calculate the field variables and their derivatives at the same point [45, 46].

$$M^{lump} \text{ x } \ddot{U} = F_{ext} - F_{int} \quad 2.7$$

M^{lump} depicts the lumped mass matrix in diagonal form, $\ddot{U}$ depicts the vector that contains all particle accelerations. F_{ext} depicts the external force vector and F_{int} depicts the regulated internal force term [47].

The above-mentioned equation, when solved, could produce spurious-energy modes in the displacement field. Thus, an additional non-residual stabilization term F_{stab} is required in the SPG formulation to avoid these modes and to have stabilization effect. Integrating this stabilization term alone would mean extra computing effort. Hence, the new equation is represented as equation 2.8 [45, 47].

$$M^{lump} \text{ x } \ddot{U} = F_{ext} - F_{int} - F_{stab} \quad 2.8$$

Since no momentum equation residual is needed in stabilizing the SPG methods, they belong to non-residual stabilization methods. Numerous integration points that match at each particle are required for integration of non-residual stabilization terms. This process is computationally inefficient. To get past these obstacles, a new type of particle stabilization method named Momentum-Consistent SPG (MC-SPG) was developed. Unlike other particle stabilization methods, smoothening is not based on residual or non-residual stabilization terms in MC-SPG. This prevents modification of system of equation, requiring just one integration point per particle [48]. MC-SPG uses a second-order pulse consistent velocity smoothing algorithm, designed for stable and accurate results in thermal structural coupling applications. This new smoothing algorithm removes stabilization term of discrete equation, leading to a system of equations in the form shown in equation 2.7 [47]. This formulation has been used in this research work for FEM-simulations in the LS-DYNA software. There are further various element formulation methods like Coupled-Eulerian Lagrangian (CEL), Element Free Galerkin (EFG), Discrete Element Method (DEM) etc. However, an explanation of all these formulations will go out of the scope of this research work.

So far, various element formulations that have been widely used by researchers over the years for the machining process simulations were discussed. Choice of element formulation becomes important as each one of them has its own advantages and disadvantages during the machining simulations. A brief literature review relevant to this research work on previously mentioned element formulations and their results is provided below.

Tay et al. [49] were one of the early researchers to simulate the temperature in an orthogonal turning process. Predicted temperature results were sufficiently in agreement with the measured temperature in their work. They also emphasized on the importance of using temperature-dependent material properties (stress-strain) in simulations for more accurate predictions.

Strenkowski et al. [50, 51] conducted orthogonal turning simulations using Eulerian formulation to predict the forces, temperature and chip geometry for different aluminum alloys. They compared the simulated results with experimental measurements and found a good correlation for both, lubricated as well as unlubricated conditions.

Childs and Maekawa [52] developed an Eulerian FEM model for a low alloy steel material in an orthogonal turning process. The focus of this research was to predict the forces, temperature and machinability of the material. They found a good agreement between the simulated and experimentally measured thrust force, but a poor agreement between the cutting forces. The simulated cutting forces were approximately twice as large as experimentally measured forces. The predicted temperatures were in range of 800°C and 1000°C. However, there were no experimentally measured temperatures to compare the predicted results.

Marusich and Ortiz [53] created an orthogonal high speed machining simulation of 34CrNiMo6 steel using lagrangian formulation. They used continuous remeshing and adaptive meshing to overcome the difficulty of mesh distortion in Lagrangian formulation. Simulations were conducted for three different cutting velocities. The model accurately depicted the observed change from continuous chips to segmented chips with an increase in cutting speed.

Ceretti et al. [54, 55] simulated the orthogonal turning process with lagrangian formulation in the Deform 2D software. For material C45, they studied the effect of cutting speed, rake angle and depth of cut on simulation results namely forces, temperature and chip shape. The simulated force results were in good correlation with the experimental results, with a deviation of 10%. For simulated chip shape, serrated or continuous, they concluded that the choice of damage model and its critical value is important.

Özel and Altan [56] developed a lagrangian FEM model in the Deform 2D software for mold steel to predict the flow stresses and friction in orthogonal turning process. In their methodology, they compared the simulated forces against the experimentally measured forces to update the input flow stress and friction model. They implemented this methodology for various cutting velocities and feed rates.

In another model, Özel and Altan [57] simulated the end milling process as a two-dimensional orthogonal turning using lagrangian formulation to predict the forces, temperature, stresses and chip flow in the Deform software. The predicted forces were in reasonable agreement when compared with measured forces. The highest tool temperature in each case was above 1000°C and was recorded on the rake face. The highest tool stresses were predicted at the secondary cutting edge around the nose radius.

Klocke et al. [58] simulated orthogonal turning for C45 material in Deform 2D using lagrangian formulation. They used El Magd and Treppmann material model [59] and used a separate program "MESHMAN" for remeshing. They found a good comparison between predicted forces and measured forces. However, in simulations, they could only simulate continuous chip and it was due to the material parameters used in simulations.

Özel [60] formed an orthogonal turning simulation with lagrangian formulation in Deform 2D to study the influence of friction models in simulation results. He concluded that friction has an influence on predicted results.

Grzesik [61] developed an orthogonal turning simulation with explicit lagrangian formulation in the AdvantEdge software for material C45 steel. The focus of the research work was to simulate four different tool cases: uncoated tool, single layer coating (TiC), two-layer coating (TiC/TiN) and three-layer coating ($TiC/TiN/Al_2O_3$) and compare the simulated temperature results with measured results. Good temperature correlation was found between simulation and experiments for uncoated and trilayer coated tool.

Kumar et al. [62] developed a 3D turning simulation model in the Deform software to study the effect of AlTiN coating in machining of 100Cr6 steel with the ceramic tool. Focus of their research work was to compare the simulated temperature results with the experimental results for different cutting velocities in both, coated and uncoated case. They found a good agreement between predicted and experimentally measured forces. Additionally, they concluded that AlTiN coating had a lower temperature on tool when compared to uncoated tool in both, simulations and experiments.

Kumar et al. [63] simulated an orthogonal turning simulation for C45 material in the Deform software using the implicit lagrangian formulation. Three-layer coated ($TiC/TiN/Al_2O_3$) tungsten carbide tool was used in the simulation to predict the temperature in simulations. For various simulated feed rates, they found an excellent agreement between the simulated and experimentally measured temperature results (maximum error below 5%).

Nilsson et al. [64] developed one of the first orthogonal cutting simulation using ALE formulation in the Exhale2D software, where they created a continuous chip during simulations. However, a comparison of simulations with experiments was not mentioned in their research work.

Movahhedy et al. [65, 66] studied the influence of different cutting speed and different chamfer angles in orthogonal turning of steel material using ALE formulation. They used this method to combine the advantages of both, lagrangian and eulerian formulations. They found that chamfer angle does not affect the chip removal process. However, it significantly influences the thrust force; with an increase in chamfer angle, thrust force also increases. In the end, they concluded that the simulation results were in reasonable agreement with the experimental results.

Madhavan and Adibi-Sedeh [67] developed a thermo-mechanical ALE model of orthogonal turning process in the ABAQUS software. In their analysis, they focused on cutting forces, chip thickness, contact length and strain. The cutting forces and shear angle from Oxley's analytical machining model were compared with the cutting forces and shear angle from FEA model and a good correlation was found between them. However, maximum strain rate and thickness of secondary shear zone predicted from Oxley's model was different from the simulated results.

Nasr et al. [68] created a time-efficient approach to simulate the machining induced residual stresses in orthogonal turning for four different steels (X40CrMoV5-1, X2CrNiMo18-14-3, 100Cr6 & 34CrNiMo6) in the ABAQUS software using ALE formulation. The major advantage of this approach was that it cut down the simulation time from order of days to minutes, and the method was implemented for both, implicit and explicit time integration. In the end, a good correlation between the simulated and experimental results was recorded.

Özel and Arrazola [69] used the ALE formulation in the ABAQUS software to study the influence of different friction models in orthogonal turning. They found that the friction models have a higher impact on thrust forces than cutting forces.

Krajinović et al. [70] simulated milling process as a two-dimensional orthogonal process using the ALE-formulation in the ABAQUS software. They investigated three different coatings and simulated forces and temperatures, where they found that coatings have a negligible influence on cutting forces, and coating with lower thermal conductivity serve as a thermal shield.

Orthogonal cutting simulations were carried out and compared with the results of experiments by Limido et al. [71, 72]. According to them, the SPH approach can accurately simulate the machining forces.

Olleak et al. [73, 74] presented a 3D model where simulation of an external longitudinal turning process for Ti6Al4V titanium alloy was developed using the coupled SPH-FEM method. They concentrated on examining the impact of various equations of state (Gruneisen and Linear polynomial function) on force components and found no significant influence, except somewhat increased force values from the Gruneisen equation of state. Instead, they discovered that the friction coefficient's value has a substantial impact and that further research in the behavior of friction in contact is necessary.

Heisel et al. [75] used the SPH method to simulate orthogonal turning process of C45 steel, placing their focus on predicting cutting forces and chip compression ratio for different initial particle density of SPH particles and timestep increase coefficient. They concluded that initial particle density and timestep increase coefficient equally influence the cutting simulation results as material or friction parameters. They found that acceptable computational time and accuracy can be achieved by using three particles along the undeformed chip thickness.

Lampropoulos et al. [76] focused their simulation research work on understanding the influence of different SPH formulations, namely standard and renormalized, on simulated cutting forces for Ti6Al4V material. For simulations, particle diameters were set at d_o=0.01mm for both formulations and an additional particle diameter of d_o=0.005mm was defined for renormalized formulation. The simulated forces and chips significantly deviated from the measured ones when the usual SPH formulation was used. However, the renormalized formulation produced chips and forces that were extremely close to the outcomes of the experiments.

Using SPG approach, Boldyrev et al. [77] simulated the orthogonal cutting of the aluminum alloy (AI6061-T6). They observed that the qualitative convergence of forces was consistent with the experimental results.

Huang et al. [78, 79, 80] also used SPG approach to simulate self-piercing rivets, and they discovered that the results of the simulations and experiments were reasonably consistent. A thorough sensitivity analysis was carried out but a comparison of simulated and experimental forces was not performed. They found that the selection of kernel update interval, critical plastic strain, particle spacing, dilation parameters, and mass-scaling factor has no appreciable influence on the simulations' force results. Application of the SPG approach to grinding process

simulations by Wu et al. [79] led to a good match between simulation and experiment for reaction forces. The comparison of chip shapes shows that both simulation and experiment produce discontinuous chips. They also discovered that the kernel update interval, particle distance, and dilation parameter refinements have little to no impact on force values [79, 80].

The suitability of the SPG approach for punching simulation was explored by Casellas et al. [81]. They discovered that the SPG approach comes close to the experimentally measured punching force. However, the quick loss of forces in case of actual material failure can only be partially depicted.

Liu et al. [82] used SPG method in a high-speed rotating cutting instrument to remove blood clots. A difference between 3 to 20 percent was found between the experimentally measured and simulated cutting force. Both, in experiment and simulation, the feed forces were quite small.

SPG modeling was used by Pan et al. [83] to simulate the friction drilling process. They found an excellent correlation between experimental results and simulated temperature, torque and feed force. On the other hand, the simulation forecasts, as compared to experimental measurements, were very low when using FEM.

2.2.1.3 Mesh for solid structures

A good quality of mesh is an important factor in the accuracy of the results that a FEM-model will produce. Mesh must be capable of representing the workpiece accurately and handling the analysis. Both structured and unstructured mesh are used by researchers for discretization of the continuum. The simulation accuracy is affected by size, number and type of elements used in a mesh. Though the accuracy of a solution could be increased by using a large number of small elements, it will lead to longer computational times. Beyond a certain threshold, further increasing the number of elements will significantly increase the time of analysis with only a marginal increase in accuracy. In machining, the plastic deformation of the material happens in the primary and secondary deformation zones (Section 2.1.3), thus a fine mesh is used in these regions to obtain accurate results. Figure 2.15 shows an example of finer mesh discretization in the above-mentioned regions for the orthogonal turning simulations [33].

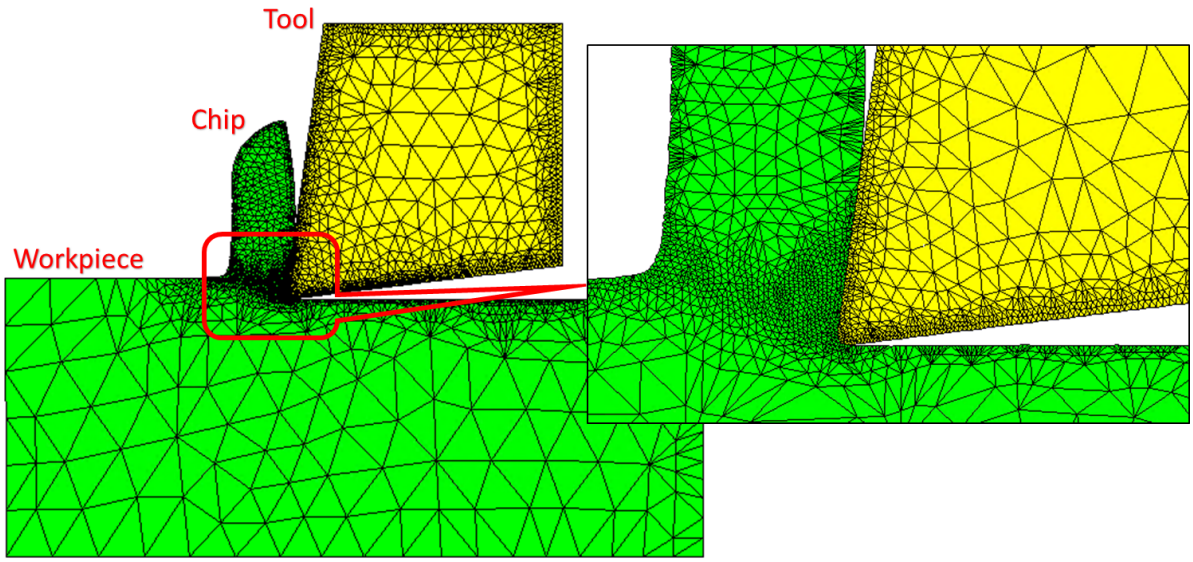

Figure 2-15: Mesh discretization (as an example)

As discussed above, lagrangian formulation cannot handle large mesh deformations. The distorted mesh may lead to numerical errors or even divergence of solution. This could be avoided by using a remeshing technique, where the existing distorted mesh is substituted by a new mesh, which in turn increases the number of elements in the concerned area by reducing the mesh size. This will improve the accuracy of solution but will also increase the computational time [33]. Niesłony et al. [84] studied the influence of tool mesh size for a 3D-turning simulation in the AdvantEdge software. They studied different mesh parameters (minimum tool element, mesh grading and segments per edge) and found that mesh size has a huge impact on simulation time; with fine mesh (number of triangles = 70,666) the simulation time was 4 times higher than with coarse mesh (number of triangles = 14,922). Finally, it was concluded that the mesh parameters have an influence on simulated forces, heat flux, and temperature. Ambati and Yuan [85] studied the dependency of orthogonal turning simulation results on mesh size in ABAQUS. They found that the cutting forces in simulations are insensitive to the mesh size. However, mesh size has a huge impact on chip morphology, with coarse mesh resulting in continuous chips, while fine mesh producing segmented chips.

2.2.1.4 Material Model

Workpiece material is subjected to a high level of strain, strain rate and heat during the machining process. This can significantly influence the flow stress of material. Jaspers et al. [86] conducted orthogonal tests to determine the strain, strain rate and temperature of C45 and aluminum AA6082-T6 material in primary shear zone, which were in the range of 1 to 2,

$2 \times 10^4 s^{-1}$ and 290°C (for steel) & 190°C (for aluminum) respectively. Several material models have been developed by researchers to determine the flow stresses and are used in modelling of machining process. Some of the commonly used material models are Johnson Cook material model, Power law model, Zerilli-Armstrong model, Usui model etc. In this research work, Power law model (in the AdvantEdge software) and Johnson-Cook model (in the LS-DYNA software) have been used. Hence, only these two material models will be discussed further in detail in this section.

Power Law model: The Power law model has three components: strain hardening, thermal softening and strain rate sensitivity. It is written as:

$$\sigma(\varepsilon^p, \dot{\varepsilon}, T) = g(\varepsilon^p) \times \Gamma(\dot{\varepsilon}) \times \Theta(T) \quad 2.9$$

where, σ is the flow stress, $g(\varepsilon^p)$ is the strain hardening, ε^p is the plastic strain, $\Gamma(\dot{\varepsilon})$ is the strain rate sensitivity, $\dot{\varepsilon}$ is the strain rate, $\Theta(T)$ is the thermal softening and T is the temperature [53,87]. All the three terms from equation 2.9 are further explained below.

$$g(\varepsilon^p) = \sigma_0 \left(1 + \frac{\varepsilon^p}{\varepsilon_0^p}\right)^{\frac{1}{n}}, if\ \varepsilon^p < \varepsilon_{cut}^p \quad 2.10$$

$$g(\varepsilon^p) = \sigma_0 \left(1 + \frac{\varepsilon_{cut}^p}{\varepsilon_0^p}\right)^{\frac{1}{n}}, if\ \varepsilon^p \geq \varepsilon_{cut}^p \quad 2.11$$

$$\Theta(T) = c_0 + c_1 T_1 + c_2 T_2 + c_3 T_3 + c_4 T_4 + c_5 T_5, if\ T < T_{cut} \quad 2.12$$

$$\Theta(T) = \Theta(T_{cut}) \left(1 + \frac{T - T_{cut}}{T_{melt} - T_{cut}}\right), if\ T \geq T_{cut} \quad 2.13$$

$$\Gamma(\dot{\varepsilon}) = \left(1 + \frac{\dot{\varepsilon}}{\dot{\varepsilon}_o}\right)^{\frac{1}{m_1}}, if\ \dot{\varepsilon} < \dot{\varepsilon}_t \quad 2.14$$

$$\Gamma(\dot{\varepsilon}) = \left(1 + \frac{\dot{\varepsilon}}{\dot{\varepsilon}_o}\right)^{\frac{1}{m_2}} \left(1 + \frac{\dot{\varepsilon}_t}{\dot{\varepsilon}_o}\right)^{\frac{1}{m_1} - \frac{1}{m_2}}, if\ \dot{\varepsilon} \geq \dot{\varepsilon}_t \quad 2.15$$

where, σ_o is the initial yield stress, ε_0^p is the reference plastic strain, ε_{cut}^p is the cut off strain and 1/n is the strain hardening exponent, c_o through c_5 are coefficients for the polynomial fit, T is the temperature, T_{cut} is the linear cut off temperature, T_{melt} is the melting temperature, $\dot{\varepsilon}_o$ is the reference plastic strain rate, $\dot{\varepsilon}_t$ is the strain rate where the transition between low and high strain rate sensitivity occurs, m_1 is the low strain rate sensitivity coefficient and m_2 is the high strain

rate sensitivity coefficient. Additionally, some other thermal and mechanical properties are also required in the material card, namely density, poisson's ration, young's modulus, specific heat, and thermal conductivity [53, 87].

Johnson-Cook model: This material model is typically employed when the strain rate varies over a wide range and the material softens as a result of plastic heating as the temperature rises [88]. This is the most commonly used material model in literature for machining process simulations. Like the Power law model, Johnson-Cook model also has three components, strain hardening, strain rate sensitivity and thermal softening. The strain hardening term represents elastic-plastic term, the strain rate sensitivity represents viscosity term and the thermal softening represents thermal effects. It is written as following [89, 90]:

$$\sigma = [A + B\,\varepsilon^{n}]\left[1 + C\,\ln\left(\frac{\dot{\varepsilon}}{\dot{\varepsilon}_o}\right)\right]\left[1 - \left(\frac{T - T_r}{T_m - T_r}\right)^{m}\right] \qquad 2.16$$

Where, A, B, C, n and m are material constants and need to be determined experimentally, σ is the flow stress, ε is the strain, $\dot{\varepsilon}$ is the strain rate, $\dot{\varepsilon}_o$is the reference strain rate, T is the Temperature, T_r is reference temperature, T_m is melting temperature.

As previously indicated, the simulations were conducted using the Johnson-Cook material model in LS-DYNA. While using the Johnson-Cook model with solid elements in LS-DYNA, an equation of state (EOS) is required. 18 different equation of state models are available in the software and this research work uses one of them, Linear polynomial equation of state. An equation of state is a mathematical description of the material behaviour for given initial conditions. The hydrostatic pressure in Linear EOS is described by the following equation [88]:

$$P = C_0 + C_1\mu_1' + C_2(\mu_1')^2 + C_3(\mu_1')^3 + (C_4 + C_5\mu_1' + C_6(\mu_1')^2)E \qquad 2.17$$

Where, P is the hydrostatic pressure, E is the internal energy, C_0 to C_6 are user defined constants and μ_1' is the volumetric parameter.

Different material models were chosen for workpiece in AdvantEdge and LS-DYNA software. Johnson-Cook model is the most commonly used material model for machining process and hence it was used in the LS-DYNA software. Since this material model was not available in the AdvantEdge software during the time of this thesis work, its default material model, Power law model, was recommended by their software support and was therefore used here. It must be noted that both the material models are quite similar to each other and their material constants are derived from flow stress measurements from the Split-Hopkinson Pressure Bar (SHPB) test.

Pervaiz et al. [91] simulated orthogonal turning process for Ti6Al4V material and compared the Power law model with Johnson-Cook material model. It was observed that Power law model based cutting simulation provided realistic chip formation, tangential and cutting forces.

If wear is not simulated in the machining process, a thermo-elastic material model is sufficient for tool. These material models only require basic thermal and mechanical properties of the tool - density, poisson's ratio, young's modulus, specific heat and thermal conductivity.

2.2.1.5 Contact & Friction model

A contact must be defined between the tool and the workpiece in order to control their interaction. In some cases, a self-contact is also necessary between the tool and the chip. Contact has a huge influence on simulation results and an incorrect contact can lead to spurious results. AdvantEdge uses the predictor-corrector method from the PRONTOD2D explicit dynamics code, which was developed and explained by Taylor and Flanagan in their work [92]. The two contacting surfaces are designated as master and slave surfaces, where tool is the master and workpiece is the slave surface [53]. Unlike AdvantEdge, LS-DYNA has numerous contact types like tied contacts, automatic contacts, forming contacts etc [93]. In this study, *CONTACT_NODE_TO_SURFACE was used to perform coupled FEM-CFD flood lubricated simulation. It uses a penalty-based approach to model the contact between the tool and the workpiece [38]. In LS-DYNA, master (tool) and slave (workpiece) surfaces must be defined manually.

In order to correctly predict the cutting forces and temperature, a friction model is as important as the material model. As with material models, there are many friction models in literature, some of which are mentioned in table 2.1.

Özel [60] studied the influence of five different friction models on orthogonal turning simulations using an updated lagrangian formulation in the Deform 2D software. After comparing his simulation results with experimental results, he concluded that the friction modelling at tool-chip interface has an impact on simulated forces, temperature and tool stresses. Among the compared models, the model with variable shear stress and coefficient of friction depicted the best results. Özel et al. [69] created an ALE model of orthogonal turning process in the ABAQUS software to study the influence of friction model (coulomb and stick-slip model). They found that the friction model has a higher impact on thrust forces as compared to cutting forces. In order to accurately forecast forces, stresses, and temperature, they also

noted that stick-slip friction models should be utilized with caution and that limiting shear stress values must be established for each cutting scenario. Malakizadi et al. [99] studied the influence of different friction models during orthogonal turning of C45 and C80 in three different software: Deform 2D, ABAQUS/Explicit and AdvantEdge. In their research, they concluded that the friction model has an impact on simulation results, with sliding-sticking and pressure dependent shear friction model providing better results than other models. Hence, it can be concluded that friction has an impact on simulation results, especially on forces.

Table 2-1: Friction models in machining simulations

Name	Equation	Reference
Coulomb	$\tau = \mu\sigma$	-
Zorev	$\tau = \begin{cases} k, 0 \le l \le l_c \\ \mu\sigma, l > l_c \end{cases}$	94
Usui	$\tau = k[1 - \exp\left(-\frac{\mu\sigma}{k}\right)]$	95
Childs	$\tau = mk\left[1 - \exp\left(-\frac{\mu\sigma}{mk}\right)^n\right]^{1/n}$	52
Iwata et al.	$\tau = \frac{H_y}{0{,}07} tanh\left(\frac{\mu\sigma}{\frac{H_v}{0{,}07}}\right)$	96
Sekhon and Chenot	$\tau = -\alpha K \lvert\lvert\vartheta_f\rvert\rvert^{\rho-1}\vartheta_f$	97
Yang and Liu	$\tau = \sum_{k=0}^{4} \mu_k \sigma^k$	98

During the course of this research work, only coulomb friction model was available in the AdvantEdge software and thus it was used in the simulations. It is written as:

$$F_{fr} = \mu * F_n \qquad 2.18$$

Where, F_{fr} is the force resulting due to friction, μ is the coefficient of friction and F_n is the normal force exerted between the surfaces.

To keep the same friction model in both software, coulomb friction model was also used in the LS-DYNA software. In LS-DYNA, an exponential interpolation function smooths the transition between static and dynamic coefficient of friction [38] and is given as:

$$\mu = \mu_d + (\mu_s - \mu_d)e^{-c'|v|} \quad 2.19$$

Where, μ_d is the dynamic coefficient of friction, μ_s is the static friction of coefficient, v is the relative velocity between slave node and master segment and c' is the decay constant.

2.2.1.6 Coupled Thermo-mechanical model

A coupled thermo-mechanical simulation of machining process can provide useful insights such as temperature calculations, which are generally not available during the experiments. This section will describe the thermo-mechanical coupling in the AdvantEdge and LS-DYNA software that were used in this thesis work.

AdvantEdge: In machining, a significant amount of heat is generated due to the plastic deformation of material and the friction at tool-chip interface. The rate of heat supply due to plastic deformation (s) of material in bulk is given in equation 2.20, whereas equation 2.21 gives the rate of heat generated at frictional contact (h''). The ratio of heat supply to chip h_1 and to tool h_2 is calculated in AdvantEdge using transient half-space solutions as seen in equation 2.22 [53]:

$$s = \beta \dot{W}^p \quad 2.20$$

$$h'' = -t'.[\![v]\!] \quad 2.21$$

$$\frac{h_1}{h_2} = \frac{\sqrt{k_1\rho_1 c_1}}{\sqrt{k_2\rho_2 c_2}} \quad 2.22$$

Where, $\dot{W}^p$ represents the plastic power per unit deformed value, β is the Taylor-Quinney coefficient of order 0.9, t' is the contact traction, $[\![v]\!]$ is the jump in velocity across the contact, k_α represents the thermal conductivity (α=1 for workpiece and 2 for tool), ρ_α is the density, and c_α is the heat capacity.

To couple the thermal and mechanical equations, a staggered approach developed by Park and Felippa is used in AdvantEdge [100]. A constant temperature during the mechanical step and a constant heat generation during the thermal step is assumed to stagger mechanical and thermal computations. Following Lemonds and Needleman [101], the heat generated is calculated using equations 2.21 and 2.22 after taking a mechanical step based on the current distribution of

temperatures. Forward-Euler method is used to recalculate the temperatures after the heat has been transferred to the thermal mesh. The recalculated temperatures are then transferred to the mechanical mesh and included into the thermal-softening model, thus completing the one time-stepping cycle.

LS-DYNA: LS-DYNA uses a two-way coupling for coupled thermo-mechanical simulation, i.e., two solvers run in parallel, with thermal time step being independent of mechanical time step, and data is shared between them. Thermal step updates the temperature field and calculates the heat from plastic work and friction, whereas in mechanical step, the plastic work is calculated, and geometry is updated. An implicit time integration is chosen for the thermal step, while both explicit and implicit time integration could be chosen for the mechanical step [102].

A coupled thermo-mechanical model of machining process can provide insights on material deformation, heat generation and temperature distribution during the machining process. This information can help in improving the predictive maintenance on tool loads. Thermo-mechanical simulations also help in understanding the complex interactions between stresses, temperature and material behavior. However, all these benefits cost high computational time, and thermo-mechanical models require a lot of information on material behavior, which can sometimes be challenging during procurement.

2.2.2 Computational fluid dynamics

As mentioned in section 2.1.3, chip formation in a machining process causes plastic deformation of workpiece material in the shear zone. This deformation generates a lot of heat energy. Even though most of the heat is taken out by the chip [103], some heat is also transferred to surroundings (tool, workpiece, air etc.) via conduction, convection and radiation. The conduction and convection heat transfer modes are more dominant than radiation. Thus, the heat transfer by radiation mode in machining process can be neglected [104]. This generated heat during the machining process has a negative influence on the tool life and finished workpiece surface quality [105, 106]. In practice, lubricants are used in machining process to take this excessive heat out of the system and to avoid the negative effects of excessive thermal load. Hence, the major function of a lubricant in machining process is tool cooling and chip evacuation. There are two types of lubrication techniques, namely [107]:

- Conventional lubrication technique (example: flood lubrication, high pressure cooling, and mist cooling)

- Alternative lubrication technique (example: minimum quantity lubrication (MQL), cryogenic cooling and hybrid cooling)

Finite element methods are widely used for simulation of structures. However, in general, fluids are simulated using the computational fluid dynamics (CFD).

2.2.2.1 CFD-Simulation: Theoretical Background

Computational fluid dynamics uses numerical methods to solve and analyze the fluid flow problems. In order to solve for fluid flow variables like velocity, pressure and temperature, CFD creates a discretized form of partial differential equations (PDE) that regulates the fluid flow. These equations are then solved on a computational grid (mesh) inside the flow domain [108].

2.2.2.2 Governing equations in CFD

The flow of a continuum such as a liquid or a gas is described by the conservation laws of mass, momentum and energy and their respective governing equations are mentioned below in equation 2.23, 2.24 and 2.27:

$$\frac{\partial \rho}{\partial t} + \nabla.(\rho \mathrm{v}) = 0 \qquad 2.23$$

This equation implies that the matter that enters the system per unit time and the mass that leaves the system are equal. This proves that the mass cannot be created or destroyed [109, 110]. In equation 2.23, ρ is the density, v is the velocity and t is the time.

$$\frac{\partial(\rho v)}{\partial t} + \nabla.(\rho v \otimes v) = \nabla.\sigma' + f_b \qquad 2.24$$

The above equation [109] states that if for a closed system there is no external force applied on the continuum, the rate of change of momentum is zero. In equation 2.24, ρ is the density, v is the velocity, t is the time, f_b is the resultant of body force (e.g. gravity) per unit volume acting on continuum, σ' is the stress tensor and $\otimes$ denotes the outer product of vector quantities.

For a fluid, stress tensor σ' is the sum of normal and shear stresses and is written as:

$$\sigma' = -pI + \zeta \qquad 2.25$$

Where, p is the pressure and ζ is the viscous stress tensor and I is the identity matrix. Using equation 2.25 in equation 2.24 leads to equation 2.26:

$$\frac{\partial(\rho v)}{\partial t} + \nabla.(\rho v \otimes v) = -\nabla.(pI) + \nabla.\zeta + f_b \qquad 2.26$$

$$\frac{\partial(\rho E)}{\partial t} + \nabla.(\rho E v) = f_b.v + \nabla.(v.\sigma') - \nabla.q + S_E \quad 2.27$$

This equation represents the first law of thermodynamics and it states that for a closed system, energy can neither be created nor be destroyed, but can only change its form. In equation 2.27, ρ is the density, E is the total energy per unit mass, t is the time, v is the velocity, f_b is the resultant of body force (e.g. gravity) per unit volume acting on continuum, σ' is the stress tensor, q is the heat flux, S_E is the energy source per unit volume.

To solve the above-mentioned equations, the ideal gas equation is required, as it connects pressure, density and temperature. The ideal gas equation is written as:

$$p = \rho RT \quad 2.28$$

where, R is the universal gas constant and is mathematically written as following:

$$R = c_p - c_v = (\Upsilon - 1)c_v \quad 2.29$$

where, c_p is specific heat at constant pressure, c_v is specific heat at constant volume and Υ is ratio of specific heat.

Coupling between solids and fluids in a CFD simulation are established through equation 2.27.

2.2.2.3 CFD-Solver

As mentioned earlier, CFD software uses PDE to solve a fluid flow problem. There are various numerical discretization methods available to solve these PDE e.g., finite volume method (FVM), finite difference method (FDM), SPH etc. In this research work, the Star-CCM+ software was used as the CFD tool and the Algebraic Multigrid (AMG) solver was used for machining simulations. AMG solver uses finite volume method to solve partial differential equations. In FVM, the continuum is divided into a finite number of control volumes (elements). At the center of these control volumes flow properties are calculated. It requires integral form of the governing equations (mass, momentum and energy) mentioned in the previous section (equation 2.23, 2.24, 2.27) [109]. One of the major advantages of FVM over FEM is conservation of flow properties like mass and momentum at a discrete level. These equations are written as following:

$$\frac{\partial}{\partial t}\int_V \rho dV + \oint_A \rho v.da = \int_V S_u dV \quad 2.30$$

$$\frac{\partial}{\partial t}\int_V \rho v dV + \oint_A \rho v \otimes v.da = -\oint_A pI.da + \oint_A \zeta.da + \int_V f_b dV + \int_V S_u dV \quad 2.31$$

$$\frac{\partial}{\partial t}\int_V \rho E dV + \oint_A \rho H v.da = -\oint_A q.da + \oint_A \zeta.da + \int_V f_b.v dV + \int_V S_u dV \quad 2.32$$

2.2.2.4 Turbulence modelling

Turbulence can be defined as a seemingly irregular and chaotic three-dimensional vorticity composed of large spectrum of eddy sizes [111]. Since most of the flows in the nature are turbulent, turbulence interests many researchers. Some of the common methods used to model turbulence are:

- Direct Numerical Simulation (DNS)
- Large Eddy Simulation (LES)
- Reynolds-Averaged Navier Stokes (RANS)

This thesis used the RANS method to model the turbulent flow in machining process and hence only RANS will be discussed further. More insights on the above-mentioned methods can be found in work of Spalart [112].

Reynolds-Averaged Navier Stokes (RANS) equation

In this method Reynolds averaging is used to decompose the primary variables in Navier-Stokes equation into two components, the mean and the fluctuation about the mean. It can be represented as:

$$U = \overline{U} + U' \tag{2.33}$$

Where, U is the primary variable from Navier-Stokes equation, $\overline{U}$ is the mean component and U' is the fluctuation about the mean component.

Substituting equation 2.33 in Navier stokes equation (equation 2.23, 2.24 and 2.27) gives the RANS equation for mass, momentum and energy for compressible flow. These equations are mentioned below [109]:

$$\frac{\partial \rho}{\partial t} + \nabla.(\rho\overline{v}) = 0 \tag{2.34}$$

$$\frac{\partial}{\partial t}(\rho\overline{v}) + \nabla.(\rho\overline{v} \otimes \overline{v}) = -\nabla.\overline{p}\mathrm{I} + \nabla.\left(\overline{\mathrm{T}} + \mathrm{T}_{\mathrm{RANS}}\right) + \mathrm{f}_b \tag{2.35}$$

$$\frac{\partial}{\partial t}\left(\rho\overline{E}\right) + \nabla.\left(\rho\overline{E}\overline{v}\right) = -\nabla.\overline{pv} + \nabla.\left(\overline{\mathrm{T}} + \mathrm{T}_{\mathrm{RANS}}\right)\overline{v} - \nabla.\overline{q} + \mathbf{f}_b\overline{v} \tag{2.36}$$

These RANS equations are similar to Navier Stokes equations. However, a new variable $\mathrm{T}_{\mathrm{RANS}}$ is present in momentum and energy equation. To provide a solution to the RANS equation, this variable term has to be solved. This variable is called as stress tensor ($\mathrm{T}_{\mathrm{RANS}}$) and is written as following:

$$T_{RANS} = -\rho \begin{pmatrix} \overline{u'u'} & \overline{u'v'} & \overline{u'w'} \\ \overline{u'v'} & \overline{v'v'} & \overline{v'w'} \\ \overline{u'w'} & \overline{v'w'} & \overline{w'w'} \end{pmatrix} + \frac{2}{3}\rho k \boldsymbol{I} \quad 2.37$$

Where, k is the turbulent kinetic energy. A transportation equation is further required to solve for kinetic energy, thus giving birth to the so-called turbulence models. Some of the common turbulence models are Standard k-ε model, realizable k-ε model, RNG k-ε model, k-ω model, k-ω-SST model, S-A-SST model etc. During this thesis work, only realizable k-ε model and k-ω-SST turbulence models are used, which are explained below.

Realizable k-ε turbulence model

Realizable k-ε model was developed in 1995 from the traditional k-ε model [113]. This model consists of a new formulation for turbulent viscosity. Similarly, a new transport equation was developed for the dissipation rate. The term realizable is used to imply that k and ε satisfy mathematical constraints for normal stress and are consistent with turbulent flow physics. For k-ε turbulence model, transport equation is written as following:

$$\frac{\partial(\rho k)}{\partial t} + \nabla.(\rho k U) = \nabla.\left[\mu_{eff} + \frac{\mu_t}{\sigma_k}\nabla(k)\right] + P_k + P_b - \rho\epsilon - Y_M \quad 2.38$$

$$\frac{\partial \rho\epsilon}{\partial t} + \nabla.(\rho\epsilon U) = \nabla.\left[\frac{\mu_t}{\sigma_\epsilon}\nabla(\in)\right] + \rho C_{1\in} S_\in - \rho C_2 \frac{\epsilon^2}{k+\sqrt{v\in}} + C_{1\in}\frac{\in}{k} C_{3\in} P_b \quad 2.39$$

Where, ρ is the density, k is turbulent kinetic energy, t is time, U is time averaged velocity field, μ_{eff} is molecular viscosity, μ_t is turbulent viscosity, σ_k is model constant, P_k is the production term for kinetic energy due to mean velocity gradients, P_b is the production term due to buoyancy, $\rho\epsilon$ is the dissipation term, Y_M is the compressibility effect, ϵ is the rate of energy dissipation, $\sigma_\in$ is model constant, $S_\in$ is the magnitude of mean strain rate, v is the kinematic viscosity, C_1, C_2 and C_3 are the model constants.

k-ω-SST turbulence model

This model is based on k-ω model which was proposed by Wilcox in 1988 [114]. The k-ω-SST model is a combination of advantages of both, k-ε and k-ω model. Menter [115] found that the solution from the k-ε model is less sensitive to assumed values in the free stream. Additionally, k-ω model performs well in near wall regions. Thus, a hybrid model was proposed that uses the standard k-ε turbulence model in fully turbulent flows and the k-ω model at near-wall regions. To obtain such an equation, the k-ε equations are transformed into a ω-equation using the substitution $\varepsilon = k\omega$. The transport equation of a k-ω-SST model is written as following:

$$\frac{\partial \rho\omega}{\partial t} + \boldsymbol{\nabla} \cdot (\rho\omega \boldsymbol{U}) = \boldsymbol{\nabla} \cdot \left[\left(\mu + \frac{\mu_t}{\sigma_{\omega,1}}\right)\boldsymbol{\nabla}(\omega)\right] + \gamma_2 \left(2\rho S_{ij} \cdot S_{ij} - \frac{2}{3}\rho\omega \frac{\partial U_i}{\partial x_j}\delta_{ij}\right) - \beta_2 \rho\omega^2 + 2\frac{\rho}{\sigma_{\omega,2}\omega}\frac{\partial k}{\partial x_k}\frac{\partial \omega}{\partial x_k} \quad 2.40$$

Where, ρ is the density, ω is the specific dissipation rate, t is time, U is time averaged velocity field, μ is molecular viscosity, μ_t is turbulent viscosity, $\sigma_{\omega,1}$ is model constant, S_{ij} is the strain rate tensor, γ_2 is model constant, δ_{ij} is Kronecker delta, β_2 is model constant, ω^2 is quadratic decay, k is turbulent kinetic energy and $\sigma_{\omega,2}$ is model constant.

2.2.2.5 Conjugate Heat Transfer (CHT)

Conjugate heat transfer methodology is used in cases where an interaction between two different materials exists on a contact surface, i.e., a contact between solid-fluid or solid-gas. During the machining process, heat is generated due to plastic deformation at the tool-workpiece interface (solid) and a lubricant (fluid) is used to take this generated heat out. Thus, conjugate heat transfer method is used in flood lubrication simulations of this thesis work.

For a conjugate heat transfer problem, equation 2.32 (energy equation) is solved over the fluid-solid interface in CFD-environment, while other conservation equations (equation 2.30 and 2.31) are solved only for fluid [116]. Since the energy is conserved in a closed domain, total heat flux is also conserved across the interface (solid-fluid contact) [117]. This can be written mathematically as following:

$$\dot{q}_0 + \dot{q}_1 = -S_u \quad 2.41$$

Where $\dot{q}_0$ is the heat flux from fluid, $\dot{q}_1$ is the heat flux leaving the solid and S_u is the user defined heat source placed at the interface. However, the temperature can be different inside the fluid and solid region. Hence, the heat flux at interface can be calculated with the following formula:

$$\dot{q}_0 = -\frac{S_u}{2} + \frac{T_{\omega 1} + T_{\omega 0}}{R'} \quad 2.42$$

Where, T_{w1} and T_{w0} are the interface temperatures on the solid side and fluid side respectively and R' is the interface thermal resistance.

The above two equations are solved to find a solution for the conjugate heat transfer problems. Further information on CHT methodology can be found in the Star-CCM+ software user guide [117].

A unidirectional coupling for flood lubricated machining has been used by many researchers in the past. To list a few of them, Pervaiz et al. [118,119] suggested an iterative method to couple FEM (for structure) and CFD (for lubricant) simulations. In this method, temperature distributions from FEM dry machining simulations were used in CFD-simulations to calculate the heat transfer coefficient (HTC) values through conjugate heat transfer analysis. The HTC values from the CFD-simulations were then taken back to the FEM-simulations for temperature calculations. This completed one cycle in iteration, and the process was repeated till temperature values were converged. Helmig et al. [120] used the same methodology while also considering chip formation. Liu et al. [121] also used this methodology along with transferring data at different time steps and chip geometry.

2.2.2.6 Mesh for fluid bodies

Mesh generation is an important part of every numerical simulation. During mesh generation, a computational domain is divided into several small elements/volumes. As mentioned in section 2.2.1.3, as per requirement, both structured and unstructured mesh can be generated in a numerical problem. Mesh element type and its size have a significant impact on the accuracy of the numerical solution and they also influence the simulation time. The most commonly used element types in CFD simulation are hexahedral and tetrahedral elements. One of the major advantages of hexahedral elements is that due to low numerical diffusion, they have the lowest discretization error in majority of the simulation cases. In contrast, it is not possible to easily generate hexahedral mesh for complex geometries. Thus, the usage of hexahedral mesh is limited in industrial applications [122] and in most commercial software, tetrahedral mesh generation algorithms are also integrated. One major advantage of tetrahedral mesh is that it can be generated entirely automatically. However, for tetrahedral mesh, computing gradients can be challenging and may lead to a poor convergence because a tetrahedral mesh neighboring node might occur in a single plane [122]. Due to this, a new mesh type called polyhedral mesh was developed. It has a low numerical diffusion and a semi-automatic generation capability, i.e., advantages of both hexahedral, and tetrahedral mesh types [123,124]. In comparison to both previously mentioned mesh types, polyhedral mesh has more neighboring elements which improves the gradient calculation. Hence, mass can flow through these element faces, resulting in the elimination of numerical diffusion effects. This mesh type's numerical stability is also increased by the fact that it is not overly sensitive to element stretching. The above mentioned three mesh types are shown in figure 2.16 [123]. Due to the mentioned benefits of polyhedral

mesh, this mesh type has been used in this thesis work for the flood lubrication simulation of turning process.

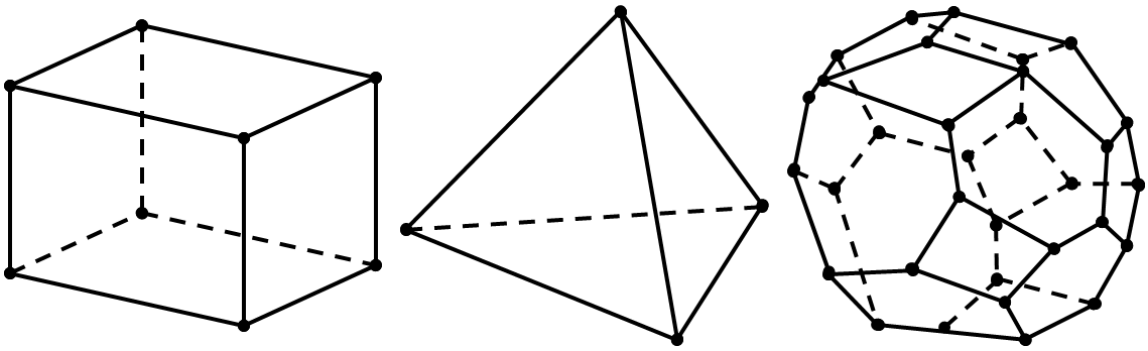

Figure 2-16: Commonly used mesh types in CFD-Simulations: Hexahedral (left), tetrahedral (center) and polyhedral (right) [123]

During FEM-machining simulations, usually an adaptive and remeshing code is written to generate a chip. This code basically contains the element separation criterion based on the material and motion of cutting tool. If a solid object must be moved inside a CFD-domain, the meshing can be quite tedious and intricate. One of the methods to overcome this difficulty is using the overset meshing technique. In this methodology, the solid object that needs to be moved is encased in a mesh (called as overset) and is moved inside the CFD-domain as per requirement [117]. In an overset meshing, a background mesh is generated for whole CFD-domain. An overset mesh containing the moving object is kept inside a background mesh. Star-CCM+ uses hole cutting procedure to connect this overset mesh with the background mesh. The mesh is grouped in three types of cells that are shown below in figure 2.17 [117]:

- Active Cells, where flow equations are solved.
- Inactive cells, which are not involved in the numerical calculations. However, these are present in the background and as the overset mesh moves, these cells can become active cells and vice-versa.
- Acceptor cells, that define the perimeter of overset mesh separating the active and inactive mesh.

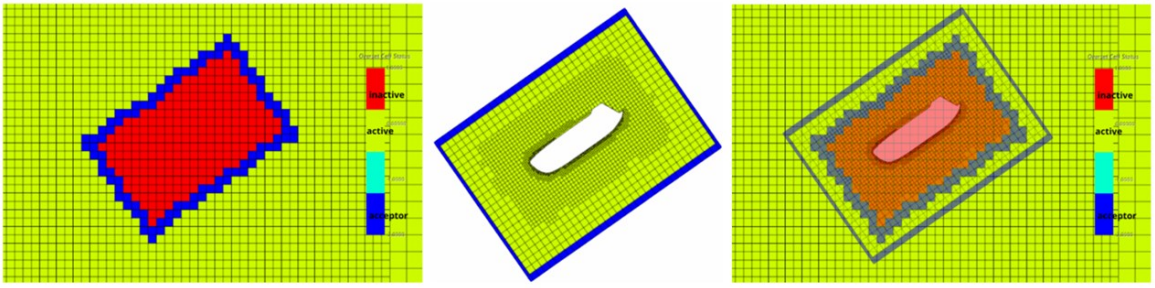

Figure 2-17: Overset meshing technique

2.2.3 Mechanistic modelling

Since the advent of Industry 4.0, companies are turning towards the digitalization of production systems. This digitalization of production system can be divided into several levels, as shown in Figure 2.18. The level of details increases from factory level to production line, to machine level, and to individual cutting edges (tool) at micro level. Various digital tools are implemented at these levels to optimize and simulate the respective process. For example, material flow simulations are used at factory and production line level, MBD and FEM simulations are used to analyze dynamic behavior and performance at machine level, and FEM and CFD simulations are used to optimize cooling channels, tool geometry, coatings etc. at tool level. There are interactions between these levels in the form of information flow. For instance, FEM-simulation results at micro level in the form of specific cutting forces serve as an input for the simulations at machine level. Similarly, more detailed simulations can be conducted at micro level with the corresponding machining parameters based on process weak points identified at macro level. Thus, an end-to-end digitalization of production processes becomes essential which could be accomplished by using integrated production and material simulations in development, design and manufacturing [125]. This integrated approach of digitalization for mass production, which has been used in this work, is divided into two major levels: micro and macro level (as shown in figure 2.18). The micro level simulations are more detailed and can represent non-linearities of material and contact between tool & workpiece. This is mainly done by numerical modelling techniques like FEM, defined in section 2.2.1. At macro level, on the other hand, machining process is represented by analytical and mechanistic modelling techniques. These models describe the relevant phenomena with mathematical expressions and thus allow comparatively faster calculation times [27]. At macro level, machining process is modelled as a function of tool geometry, material, cutting speed, and machined volume. Additionally, specific cutting

force coefficients are required as an input to the simulations. [126]. Typical simulation outputs from these simulations are forces, spindle power, torque and stability charts.

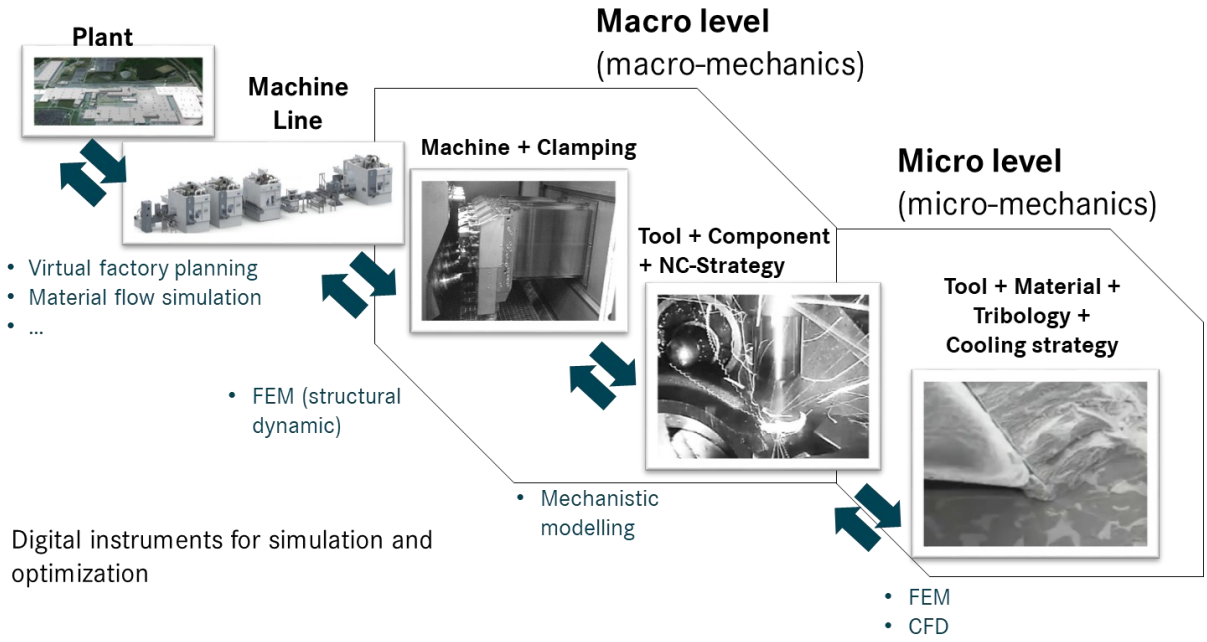

Figure 2-18: Levels of machining production and suitable simulation tools

Since all the mechanistic & analytical modelling techniques that can be used at macro level will go out of the scope of this thesis work, only the methodology used in this work will be discussed further.

In this work, simulations at macro level are carried out with the MACHpro software tool. Unlike other software using mechanistic modelling approach, one of the advantages of MACHpro is the ability to simulate various machining processes using a single force model. This is made possible by the use of so-called orthogonal-to-oblique (O-to-O) transformation in the engine of software, which is defined in section 2.2.3.2. To understand this transformation better, orthogonal machining is defined briefly in section 2.2.3.1.

2.2.3.1 Orthogonal Machining

Machining processes with defined cutting edges can be divided into three categories according to the type of cut, namely [7]:

- Free, orthogonal cuts
- Free, oblique cuts
- Bound, oblique cuts

These three process variants are shown below in figure 2.19.

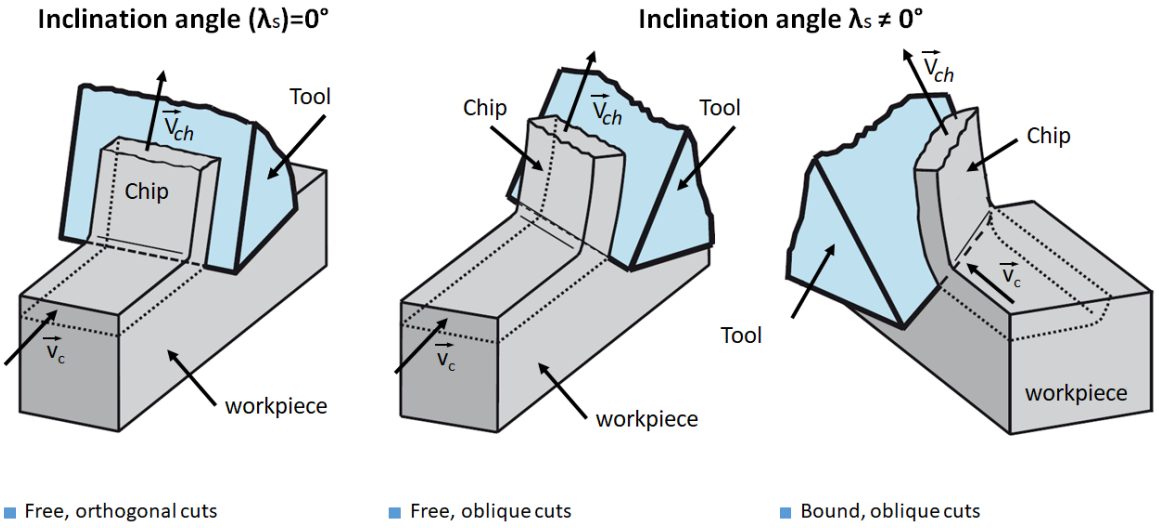

Figure 2-19: Machining process variants [127]

In the fundamental research of machining process, orthogonal cut is the most basic and important process variant, since the geometrical relationships are much less complex than the oblique cuts. An orthogonal cut can be realized only if the major cutting edge is engaged, the tool cutting edge angle (κ_r) is 90° and tool cutting edge inclination angle (λ_s) is 0° [7].

2.2.3.2 Orthogonal to Oblique transformation

Armarego [128] was able to transfer Merchant's analytical shear plane theory from orthogonal to oblique cut. He could transfer forces from an orthogonal cut to any oblique cut by developing the so-called orthogonal-to-oblique transformation (O-to-O). With this method, cutting force coefficients can be defined as a function of friction angle ρ', shear stress τ_S, shear angle ϕ, rake angle γ_o and inclination angle λ_S. The inclination angle takes oblique cut into account, whereas other physical quantities are derived from the orthogonal cut. This method can be used in common industrial machining processes like milling, turning, or drilling because the cutting force is defined by friction force and shear force [128]. Budak et al. [129] validated this approach experimentally and MAL Inc. implemented this approach in MACHpro [130].

To use the O-to-O method in MACHpro software for simulating the machining process, following specific cutting force coefficients are required. Additionally, shear angle, friction angle, and shear stress are required to transform the orthogonal cutting data into realistic oblique cutting conditions.

K_{te} (N/mm):	Edge cutting force coefficient in tangential direction
$K_{re}(K_{fe})$ (N/mm):	Edge cutting force coefficient in radial direction
K_{ae} (N/mm):	Edge cutting force coefficient in axial direction
ϕ (°):	Shear angle
τ_s (MPa):	Shear stress in shear plane
ρ' (°):	Friction angle

In orthogonal cutting, uncut chip thickness h (figure 2.4) corresponds to feed per revolution. A mathematical relationship is obtained for tangential (F_t) and feed (F_f) forces as a function of uncut chip thickness h and width of cut b, respectively, by drawing an average line through the recorded average cutting forces. The lines are expressed by the following equations:

$$F_t = F_{tc} + F_{te} = K_{tc}bh + K_{te}b \quad 2.43$$
$$F_f = F_{fc} + F_{fe} = K_{fc}bh + K_{fe}b \quad 2.44$$

Here, $K_{tc}b$ and $K_{fc}b$ are the slopes of averaged lines for the tangential and feed forces, $K_{te}b$ and $K_{fe}b$ are the edge forces in tangential and feed direction. These edge forces are due to the friction between the flank face of the tool and the newly created machined surface of the workpiece. Hence, they are not dependent on feed rate. As edge forces do not contribute to the shearing of the material, the above-mentioned equations 2.43 and 2.44 can be written as:

$$F_{tc} = F_t - F_{te} = K_{tc}bh \quad 2.45$$
$$F_{fc} = F_f - F_{fe} = K_{fc}bh \quad 2.46$$

Tangential and feed forces are linearly dependent on width of cut b. Hence, the cutting force coefficients (shear coefficient and edge force coefficient) can be calculated using equation 2.45 and 2.46, which are mentioned in equation 2.47 and 2.48 respectively:

$$\frac{F_{tc}}{h} = K_{tc}b\,,\boldsymbol{K_{tc}} = \frac{\boldsymbol{F_{tc}}}{\boldsymbol{bh}}; \qquad \frac{F_{fc}}{h} = K_{fc}b\,,\boldsymbol{K_{fc}} = \frac{\boldsymbol{F_{fc}}}{\boldsymbol{bh}} \quad 2.47$$

$$F_{te} = K_{te}b\,,\boldsymbol{K_{te}} = \frac{\boldsymbol{F_{te}}}{\boldsymbol{b}}; \qquad F_{fe} = K_{fe}b\,,\boldsymbol{K_{fe}} = \frac{\boldsymbol{F_{fe}}}{\boldsymbol{b}} \quad 2.48$$

Additionally, the chip ratio must be calculated for mechanistic modelling and is defined as the ratio of uncut chip thickness h to cut chip thickness h' [10] and is mentioned below in equation 2.49:

$$\lambda_{ch} = \frac{h}{h'} \quad 2.49$$

Shear angle (ϕ) can be calculated from equation 2.50, if chip ratio λ_{ch}, and rake angle γ are known:

$$\tan(\phi) = \frac{\lambda_{ch}\cos(\gamma)}{1-\lambda_{ch}\sin(\gamma)} \quad 2.50$$

Since chips have three dimensional curvatures, the chip thickness h' must be measured manually. For this, weighing method is used by assuming that the chip has constant volume and is calculated as per equation 2.51:

$$h' = \frac{m}{\rho \cdot b \cdot l_{ch}} \quad 2.51$$

Where, m is the mass of chip, ρ is the density of material and l_{ch} is the chip length.

Friction angle ρ',, shear angle ϕ and shear stress τ_s can be calculated using the following equations (2.52 to 2.57) for mechanistic modelling:

Feed force component without friction on flank face is given by the following equation:

$$F_{fc} = F_f - F_{fe} \quad 2.52$$

Cutting force component without friction on flank face is given as following:

$$F_{tc} = F_t - F_{te} \quad 2.53$$

Resulting cutting force can be obtained from the above mentioned two force components as:

$$F_c = \sqrt{F_{tc}^2 + F_{fc}^2} \quad 2.54$$

Friction angle is given as following:

$$\rho' = \gamma + \tan^{-1}\frac{F_{fc}}{F_{tc}} \quad 2.55$$

Shear angle is deduced from the following equation:

$$\phi = \tan^{-1}\frac{\lambda_{ch}\cos(\gamma)}{1-\lambda_{ch}\sin(\gamma)} \quad 2.56$$

Shear stress in shear plane is obtained from the following equation:

$$\tau_s = \frac{F_c\sin(\phi+\rho'-\gamma)}{bh} \quad 2.57$$

2.3 Workpiece and tool material

In the era of digitalization, modern digital tools are used by companies to develop better and sustainable products. This leads to the research of novel materials that are cost effective and have a longer lifespan. Automotive industry is no exception here and thus, the workpiece material used in this thesis work is a material specially developed by Mercedes-Benz AG for the turbine housing of exhaust gas turbochargers for gasoline engines. Similar situation exists in the Hardmetal industry, where the focus is always on improving tool-life, either by enhancing the tool material or finding novel materials that can be used in making the tool. Next two sections discuss the workpiece and tool material, respectively, in detail.

2.3.1 Machining of low nickel-based alloy GX30NiCrSiWNbN12-23 (1.4837D)

Turbine housings are exposed to a variety of thermal, mechanical and corrosive stresses due to a constant contact with exhaust gases, demanding the turbine housing material to be resistant to heat and corrosion [2]. Since the turbochargers have to withstand high stresses, high-temperature materials above 550°C are required [131]. These high-temperature materials include iron, cobalt or nickel-based alloys, refractory alloys and precious metal alloys. High temperature steels are either martensitic CrMoV steels or austenitic high-temperature steels, also called as iron-based superalloys [3,7]. Inside a gasoline engine exhaust gas, temperatures rise up to T=1050°C and are subjected to extreme fluctuations. Compressive yield point of the material can be exceeded because of high thermal and mechanical stresses, causing the material to deform plastically. On the other hand, subsequent cooling of a turbocharger can cause the material to crack. High alloy, carbide reinforced austenitic steels are used to meet these demands. Such steels contain high chromium and nickel content to keep the austenitic structure stable. These steels also have dendritic structure with carbide precipitates at the dendrite boundaries. Strength of the material is enhanced by the carbide reinforcements as they restrain the dislocation movements [2, 3, 17, 132, 133, 134]. Traditionally, GX40NiCrSiNb38-19 (1.4849) material, defined in DIN EN 10295 [135], has been used in the production of turbochargers. This material has 36-39% nickel content. However, due to high nickel prices and its price fluctuations, a new material GX30NiCrSiWNbN12-23 (1.4837D) was developed by Mercedes-Benz AG by drastically reducing the nickel content to 11-12%. Comparable properties between 1.4837D and 1.4849 were achieved by adapting other alloying materials in

the 1.4837D material. Table 2.2 shows the comparison between chemical compositions of the two materials [132].

Table 2-2: Comparison of alloy composition [17, 135]

	Mass fraction (%)							
Material	**Ni**	**Cr**	**Si**	**Nb**	**C**	**W**	**Mn**	**N**
1.4849	36 - 39	18 - 21	1.0 - 2.5	1.20 - 1.80	0.30 - 0.50	-	< 2.0	-
1.4837D	11 - 12	23 - 24	1.1 - 1.3	0.30 - 0.45	0.28 - 0.35	0.8 - 1.0	0.05 - 0.2	0.23 - 0.26

Due to their mechanical properties, high-alloy austenitic materials pose a major challenge in machining. Both 1.4849 and 1.4837D have austenitic microstructure with dendritic structure. However, the carbide precipitation in 1.4837D is not uniform, causing it to be more difficult to machine [17]. 1.4837D material has higher toughness in comparison to 1.4849, and it causes more vibrations in the machine tool system, leading to a higher alternating load on the cutting edge of tool, ultimately producing long and less favorable chips. The hardness of material 1.4837D also increases by 20%, which promotes tool wear. All these material characteristics reduce tool life significantly in the machining of 1.4837D material [17]. The important physical properties of the two materials are compared in Table 2.3. Since 1.4837D material is used in the production of over 1 million turbine housings every year, the focus of this thesis will be on tool optimization for this material.

Table 2-3: Physical properties of 1.4849 and 1.4837D [17, 132]

Physical properties of material	**1.4849**	**1.4837D**
Highest application temperature (T)	1050 [°C]	1050 [°C]
Thermal conductivity (k)	11 [W/mK]	14 [W/mK]
Tensile strength (R_m)	479 [N/mm²]	626 [N/mm²]
Yield strength (Y_m)	260 [N/mm²]	365 [N/mm²]
Young's Modulus (Y)	131 [kN/mm²]	137 [kN/mm²]
Elongation at break (A)	10%	25%
Fracture necking (Z)	6%	12%

2.3.2 Tool material

The workpiece material discussed in earlier section causes high thermo-mechanical stress in the cutting tools. For economical machining of such a workpiece material, cutting tool material should be selected carefully. Most common cutting tool materials are tool steels, hardmetals, ceramics and boron nitride [7]. Hardmetals, with or without coating, are generally used for machining difficult-to-machine materials. This is due to the fact that hardmetals are sufficiently wear and heat resistant even at a high temperature, and do not soften with an increase in temperature [9,136,137].

Table 2-4: Application and classification of hard metals cutting tool materials according to DIN ISO 513 [139]

Code-letter	Code-color	Workpiece material	Hard cutting tool material
P	Blue	Steel: All kind of steel and cast-steel, except stainless steel with austenitic structure	P01, P05, P10, P15, P20 …. P45, P50
M	Yellow	Stainless steel: Stainless austenitic and austenitic-ferritesteel and cast-steel	M01, M05, M10, M15 … M35, M40
K	Red	Cast-iron: cast-iron with flake-graphite, cast-iron with ductile graphite, annealed cast-iron	K01, K05, K10, K15 … K35, K40
N	Green	Non-ferrous metals: Aluminum and other nonferrous metals, non-metal materials	N01, N05, N10, N15 … N25, N30
S	Brown	Specializations and titanium: Highly heat resisting special-alloys based on iron, nickel and cobalt, titanium and titanium based alloys	S01, S05, S10, S15 … S25, S30
H	Grey	Hard materials: Hardened steel, hardened cast-iron-materials, cast-iron for chill-casting	H01, H05, H10, H15 … H25, H30

Hardmetals are a composite material produced via powder metallurgy process. These hardmetal composites are made of transition metal carbides embedded in a cobalt- or nickel-based soft metallic binder phase. The most general hardmetal is WC-Co, where tungsten (W) is used to

form carbide and cobalt (Co) is used as the binder. Titanium (Ti), tantalum (Ta) and niobium (Nb) can also be used to form special carbides [7,9]. The properties of hardmetals can be influenced by adjusting the percentage of carbide and binder. In addition to this, their properties can also be modified by adjusting the grain size; for the same cobalt content, smaller the grain size, more the hardness and bending strength. It also increases the hot hardness of hardmetal. This leads to a higher tool edge strength, but causes a reduction in fracture toughness [138]. According to ISO 513, hardmetals are divided into six major categories as shown in table 2.4.

Habermeier [17] evaluated over 500,000 coated and uncoated indexable inserts for turning, milling and drilling processes for Mercedes-Benz AG. This was done internally in the powertrain area. The analysis reveals that the majority of cutting materials used in machining of powertrain components are from the ISO-P and -M, application groups and its percentage distribution is shown in Table 2.5. Habermeier [17] tested these hardmetal application groups for different machining processes for 1.4837D material and found that the ISO-K application group had lower wear in comparison to the ISO-P and -M groups. Based on these results, ISO-K cutting inserts were chosen as tool material in this thesis work.

Table 2-5: Percentage distribution of ISO indexable inserts in powertrain [17]

Main area of application	Percentage application in Powertrain	Milling	Turning	Drilling
P	66.00%	97.13%	55.41%	100.00%
M	27.61%	0.00%	36.90%	0.00%
K	5.80%	0.81%	7.51%	0.00%
N	0.02%	0.09%	0.00%	0.00%
S	0.51%	1.81%	0.15%	0.00%
H	0.05%	0.16%	0.03%	0.00%

Exceptionally, uncoated tools are used in the machining process, thus making the coatings an inherent part of a large-scale production in automotive companies. Coatings enhances the wear resistance [140,141] and acts as a thermal barrier [142, 143], positively influencing the tool performance. Higher process parameters can be used in the machining process with coated tools, despite higher thermal and mechanical load on tool, which increases the tool productivity.

Majorly there are two requirements from coating: first, toughness and bond strength of hardmetal substrate should not be reduced, and second, the wear mechanism should slow down [7]. Thus, coatings usually have a higher hardness than the hardmetal substrate [127]. Some examples of commonly used industrial coatings are titanium nitride (TiN), titanium carbide (TiC), aluminum oxide (Al_2O_3), titanium carbon nitride (Ti(C,N), aluminum titanium nitride (AlTiN) [144]. Coatings can be produced by two methods: Chemical vapour deposition (CVD) and Physical vapour deposition (PVD). In CVD process, under rough vacuum conditions, chemical reactions happen in gaseous phase, creating a hard layer forming substance and volatile products. The process is controlled by different temperatures, pressures and ways of activating chemical reaction. CVD coatings can be produced via three different ways [7]:

- HT-CVD (High temperature CVD, process temperature: 900-1100°C)
- MT-CVD (Medium temperature CVD, process temperature: 700-900°C)
- PA-CVD (Plasma activated CVD, process temperature: 450°C-650°C)

Conversely, PVD procedures rely on condensation of ions, molecules, or atoms on the surface of substrate [145]. Due to compressive residual stresses, PVD coatings are generally limited to a thickness of 3-6µm [7]. However, a higher coating thickness can be achieved with CVD coatings [146]. Like CVD, PVD also has three process variants [7]:

- Thermal evaporation (vacuum evaporation)
- Arc evaporation (arc-PVD)
- Cathode evaporation (Sputtering)

In the last decade, many researchers have focused on developing the coatings for various machining processes through simulations. The temperature at tool-chip interface was measured and simulated by Grzesik et al. [61,143] for different coated inserts, TiC, TiC/TiN, and TiC/TiN/Al_2O_3 coating and an uncoated insert. They used the AdvantEdge software to model a coupled thermo-mechanical orthogonal cutting process with a continuous chip generation and found that thermal properties of the work material and the coating have an impact on percentage of heat transferred into the tool/chip. Additionally, they found a strong correlation between simulated and measured temperatures. For the purpose of examining effects of various coating layers, Kone et al. [147] examined the dry orthogonal turning process by investigating four different cases. These cases were modelled in the Deform software and included an uncoated tungsten carbide tool and three coated tungsten carbides: a single layer TiN coating, a hypothetical carbide insert with an Al_2O_3/TiN bilayer, and a tri-layer TiCN/Al_2O_3/TiN. By

analyzing the temperature distribution, it was found that the presence of coatings affects heat transfer at the interface. They concluded that the low thermal conductivity of coatings restricts conductive heat transfer at the tool surface. A milling process was modelled as a 2D-orthogonal process in Abaqus by Krajinovi et al. [70]. Three distinct coatings, namely a single layer TiAlN formed by arc evaporation, a bilayer of TiCN and Al_2O_3 formed by chemical vapor deposition, and a bilayer of TiAlN and Al_2O_3 formed by chemical vapor deposition, along with an uncoated tool were investigated. They computed the forces and temperatures on the tools and found that coatings have a negligible effect on cutting forces, but function as a thermal shield on the tool, causing higher temperatures on the tool surface and lower temperatures in the substrate. Sargade et al. [148] conducted experimental research on the impact of coating thickness on dry machining performance of C40 steel. TiN coating with varying thickness, from 1.8µm to 6.7µm, was used in their research work. They found that inserts with TiN coating performed better because of smaller crater wear area, in contrast to the larger crater size of an uncoated carbide insert. Additionally, they found that among the various studied coating thicknesses, 4µm demonstrated the best performance, which is attributable to this thickness's superior coating adhesion characteristics. The performance of AlCrN and AlTiN coated (coating thickness varying from 2 to 4 µm) Al_2O_3-TiCN composite (mixed) ceramic cutting tools was studied by Kumar et al. [149,150] for hard turning of 100Cr6 steel. They concluded that the performance of coating was significantly influenced by coating adhesion.

2.4 Summary

In this chapter, the basics of turning process, workpiece & tool material and different modelling techniques were introduced. The current state of the art theoretically provides various possibilities to model the machining process. Comprehensive description of two modelling techniques used in this thesis, i.e., numerical (FEM and CFD) and mechanistic modelling was provided. A detailed literature review showed that the choice of element formulation impact the effort required to model a simulation. Additionally, in some cases, element formulation also has an influence on the accuracy of model. Finally, a thorough literature review on modelling of coating and hardmetals was provided. This review indicated that most of the research work on coating simulations in past was done as 2D-FEM-simulations and majority of them were limited to orthogonal machining process. This thesis research work will focus on modelling different coatings and coating thicknesses in 3D for a turning process. Finally, it will be

investigated how different modelling techniques can be used in providing digital solutions to mass-production problems.

3 Initial situation and objective

3.1 Motivation, objective and challenges in mass production

As mentioned in section 2.3.2, current state of the art allows all carbides and coatings to be combined with each other. But the tool manufacturers of ISO inserts limit themselves to a defined number of possible combinations as effort required to produce indexable inserts to customer specifications would not be feasible in large-scale tool production [17]. Though the tool suppliers restrict themselves to a limited combination of hardmetal and coatings, there are several tool manufacturers that provide various tool variants for the turning process. Figure 3.1 shows the name of German tool manufacturers and the approximate number of turning inserts provided by them [151]. It can be seen in this figure that there are around 50 tool suppliers in Germany providing approximately 800 tool variants. This existing diversity of variants poses a significant challenge to the company in terms of time and cost when it comes to the optimization of machining process for a novel material like 1.4837D.

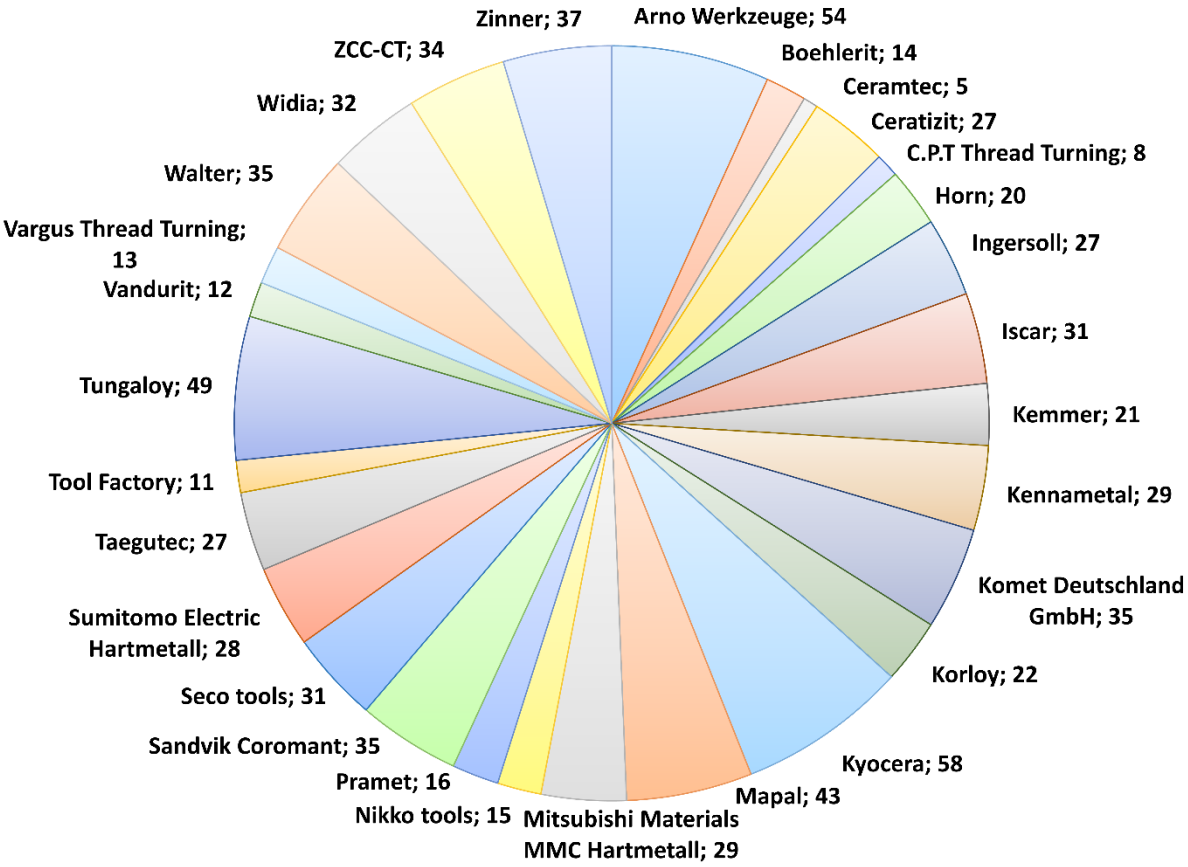

Figure 3-1: Various carbide turning tool manufacturers and the number of their turning tools [151]

One of the possible solutions to the above-mentioned challenge is using digital tools to reduce the number of tool variants that need to be tested in mass production. But, as mentioned in section 2.2.3, modelling of machining process can be done from macro to micro level. Depending on the end goal, the modelling level and technique can be chosen. Additionally, for any modelling level, different modelling techniques are available, for example at macro level, both FEM and mechanistic modelling techniques can be used, depending on the problem statement. Even for a single modelling technique like FEM, several important input factors such as element formulation and time integration need to be considered. Thus, choosing the incorrect modelling technique can also pose a challenge in implementing the digitalization in the production systems.

A major objective of this research work is to provide a digital strategy that can be implemented for various machining processes at different levels and is suitable for implementation in mass-production. Another objective is to find out whether simulation tools could aid in tool selection and optimization in case of subtle variations, such as change in coating, coating thickness and cutting edge radius. This will not only reduce the number of experiments to be conducted but also minimize the development time and material costs. In the end, goal of this digital strategy is to optimize the turning process in mass-production by using turbocharger as an example.

3.2 Initial Situation and approach

As mentioned in section 2.3.1, 1.4837D casted low nickel alloy has a reduced machinability when compared to its predecessor 1.4849 material. This deterioration in machinability has a direct impact on the economic efficiency of tools. Turbocharger housings rank among the most expensive parts of the powertrain in terms of tool costs. For example, tooling costs for crankcases, cylinder heads, connecting rods, camshafts, etc. are in the cent range. However, tooling costs for the manufacturing of turbine housings typically vary from 3 to 10 euros per component [17]. Since at the start of this research work, over 1 million turbine housings were produced per year, optimizing machining process of turbine housing could create a significant impact on overall cost savings for the company. Due to this reason, the inner contour turning process was taken as a problem statement in this research work.

Due to the above-mentioned challenges like numerous tool suppliers, various cutting inserts, novel material and high cost of material, it became evident that the traditional approach of

conducting experiments was not enough to find a solution in time. Thus, the solution strategy had to consider alternative approaches like digitalization in mass-production.

3.3 Strategical solution to problem statement

The important factors that are usually optimized by researchers in a machining process include cutting parameters and strategy, tool material (hardmetal and coating), tool micro-geometry, tool macro-geometry, cooling strategy, and dynamic structural behavior of machine, tool and workpiece. To improve the tool life of inner contour machining process, initial focus was laid on all these mentioned factors. However, scale of these factors ranges from micro-meter (in case of tool micro-geometry) to meter (in case of complete machine). Therefore, a single digital system cannot be used for optimizing all these factors because it will be time consuming as well as cost ineffective. Since economic efficiency is a key feature in the industrial environment, it is important to consider which level (micro or macro) of modelling technique from an economic and technical standpoint makes the most sense while implementing machining simulations. Figure 3.2 shows the strategy used in this thesis to optimize the above-mentioned parameters. The core of this strategy is FEM simulations, which can be used to optimize the tool material (hardmetal and coatings), tool micro-geometry, tool macro-geometry, cutting parameters and cooling strategy.

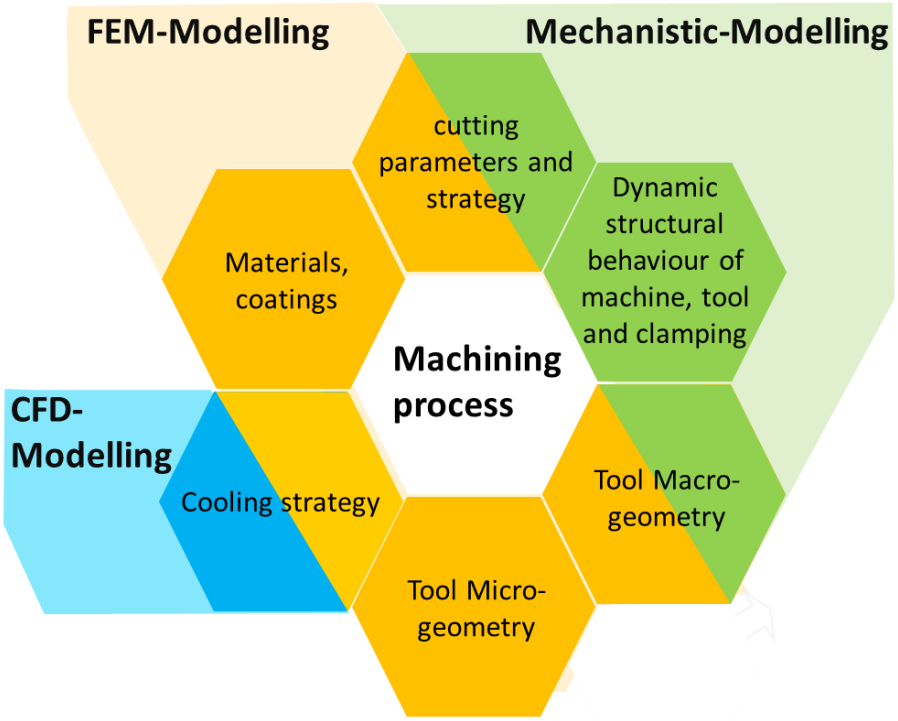

Figure 3-2: Factors during optimization of machining process

The three different modelling techniques mentioned in Figure 3.2 have one or few assumptions that may or may not exist. Thus, it becomes essential to calibrate and validate the simulations. Since 1.4837D turbine housing material was never simulated earlier, each FEM simulation was validated against experiments initially. It must be mentioned here that during this thesis work, simulations were conducted earlier than experiments. The FEM-simulations were used to optimize coating, coating thickness and micro-geometry of the tool. A design of experiment was created to optimize the cutting parameters via FEM simulations. Results of these simulations and experimental results for dry turning process are documented in chapter 4. Additionally, all these experiments were conducted on casted low nickel blanks of 1.4837D material due to the high cost of turbine housing part.

However, traditional FEM-simulations cannot model the lubricants and hence two coupling approaches were developed for cooling strategy, which are mentioned in detail in chapter 5. In the first approach two software were coupled with each other to simulate the flood lubricated internal turning simulations which were validated with experiments. To overcome the shortcomings of this approach, a second approach was developed in a single software to model the flood lubricated orthogonal turning simulations.

Mechanistic modelling techniques were used to optimize the cutting strategy and NC-program in this thesis work. Traditionally, orthogonal turning experiments were required to determine the force model in mechanistic modelling simulations, as defined in section 2.2.3.2. But in this thesis, FEM-simulations of orthogonal turning process were conducted to determine the force coefficients required for force model in mechanistic simulations, which is further explained in chapter 6. In the end, mass production hardmetal was combined with the best performing coating and coating thickness from chapter 4. Both, the existing mass-production tool and the new tool were simulated, and on comparison it was found that the new tool performed better than the existing tool, which is further mentioned in detail in chapter 6.

4 Simulation of dry turning process

One of the major steps to bring digitalization in product development and production optimization is by initially validating every simulation result with the corresponding experimentally measured values, which has also been done extensively in this research work. During this research work, all the simulations were conducted initially and then validated with the experimental results.

To reduce the workpiece material cost of casted turbine housing, experiments were conducted on casted blanks of the same material (1.4837D). Due to this reason, FEM-simulations were also conducted on simple workpiece geometry. The experiments and simulations were conducted according to the Design of Experiments (DoE) plan and it will be discussed in the next section.

The central question in this chapter is how well the predictions of a simulation correspond to reality (experiments) in the event of fine differences. Two DoEs were created to analyze and optimize the turning process of the 1.4837D material. In the first DoE, two different tool coatings were analyzed and in the second DoE, different coating thicknesses and cutting edge radii for the better performing coating from the first DoE were analyzed.

4.1 Design of Experiment (DoE) for simulations and experiments

To ensure a good comparability of all the experiments, a DoE plan was created in the first step which defines factors and their range. This is shown in Figure 4.1 as a cube plot diagram. The focus of the first DoE was to compare the two coatings, but the cutting speed, feed and depth of cut were also varied. Each corner point together with the center of the cube represents a parameter set for a test. This covers all combinations to ensure good informative value. The parameter set in the center of the cube was used to check whether the influence of the parameters between the corner points had a linear progression. If the results suggested a different course, additional parameter sets could be defined on the cube later. The ranges for the parameters are defined as follows: Feed $f = 0.1 - 0.25mm$, cutting speed $v_c = 90 - 170\,\frac{m}{min}$, depth of cut $a_p = 0.1 - 0.3mm$. All the DoE were built and analyzed in the Minitab software. Following the initial tests, the better performing coating was used to create a second DoE, whereby two different cutting edge radii and two different coating layer thicknesses were used. A coating layer thickness of 2 µm and 4 µm was applied to the two basic geometries with

cutting edge radius of 20 µm and 40 µm. This resulted in four sets of parameters with edge radii of 22 µm, 24 µm, 42 µm and 44 µm.

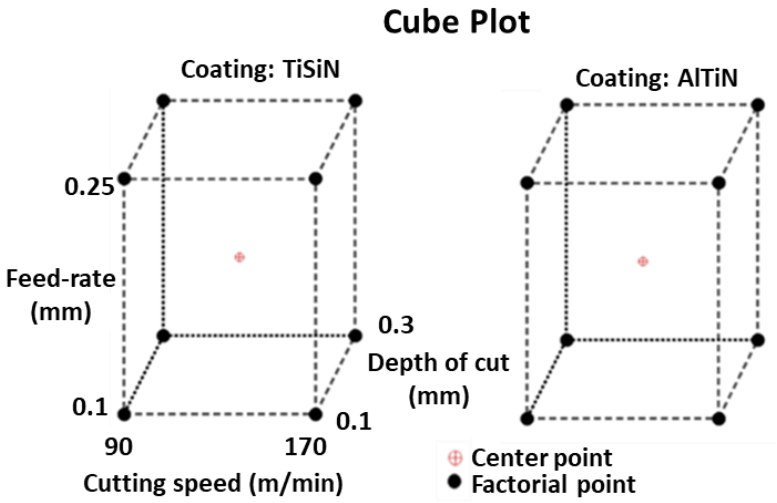

Workpiece material: 1.4837D Cooling: None	Cutting depth : a_p = var. Feed-rate : f = var. Cutting speed : v_c = var.	α_o	γ_o	ε_r	κ_r	Tool material: ISO-K10 Geometry: DCGT11T304-F Cutting edge radius: 12µm Corner radius: 0.4mm Coating: var.
Longitudinal turning		7°	15°	55°	93°	

Figure 4-1: Design of Experiment

4.2 Experimental setup of dry turning process

During this research work, experiments for two different turning processes were conducted: longitudinal cylindrical turning, and internal turning process. DCGT11T304-F inserts (α_o=7°, γ_o= 15°, ε_r= 55° and κ_r=93°) with substrate material ISO K10 and with different coatings and coating thicknesses were used in the experiments. Tool holder used in longitudinal turning experiments was SDJCL2020K11JET. The longitudinal cylindrical turning experiments were conducted on a CNC lathe Gildemeister CTX310. The machine specifications are mentioned in table A1 in appendix. During longitudinal turning experiments, process forces (cutting, feed and passive forces) and averaged surface roughness were measured for each parameter as per the DoE plan. Additionally, chips were collected for comparison with simulated chips. For each cutting parameter in the DoE plan, a new cutting edge was used so that wear doesn't influence the measured results. All the experiments were conducted without lubricants. Figure 4.2 shows the experimental setup of longitudinal turning process. During experiments, workpiece was rotated according to the cutting speed, whereas feed was given to the tool by its translational movement at a particular depth of cut. Additionally, for a cutting parameter (reference parameter) width of flank wear (VB) was measured to get an insight on tool life.

Process forces (cutting, feed and passive forces) were measured during experiments using quartz crystal 3-component-dynamometer type 9121 from Kistler. Recorded signals were converted into electrical voltages using the charge amplifier type 5017A from Kistler [152]. The electrical voltages were proportional to force components, and the measured force components were analyzed in the DIAdem software from National instruments. Averaged surface roughness were measured using the MarSurf M300 + RD18 device. Width of the flank wear (VB) and chips were analyzed with the Keyence VHX-5000 microscope.

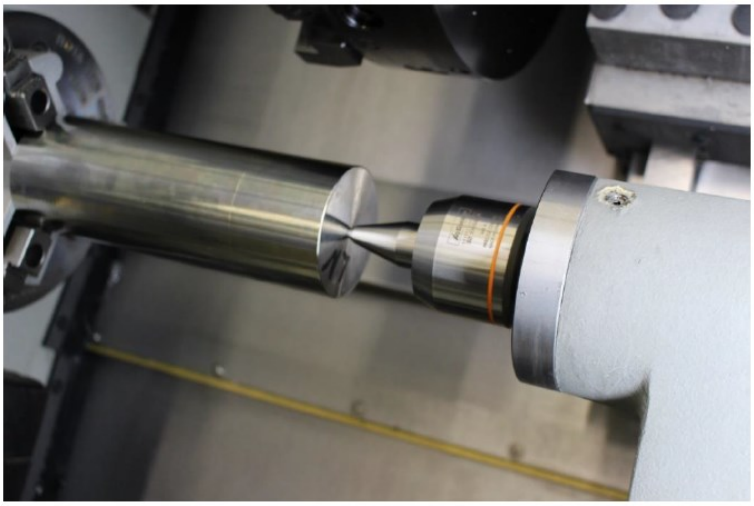

Figure 4-2: Experimental setup of longitudinal turning process

A two-color pyrometer FIRE-3 was used for temperature measurements during this work and the recorded results were analyzed in the OriginPro software. One of the major problems during temperature measurements in the research work mentioned in section 2.1.4 was the placement of thermocouple or pyrometer inside the tool, which was not exactly on the tool edge. This, on one hand, causes the tool to lose its strength and on the other hand, the temperature at the tool edge is not directly measured. To resolve this issue, a hole with a diameter of 700 µm, shown in figure 4.3 on the right side, was drilled in the workpiece and the pyrometer fiber was then placed inside this hole to record the temperature at the tool tip during the internal turning process. The experiments were conducted on a 4-axis Heller MC12 machining center and the experimental setup is shown in figure 4.3. The machine specifications for Heller MC12 are mentioned in table A1 in appendix. ISO K10 substrate DCGT11T304-F coated inserts (with α_o=7°, γ_o= 15°, ε_r= 55° and κr=93°) with tool holder SDJCL2525M11 were used in the experiments. Unlike longitudinal turning, both rotational and translational movement were provided to the tool here.

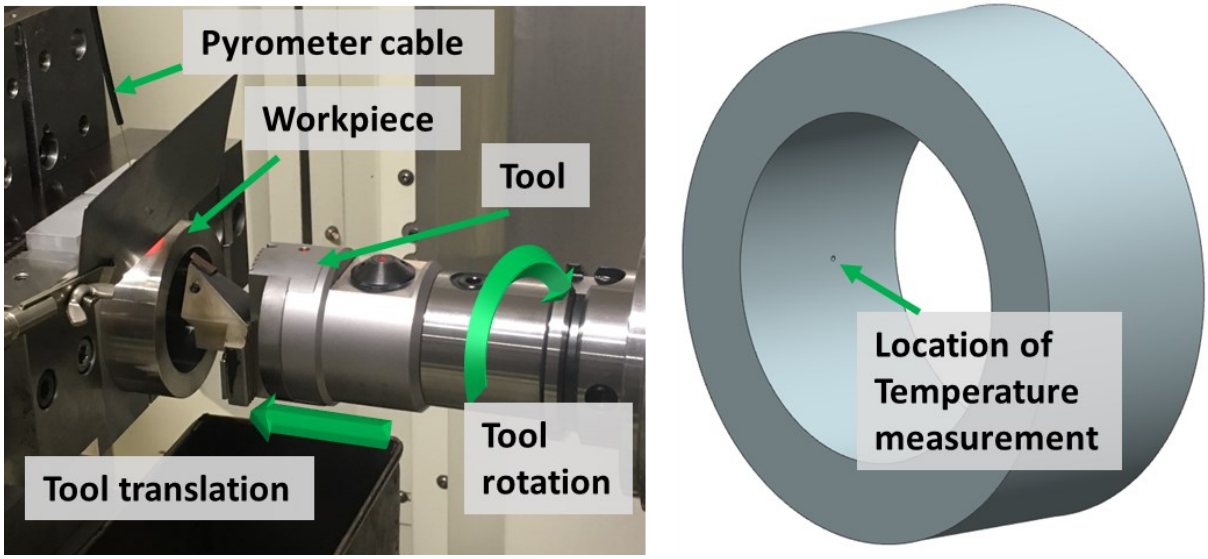

Figure 4-3: Experimental setup of internal turning process

4.3 Simulation setup of dry turning process

In this section, the simulation setup for both longitudinal cylindrical turning and internal turning process are described. The simulations were run without lubricant and were performed in AdvantEdge v7.9 software from the Third Wave Systems company. Since AdvantEdge only allows lagrangian formulation and explicit time integration method, they were used in FEM simulations. All the simulations were run at 16 core Dell Precision T7810 tower with Intel (R) Xeon (R) CPU E5-2667 computer system and 32 GB RAM. In simulations, simplifications are always made, in form of assumptions, as the exact representation of reality can be quite challenging because of the complex physics involved or due to high computational cost. These simplifications must be chosen carefully so that they do not affect the end simulation results by a huge percentage. Following assumptions were made during FEM-simulations:

- Both tool and workpiece were considered as homogenous materials
- Tool was considered as a thermo-elastic body and thus tool-wear was not considered in simulations
- Radiation heat transfer effects were neglected during FEM-simulations

The unit system used for FEM-simulations is mentioned in table 4.1:

Table 4-1: Unit system used in FEM-Simulations

Mass	Length	Time	Force	Stress	Temperature	Thermal conductivity	Heat Capacity
kg	mm	s	N	Pa	°C	$\frac{W}{m * °C}$	$\frac{J}{kg * °C}$

4.3.1 CAD-Modelling of dry turning process simulations

Due to the simplicity of workpiece geometry in simulations, they were prepared directly inside AdvantEdge. The workpiece dimensions used in linear longitudinal turning process (explained in section 4.5.1) were 30mm length, 5mm height and 2mm width, whereas workpiece dimensions used in internal turning process were 43mm inner diameter, 47mm outer diameter and 6mm length. CAD geometry of tool was provided by the tool supplier and only cutting edge radius was integrated on tool CAD model inside the Siemens NX software. For measurement of cutting edge radius, Alicona Infinite Focus G5 machine was used. For both turning processes (longitudinal and internal turning), tool holder CAD model was also provided by the tool supplier. However, to save the computational time, the CAD model was simplified by reducing the size of the tool to half for both the processes. CAD model of the tool was imported in .stp file format to the AdvantEdge software. Since during machining simulations, the focus was on the tool workpiece contact area, the above-mentioned simplification does not affect the simulation accuracy. The simplified version of CAD used in simulations for both turning processes is shown below in figure 4.4. It must also be observed in the same figure that longitudinal turning workpiece (right image) does not look like a traditional cylindrical turning workpiece from the experiments. The workpiece was simplified to save the computational time during simulations which will be discussed later in section 4.5.1 in detail.

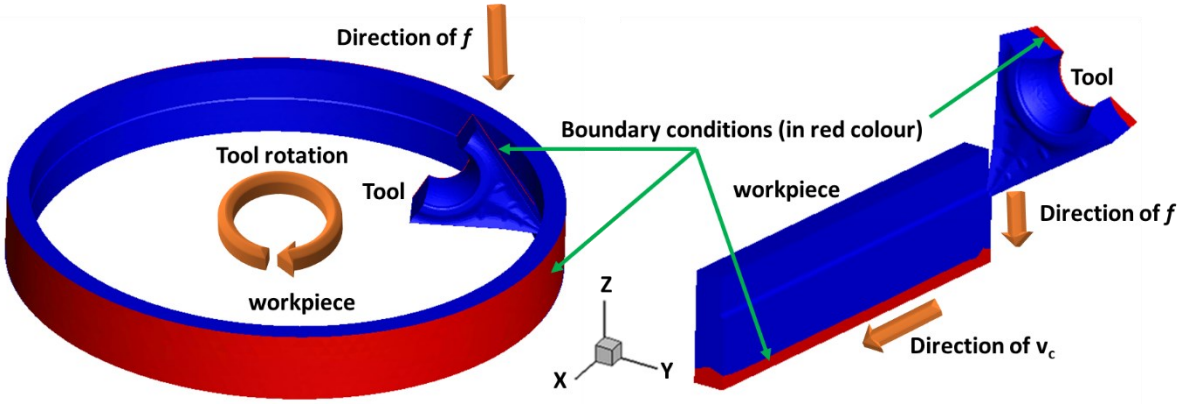

Figure 4-4: Simulation model setup of internal turning process (left) and linear longitudinal turning (right)

4.3.2 Material modelling of dry turning process simulations

A thermal and mechanical material model had to be defined for the simulation of the turning processes. During machining, plastic deformation of workpiece happens under high strain, strain-rate and temperature. This affects the flow stress of the material. Hence, for accurate prognosis via simulations, defining strain hardening, strain rate sensitivity and thermal softening material parameters of the workpiece becomes essential. As mentioned in section 2.2.1.4, there are various material models used by the researchers in past to define these flow stresses. In this research work, Power law is used for simulations. The selection of this material model (explained in section 2.2.1.4) was based on suggestions and research from the AdvantEdge support team. Like Johnson-Cook material model, material constants for Power-law model (mentioned in equation 2.9-2.15) are also found by the SHPB test. The SHPB test for material 1.4837D was performed at Leibniz Universität, Hannover. Based on the experimental raw data, the Power-law model was developed. From this measured data, flow curves for the material 1.4837D were plotted at different strain rate (from 0.001 to 100,000 s^{-1}) and at cut off strain of 3, which is shown in figure 4.5. Table 4.2 depicts the other experimentally measured material properties required to find the Power law constants.

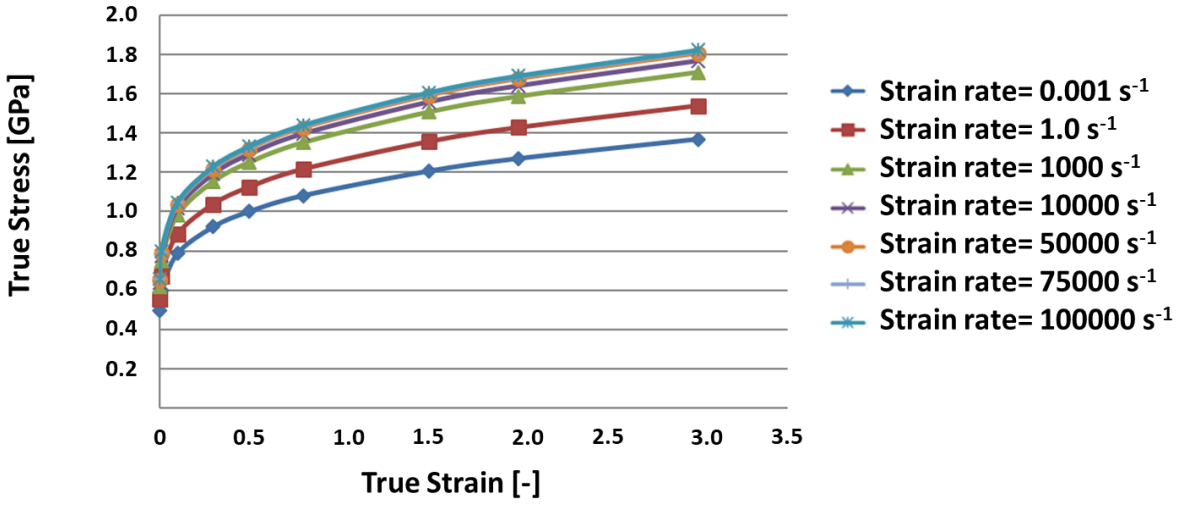

Figure 4-5: Flow Curve: 1.4837D material

Table 4-2: Material properties of 1.4837D material for FEM-simulations

Thermal conductivity (k)	13.4 $\frac{W}{m*°C}$
Heat capacity (c)	525 $\frac{J}{kg*°C}$
Density (ρ)	7820 $\frac{kg}{m^3}$
Young's Modulus (Y)	137 GPa
Poisson's ratio (υ)	0.3
Reference temperature (T)	20 °C
Melting temperature (T)	1590 °C
Yield Stress (σ_y)	350 MPa
Reference plastic strain (ε_0^p)	0.001

Polynomial fitting was used to determine the power law constants (strain hardening coefficient, thermal softening coefficients and strain rate coefficient) mentioned in equations 2.10-2.15. Equations 2.10 and 2.14 were modified by using logarithmic function to find strain hardening coefficient and strain rate coefficient. The modified equations are written as following:

$$\log\left(g(\varepsilon^p)\right) - \log\left(\sigma_0\right) = \frac{1}{n} * \log\left(1 + \frac{\varepsilon^p}{\varepsilon_0^p}\right) \quad 4.1$$

$$\log\left(\Gamma(\dot{\epsilon})\right) = \frac{1}{m_1} * \log\left(1 + \frac{\dot{\varepsilon}}{\dot{\varepsilon}_o}\right) \quad 4.2$$

Equation 4.1 and 4.2 are plotted in figure 4.6 and their slope gives the strain hardening coefficient (top figure) and strain rate coefficient (bottom figure).

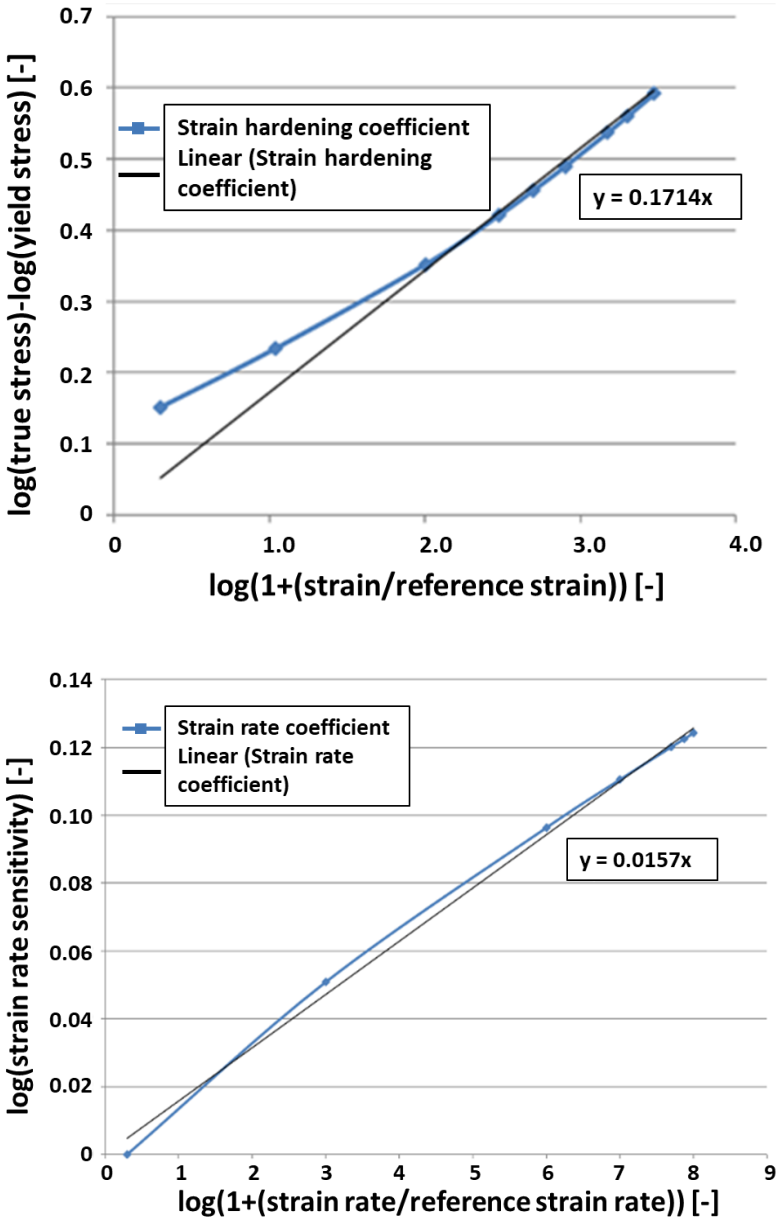

Figure 4-6: Strain hardening coefficient diagram (top), strain rate coefficient diagram (bottom)

For thermal softening coefficient (c_o to c_5), normalized stress vs temperature graph was plotted (as shown in figure 4.7) and a fifth order polynomial fit was used to find the coefficients.

Since no wear was considered on the tool during simulations, only elastic properties of tool and coatings were sufficient here. For tool ISO K10, substrate material was used in simulations with AlTiN and TiSiN PVD coatings of 3µm coating thickness.

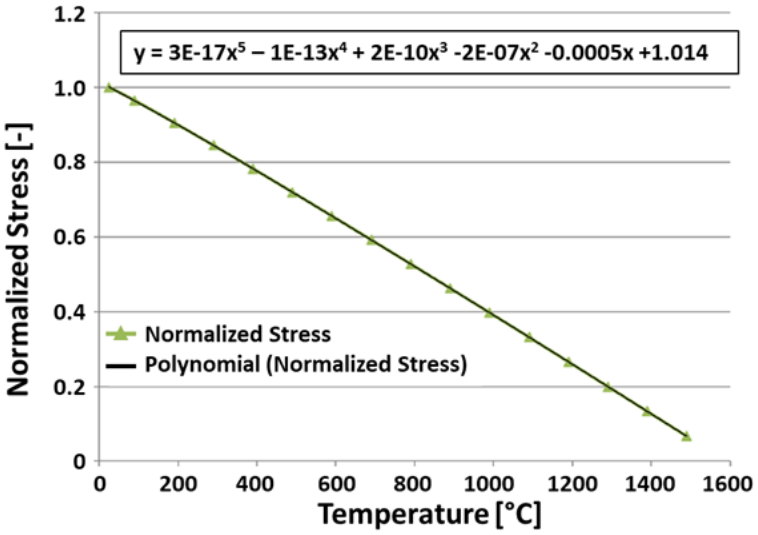

Figure 4-7: Thermal softening coefficients

4.3.3 Boundary conditions for dry turning process simulations

Cutting parameter (cutting speed, feed-rate and depth of cut) values used in simulations were same as those set on CNC machine during experiments. In longitudinal turning and internal turning simulations, cutting parameters were provided to the tool. During longitudinal turning simulations, the tool was also provided with translational constraints in Y and Z-directions (shown in figure 4.4 on right side) and rotational constraints were set in all the three directions. Bottom of workpiece was kept fixed in all the three directions for both, translational and rotational movement. On the contrary, in internal turning simulations, rotational and translational movement were constrained for the tool in X and Y-direction. The feed per revolution was provided to the tool as a translational movement, and cutting speed as a rotational movement along the Z-axis (as shown in figure 4.4, left side). Like the longitudinal turning process, workpiece was kept fixed in all the three directions for both, rotational and translational movement.

Since thermo-mechanical simulations were conducted, an initial room temperature of 20°C was defined in the simulation environment. AdvantEdge defines an automatic contact between the tool-workpiece, workpiece-chip and chip-tool. During this research work, only coulomb friction model was available in AdvantEdge and hence it was used to define the friction between the tool and workpiece. Coefficient of friction (COF) values for both coatings were provided by the supplier. For AlTiN coating, a friction coefficient of COF= 0.6 was defined in simulations, whereas for TiSiN coating, a friction coefficient of COF= 0.65 was used. To attain

a one-on-one comparison with experiments, all the simulations were conducted without any lubricant, i.e., dry machining simulations were conducted.

4.3.4 Meshing for dry turning process simulations

During any numerical simulation, meshing plays an important role, as the accuracy of simulation depends on it. A coarse mesh can lead to incorrect prognosis of the results, whereas a very fine mesh can increase the simulation time enormously, especially in case of explicit simulations where simulation time step depends on the smallest element size. Due to this reason, sensitivity of mesh was analyzed and is discussed in detail in the section 4.5.2. For both, tool and workpiece, tetrahedral mesh was used in the simulations and mesh was created in the AdvantEdge software. In AdvantEdge, remeshing of distorted elements during machining simulations was created automatically based on set initial mesh parameters. The final mesh used in two process simulations after mesh sensitivity analysis is shown figure 4.8.

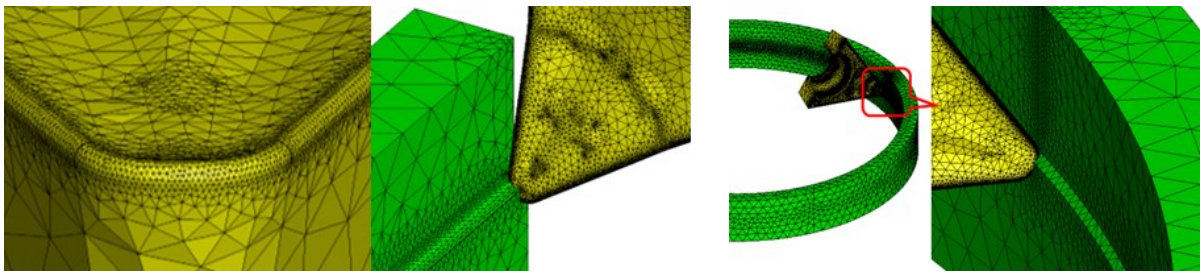

Figure 4-8: Mesh used in simulations: longitudinal turning (left) and internal turning process (right)

4.4 Experimental results of first DoE

4.4.1 Comparison of different coatings

In the first set of experiments, two different PVD coatings namely AlTiN and TiSiN of coating thickness 3µm each were used. The other test parameters were defined by DoE and they correspond to the eight corner points and the center point from Figure 4.1. This results in a total of nine parameter sets for each coating. To eliminate external influences, each experiment was conducted twice, and they were conducted randomly.

Figure 4.9 shows an example of a force curve measured from longitudinal turning experiments. To compare the machining forces occurring from individual experiments, a representative force was determined for each of the DoE parameters. For this purpose, a 10s segment from the force

measurements was used as soon as the tool cutting edge reached the defined engagement. The measured forces were then sorted in descending order and the force at 95% of the value was read out as the representative force. This means that 5% of the forces were greater than this read out force value. This method filters out extreme force values and ensures good comparability between the force values from different DoE parameters and tools.

It can be observed from the same figure that the cutting force was the dominant force component among the three components. The cutting force F_c= 114N, passive force F_p= 32N and feed force F_f= 64N were recorded for the TiSiN coated tool with cutting parameter v_c=130m/min, f=0.175mm and a_p=0.2mm. In this figure, high fluctuations in force values can be observed for all the three force components. These fluctuations are due to high toughness of the 1.4837D material. The high toughness of material allows it to store more elastic energy, resulting in excitation of tool system which ultimately leads to force fluctuations. Such force fluctuations were also observed in other machining processes of 1.4837D material [17].

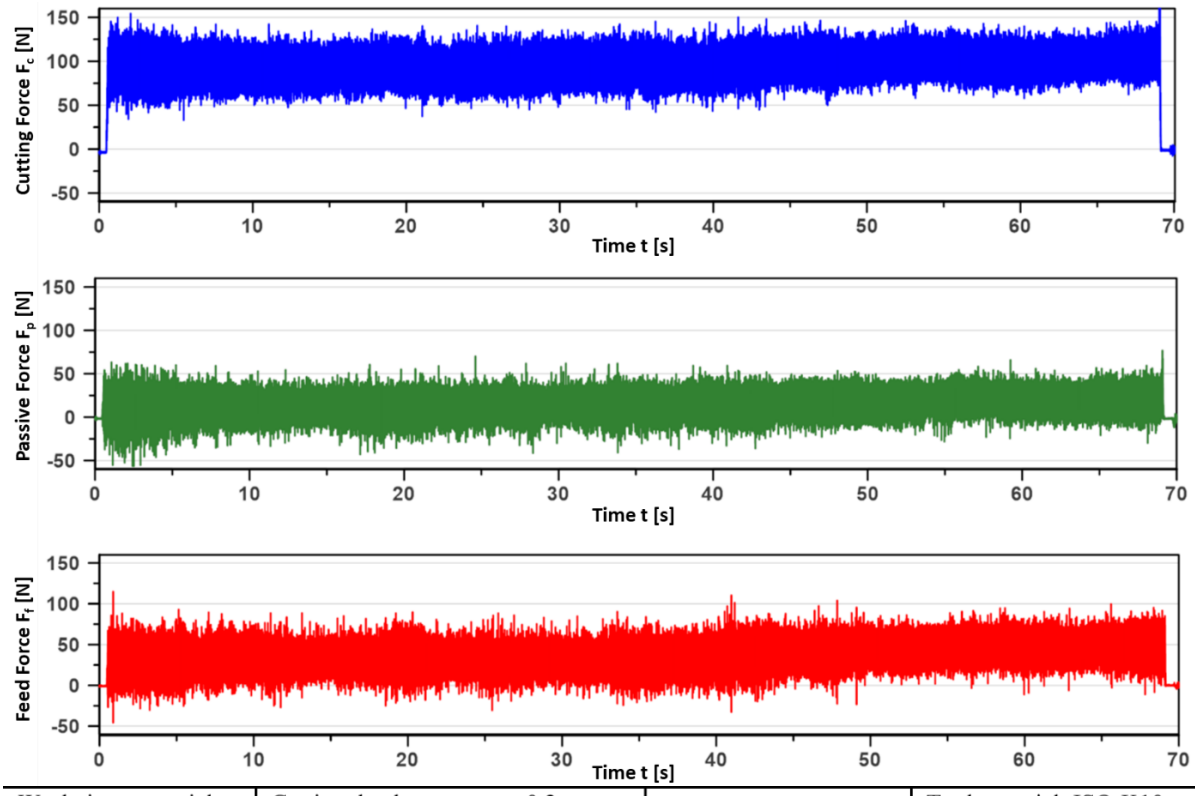

Workpiece material: 1.4837D Cooling: None	Cutting depth : a_p = 0.2mm Feed-rate : f = 0.175mm Cutting speed : v_c = 130m/min	α_o	γ_o	ε_r	κ_r	Tool material: ISO-K10 Geometry: DCGT11T304-F Cutting edge radius: 12µm Corner radius: 0.4mm Coating: TiSiN Coating thickness: 3µm
Longitudinal turning		7°	15°	55°	93°	

Figure 4-9: Example of a force measurement, parameters of this measurement: TiSiN-Coating, v_c=130m/min, f=0.175mm, a_p=0.2mm

Figure 4.10 shows the results of cutting forces for each DoE parameter and both the coatings. The color bar in the diagram represents the mean value of the parameter. The table at the bottom of the image shows the corresponding machining parameters. The maximum cutting force occurs with the maximum feed-rate of f=0.25mm and depth of cut of a_p=0.3mm. The majority of cutting parameters with AlTiN coating had lower forces in comparison to the TiSiN coating. This is due to the low coefficient of friction of AlTiN coating. This lower coefficient of friction reduces the tool-workpiece adhesion and material sticking, which in turn reduces the cutting forces. For TiSiN coating, when the cutting forces were compared for first three set of cutting parameters from DoE (as shown in figure 4.10), it was observed that the forces decreased with an increase in the feed-rate or depth of cut. This reduction in force was because at very small chip thickness (relative to 12µm cutting edge radius), ploughing effect dominated and specific cutting force was high. Increasing depth of cut or feed increased effective chip thickness, reduced ploughing effect, and made cutting more efficient, hence lowering the measured force.

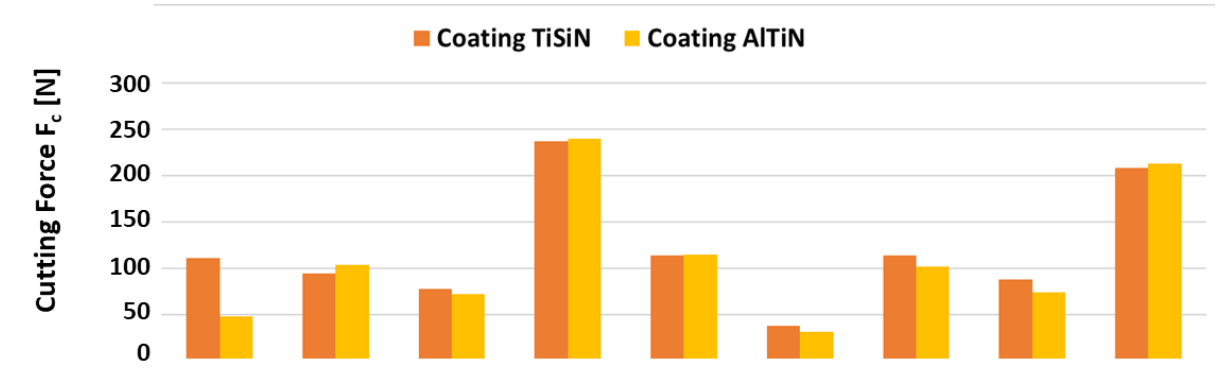

v_c (m/min)	90	90	90	90	130	170	170	170	170
f (mm)	0.1	0.1	0.25	0.25	0.175	0.1	0.1	0.25	0.25
a_p (mm)	0.1	0.3	0.1	0.3	0.2	0.1	0.3	0.1	0.3

Workpiece material: 1.4837D
Cooling: None
Longitudinal turning

α_o	γ_o	ε_r	κ_r
7°	15°	55°	93°

Tool material: ISO-K10
Geometry: DCGT11T304-F
Cutting edge radius: 12µm
Corner radius: 0.4mm
Coating: var.
Coating thickness: 3µm

Figure 4-10: Comparison of the cutting forces during longitudinal cylindrical turning

The roughness measurements from longitudinal cylindrical turning are shown in Figure 4.11 below. Roughness profile height Rz was determined as roughness parameter for the surfaces. A high value corresponds to a poor surface quality. High roughness was measured for parameter sets with the maximum feed-rate and depth of cut, where higher forces also played their part. It must be noted in this diagram that TiSiN coating is worse than AlTiN coating in six out of nine

cases, with a difference of more than 30% in four cases. Low roughness values were measured for low tool engagements.

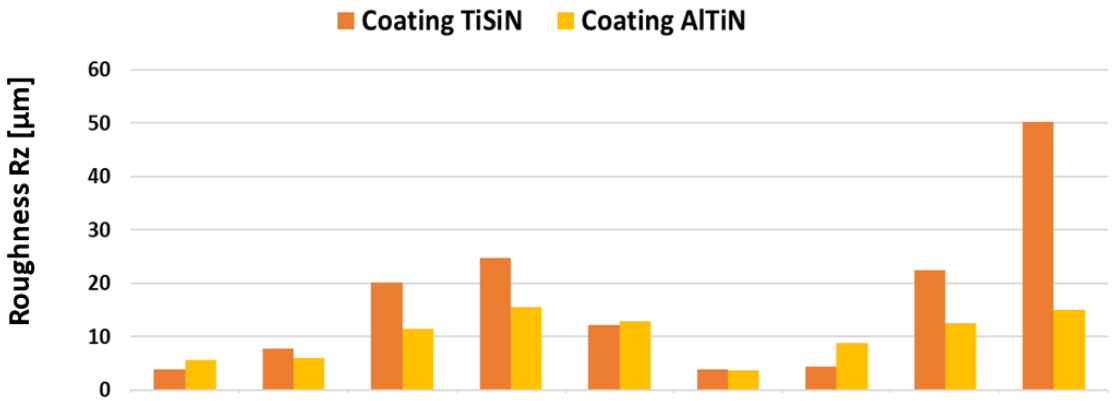

v_c (m/min)	90	90	90	90	130	170	170	170	170
f (mm)	0.1	0.1	0.25	0.25	0.175	0.1	0.1	0.25	0.25
a_p (mm)	0.1	0.3	0.1	0.3	0.2	0.1	0.3	0.1	0.3

Workpiece material: 1.4837D
Cooling: None
Longitudinal turning

α_o	γ_o	ε_r	κ_r
7°	15°	55°	93°

Tool material: ISO-K10
Geometry: DCGT11T304-F
Cutting edge radius: 12µm
Corner radius: 0.4mm
Coating: var.
Coating thickness: 3µm

Figure 4-11: Comparison of the averaged surface roughness profile (Rz) during longitudinal cylindrical turning

Figure 4.12 shows the image of chips for every cutting parameter of TiSiN coated inserts. It can be noticed that during machining, spiral chips were produced with most of the cutting parameters and these chips were acceptable. Comparable spiral chips were also produced with AlTiN coated cutting inserts. Chip shapes will be compared with simulated chip shapes in the upcoming sections.

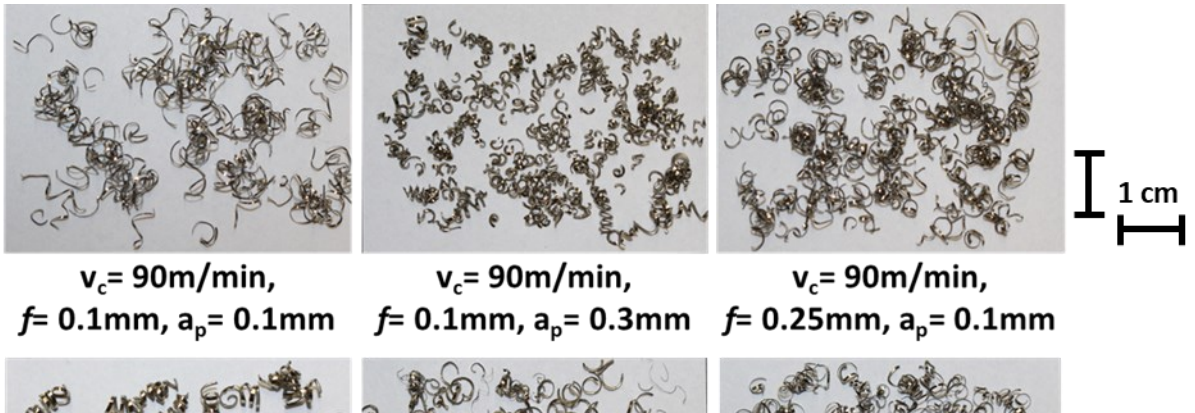

v_c= 90m/min, f= 0.1mm, a_p= 0.1mm | v_c= 90m/min, f= 0.1mm, a_p= 0.3mm | v_c= 90m/min, f= 0.25mm, a_p= 0.1mm

v_c= 90m/min, f= 0.25mm, a_p= 0.3mm | v_c= 130m/min, f= 0.175mm, a_p= 0.2mm | v_c= 170m/min, f= 0.1mm, a_p= 0.1mm

v_c= 170m/min, f= 0.1mm, a_p= 0.3mm | v_c= 170m/min, f= 0.25mm, a_p= 0.1mm | v_c= 170m/min, f= 0.25mm, a_p= 0.3mm

Workpiece material: 1.4837D Cooling: None Longitudinal turning	α_o | γ_o | ε_r | κ_r 7° | 15° | 55° | 93°	Tool material: ISO-K10 Geometry: DCGT11T304-F Cutting edge radius: 12µm Corner radius: 0.4mm Coating: TiSiN Coating Thickness: 3µm

Figure 4-12: Experimental chips for TiSiN coated insert

As mentioned in section 4.2, temperature has a major influence on the machining process. Therefore, it was additionally measured in the internal turning process on the cutting edge of the tool using a two-color pyrometer. Figure 4.13 shows an example of a temperature curve recorded for the TiSiN coated tool with cutting parameter v_c=130m/min, f=0.175mm and a_p=0.2mm measured during internal turning experiments. On the left side in the figure, voltage measurements from pyrometer are plotted. The number of voltage measurements changed based on the feed-rate. For example, for the feed-rate f=0.1mm, around 7 measurements were recorded (as the measuring hole diameter was 700µm in each experiment as shown in figure

4.3), whereas for the feed-rate f=0.25mm, only three measurements were recorded. The temperature result corresponding to the second peak is shown on the right side of figure 4.13. It can be observed that when the tool cutting edge passes over the measurement hole, the temperature rises sharply to the peak value and as the tool moves away from the measuring hole, the temperature reduces slowly because of the specific heat and thermal conductivity of 1.4837D material. To get the representative temperature value from each temperature curve, only the initial temperature peak curve was considered and the temperature at 95% of the value was read out as the representative value. This means that 5% of the temperature was greater than this read out value. This method filtered out extreme temperature values and ensured good comparability between the temperature results from different DoE parameters and tools. Lastly, all four voltage measurements were visualized and the mean value of representative temperature from each curve was taken as the final temperature value and compared with simulations.

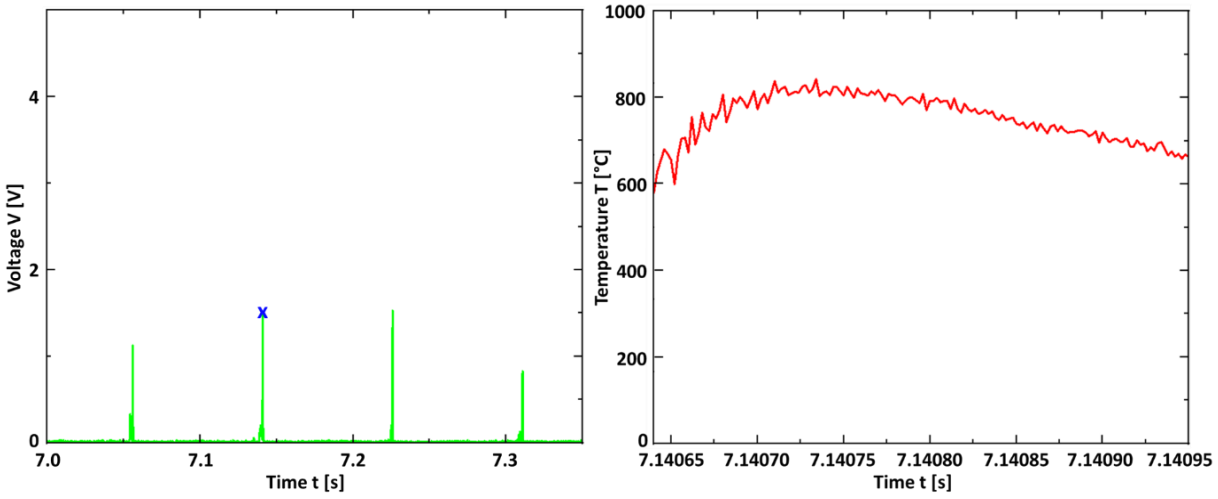

Figure 4-13: Example of a temperature measurement, parameters of this measurement: TiSiN-Coating, v_c=130m/min, f=0.175mm, a_p=0.2mm

In Figure 4.14, temperature results are plotted for both the coatings and each of the DoE parameters. The maximum temperatures were recorded in the tests with larger cutting parameters. In six of the nine parameter sets, the AlTiN coating has a lower temperature than the TiSiN coating. This difference in temperature is due to the lower coefficient of friction for AlTiN coated cutting inserts than TiSiN coated inserts.

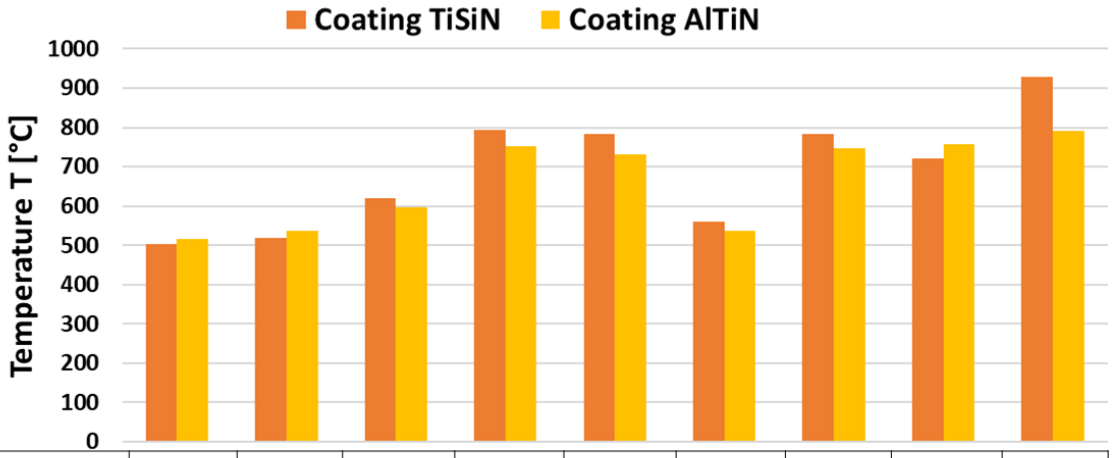

v_c (m/min)	90	90	90	90	130	170	170	170	170
f (mm)	0.1	0.1	0.25	0.25	0.175	0.1	0.1	0.25	0.25
a_p (mm)	0.1	0.3	0.1	0.3	0.2	0.1	0.3	0.1	0.3

Workpiece material: 1.4837D
Cooling: None
Internal turning

α_o	γ_o	ε_r	κ_r
7°	15°	55°	93°

Tool material: ISO-K10
Geometry: DCGT11T304-F
Cutting edge radius: 12µm
Corner radius: 0.4mm
Coating: var.
Coating thickness: 3µm

Figure 4-14: Comparison of temperatures during internal turning process

Wear width (VB) was measured on the flank face of coated inserts to further investigate the tool lives of two coatings. Wear was not measured on all the cutting parameters from DoE plan but on a particular cutting parameter (like production parameter): v_c= 140m/min, f = 0.22mm and a_p = 0.1mm. These experiments were also carried out twice to eliminate the external influences. Wear experiments were conducted on 1.4837D material casted blanks and not on a real turbine housing.

The goal during these experiments was to produce around 90 turbine housing parts and the maximum tool wear criteria was set to VB=100µm. The VB curve for the two coatings at v_c= 140m/min, f = 0.22mm and a_p= 0.1mm is shown below in figure 4.15.

The result depicts that for both the coatings, the tool was severely worn. It can be observed that both the inserts reach the wear criteria of VB= 100µm at machining of around 40 parts. This indicates that the wear of both the tool coatings exceeded the specified wear criteria for the target parts that were to be manufactured. Additionally, it was noticed that after 50 parts were machined, there was a sharp increase in wear for the TiSiN coated inserts as compared to the AlTiN coated inserts. This sudden increase in wear was because of the delamination of TiSiN coating from the cutting insert. This implies that for this cutting parameter, AlTiN coating had

lesser wear in comparison to TiSiN coating once the target parts were produced. Figure 4.16 shows the flank wear width of two coatings after the production of target of 90 parts. After the production of 90 parts, AlTiN coated inserts had a flank wear width of 235µm whereas for TiSiN coating inserts, the flank wear width was 588µm.

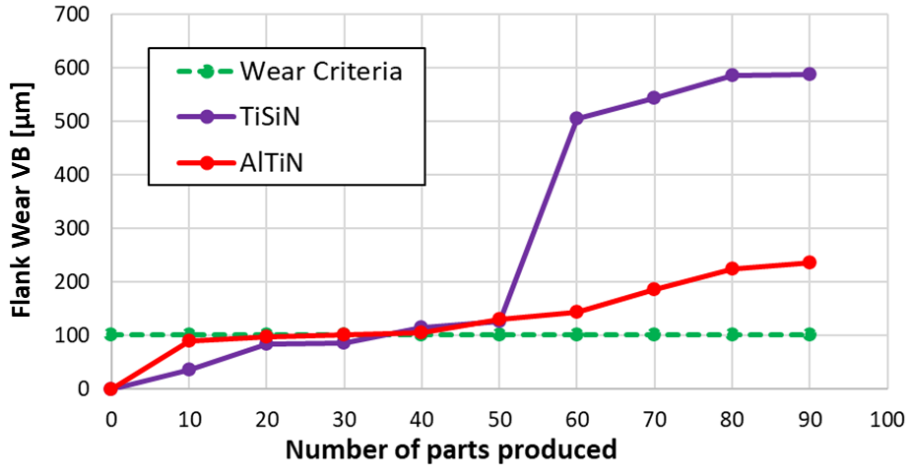

Workpiece material: 1.4837D Cooling: None	Cutting depth : $a_p = 0.1$mm Feed-rate : $f = 0.22$mm Cutting speed : $v_c = 140$m/min	α_o	γ_o	ε_r	κ_r	Tool material: ISO-K10 Geometry: DCGT11T304-F Cutting edge radius: 12µm Corner radius: 0.4mm Coating: var. Coating thickness: 3µm
Longitudinal turning		7°	15°	55°	93°	

Figure 4-15: Flank wear curve for TiSiN and AlTiN coating

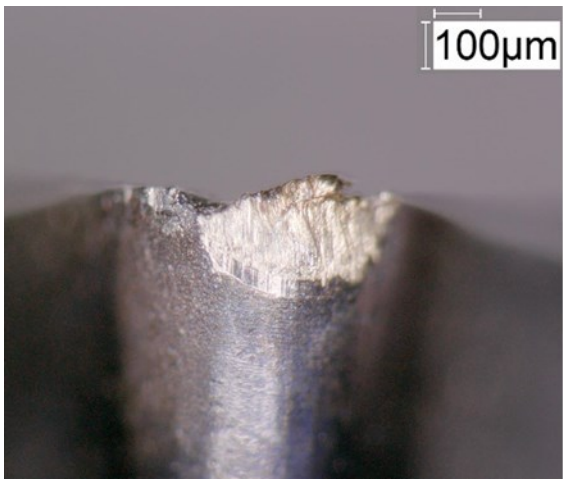

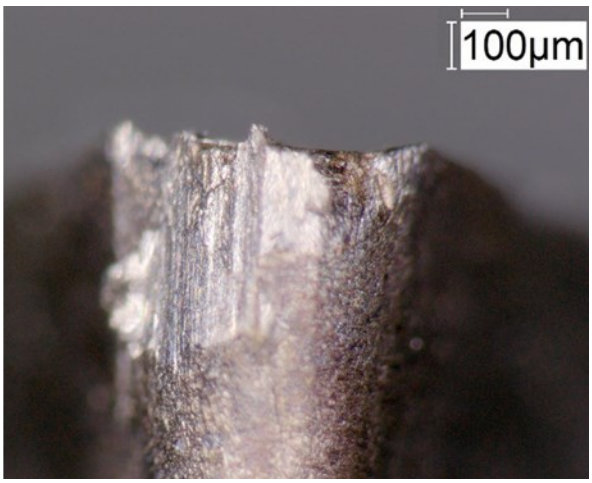

Workpiece material: 1.4837D Cooling: None	Cutting depth : $a_p = 0.1$mm Feed-rate : $f = 0.22$mm Cutting speed : $v_c = 140$m/min	α_o	γ_o	ε_r	κ_r	Tool material: ISO-K10 Geometry: DCGT11T304-F Cutting edge radius: 12µm Corner radius: 0.4mm Coating: var. Coating thickness: 3µm
Longitudinal turning		7°	15°	55°	93°	

Figure 4-16: Wear on the tool cutting edge after 90 parts AlTiN coating (left), TiSiN coating (right)

4.4.2 Evaluation of first DoE results

The influence of an individual test parameter is not always apparent. Therefore, linearized correlations between the measured variables and input factors from the DoE plan are shown in following diagrams. These diagrams were created through analysis of DoE results in the Minitab software. To create these diagrams, the mean value of measured variables (forces, roughness and temperature) was chosen for both, corner points and center point, in the DoE plan. The corner points create a straight line and the distance of the center point from this straight line indicates whether a linear relationship exists. In case there is a significant distance of center point from the straight line, it implies that the measured variable does not indicate a linear relationship and hence no statements can be made about that parameter.

In the following figure 4.17, influence of input parameters on cutting force F_c, feed force F_f and passive force F_p is examined. For cutting speed, a similar relationship can be seen for all the three force components. With an increase in cutting speed, the forces decrease. This reduction in force values is due to the thermal softening of material caused by a high temperature of machining system at a high cutting speed. This behavior therefore corresponds to what is defined and expected in literature [153]. It can also be observed that cutting force F_c is the dominant force among the three force components and thus will play a major role in the tool-life.

The feed-rate and depth of cut determine the chip cross-section area during the machining process. This has a significant influence on forces, whereby the forces increase with the larger chip cross-section area, i.e., a large feed-rate or a large depth of cut. This effect can be clearly seen in the diagrams below. The influence of the depth of cut on the cutting force is higher than that of the feed-rate. This is in line with the expectations and information from the literature [153].

Additionally, the center point of DoE (red color dot in figures) is very close to the straight line for cutting and feed force. Therefore, a linear relationship between the two forces can be assumed with all the four input parameters from the DoE plan. However, passive force has minor deviations, but they are insignificant. Lastly, the AlTiN coated inserts have lower forces for all three components in comparison to the TiSiN inserts. The low forces for AlTiN coated inserts are because of the low tool temperatures (caused by low coefficient of friction), which is explained in figure 4.14. This low tool temperature reduces the tool-workpiece adhesion and material sticking, in turn reducing the cutting forces.

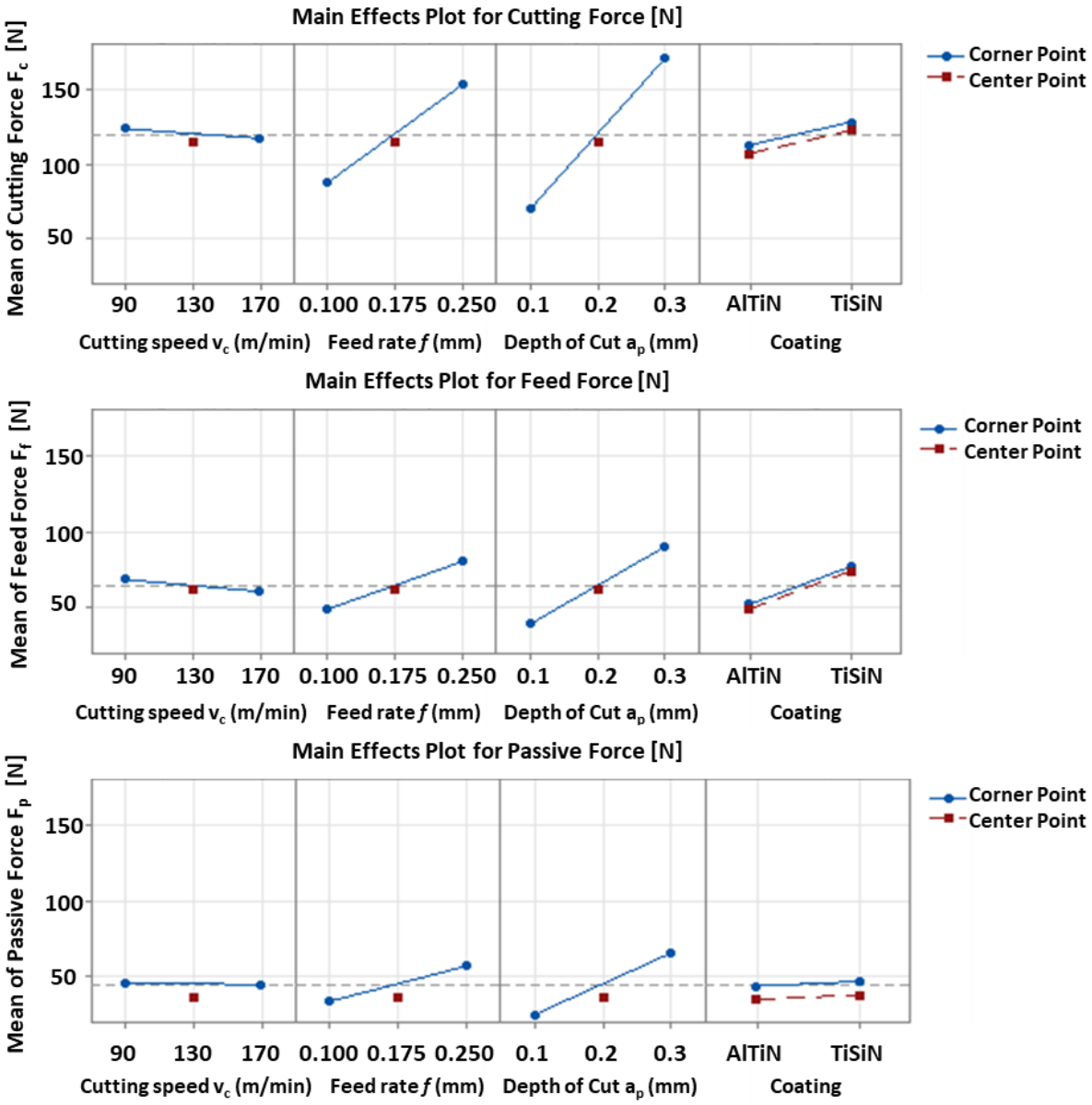

Workpiece material: 1.4837D Cooling: None	Cutting depth Feed-rate Cutting speed	a_p = var. f = var. v_c = var.	α_o	γ_o	ε_r	κ_r	Tool material: ISO-K10 Geometry: DCGT11T304-F Cutting edge radius: 12µm Corner radius: 0.4mm Coating: var. Coating thickness: 3µm
Longitudinal turning			7°	15°	55°	93°	

Figure 4-17: Linearized relationships between the test factors, cutting speed, feed-rate, depth of cut and coating to the measured variable: Cutting force (Top), Feed force (middle) and passive force (bottom)

For turbine housing inner contour turning process, Rz =12.5µm is the averaged surface roughness requirement in bearing seat area. Hence, it was measured and analyzed. Figure 4.18 shows the influence of test parameters on the averaged surface roughness profile height Rz. A lower Rz value represents a better surface quality. This good surface quality was clearly

measured for all the three cutting parameters at their respective lower limits, which implies that a lower cutting speed, lower feed-rate and lower depth of cut provide better results.

However, the feed-rate has a dominating effect on the averaged surface roughness (Rz). The roughness measurements were in accordance with the theoretical roughness depth (R_{th}) given by the following equation [9]:

$$R_{th} = \frac{f^2}{8r_\epsilon} \qquad 4.3$$

where r_ϵ is the corner radius of the tool.

The theoretical surface roughness for the three feed-rates (0.1mm, 0.175mm and 0.25mm) used in this DoE were calculated by using equation 4.3 as 3.125µm, 9.57µm and 19.53µm respectively. These calculations were in good correlation with the measured values in figure 4.19. It can also be observed from figure 4.18 and 4.19 that coating had a major influence on the surface profile. When comparing the two coatings, AlTiN was again found to be better. Figure 4.19 shows the measured roughness profile heights in a cube diagram. Each roughness value in this diagram corresponds to the mean values of the measurements taken twice in experiments.

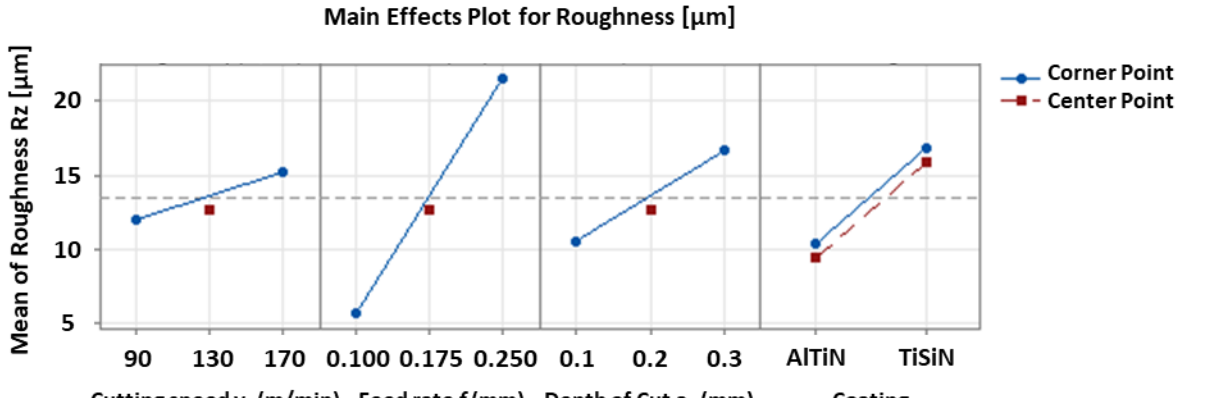

Workpiece material: 1.4837D Cooling: None Longitudinal turning	Cutting depth Feed-rate Cutting speed	a_p = var. f = var. v_c = var.	α_o	γ_o	ε_r	κ_r	Tool material: ISO-K10 Geometry: DCGT11T304-F Cutting edge radius: 12µm Corner radius: 0.4mm Coating: var. Coating thickness: 3µm
			7°	15°	55°	93°	

Figure 4-18: Linearized relationships between the test factors, cutting speed, feed-rate, depth of cut and coating to the measured variable: averaged surface roughness Rz

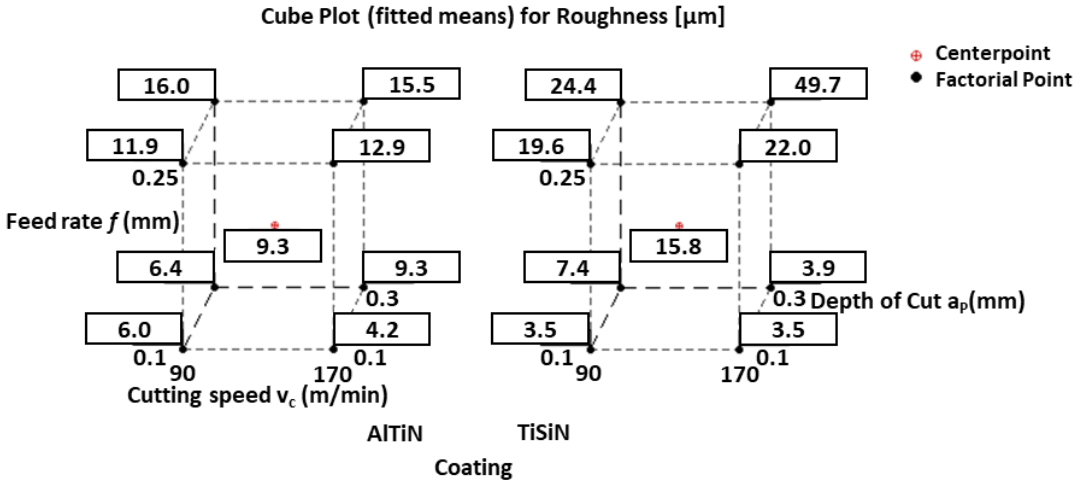

Figure 4-19: Representation of the measured roughness Rz for the parameter sets in the cube diagram

One of the major roles of a coating on substrate material is to protect the tool from thermal loads, as it affects the tool life. A lower tool temperature tends to be better for the tool life. Therefore, analyzing temperature on tools become vital during the optimization of machining process. The temperature results from internal turning process were analyzed like forces and surface profile roughness in the Minitab software. Figure 4.20 shows relationships between cutting speed, feed-rate, depth of cut, both coatings and measured mean temperature values. It can again be observed that lower cutting parameters provide better results, i.e., low temperatures. Additionally, an increase in cutting parameters lead to high temperatures.

It should be noted that the center point (red dot) in figure 4.20 is far away from straight line that joins the corner points. This indicates a non-linear relationship of temperature with the set of tested parameters [154]. In the case of coatings, AlTiN again performed better and was therefore also selected for further tests in the second DoE. Figure 4.21 shows the measured temperature results for the corresponding cutting parameters from the DoE plan. Highest temperature (worst results) occurred with TiSiN coated inserts at v_c=170m/min, f=0.25mm and a_p=0.3mm.

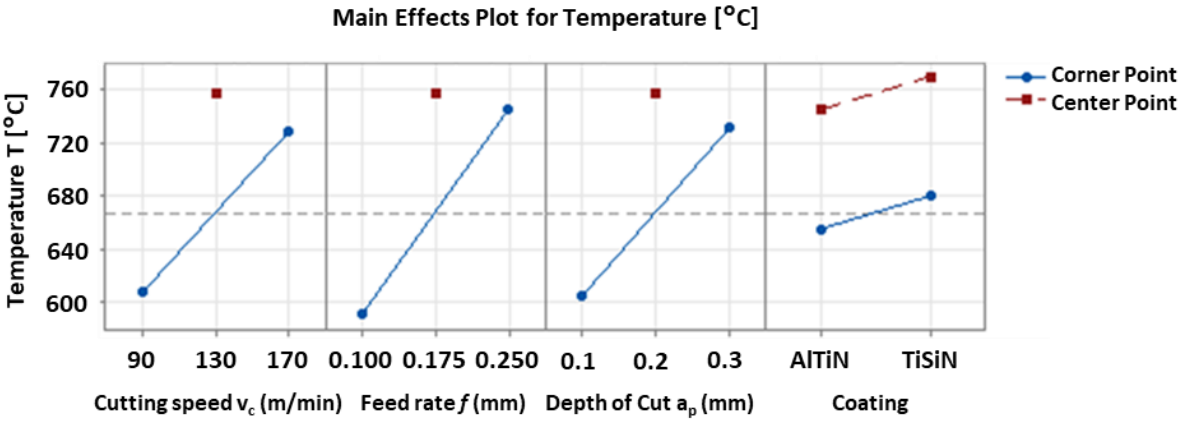

Workpiece material: 1.4837D Cooling: None Internal turning	Cutting depth : a_p = var. Feed-rate : f = var. Cutting speed : v_c = var.	α_o | γ_o | ε_r | κ_r 7° | 15° | 55° | 93°	Tool material: ISO-K10 Geometry: DCGT11T304-F Cutting edge radius: 12µm Corner radius: 0.4mm Coating: var. Coating thickness: 3µm

Figure 4-20: Linearized relationships between the test factors, cutting speed, feed-rate, depth of cut and coating to the measured variable: Temperature

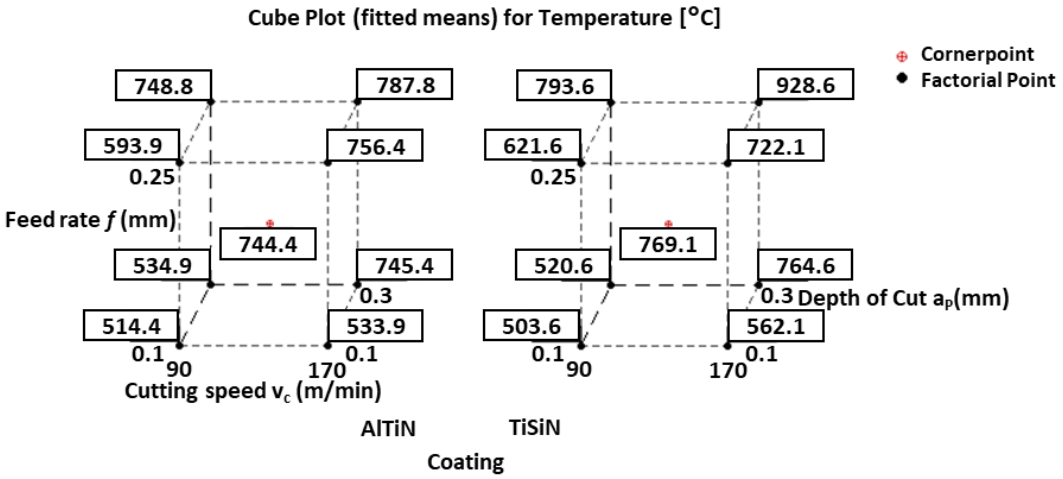

Figure 4-21: Representation of the measured temperatures for the parameter sets in the cube diagram

4.5 Simulation results: Comparison of coatings (DoE 1)

Two parametric studies were conducted with an aim to save the computational cost (simulation time) during simulations and to find the best suitable mesh size. They served as a base for all the dry longitudinal turning and internal turning process FEM-simulations. These studies were conducted on a 3µm AlTiN coated DCGT11T304-F (α_o=7°, γ_o= 15°, ε_r= 55° and κ_r=93°) tool with ISO-K10 hardmetal for the cutting parameter v_c=90m/min, f=0.25mm and a_p=0.3mm. The

results of these parametric studies are mentioned below. The FEM-simulation results of longitudinal turning and internal turning process from the DoE plan will be discussed in detail after that.

4.5.1 Parametric study: Longitudinal turning vs linear longitudinal turning

In the first parametric study, a 3D-longitudinal turning simulation was run in two different variants available in the AdvantEdge software: one, longitudinal turning and two, a simplified version of longitudinal turning based on process kinematics, as shown in figure 4.22. Longitudinal turning (right image in figure 4.22) was a direct replica of the real experiments conducted in the previous section. During longitudinal turning simulations, cutting speed was provided to the workpiece, whereas feed-rate and depth of cut was given to the tool. In the linear longitudinal turning, it was assumed that the diameter of the workpiece was high enough to neglect the curvature effect of the workpiece. Thus, in contrast to reality, the simulation used a linear workpiece. The process kinematics from the experiment was, however, replicated in this process. The workpiece was in a cuboid form for linear longitudinal turning process as shown in figure 4.22 (left). All the cutting parameters (v_c, f and a_p) were provided to the tool during simulation. The major benefit of linear longitudinal turning simulations over outer turning simulations is that if the meshing parameters are kept identical in the two simulations, linear longitudinal turning takes less computational time. To keep the simulation time to a minimum, both the longitudinal turning simulations were carried out for a corresponding length of 15.7mm. A comparison of process kinematics of the longitudinal turning and linear longitudinal turning process was provided by AdvantEdge support and is shown in figure A1 in the appendix chapter.

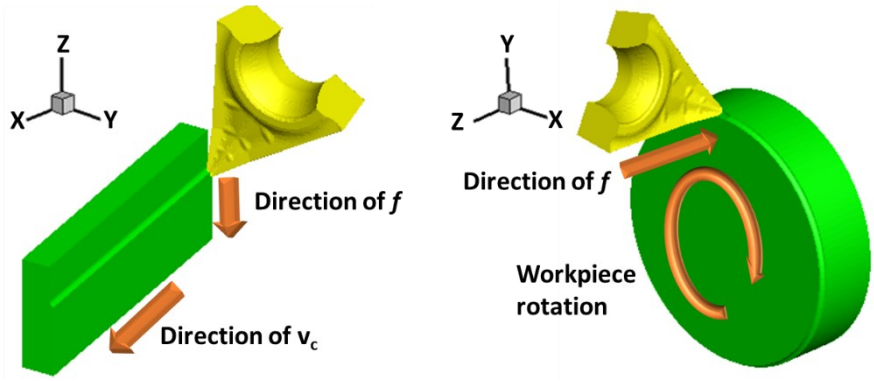

Figure 4-22: Linear longitudinal turning (left), Longitudinal turning (right)

The post-processing of simulation results was conducted in the Tecplot software. For this parametric study, cutting force and temperature curves from linear longitudinal turning and outer turning were plotted against each other, which is shown in figure 4.23. The other two force coefficients, i.e., feed force and passive force were also compared and are shown in appendix in figure A2. It can be observed from figure 4.23 that magnitude of the cutting force is similar (difference of approximately 2%) in both the simulations. However, due to the difference in cutting axis direction, cutting force for outer turning is in negative direction. On the other hand, feed-rate and depth of cut directions were same in both the simulations and thus feed force and passive force values overlap each other in figure A2 in appendix.

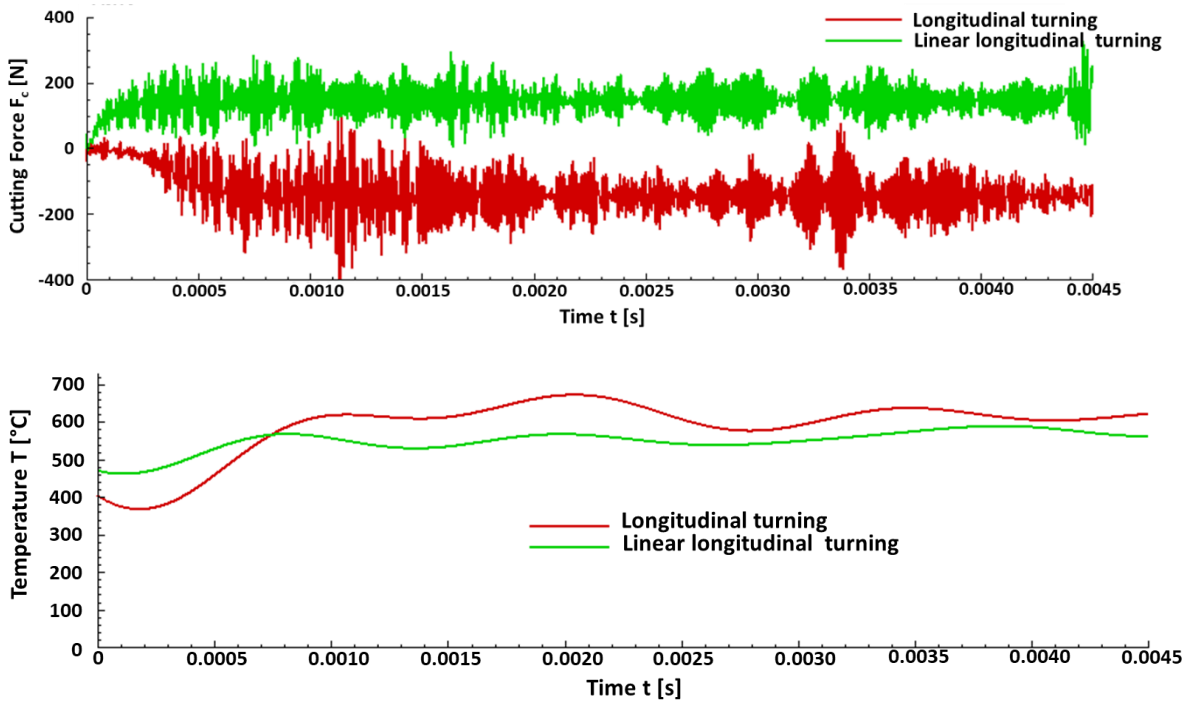

Workpiece material: 1.4837D Cooling: None	Cutting depth : $a_p = 0.3$mm Feed-rate : $f = 0.25$mm Cutting speed : $v_c = 90$m/min	α_o | γ_o | ε_r | κ_r 7° | 15° | 55° | 93°	Tool material: ISO-K10 Geometry: DCGT11T304-F Cutting edge radius: 12µm Corner radius: 0.4mm Coating: AlTiN Coating thickness: 3µm
Longitudinal turning Simulation method: FEM			

Figure 4-23: Comparison of cutting force curve (top) and temperature curve (down) between linear longitudinal turning and longitudinal turning process simulations

From temperature curves in figure 4.23, it can be noticed that there is a slight difference in temperature values between the two simulations. The temperature curve is constant in the linear longitudinal turning simulation, while it is fluctuating in the outer turning simulation. This can be explained by visualizing the chip and tool profile in figure 4.24. For the same mesh settings

in the linear longitudinal turning, a smooth chip formation was developed in simulation, whereas in the outer turning simulation, the chip mesh was distorted, which causes a numerical error in the temperature calculations. This numerical error results in the fluctuation in temperature curve (shown in figure 4.23) and the higher temperature profile (shown in figure 4.24) on tool. Additionally, it can be observed that except fluctuation, the two simulations had similar temperature curves. This fluctuation can be avoided by further refining the mesh during outer turning simulations but it is accompanied with computational cost. AdvantEdge required 9 hour and 55 minutes of simulation time for linear longitudinal turning whereas 14 hour and 17 minutes of simulation time was required for the outer turning simulations. To save computational time and cost, longitudinal turning process was simulated as linear longitudinal turning in AdvantEdge as it showed similar results to outer turning simulations and was computationally less expensive.

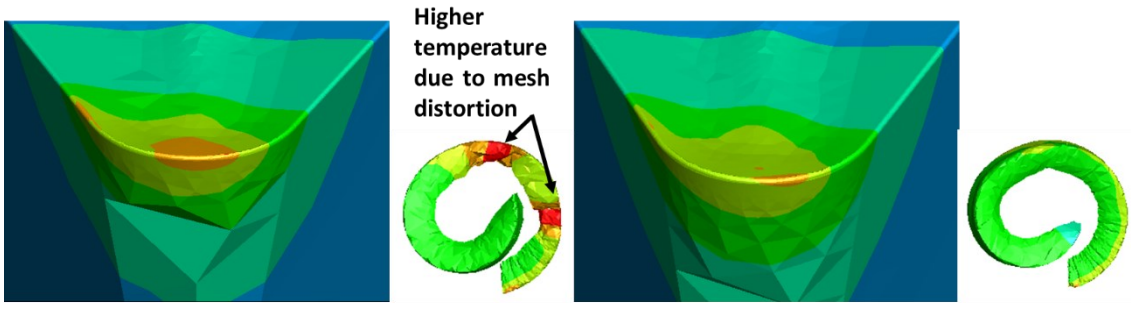

Workpiece material: 1.4837D Cooling: None	Cutting depth Feed-rate Cutting speed	: : :	$a_p = 0.3$mm $f = 0.25$mm $v_c = 90$m/min	α_o	γ_o	ε_r	κ_r	Tool material: ISO-K10 Geometry: DCGT11T304-F Cutting edge radius: 12µm Corner radius: 0.4mm Coating: AlTiN Coating thickness: 3µm
Longitudinal turning Simulation method: FEM				7°	15°	55°	93°	

Figure 4-24: Comparison of temperature profile longitudinal turning (left) and linear longitudinal turning (right) simulations

4.5.2 Parametric study: Mesh sensitivity analysis

To adequately capture the thermal and mechanical load on tool and workpiece, a certain mesh size is required. However, refining the mesh to a very small size can increase the computational cost enormously. Various mesh sizes were defined for the tool and workpiece. The smallest mesh size on the tool was calculated based on the cutting edge radius of the tool, as edge radius came in contact with the workpiece and chip. To capture the generated heat and temperature during machining, at least 3 elements were defined on the tool cutting edge radius. This implies

that the cutting tool with edge radius 12µm had the smallest element size of 4µm on the tool. For the workpiece, four different mesh sizes were analyzed to find the optimal mesh size during turning simulations. These parameters are named here as Mesh 1 (default mesh suggested by AdvantEdge), Mesh 2 (mesh size equals feed-rate (*f*)), Mesh 3 (mesh size equals *f* /10) and Mesh 4 (mesh size equals *f* /15). This mesh sensitivity analysis was conducted for finishing insert DCGT11T304-F with ISO-K10 hardmetal and 3µm AlTiN coating. The cutting parameter used for the mesh-sensitivity were: v_c=90m/min, *f*=0.25mm and a_p=0.3mm. All four simulations were conducted for a cutting length of 5mm of the workpiece. This short cutting length was chosen to keep the simulation time low. The simulation results were then compared with the experimental results and are mentioned below in table 4.3. Additionally, force curves and temperatures are shown in figure 4.25.

Table 4-3: FEM-Mesh sensitivity analysis and comparison with experimental results

	Smallest element size	Total number of elements	Simulation time [Min]	Cutting force [N]	Feed force [N]	Passive force [N]
Mesh 1	0.075mm	107063	101	393	309	273
Mesh 2	0.25mm	80897	89	477	480	475
Mesh 3	0.025mm	142078	172	220	98	70
Mesh 4	0.0167mm	200277	261	221	101	75
Experiment				239	107	88

Table 4.3 and figure 4.25 show that for mesh 1 and mesh 2, force components and temperature values are significantly different from the experimentally measured values. The large variations in force and temperature results of mesh 1 and mesh 2 can be seen in figure 4.25 and therefore these mesh sizes should not be used. Mesh 3 and Mesh 4 were in good correlation with the experimentally measured results. However, simulation of Mesh 4 took much longer time (over four hours) than Mesh 3 (under three hours). This is because Mesh 4 had the smallest size among four meshes used in sensitivity analysis.

Additionally, it must be noted that these simulations were conducted for a workpiece of cutting length of 5mm, and such a small length is not sufficient for chip generation simulations. For chip generation, cutting length of a workpiece should be at least 20mm. In such a case, the gap

between computational time for Mesh 3 and 4 will increase significantly for chip generation simulations. Taking this point into account and knowing that Mesh 4 had no significant impact on the results and only caused extra computational cost, Mesh 3 was chosen for further simulations in this work, i.e., mesh equals $f/10$ was used in simulations.

It must be noted that if the value of depth of cut was smaller than the feed-rate, workpiece mesh was chosen as $a_p/10$. This means that the smallest mesh size for workpiece is one tenth of the feed-rate or depth of cut, depending on which of the two is smaller. These mesh parameters were used for all the simulations.

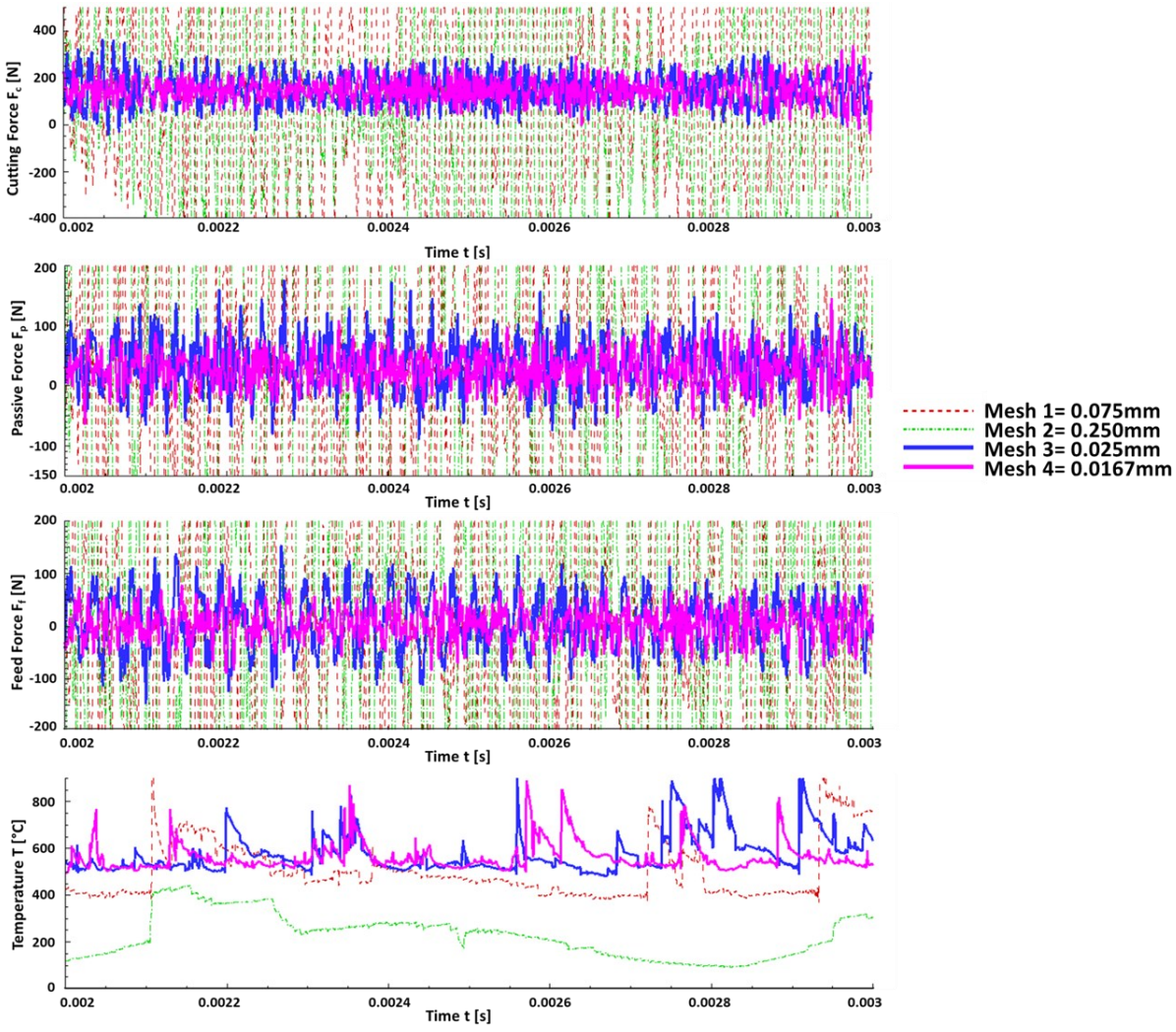

Workpiece material: 1.4837D Cooling: None	Cutting depth : $a_p = 0.3$mm Feed-rate : $f = 0.25$mm Cutting speed : $v_c = 90$m/min	α_o | γ_o | ε_r | κ_r 7° | 15° | 55° | 93°	Tool material: ISO-K10 Geometry: DCGT11T304-F Cutting edge radius: 12µm Corner radius: 0.4mm Coating: AlTiN Coating thickness: 3µm
Longitudinal turning Simulation method: FEM			

Figure 4-25: Force and temperature results for different mesh sensitivity analysis

4.5.3 Simulation results for different coatings

Although FEM-simulations have some disadvantages like roughness or tool wear cannot be simulated and they are carried out only for a few milliseconds, they also have advantages like the temperature at the tool edge can be precisely determined at any given time and the temperature distribution is known in the entire tool and workpiece. The same applies to the stresses in the tool and workpiece. The simulation results in this section, therefore, contain force curves, temperature, stresses in tool and formation of chips. An example of simulated force curves is shown in Figure 4.26. The cutting force is shown at the top, the passive force at the center and the feed force at the bottom. The cutting speed is v_c=130m/min, feed-rate is f =0.175mm and the depth of cut is a_p =0.2mm. To create chips, workpiece cutting length was set to 25mm for all the simulations. Additionally, to keep the computational time in check, the tool mesh was refined only in the tool-workpiece engagement area. The tool mesh was defined as one-third of the cutting edge radius. The workpiece mesh was created as per parametric study mentioned in section 4.5.2.

To read out a representative force value from the curves shown in figure 4.26, the simulated forces were sorted in a similar way like experiments. The force at 95% of the value was read out as the representative force. This means that 5% of the forces were greater than this read out force value. This method filters out extreme force values and ensures good comparability between the force values from different DoE parameters and tools. From the figure, it can be observed that the cutting force is the dominant force component among the three force components.

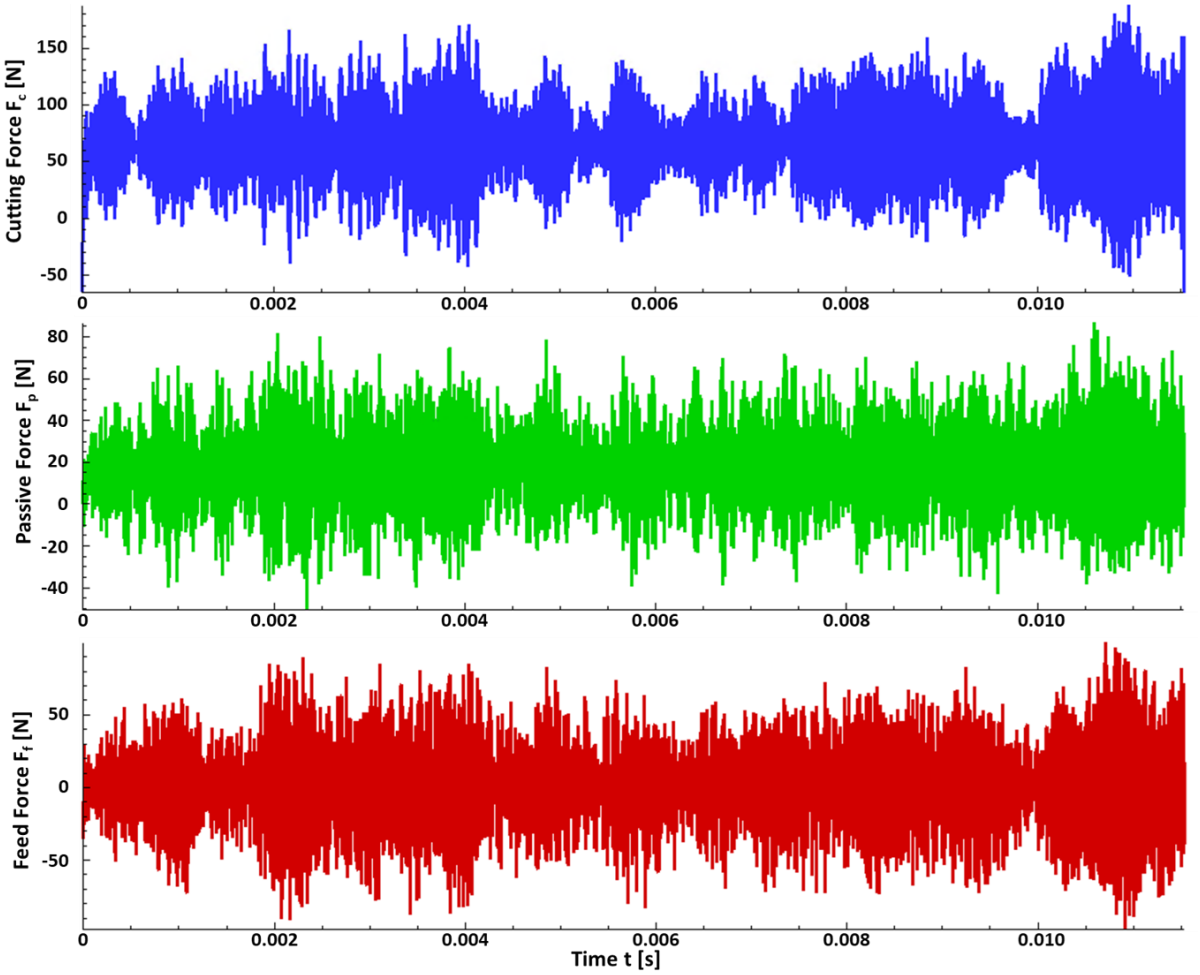

Workpiece material: 1.4837D Cooling: None	Cutting depth : a_p = 0.2mm Feed-rate : f = 0.175mm Cutting speed : v_c = 130m/min	α_o	γ_o	ε_r	κ_r	Tool material: ISO-K10 Geometry: DCGT11T304-F Cutting edge radius: 12µm Corner radius: 0.4mm Coating: TiSiN Coating thickness: 3µm
Longitudinal turning Simulation method: FEM		7°	15°	55°	93°	

Figure 4-26: Force curve for the cutting force, passive force and feed force

Figure 4.27 shows the results of simulated cutting forces for both the coatings and for each DoE parameter. The table at the bottom of the image shows the corresponding machining parameters. The maximum cutting force occurs with the maximum tool-workpiece engagement, i.e., with a feed of f=0.25mm and a depth of cut of a_p=0.3mm. It can also be observed that the forces are higher at lower cutting speeds. It can be noted that AlTiN coating had lower cutting forces in comparison to the TiSiN coating. Similar trend for forces was observed in experiments and this is because of the lower coefficient of friction of AlTiN coating. For the TiSiN coating, a similar comparison of cutting forces was seen in simulations as experiments, i.e. the forces decreased with an increase in the feed-rate or depth of cut for first three set of cutting parameters from DoE. It can be well observed in figure 4.27. These results prove that simulations can replicate

the mechanical loads on tools very well when it comes to fine changes in tool like different coatings.

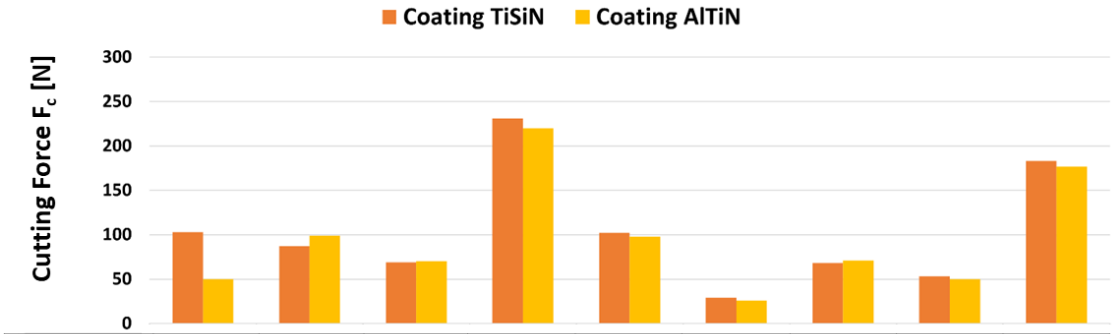

v_c (m/min)	90	90	90	90	130	170	170	170	170
f (mm)	0.1	0.1	0.25	0.25	0.175	0.1	0.1	0.25	0.25
a_p (mm)	0.1	0.3	0.1	0.3	0.2	0.1	0.3	0.1	0.3

Workpiece material: 1.4837D
Cooling: None

Longitudinal turning
Simulation method: FEM

α_o	γ_o	ε_r	κ_r
7°	15°	55°	93°

Tool material: ISO-K10
Geometry: DCGT11T304-F
Cutting edge radius: 12µm
Corner radius: 0.4mm
Coating: var.
Coating thickness: 3µm

Figure 4-27: Comparison of simulated cutting forces for AlTiN and TiSiN coating

In addition to the machining forces, the stresses on tool can also be evaluated using simulations. The stress analysis can indicate the tool cutting areas that are subject to greater impact of the machining loads and thus also serve as an indicator of wear. Figure 4.28 shows the von-Mises equivalent stresses acting at the cutting edge radius of the AlTiN coated tool for all the DoE parameters. The locations of high stress on the tool cutting edge change depending on the engagement between the tool and the workpiece. It can also be seen that the stresses increase as the cutting parameter increases (cutting speed, feed-rate, and depth of cut).

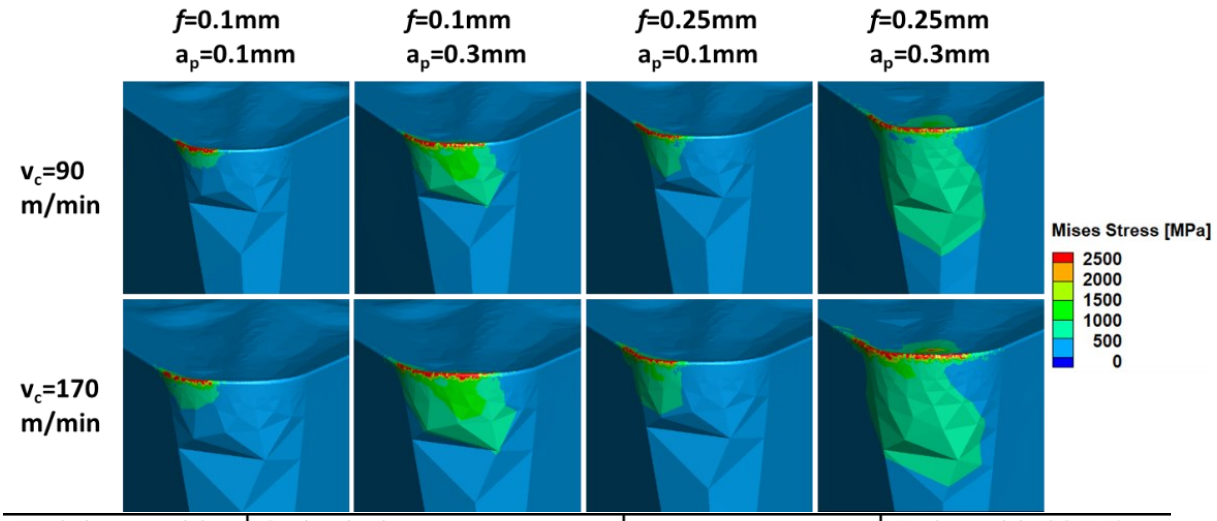

Workpiece material: 1.4837D Cooling: None	Cutting depth : a_p = var. Feed-rate : f = var. Cutting speed : v_c = var.	α_o	γ_o	ε_r	κ_r	Tool material: ISO-K10 Geometry: DCGT11T304-F Cutting edge radius: 12µm Corner radius: 0.4mm Coating: AlTiN Coating thickness: 3µm
Longitudinal turning Simulation method: FEM		7°	15°	55°	93°	

Figure 4-28: von-Mises stress at tool cutting edge for AlTiN coating

During experiments, measurement of temperature at the tool tip was only possible with an internal turning process through a bored hole in the workpiece. This was done with a two-color pyrometer. The measurement time in experiments was very short as the tool passed the bored hole of 700µm very quickly (t=700µm/v_f). Contrastingly, the temperature at the tool cutting edge could be observed in the simulation over the entire simulation period. To ensure good comparability, like experiments, internal turning process was also simulated. An example of the resulting temperature pattern can be seen in Figure 4.29.

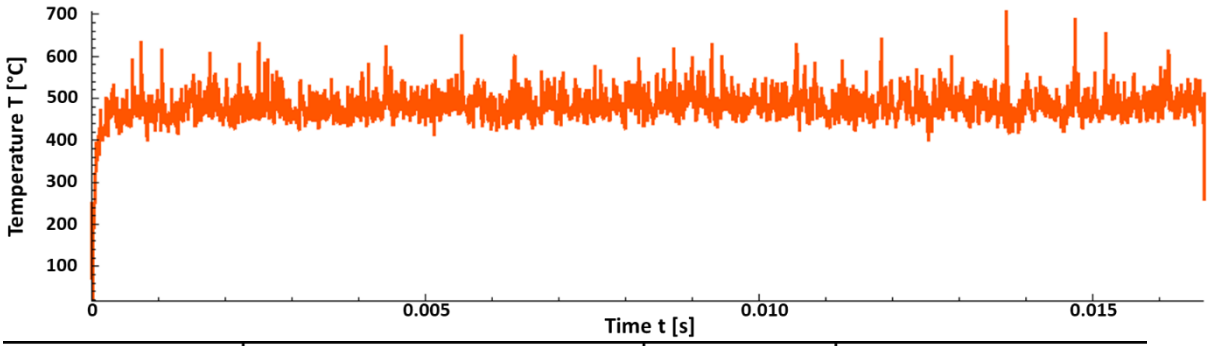

Workpiece material: 1.4837D Cooling: None	Cutting depth : a_p = 0.1mm Feed-rate : f = 0.1mm Cutting speed : v_c = 90m/min	α_o	γ_o	ε_r	κ_r	Tool material: ISO-K10 Geometry: DCGT11T304-F Cutting edge radius: 12µm Corner radius: 0.4mm Coating: TiSiN Coating thickness: 3µm
Internal turning Simulation method: FEM		7°	15°	55°	93°	

Figure 4-29: Temperature curve for the simulation with v_c=90m/min, f=0.1mm, a_p=0.1mm and TiSiN coating

The maximum representative temperature (neglecting simulation outliers) was determined from such temperature curves for each DoE parameter set. The temperature results for the comparison of the two coatings are shown below in Figure 4.30. The highest temperature for both the coatings was found with the cutting speed of v_c=170m/min. On comparing the two coatings, AlTiN coated inserts had lower temperature than the TiSiN coated inserts due to the lower coefficient of friction for AlTiN coating. These temperature results for coatings are similar to experimental results presented in section 4.4.1. and they prove that simulations can also build thermal loads quite well for different coatings and cutting parameters. A detailed comparison of experimental and simulations results will be discussed in section 4.6.

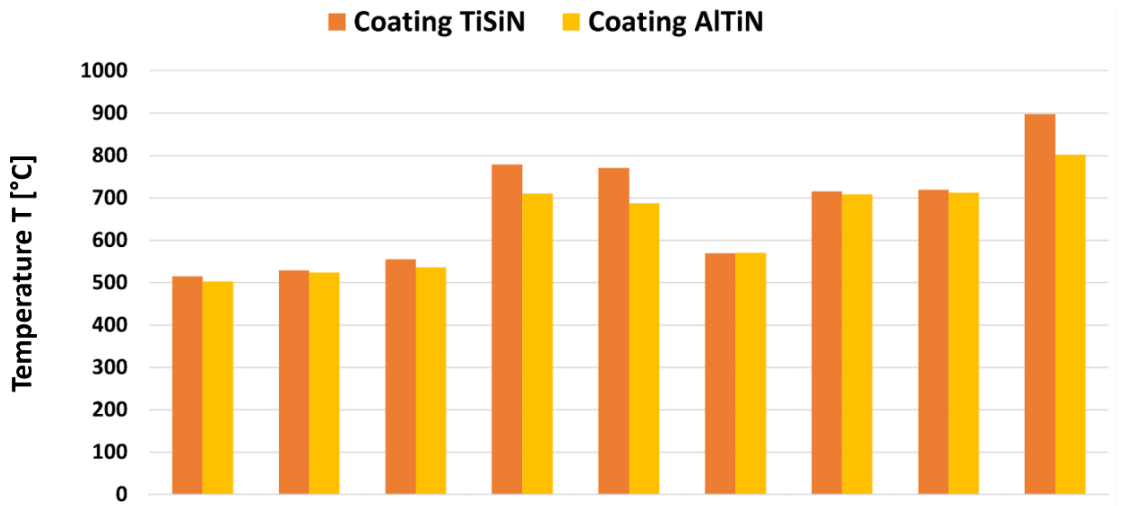

v_c (m/min)	90	90	90	90	130	170	170	170	170
f (mm)	0.1	0.1	0.25	0.25	0.175	0.1	0.1	0.25	0.25
a_p (mm)	0.1	0.3	0.1	0.3	0.2	0.1	0.3	0.1	0.3

Workpiece material: 1.4837D
Cooling: None

Internal turning
Simulation method: FEM

α_o	γ_o	ε_r	κ_r
7°	15°	55°	93°

Tool material: ISO-K10
Geometry: DCGT11T304-F
Cutting edge radius: 12µm
Corner radius: 0.4mm
Coating: var.
Coating thickness: 3µm

Figure 4-30: Maximum temperature at tool cutting edge from simulations for two coatings

In addition to the representative temperature shown in the figure above, simulations can also display the temperature distribution at the cutting edge of the tool. This is shown for the AlTiN coating in Figure 4.31. This image shows which area of the tool cutting edge was engaged during machining. The plastic deformation of the workpiece material and friction serve as a source of heat generation. The maximum temperature on the tool is slightly behind the cutting edge on rake face due to a delay in heat transfer. It can be observed (from top to bottom in figure 4.31) that the increase in cutting speed, when feed-rate and depth of cut is kept constant,

leads to a rise in temperature. Additionally, it is also evident that based on feed-rate and depth of cut, the tool-workpiece engagement changes, leading to a shift in point with maximum temperature on tool.

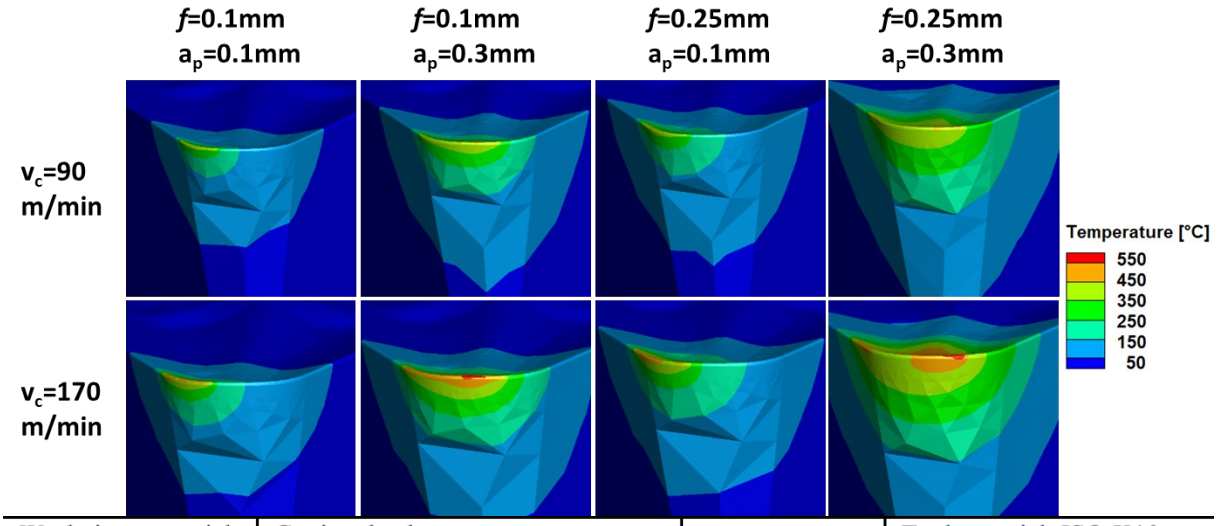

Workpiece material: 1.4837D Cooling: None	Cutting depth : a_p = var. Feed-rate : f = var. Cutting speed : v_c = var.	α_o	γ_o	ε_r	κ_r	Tool material: ISO-K10 Geometry: DCGT11T304-F Cutting edge radius: 12µm Corner radius: 0.4mm Coating: AlTiN Coating thickness: 3µm
Internal turning Simulation method: FEM		7°	15°	55°	93°	

Figure 4-31: Temperature at tool cutting edge for AlTiN coating

Chip formation is an important factor in determining the optimum cutting parameters. The aim is generally to produce short chips that break at suitable chip length. The temperature and chips formed in the simulation can be seen in Figure 4.32. It can be observed that the simulated chip shape also changes (like experiments) with respect to the cutting parameters. For example, for cutting parameter v_c=90m/min, f=0.1mm and a_p=0.1mm, a thin simulated chip is produced, whereas for v_c=90m/min, f=0.25mm and a_p=0.3mm, a thicker simulated chip is produced. This variation in chip thickness was also observed in experiments. It must be noted, however, that the chip breakage was not simulated in this work.

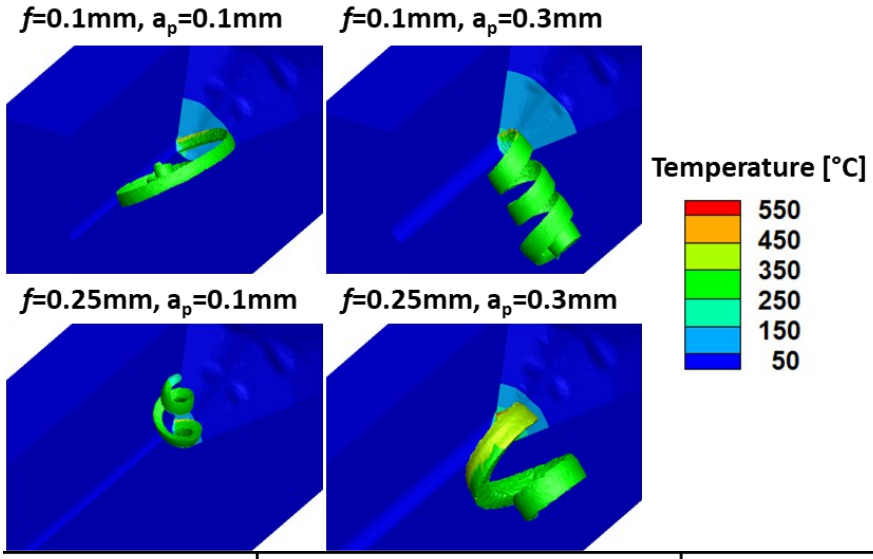

Workpiece material: 1.4837D Cooling: None	Cutting depth : a_p = var. Feed-rate : f = var. Cutting speed : v_c = 90m/min	α_o	γ_o	ε_r	κ_r	Tool material: ISO-K10 Geometry: DCGT11T304-F Cutting edge radius: 12µm Corner radius: 0.4mm Coating: AlTiN Coating thickness: 3µm
Longitudinal turning Simulation method: FEM		7°	15°	55°	93°	

Figure 4-32: Chip formation for AlTiN coating

4.5.4 Evaluation of DoE results

Like earlier in real measurements, linearized influence of cutting parameters on all the three simulated force components was visualized. Figure 4.33 shows the main effect plot for the simulated cutting forces. Only the plot for cutting force is shown here as it is the dominant component among the three forces. It can be noticed that the cutting force decreases with an increase in cutting speed, a decrease in feed-rate and a decrease in depth of cut. A similar trend was observed in the experiments and mentioned in section 4.4.2. However, in simulations, the influence of cutting speed is greater than experiments. This could be due to either the friction model or the consideration of homogenous material model for workpiece. Additionally, the forces of AlTiN coated inserts are on average lower than those with TiSiN coating. The same effect was observed in the experiments and the reason for this effect is the lower value of friction coefficient for AlTiN coated tools.

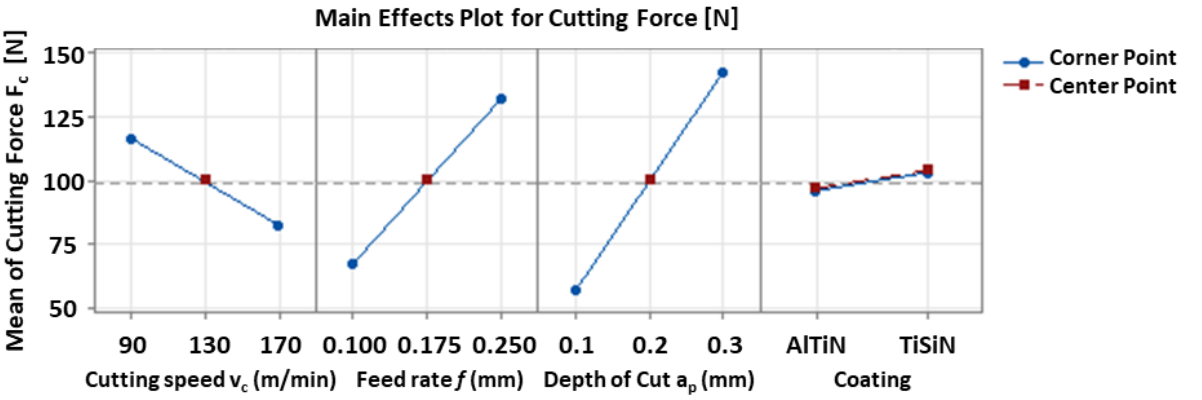

Workpiece material: 1.4837D Cooling: None	Cutting depth : a_p = var. Feed-rate : f = var. Cutting speed : v_c = var.	α_o | γ_o | ε_r | κ_r 7° | 15° | 55° | 93°	Tool material: ISO-K10 Geometry: DCGT11T304-F Cutting edge radius: 12µm Corner radius: 0.4mm Coating: var. Coating thickness: 3µm
Longitudinal turning Simulation method: FEM			

Figure 4-33: Linearized relationships between the test factors v_c, f, a_p and coating to the measured variable: Cutting force from simulations

Additionally, like experiments, the inner turning process was also simulated to visualize the temperature for each DoE parameter. Figure 4.34 shows the main effect plot for temperature. The simulated results are similar to the experimental results. Temperature increases with an increase in cutting speed, feed-rate and depth of cut. Broadly, due to its lower coefficient of friction, AlTiN coating had lower temperature than TiSiN coating. The lower temperatures led to the better performances of AlTiN coated tools.

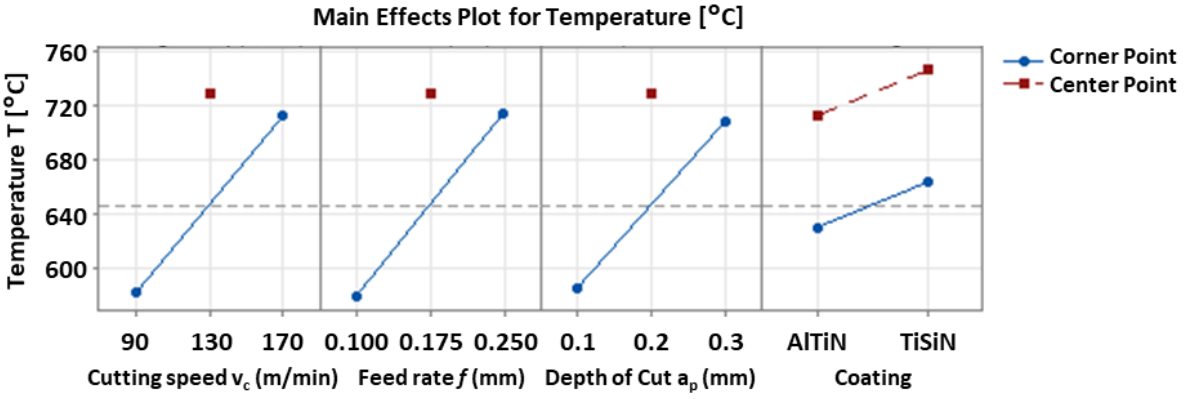

Workpiece material: 1.4837D Cooling: None	Cutting depth : a_p = var. Feed-rate : f = var. Cutting speed : v_c = var.	α_o | γ_o | ε_r | κ_r 7° | 15° | 55° | 93°	Tool material: ISO-K10 Geometry: DCGT11T304-F Cutting edge radius: 12µm Corner radius: 0.4mm Coating: var. Coating thickness: 3µm
Internal turning Simulation method: FEM			

Figure 4-34: Linearized relationships between the test factors cutting speed, feed-rate, depth of cut and coating to the measured variable: Temperature from Simulations

4.6 Comparison of simulation and experiments for DoE 1

Figures 4.9 and 4.26 show the force curves from the experiments and simulations respectively. These force curves exhibit large fluctuations between the maximum and minimum values compared to the mean value. In experiments, these fluctuations may occur due to the formation of chips, inhomogeneities in the material, wear mechanisms, surface roughness etc. In simulations, these fluctuations may arise due to initial mesh, remeshing while chip creation, coupled thermo-mechanical step and numerical errors. Initially, the validation of simulation results with the experimentally measured values was necessary to implement simulations in production, in order to achieve the goal of reducing the number of experiments in future. For this reason, relative error was calculated between experimental and simulation results. Measured values were considered as true values for the calculation of relative error.

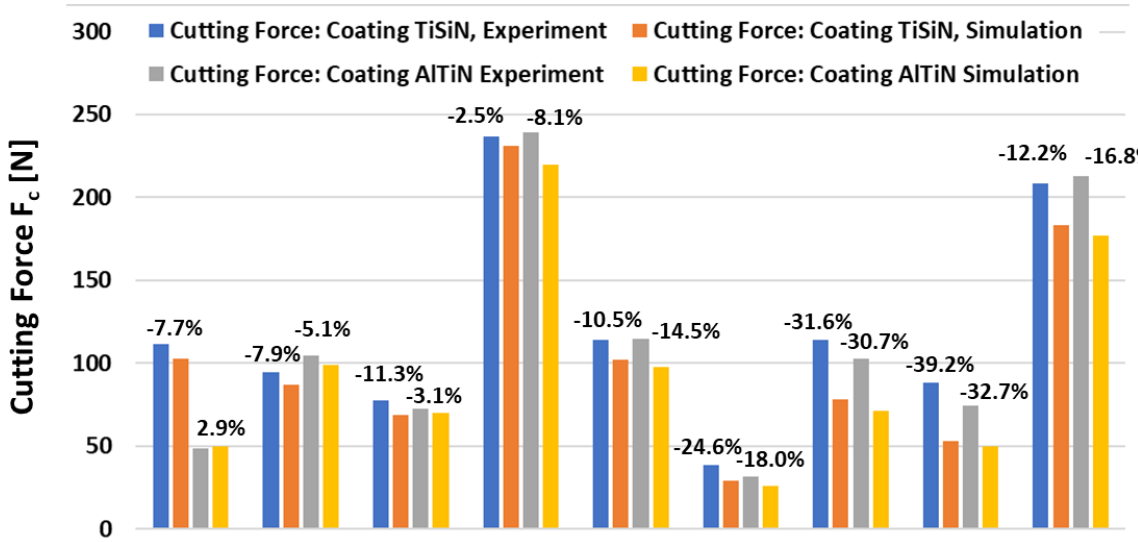

v_c (m/min)	90	90	90	90	130	170	170	170	170
f (mm)	0.1	0.1	0.25	0.25	0.175	0.1	0.1	0.25	0.25
a_p (mm)	0.1	0.3	0.1	0.3	0.2	0.1	0.3	0.1	0.3

Workpiece material: 1.4837D Cooling: None	α_o | γ_o | ε_r | κ_r 7° | 15° | 55° | 93°	Tool material: ISO-K10 Geometry: DCGT11T304-F Cutting edge radius: 12µm Corner radius: 0.4mm Coating: var. Coating thickness: 3µm
Longitudinal turning Simulation method: FEM		

Figure 4-35: Cutting force comparison and relative error for AlTiN and TiSiN coatings between experiments and simulations

Figure 4.35 shows a direct comparison of cutting force between simulations and experiments for both the coatings and each DoE parameter set. It can be noted that the forces match well for

both coating inserts in experiments as well as simulations. It can also be noticed that simulations have either under predicted the force values or the simulated values are almost equal to the measured values. The reason for underprediction of force values is the coulomb friction model, which also corresponds to the literature [155]. This figure also presents the relative error in cutting force between simulations and experiments for each cutting parameter for both the coatings. The worst results for both the coatings were observed for the highest cutting speed v_c=170m/min. This difference in results is because of high wear on tools during experiments, which was not considered in simulations. For other cutting parameters, the relative error was approximately 10%. For feed and passive forces, similar relative error was observed.

One of the major questions that arose during DoE1 was if simulations were good enough to predict the coating performance. The above figure depicts that simulations and experiments have similar tendencies towards cutting force, and both predicted that the AlTiN coated inserts have lower forces in comparison to the TiSiN coated inserts.

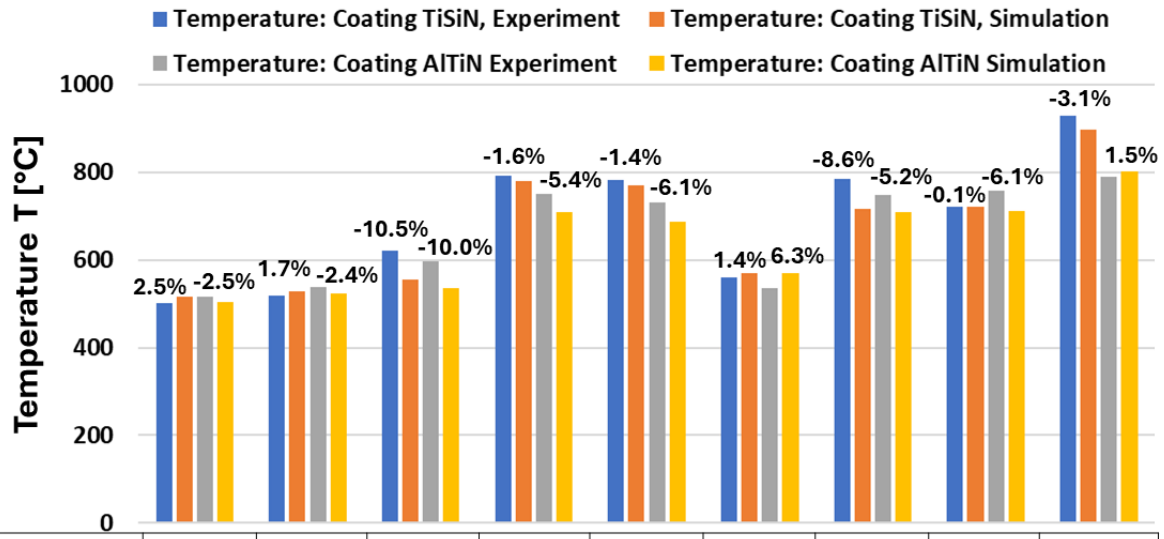

v_c (m/min)	90	90	90	90	130	170	170	170	170
f (mm)	0.1	0.1	0.25	0.25	0.175	0.1	0.1	0.25	0.25
a_p (mm)	0.1	0.3	0.1	0.3	0.2	0.1	0.3	0.1	0.3

Workpiece material: 1.4837D
Cooling: None

Internal turning
Simulation method: FEM

α_o	γ_o	ε_r	κ_r
7°	15°	55°	93°

Tool material: ISO-K10
Geometry: DCGT11T304-F
Cutting edge radius: 12µm
Corner radius: 0.4mm
Coating: var.
Coating thickness: 3µm

Figure 4-36: Temperature comparison for AlTiN and TiSiN coatings between experiments and simulations

Simulated and measured temperature from internal turning DoE for both the coatings were compared and are shown in figure 4.36. A very good comparison between the real measurements and simulations can be seen here. The average relative error for the TiSiN coating was 2.2% and for the AlTiN coating, it was 3.8%. However, in some cases, the temperatures were slightly underpredicted and in the others, they were mildly overpredicted.

The chips collected from the cylindrical longitudinal turning were compared with the simulated chips from the linear longitudinal turning process. Figure 4.37 shows the chips for AlTiN coated inserts from the real experiments at the top and from the simulation at the bottom. All are spiral chips, whereby the variations in chip thickness and curvature radius depend on the cutting parameters. Overall, a very good prediction was achieved for the chips between simulation and experiments.

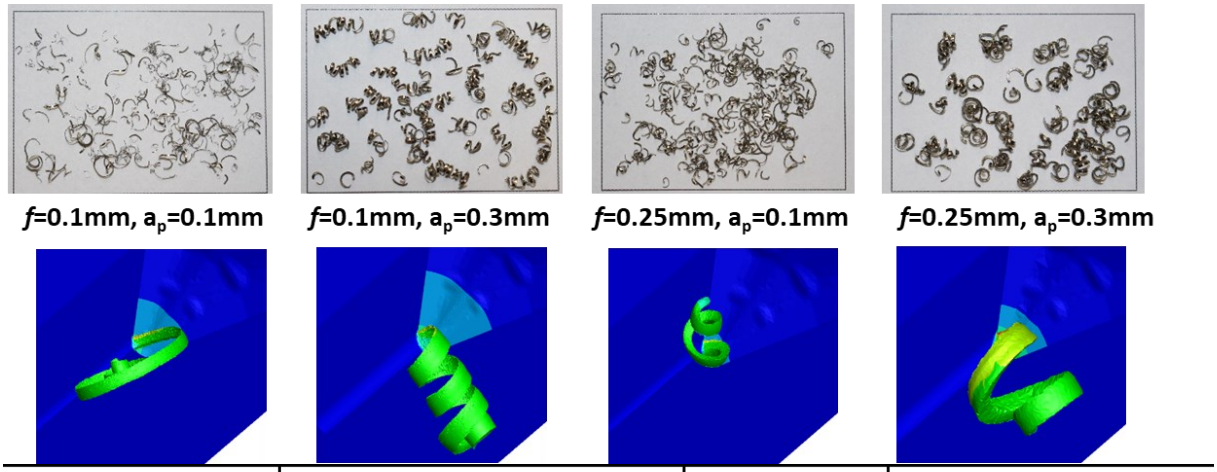

Workpiece material: 1.4837D Cooling: None	Cutting depth : a_p = var. Feed-rate : f = var. Cutting speed : v_c = 90m/min	α_o | γ_o | ε_r | κ_r 7° | 15° | 55° | 93°	Tool material: ISO-K10 Geometry: DCGT11T304-F Cutting edge radius: 12µm Corner radius: 0.4mm Coating: AlTiN Coating thickness: 3µm
Longitudinal turning Simulation method: FEM			

Figure 4-37: Chip comparison between experiments and simulations

4.7 Conclusion of first DoE results

One of the central objectives of this work was to determine whether simulation could aid in tool selection and optimization in case of subtle variations, such as change in coating. This was investigated using an external and an internal turning process. For force predictions in outer turning, the tendency in simulations was similar to experiments. However, for a few cutting parameters there was a difference between the simulated and measured forces. On the other hand, chips were very well predicted and resembled experimental chips. Simulated

temperatures from the internal turning process were in very good correlation with experiments. Temperatures have a major influence on tool wear [153] but the effort to measure temperature in experiments is very high and therefore it is not possible to measure it in some cases, like in outer turning. The simulation, thus, offers a major advantage here.

On the other hand, a major objective of this DoE was to optimize the turning process. It was noticed that AlTiN coating performed better than TiSiN coating. Nevertheless, both coatings exceeded the tool wear criteria of VB=100µm and could not achieve the target of producing 90 parts. Thus, to optimize turning process, another DoE was created by increasing the tool cutting edge radius and coating thickness with an aim to stabilize the tool cutting edge.

4.8 Experimental results of second DoE

4.8.1 Comparison of coating thickness and cutting edge radius

Due to excessive wear, the turning process was further optimized. For the next experimental design, the cutting edge radius (ER= Cutting edge radius) and the coating layer thickness (CT = Coating thickness) were altered. Since AlTiN coating performed better in the first DoE, it was used in DoE 2.

Initially, the uncoated DCGT11T304-F tungsten carbide inserts from substrate material ISO K10 with cutting edge radii of r_β= 20µm and r_β= 40µm were prepared. These tools were coated with CT= 2µm and CT= 4µm thick layer of AlTiN coating. This resulted in the manufacturing of four coated inserts with the cutting edge radii of 22µm, 24µm, 42µm and 44µm. Cutting parameters remained unchanged from the first experimental design, i.e., cutting speed v_c= 90-170m/min, feed-rate f= 0.1-0.25mm and depth of cut a_p= 0.1-0.3mm. Likewise all the three force components, surface roughness profile and chips were measured during the external turning process and the temperatures were measured during the internal turning process. Experimental setup for both, external and internal turning process remained same as described in section 4.2.

The measurement results from the external turning process with coating layer thickness of 4 µm are presented henceforth. Figure 4.38 compares the cutting forces for cutting edge radii of 24µm and 44µm. The cutting force was proportional to the tool-workpiece engagement, a similar trend as observed in DoE1. This means that a higher feed-rate and depth of cut led to higher forces. However, there was no significant change in forces with an increase in cutting

speed. These influences of cutting parameters on the cutting force are expected according to the relevant literature [7].

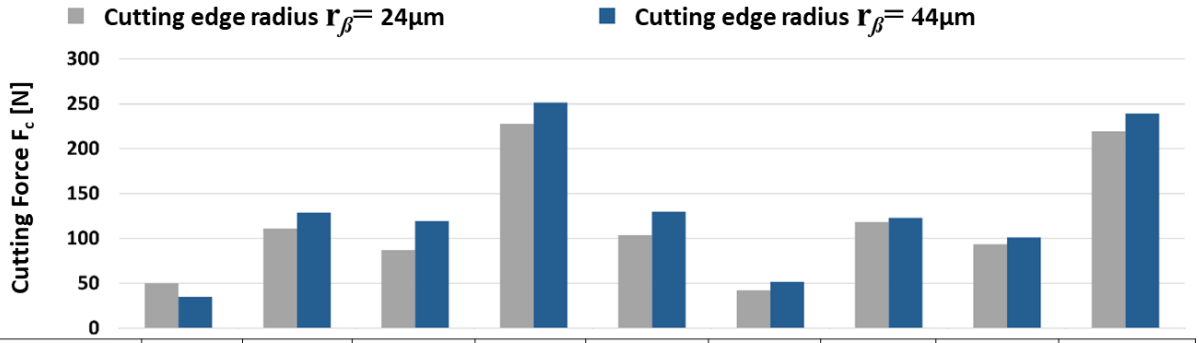

v_c (m/min)	90	90	90	90	130	170	170	170	170
f (mm)	0.1	0.1	0.25	0.25	0.175	0.1	0.1	0.25	0.25
a_p (mm)	0.1	0.3	0.1	0.3	0.2	0.1	0.3	0.1	0.3

Workpiece material: 1.4837D
Cooling: None
Longitudinal turning

α_o	γ_o	ε_r	κ_r
7°	15°	55°	93°

Tool material: ISO-K10
Geometry: DCGT11T304-F
Cutting edge radius: var.
Corner radius: 0.4mm
Coating: AlTiN
Coating thickness: 4µm

Figure 4-38: Comparison of measured cutting forces for AlTiN coating with cutting edge radii r_β 24µm and 44µm

Averaged surface roughness measurements for two tools are presented in figure 4.39. The best surface finish was recorded with the feed-rate f= 0.1mm and worst profile was recorded with the feed-rate f= 0.25mm. It can also be noticed that in some cases, the tool with high cutting edge radius has produced slightly rougher surface. A large tool cutting edge radius creates a rough surface as the tool transitions from a sharp cutting action to a plowing or rubbing action. However, due to the built up edges, some experiments recorded high surface roughness even with a sharp tool cutting edge radius. This was also observed by other researchers [156].

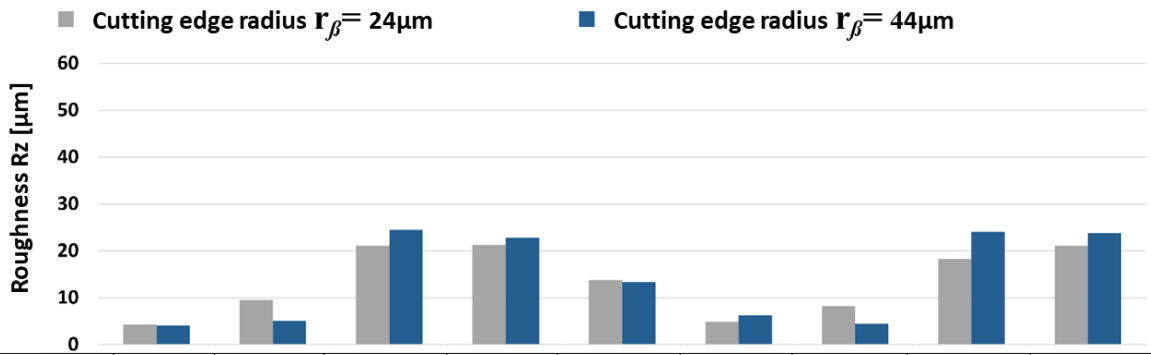

v_c (m/min)	90	90	90	90	130	170	170	170	170
f (mm)	0.1	0.1	0.25	0.25	0.175	0.1	0.1	0.25	0.25
a_p (mm)	0.1	0.3	0.1	0.3	0.2	0.1	0.3	0.1	0.3

Workpiece material: 1.4837D
Cooling: None
Longitudinal turning

α_o	γ_o	ε_r	κ_r
7°	15°	55°	93°

Tool material: ISO-K10
Geometry: DCGT11T304-F
Cutting edge radius: var.
Corner radius: 0.4mm
Coating: AlTiN
Coating thickness: 4µm

Figure 4-39: Comparison of measured averaged surface roughness for AlTiN coating with cutting edge radii r_β 24µm and 44µm

Figure 4.40 shows the measured temperature values for the two tools with a 2-color pyrometer in the internal turning process. An increase in depth of cut, feed-rate or cutting speed causes an increase in tool temperature, the same trend was observed in DoE 1. Tools with the radius of 44µm mostly recorded higher temperatures than tools with the radius of 24µm. At low cutting speed (v_c=90m/min), the larger 44µm cutting edge radius produces more ploughing and friction, increasing heat generation on the tool. When the cutting speed is high (v_c=170m/min), shear heat becomes predominant and the chip carries more heat; additionally, the larger radius spreads heat over a broader contact area and increases heat partition into the chip, resulting in reduced tool temperature in comparison to the 24µm edge.

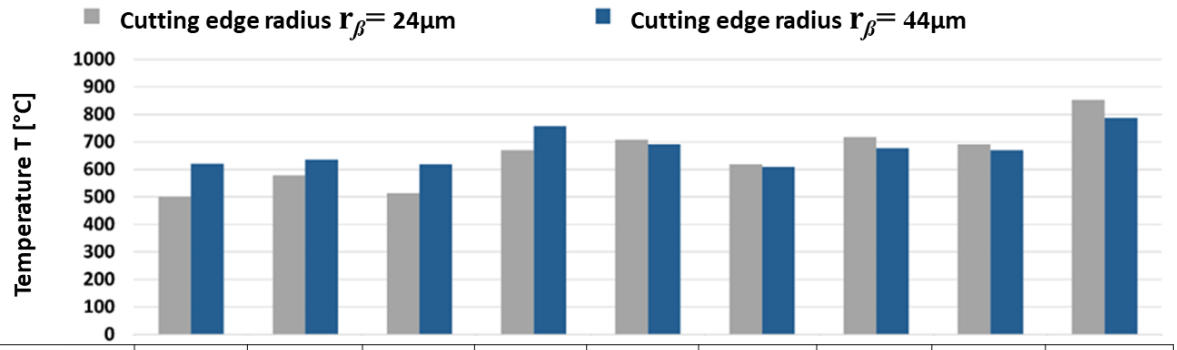

v_c (m/min)	90	90	90	90	130	170	170	170	170
f (mm)	0.1	0.1	0.25	0.25	0.175	0.1	0.1	0.25	0.25
a_p (mm)	0.1	0.3	0.1	0.3	0.2	0.1	0.3	0.1	0.3

Workpiece material: 1.4837D
Cooling: None
Internal turning

α_o	γ_o	ε_r	κ_r
7°	15°	55°	93°

Tool material: ISO-K10
Geometry: DCGT11T304-F
Cutting edge radius: var.
Corner radius: 0.4mm
Coating: AlTiN
Coating thickness: 4µm

Figure 4-40: Comparison of measured temperature for AlTiN coating with cutting edge radii r_β 24µm and 44µm

Analogous to these measurements, for the tools with cutting edge radii 22µm and 42µm, the force components and surface roughness profile were measured in the external turning process and the temperature was measured in the internal turning process. In appendix chapter figure A3, A4 and A5 represent the cutting forces, averaged surface roughness and temperatures for r_β= 22µm and r_β= 42µm tools respectively. The result trends for these tools were comparable to the tools with the cutting edge radii of 24µm and 44µm and thus are not discussed again.

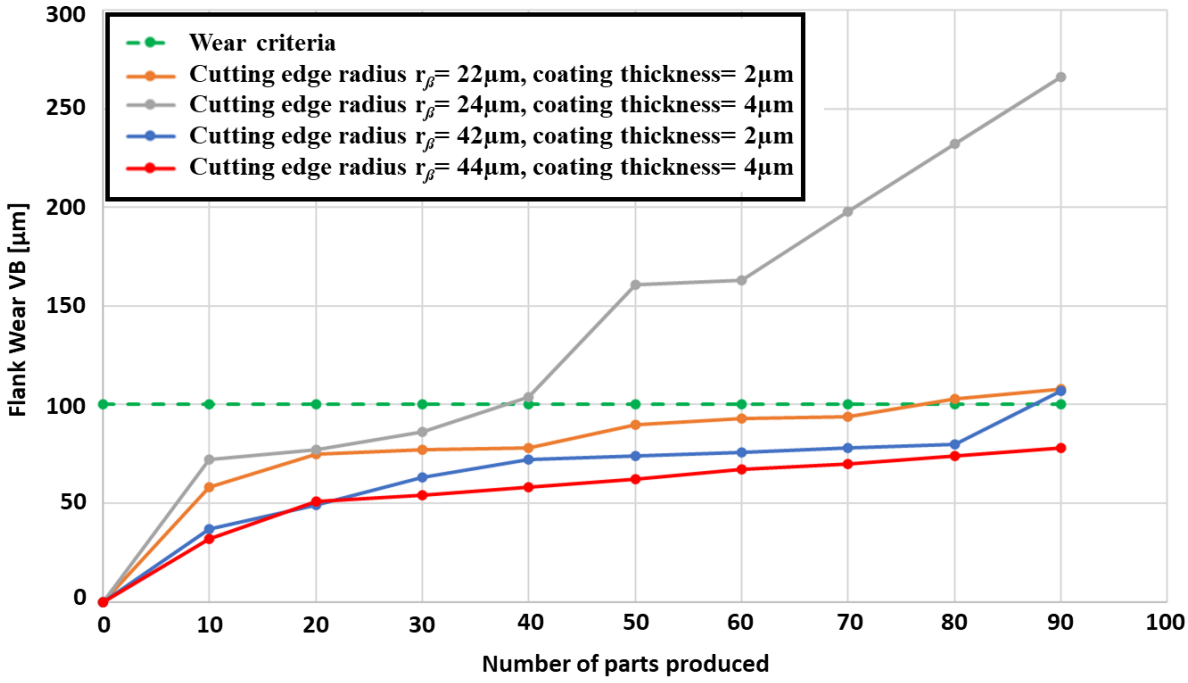

Workpiece material: 1.4837D Cooling: None	Cutting depth : a_p = 0.1mm Feed-rate : f = 0.22mm Cutting speed : v_c = 140m/min	α_o	γ_o	ε_r	κ_r	Tool material: ISO-K10 Geometry: DCGT11T304-F Cutting edge radius: var. Corner radius: 0.4mm Coating: AlTiN Coating thickness: var.
Longitudinal turning		7°	15°	55°	93°	

Figure 4-41: Flank wear curve for cutting edge radii r_β 22µm (CT=2µm), 24µm (CT=4µm), 42µm (CT=2µm) and 44µm (CT=4µm)

Flank face wear width (VB) was also measured for each tool on a cutting parameter (v_c=140m/min, f=0.22 and a_p=0.1mm) to study the tool-life. Tool wear tests were conducted in the external turning process and the wear criteria for these tools remained same as mentioned in section 4.4.1, i.e., tool wear should not exceed VB= 100µm and tool life quantity of 90 parts should be achieved. The test results are shown in figure 4.41. The maximum tool wear limit is shown with the green dashed line and the other four lines represent the four tools. It can be clearly seen that the tools with cutting edge radii 42µm and 44µm had similar tool wear till 80 parts. However, after 80 parts, there was a sudden increase in tool wear for the tool with 42µm cutting edge radius and it crossed the tool wear criteria mark. In the end, at 90 target parts, the tool with the radius of 44µm had flank wear width (VB) of 78µm and it had the best performance among the four tools. The tool with the cutting edge radius of 22µm reached the wear criteria of 100µm at 80 parts, whereas the tool with the cutting edge radius of 24µm had the worst performance and it reached the wear criteria mark at 40 parts.

To measure the flank wear width, tool images at an interval of production of 10 parts were captured with Keyence microscope and figure 4.42 below shows these wear images for tool with the cutting edge radius of 24µm at the top and tool with the edge radius of 44µm at the bottom.

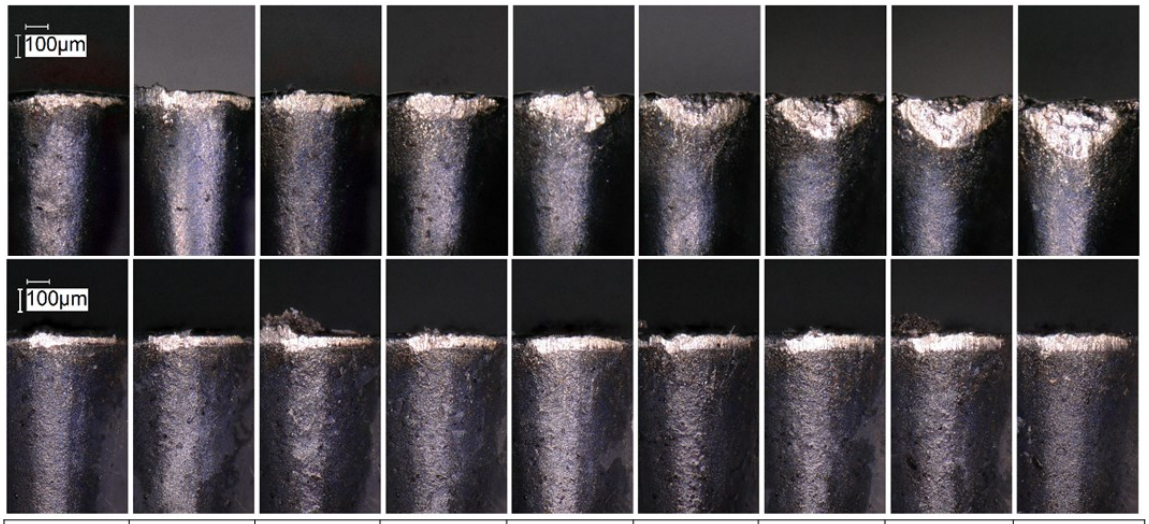

10 parts	20 parts	30 parts	40 parts	50 parts	60 parts	70 parts	80 parts	90 parts

Workpiece material: 1.4837D Cooling: None	Cutting depth : $a_p = 0.1$mm Feed-rate : $f = 0.22$mm Cutting speed : $v_c = 140$m/min							Tool material: ISO-K10 Geometry: DCGT11T304-F Cutting edge radius: var. Corner radius: 0.4mm Coating: AlTiN Coating thickness: 4µm
Longitudinal turning		α_o	γ_o	ε_r	κ_r			
		7°	15°	55°	93°			

Figure 4-42: Wear on the tool cutting edge after 90 parts for cutting edge radii r_β 24µm (top) and 44µm (bottom)

4.8.2 Evaluation of second DoE results

The Minitab software was used to analyze the above-mentioned results and create linearized correlations between input parameters and outputs. Overall, three diagrams were created: one for force components, one for surface roughness profile and one for temperature. Figure 4.43 shows the linearized correlation of cutting force F_c, feed force F_f and passive force F_p. The change in feed-rate and depth of cut have a similar effect on forces as described earlier in section 4.4.2, i.e., they are directly proportional. On the other hand, with an increase in cutting speed, cutting force and passive force decrease but there is a marginal increment in feed force. The reduction of forces is due to the thermal softening of the material, caused by high temperature during machining with high cutting speeds. Additionally, it must be noted that an increase in the cutting edge radius has a marginal incremental effect on cutting force, passive force and

feed force. Similarly increase of coating thickness from 2µm to 4µm for both cutting edge radii leads to an increase in all the three force components. The cutting force is the dominant force among the three forces.

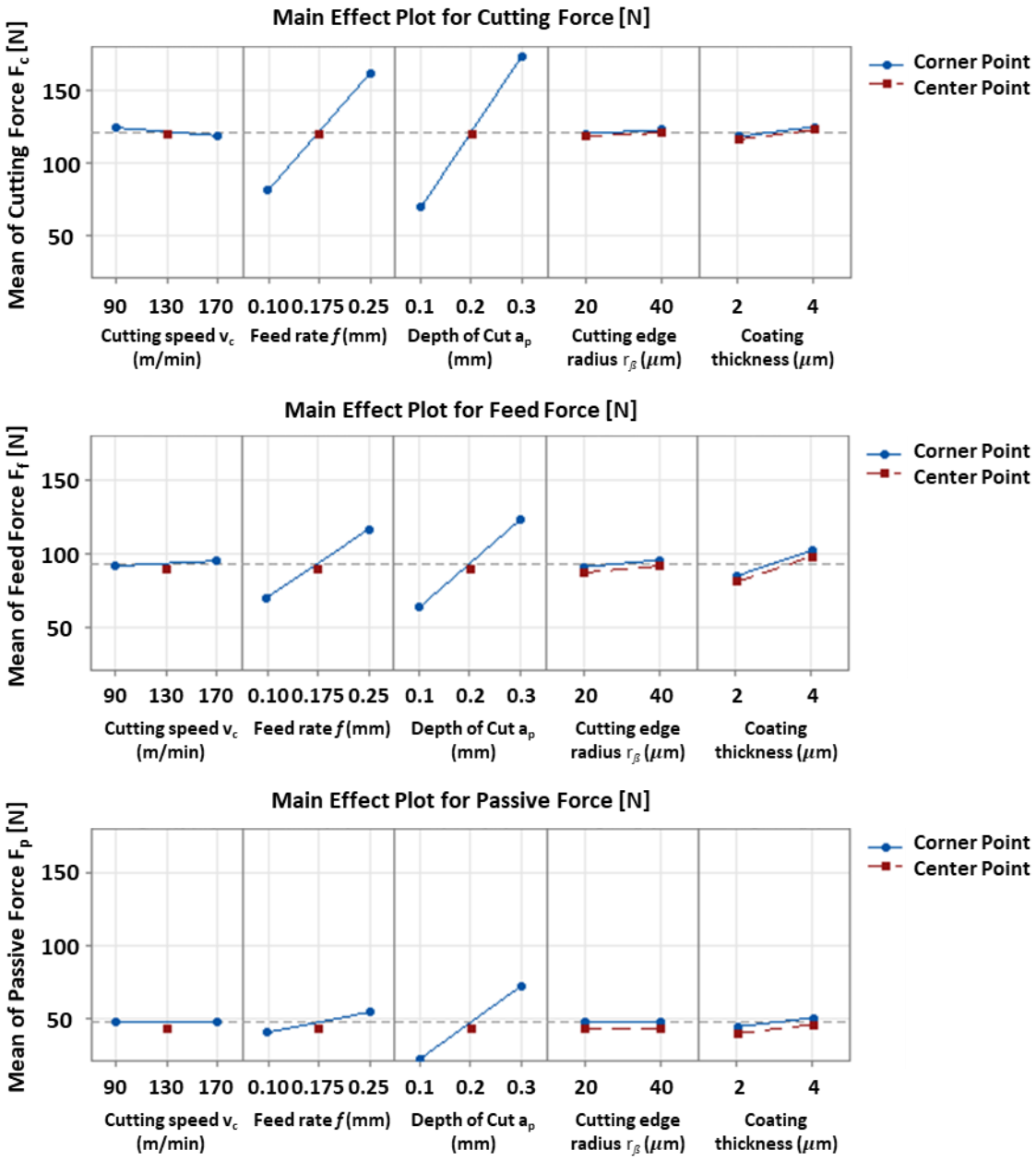

Workpiece material: 1.4837D Cooling: None Longitudinal turning	Cutting depth : a_p = var. Feed-rate : f = var. Cutting speed : v_c = var.	α_o | γ_o | ε_r | κ_r 7° | 15° | 55° | 93°	Tool material: ISO-K10 Geometry: DCGT11T304-F Cutting edge radius: var. Corner radius: 0.4mm Coating: AlTiN Coating thickness: var.

Figure 4-43: Linearized relationships between forces (F_c, F_f and F_p) and corresponding test factors (v_c, f, a_p, r_β and coating thickness): Experiments

It can be observed that the center point of DoE is very close to the straight line for all the three force components. This means that a linearized relationship of forces can be assumed for the analyzed DoE parameters.

Figure 4.44 shows the linearized correlation between averaged surface roughness (Rz) and cutting parameters, cutting edge radius and coating thickness. In this figure, it is evident the feed-rate is strongly correlated with the averaged surface roughness, and it is dominating the other input parameters. This behavior corresponds to what is defined and expected in literature [7, 9]. On the other hand, cutting speed, depth of cut and cutting edge radius have a minor impact on the averaged surface roughness. In comparison to tools with a coating thickness of 2µm, tools with a coating thickness of 4µm provided better results with a lower averaged surface roughness value. This is because the 2µm AlTiN coated inserts had built up edges during machining and in some cases also had high wear.

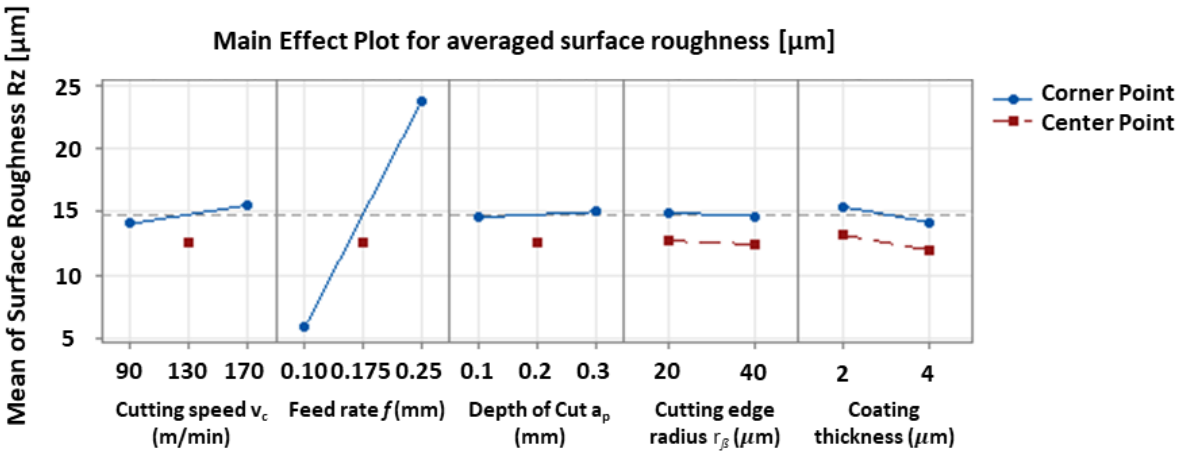

Workpiece material: 1.4837D Cooling: None Longitudinal turning	Cutting depth : a_p = var. Feed-rate : f = var. Cutting speed : v_c = var.	α_o | γ_o | ε_r | κ_r 7° | 15° | 55° | 93°	Tool material: ISO-K10 Geometry: DCGT11T304-F Cutting edge radius: var. Corner radius: 0.4mm Coating: AlTiN Coating thickness: var.

Figure 4-44: Linearized relationships between averaged surface roughness and corresponding test factors (v_c, f, a_p, r_β and coating thickness): Experiments

The linearized correlation of temperature with cutting parameters, edge radius and coating thickness are plotted in figure 4.45. The cutting parameters (v_c, f and a_p) have a dominating effect on the tool temperature compared to the cutting edge radius and coating thickness. The temperature increases significantly with increasing cutting parameters. These effects are similar to what was observed in first DoE. A larger tool cutting edge radius also leads to a higher

temperature. The increase in tool temperature with increasing tool cutting edge radius can be explained by the energy balance in the machining process. A larger cutting edge radius increases the friction and shear components, which are the dominant energy components and are almost entirely generated as heat in the tool [9] leading to an increase in tool temperature. In contrast, for a thicker coating of 4µm, lower temperatures were recorded than for a coating thickness of 2µm.

Additionally, it must be noted that the center point for all the five input parameters deviate significantly from the linearized straight line. A similar behavior was observed in DoE 1. This deviation indicates that there is no linear relationship between the tested input parameters and temperature [154]. The cube plot diagram showing temperature results for all the four coatings at each DoE parameter is shown in figure A6 in appendix.

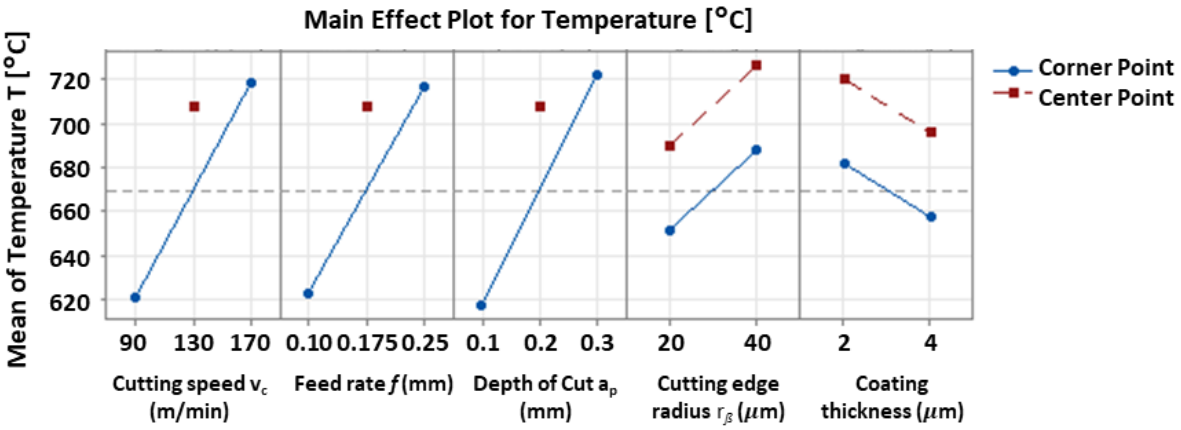

Workpiece material: 1.4837D	Cutting depth : a_p = var.	α_o	γ_o	ε_r	κ_r	Tool material: ISO-K10
Cooling: None	Feed-rate : f = var.	7°	15°	55°	93°	Geometry: DCGT11T304-F
Internal turning	Cutting speed : v_c = var.					Cutting edge radius: var.
						Corner radius: 0.4mm
						Coating: AlTiN
						Coating thickness: var.

Figure 4-45: Linearized relationships between temperature and corresponding test factors (v_c, f, a_p, r_β and coating thickness): Experiments

4.9 Simulation results: Comparison of coating thickness and cutting edge radius (DoE 2)

The FEM-simulation setup for longitudinal turning and internal turning process used in this DoE was identical to DoE 1. The only difference here was that the different cutting edge radii, i.e., 22µm, 24µm, 42µm and 44µm, were modelled in Siemens NX and then these CAD models were imported to the first DoE AdvantEdge simulation setup for carrying out new calculations.

To create chips, the length of cut was defined as 25mm for all the simulations. Tool mesh size was refined only in the tool-workpiece engagement area and was defined as one-third of the tool cutting edge radius. Workpiece mesh was defined in accordance with parametric study of mesh sensitivity analysis explained in section 4.5.2.

A comparison of the dominant force, i.e., cutting force from longitudinal turning simulations for the tools with cutting edge radii of r_β= 24µm and r_β= 44µm is plotted below in figure 4.46. For the other two tools (cutting edge radii r_β= 22µm and r_β= 42µm), results of cutting force are shown in figure A7 in appendix. Analogous to experiments, simulation results do not deviate significantly from basic proportionalities and magnitude of forces. Linearized correlation of forces was visualized using Minitab software for all the input parameters (three cutting parameters, edge radius and coating thickness) and is shown in figure 4.47.

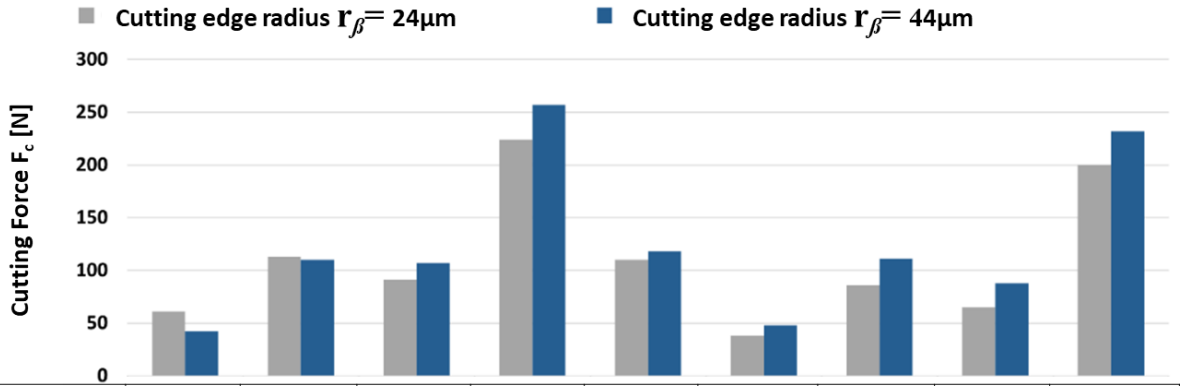

v_c (m/min)	90	90	90	90	130	170	170	170	170
f (mm)	0.1	0.1	0.25	0.25	0.175	0.1	0.1	0.25	0.25
a_p (mm)	0.1	0.3	0.1	0.3	0.2	0.1	0.3	0.1	0.3

Workpiece material: 1.4837D Cooling: None	α_o	γ_o	ε_r	κ_r	Tool material: ISO-K10 Geometry: DCGT11T304-F Cutting edge radius: var. Corner radius: 0.4mm Coating: AlTiN Coating thickness: 4µm
Longitudinal turning Simulation method: FEM	7°	15°	55°	93°	

Figure 4-46: Cutting forces for tools with a 4µm coating layer thickness (CT) and cutting edge radii of r_β= 24µm and r_β= 44µm

As it can be seen in figure 4.46 and 4.47, the cutting force increases with an increase in feed-rate and depth of cut and the forces decrease with an increase in the cutting speed. However, the influence of cutting speed is more in simulations than in experiments. Furthermore, forces increase with an increase in cutting edge radius and coating thickness. In main effect plot diagram for simulated forces, it can be observed that the center point (red dot) is close to the

straight line joining the corner points of DoE. This closeness indicates that a linear relationship exists between forces and input parameters of DoE.

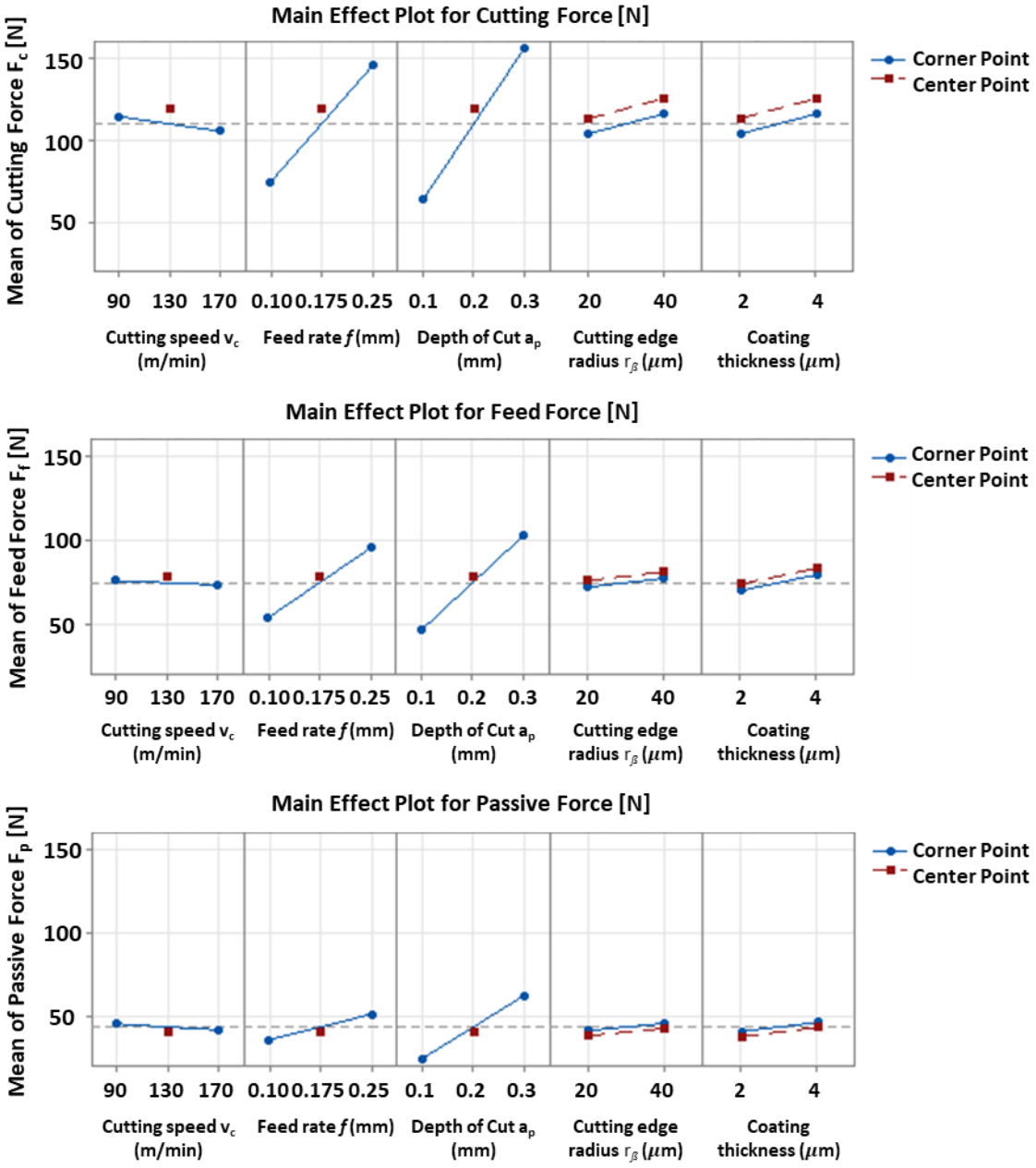

Workpiece material: 1.4837D Cooling: None	Cutting depth : a_p = var. Feed-rate : f = var. Cutting speed : v_c = var.	α_o | γ_o | ε_r | κ_r 7° | 15° | 55° | 93°	Tool material: ISO-K10 Geometry: DCGT11T304-F Cutting edge radius: var. Corner radius: 0.4mm Coating: AlTiN Coating thickness: var.
Longitudinal turning Simulation method: FEM			

Figure 4-47: Linearized relationships between forces (F_c, F_f and F_p) and corresponding test factors (v_c, f, a_p, r_β and coating thickness): Simulations

Figure 4.48, and figure A8 in appendix compare the simulated temperature results of cutting inserts with coating thicknesses of 4µm and 2µm, respectively, from the internal turning process. Figure 4.49 shows the main effect diagram for temperatures based on input parameters of the DoE. The influence of cutting parameters is same as mentioned earlier in DoE 1. However, with an increase in cutting edge radius, the temperature increases in most of the cases. On the contrary, the tool temperature reduces from 2µm coating thickness to 4µm coating thickness, i.e., the tool with a radius of 44µm observes lower temperatures than the tool with a radius of 42µm. This happened because the tool with thicker coating of 4µm acts as thermal barrier, reducing the heat conduction in the substrate material. Since the center point in figure 4.49 is away from the straight line joining the corner points, no linear relationship exists for temperatures on the tested set of parameters. Similar results were observed for the measured experimental temperature results.

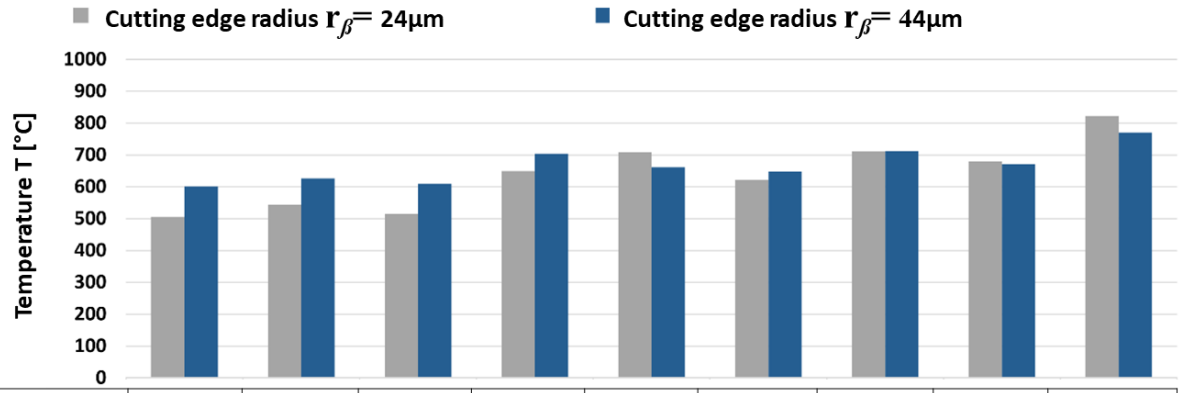

v_c (m/min)	90	90	90	90	130	170	170	170	170
f (mm)	0.1	0.1	0.25	0.25	0.175	0.1	0.1	0.25	0.25
a_p (mm)	0.1	0.3	0.1	0.3	0.2	0.1	0.3	0.1	0.3

Workpiece material: 1.4837D
Cooling: None

Internal turning
Simulation method: FEM

α_o	γ_o	ε_r	κ_r
7°	15°	55°	93°

Tool material: ISO-K10
Geometry: DCGT11T304-F
Cutting edge radius: var.
Corner radius: 0.4mm
Coating: AlTiN
Coating thickness: 4µm

Figure 4-48: Tool temperature with 4µm coating layer thickness and cutting edge radius of 24µm and 44µm

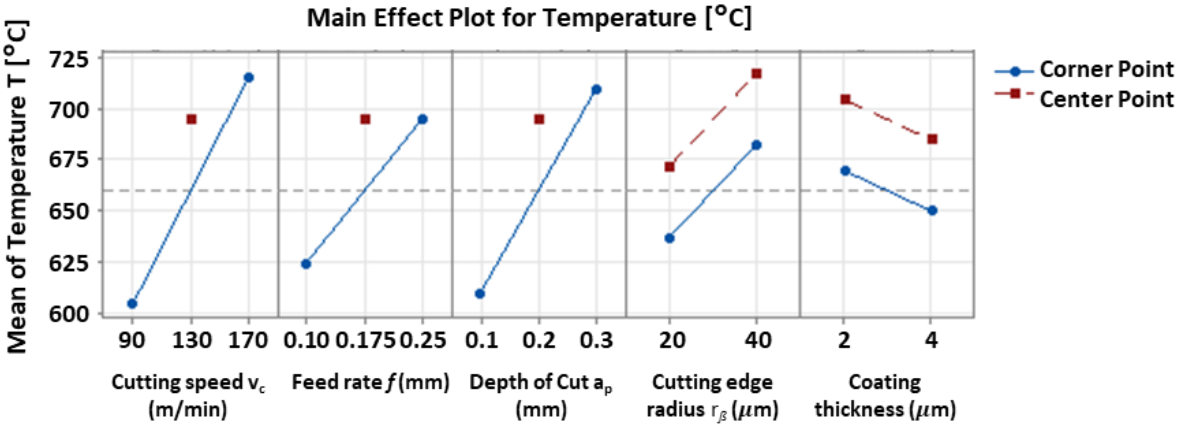

Workpiece material: 1.4837D Cooling: None Internal turning Simulation method: FEM	Cutting depth : a_p = var. Feed-rate : f = var. Cutting speed : v_c = var.	α_o | γ_o | ε_r | κ_r 7° | 15° | 55° | 93°	Tool material: ISO-K10 Geometry: DCGT11T304-F Cutting edge radius: var. Corner radius: 0.4mm Coating: AlTiN Coating thickness: var.

Figure 4-49: Linearized relationships between temperature and corresponding test factors (v_c, f, a_p, r_β and coating thickness): Simulations

One of the major advantages of machining simulations over experiments is that temperature, which is vital information in selection of a tool, can be determined and visualized at any given point of time over the tool's cutting edge. Figure 4.50 compares the temperature of all the four tools with the cutting parameter v_c=90m/min, f=0.25mm and a_p=0.3mm. This figure shows the tool with cutting edge radius r_β=22µm (CT=2µm) on the top left, the tool with cutting edge radius r_β=24µm (CT=4µm) on the top right, the tool with cutting edge radius r_β=42µm (CT=2µm) on the bottom left and the tool with cutting edge radius r_β=44µm (CT=4µm) on the bottom right. While comparing the temperature results from left to right in figure 4.50, it can be noticed that the right side of tools (4µm coating) has lower temperature in comparison to the left side of tools (2µm coatings). On the other hand, it can be observed that the area of high temperature zone (in red color in figure 4.50) increases from top (tools with cutting edge radii 22µm and 24µm) to bottom (tools with cutting edge radii 42µm and 44µm). This increase in temperature is because of the large contact area between the tool and workpiece for bottom tools as compared to top tools. An increase in tool temperature here is not necessarily bad because an increase in contact length between tool and workpiece increases the area for heat dissipation. For this reason, maximum temperature for each DoE parameter and each tool was plotted on the DoE cube plot. This is shown in figure A9 in appendix. From this figure, it can be noticed that temperatures for all the four tools lie in the same range and thus, higher

temperatures for tools with radii of 42µm and 44µm are not detrimental as the tool-workpiece contact also increases.

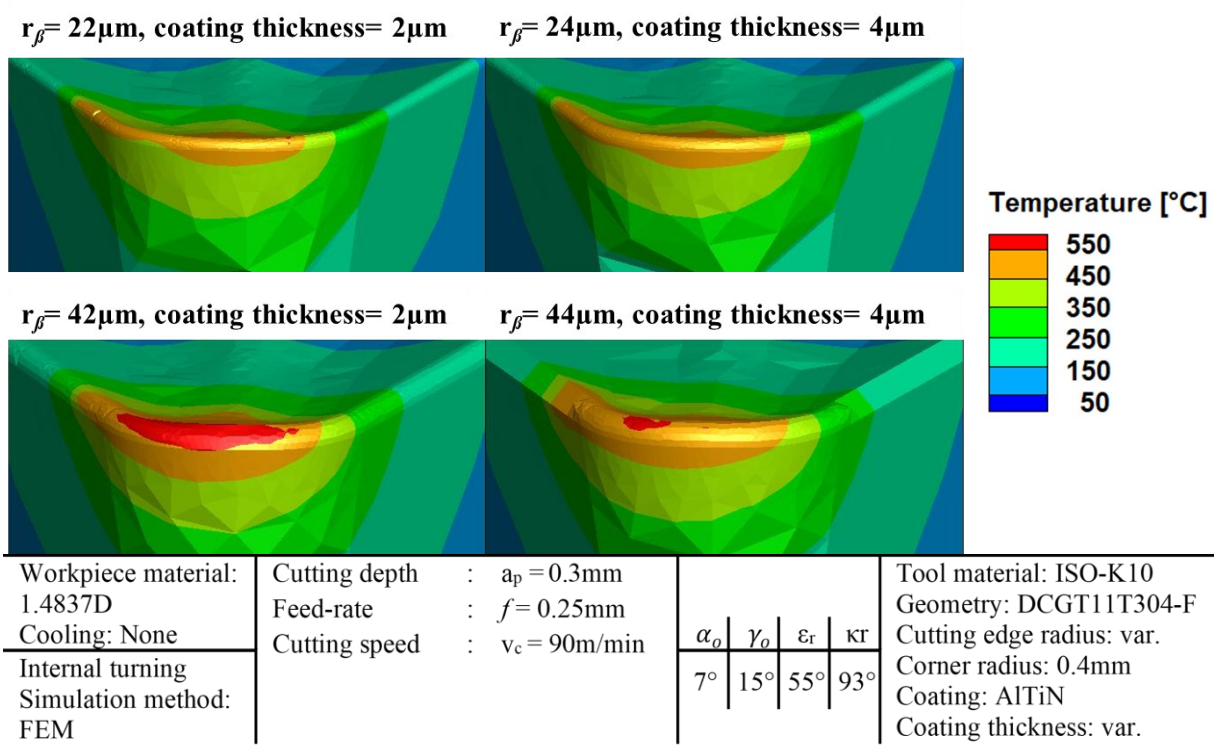

Workpiece material: 1.4837D Cooling: None	Cutting depth : a_p = 0.3mm Feed-rate : f = 0.25mm Cutting speed : v_c = 90m/min	α_o	γ_o	ε_r	κ_r	Tool material: ISO-K10 Geometry: DCGT11T304-F Cutting edge radius: var. Corner radius: 0.4mm Coating: AlTiN Coating thickness: var.
Internal turning Simulation method: FEM		7°	15°	55°	93°	

Figure 4-50: Temperature at tool cutting edge: 22µm tool (top-left), 24µm tool (top-right), 42µm tool (bottom-left) and 44µm tool (bottom-right) with v_c=90m/min, f=0.25 and a_p=0.3

The rise in temperature (in Figure 4.50) is not detrimental for the tools with higher cutting edge radius (42µm and 44µm) as the tool and chip contact area is increased and more heat is absorbed by the chip. Additionally, the higher (blunt) cutting edge radius is more stable than the lower (sharp) cutting edge radius. Thus, 44µm tool had the lowest wear among the tested tools.

4.10 Comparison of simulation with experiments for DoE 2

In this section, the simulation results from DoE 2 will be compared with the experimental results. This comparison was carried out to determine the accuracy of simulation models with experiments and to find out whether simulations can capture the effect of change in cutting edge radii and coating thicknesses. Figure 4.51 shows comparison of cutting forces between simulations and experiments for the tool with cutting edge radius of 44µm and a coating thickness of 4µm. For other three tools and two force components, the results were similar.

For most of the cutting parameters, simulations have lower values of cutting forces than experiments and a similar behavior was observed earlier in DoE 1. Relative error between

simulations and experiments was calculated, taking experimental results as true values. The relative error of cutting force for four tools with the cutting edge radii of 22µm, 24µm, 42µm and 44µm were -13.2%, -5%, -2.9% and -5.3% respectively. These relative errors prove that the simulation results are in good correlation with the measured values.

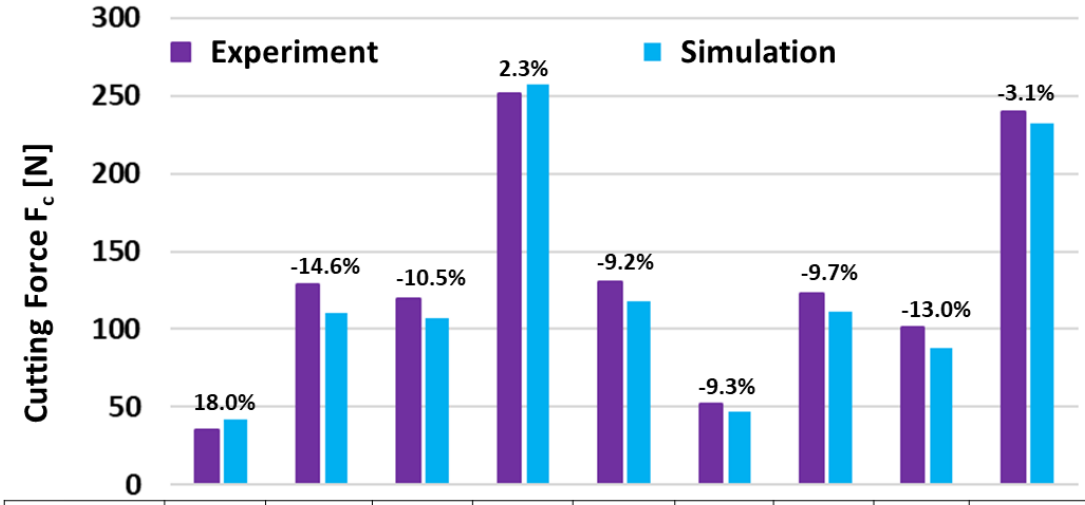

v_c (m/min)	90	90	90	90	130	170	170	170	170
f (mm)	0.1	0.1	0.25	0.25	0.175	0.1	0.1	0.25	0.25
a_p (mm)	0.1	0.3	0.1	0.3	0.2	0.1	0.3	0.1	0.3

Workpiece material: 1.4837D Cooling: None	Cutting depth : a_p = var. Feed-rate : f = var. Cutting speed : v_c = var.	α_o | γ_o | ε_r | κ_r 7° | 15° | 55° | 93°	Tool material: ISO-K10 Geometry: DCGT11T304-F Cutting edge radius: 44µm Corner radius: 0.4mm Coating: AlTiN Coating thickness: 4µm
Longitudinal turning Simulation method: FEM			

Figure 4-51: Cutting force comparison between measured and simulation results for 44µm cutting edge radius and 4µm AlTiN coating thickness

The simulated and measured temperature results from internal turning were also compared with each other. Figure 4.52 shows comparison of temperature results for the tool with cutting edge radius of 44µm and a coating thickness of 4µm. For most cutting parameters, temperatures were slightly underpredicted, whereas for a few cutting parameters, there was a marginal overprediction. Relative error between experiments and simulations was also calculated and on average it accounts for -4.1%, -2.5%, -3% and -3.5% for tools with the cutting edge radii of 22µm, 24µm, 42µm and 44µm respectively. From relative error percentage it can be concluded that for temperature calculations, simulations have a very good correlation with experiments.

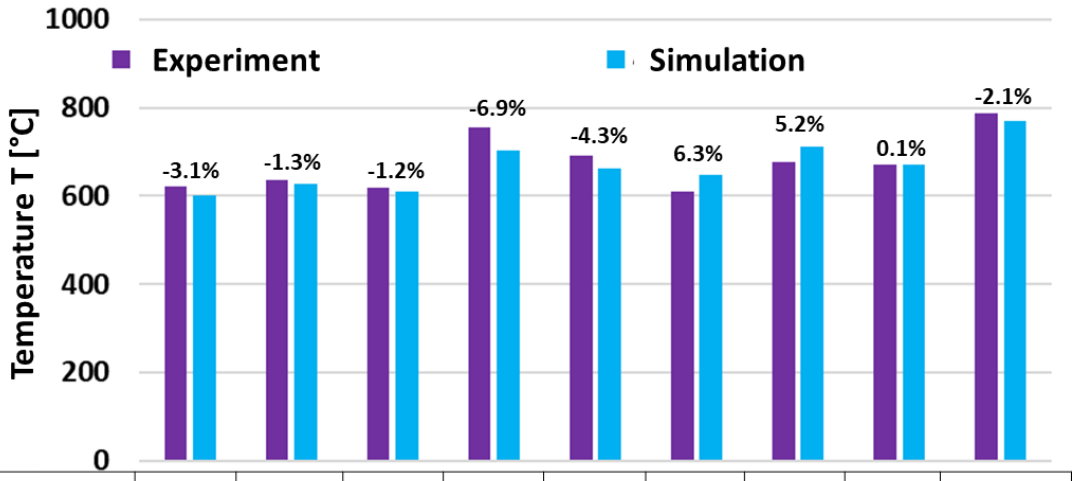

v_c (m/min)	90	90	90	90	130	170	170	170	170
f (mm)	0.1	0.1	0.25	0.25	0.175	0.1	0.1	0.25	0.25
a_p (mm)	0.1	0.3	0.1	0.3	0.2	0.1	0.3	0.1	0.3

Workpiece material: 1.4837D
Cooling: None

Internal turning
Simulation method: FEM

Cutting depth : a_p = var.
Feed-rate : f = var.
Cutting speed : v_c = var.

α_o	γ_o	ε_r	κ_r
7°	15°	55°	93°

Tool material: ISO-K10
Geometry: DCGT11T304-F
Cutting edge radius: 44µm
Corner radius: 0.4mm
Coating: AlTiN
Coating thickness: 4µm

Figure 4-52: Temperature comparison between measured and simulation results for 44µm cutting edge radius and 4µm AlTiN coating thickness

It is very important for simulations to reliably predict the chip formation during machining process calculations. For this reason, chips collected from the experiments were compared with the simulated chips. Figure 4.53 shows the chips for two depth of cut a_p=0.1mm (left side in image) and a_p=0.3mm (right side in image) on the tool with cutting edge radius of 44µm and a coating thickness of 4µm. In experiments, long continuous chips were produced for depth of cut a_p= 0.1mm whereas spiral chips were produced for the other depth of cut. At the bottom of the image, simulated chips are presented. In simulations too, spiral chips were obtained for the depth of cut a_p=0.3mm and it is in very good correlation with the experiments. For the other cutting parameter with depth of cut a_p=0.1mm, cutting length of the workpiece, which was set to 25mm for all the simulations, was probably not enough to produce the same chips. However, chip produced till the cutting length of 25mm looked comparable to the experimental chips. On comparing the two chip shapes, spiral chips were more suitable for machining process.

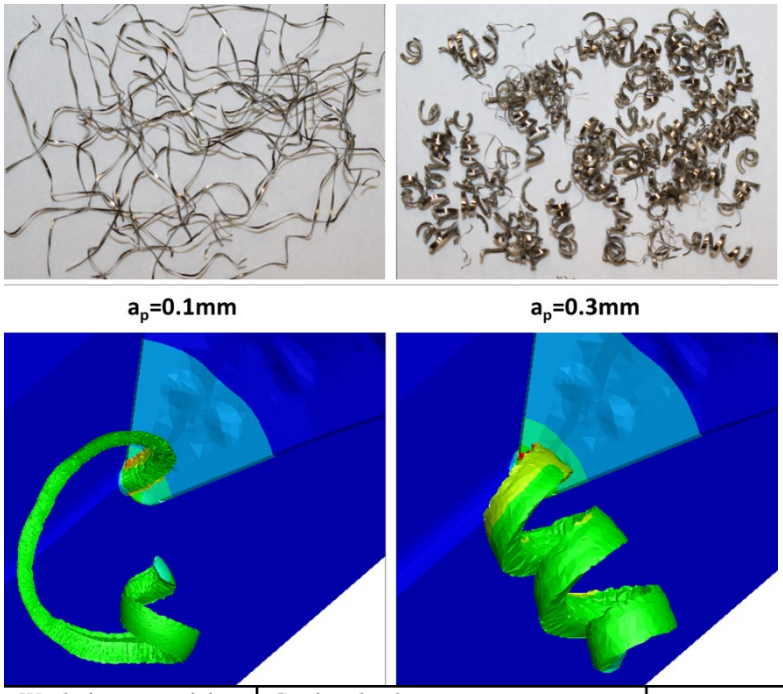

Workpiece material: 1.4837D Cooling: None	Cutting depth : a_p = var. Feed-rate : f = 0.25mm Cutting speed : v_c = 90m/min	α_o | γ_o | ε_r | κ_r 7° | 15° | 55° | 93°	Tool material: ISO-K10 Geometry: DCGT11T304-F Cutting edge radius: 44µm Corner radius: 0.4mm Coating: AlTiN Coating thickness: 4µm
Longitudinal turning Simulation method: FEM			

Figure 4-53: Chip comparison between experiments and simulations for 44µm cutting edge radius and 4µm coating thickness

4.11 Summary

The aim of the two DoEs in this chapter was to find out how well simulations can depict fine changes like coatings, coating thicknesses or edge radii. It has been shown that these influences can be reflected well digitally. Whether a change leads to a reduction or increase in the forces or temperatures was evident to a great extent. It could be concluded from both the DoEs that a major advantage of simulations over experiments was that the temperatures could be visualized for the whole simulation time. This helped in understanding thermal loads on the tool during the machining process.

On the other hand, a major objective of these two designs of experiments was to optimize the turning process. This has been achieved by simulations to some extent because tool wear and surface roughness cannot be simulated yet. For these two outputs (surface roughness and wear), practical experiments are still necessary. Nevertheless, for future, simulations can narrow down the test parameters and help in tool selection beforehand to reduce effort and cost. Additionally,

turning process optimization was achieved in DoE 2 with 44µm tool cutting edge radius and 4µm AlTiN coating thickness because this tool was able to produce 90 target parts, keeping the tool wear lower than the defined tool-wear criteria. Therefore, it can be concluded that instead of experiments, FEM-simulations can be used in future to determine forces and temperature.

5 Simulation of flood lubricated turning process

During machining, a tool undergoes severe mechanical and thermal loading conditions. During chip removal, due to friction a lot of heat is generated which can pose detrimental effects on the tool. Due to this reason, tools are coated, so that coating can shield the hardmetal by acting as a thermal barrier and improve the tool life. In chapter 4, it was noticed that the tool temperatures (both measured and simulated) reached above 700°C for most of the cutting parameters, especially with a high cutting speed. To mitigate these thermal issues on the tool, lubricants are widely used during the machining process.

Through FEM-Simulations, a prognosis can be made for various aspects of machining process, for example cutting forces, induced stress in tool and workpiece, chip shape, and temperature. However, accurate temperature of only dry machining can be predicted because FEM simulations cannot effectively model the lubricant, i.e., fluid. In experiments also it is difficult to understand the behavior of a coolant in the cutting area due to high rotational speed of tools. In this scenario, CFD-simulations present an optimal solution where lubricant can be modelled inside a virtual environment. This makes it easier to study the flow of lubricant inside the system and more information can be gathered on heat exchange between the tool, workpiece and lubricant.

5.1 Experimental setup & results of flood lubricated internal turning process

To verify the usefulness and accuracy of simulations, it is necessary to validate them with the experimentally measured values. For this reason, the simulated temperatures from flood lubricated internal turning process in this chapter were validated with the experimental results. The same internal turning process experimental setup mentioned in section 4.2 was used to measure temperatures in both, dry and flood lubricated machining, i.e., experiments were conducted using Heller MC12, 4-axis machining center. The only difference in these experiments, as compared to dry machining experiments (as shown in figure 4.3), was that the sealing air was blown through the 700µm hole to prevent the lubricant from entering the hole, so that the lubricant does not falsify the temperature measurement results. DCGT11T304-F coated inserts were used in experiments with 3µm AlTiN coating and 12µm cutting edge radius. The cutting parameter: cutting speed, feed-rate and depth of cut were analyzed. Each experiment was repeated twice, and a new tool was used for every cutting parameter.

Temperature was measured with a 2-color pyrometer and measured results were analyzed with the OriginPro software. The experimentally measured temperature for the cutting parameter, cutting speed (v_c) =90m/min, feed-rate (f) =0.1mm and depth of cut (a_p) =0.1mm is illustrated in figure 5.1. To compare the temperature recorded from individual experiments, a representative temperature value was determined in the same way as mentioned in section 4.4.1. Different cutting parameters tested during experiments along with their mean temperature results are shown below in table 5.1. It can be observed from the table that the temperature increases with an increase in depth of cut, feed-rate and cutting speed. Additionally, the cutting speed has dominant effect on the temperature results, which is similar to the observation in chapter 4 in dry internal turning experiments.

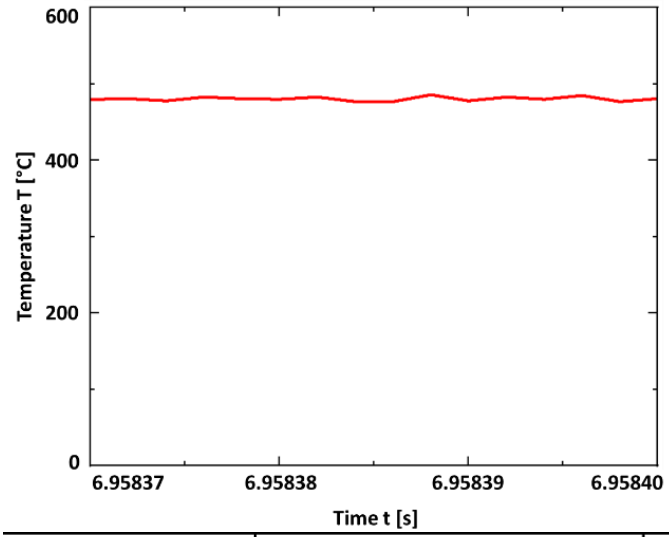

Workpiece material: 1.4837D Cooling: Flood Internal turning	Cutting depth : a_p = 0.1mm Feed-rate : f = 0.1mm Cutting speed : v_c = 90m/min	α_o | γ_o | ε_r | κ_r 7° | 15° | 55° | 93°	Tool material: ISO-K10 Geometry: DCGT11T304-F Cutting edge radius: 12µm Corner radius: 0.4mm Coating: AlTiN Coating thickness: 3µm

Figure 5-1: Temperature measurement results from flood lubricated internal turning process

Table 5-1: Measured temperature results from flood lubricated internal turning process

Cutting speed [m/min]	Feed-rate [mm]	Depth of cut [mm]	Temperature [°C]
90	0.1	0.1	482
90	0.25	0.1	542
90	0.1	0.3	514
170	0.1	0.3	695

5.2 CFD-Simulation of lubricated internal turning process

Due to shearing of material, a lot of heat is generated in the machining process. This heat is dissipated via conduction, convection and radiation. The heat dissipation can be quantified if the heat transfer coefficient (HTC) at the tool surface is known. Since flood lubrication involves both lubricant (fluid) and tool-workpiece (structure), it makes flood lubrication machining process a multi-physics problem. This multi-physics problem was solved with two different approaches in this work:

1.) Unidirectional coupling approach between two different FEM- and CFD- software.

2.) Bidirectional FEM-CFD coupling using a single software.

In the first approach, flood lubricated internal turning process was modelled using coupling between AdvantEdge (for FEM-simulations) and Star-CCM+ (for CFD-simulations). The results from this approach were validated with the experimental results mentioned in section 5.1. In the second approach, an orthogonal turning process for flood lubrication was modelled using SPH formulation in the LS-DYNA software. These results were compared to the results of dry orthogonal turning simulations because no experimental results from flood lubricated orthogonal turning process were available for validation.

The first approach is based on one-way coupling between FEM- and CFD-software, whereas the second approach used a two-way coupling in a single software. Both approaches were tested to find the one approach that can be used in future to understand the cooling mechanism during flood lubricated machining.

5.2.1 Unidirectional coupling for flood lubrication using FEM- and CFD-Software

In this approach, two methodologies were used to achieve the FEM-CFD coupling for flood lubricated internal turning process. The first methodology is based on the research work mentioned in section 2.2.2, where the temperature in flood lubricated internal turning process was calculated in the FEM-software. Due to some shortcomings in this approach, a second methodology, where the above-mentioned temperature was calculated in the CFD-software, was used later in the simulations. These two methodologies will be defined in detail below in sections 5.2.1.4 and 5.2.1.5. For both the methodologies in this approach, same simulation setup, mesh and turbulence model were used.

5.2.1.1 Simulation setup

The simulation setup for flood lubricated internal turning process is described. ISO K10 substrate material and DCGT11T304-F coated inserts (α_o=7°, γ_o= 15°, ε_r= 55° and κ_r= 93°) were used in the turning process. The inserts were coated with a 3µm thick PVD-AlTiN layer. The simulations for the FEM part (structure) were performed in AdvantEdge v7.9 and for the CFD part (fluid) were performed in Star-CCM+ version 2302. The FEM-simulation setup in flood lubrications is same as mentioned in chapter 4 and thus here only the CFD-model setup is explained. Few assumptions were made in the CFD-simulations:

- Lubricant does not change its properties with respect to temperature,
- Wear during the flood lubrication internal turning process can be neglected as simulations were run only till 1.1s,
- Radiation effects were neglected.

All the CFD-simulations were run on high performance cluster with 576 cores. The material properties and process parameters of lubricant used are mentioned below in table 5.2. The material properties of the tool and workpiece are same as mentioned earlier in chapter 4. The unit system used in CFD simulations is mentioned in table 5.3.

Table 5-2: Material properties of lubricant in CFD-simulations

Object	**Density (kg/m³)**	**Viscosity (mm²/s)**	**Pump pressure (bar)**	**Flow rate (l/min)**
Lubricant	997.56	60	5	28

Table 5-3: Unit system used in CFD-simulations

Mass	Length	Time	Energy	Temperature	Thermal conductivity	Heat capacity
kg	mm	ms	kN-mm	K	$\frac{kg\ mm}{ms^3°C}$	$\frac{mm^2}{ms^2°C}$

CAD models were prepared in the Siemens NX software. Due to the complex shape of the tool holder, CAD model was simplified for CFD simulations by removing unnecessary parts like screws. This simplified CAD model used in simulations is shown in figure 5.2.

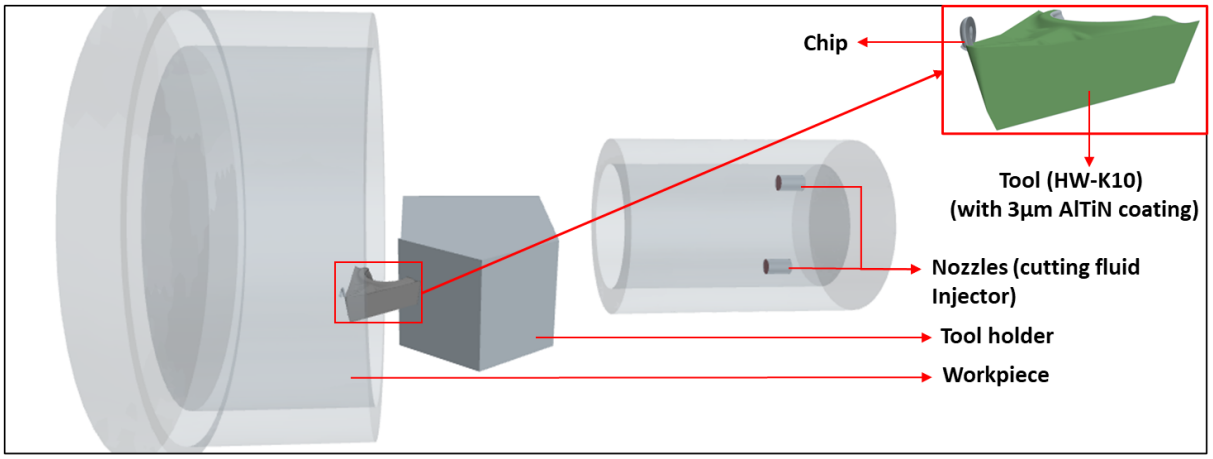

Figure 5-2: Flood lubrication simulation model setup

During CFD-simulation of internal turning process, the workpiece was kept stationary and the tool was given both, cutting speed (v_c) and feed-rate (f), i.e., the tool was rotated as well as translated. An inlet flow rate of 28 l/min was given to the lubricant coming out of the nozzles in the tool holder. Atmospheric pressure was defined as an outlet boundary. Along with that, a no slip boundary condition was defined on all the solid walls, i.e., on the workpiece surface, tool surface and tool holder surface. A no slip condition means that the velocity of fluid at a solid interface is equal to the velocity of that solid surface. An initial temperature of 20°C was also provided as a thermal condition to the entire CFD-domain.

5.2.1.2 Mesh methodology

A polyhedral mesh was used along with an overset meshing technique for the moving objects in CFD domain. In total three overset regions for cutting fluid injectors, tool and tool holder were defined in simulations, as shown in figure 5.3. A mesh sensitivity analysis was conducted to get the adequate mesh size for simulations.

Analogous to FEM-simulations, mesh sensitivity analysis was conducted to get the correct meshing parameters for flood lubricated internal turning process simulations. Four different mesh parameter settings were used to find the optimal mesh setting. In all the four cases, polyhedral mesh was used for CFD-background with mesh size of 5mm. Along with that, overset mesh technique was used for the rotating parts. The values of these four different mesh

parameters along with the results are mentioned below in table 5.4. The cutting parameters used in this mesh sensitivity analysis were cutting speed (v_c) =90m/min, feed-rate (f) =0.1mm and depth of cut (a_p) =0.1mm.

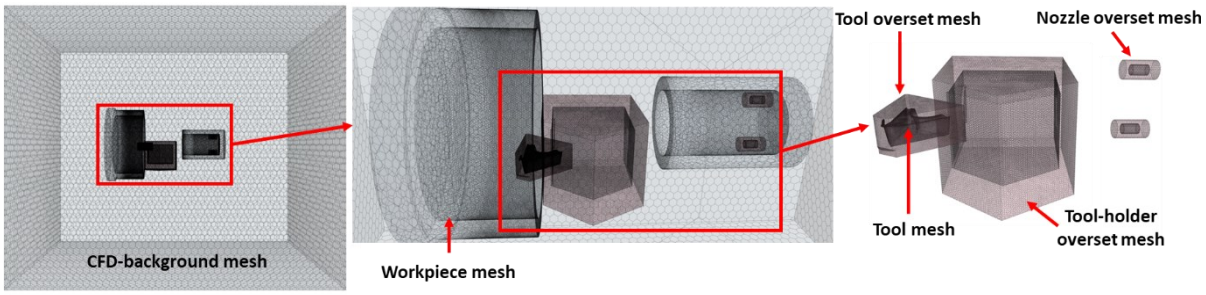

Figure 5-3: Mesh used in CFD-simulations

Table 5-4: CFD-Mesh sensitivity analysis

Name	Tool mesh [mm]	Tool overset mesh [mm]	Simulation time [min]	Tool Temperature [°C]
Mesh 1	0.5	0.5	210	470
Mesh 2	0.5	0.2	250	465
Mesh 3	0.2	0.2	906	449
Mesh 4	0.2	0.1	987	466
Measured Temperature result				514

Table clearly illustrates that mesh has a negligible impact on temperature results. However, it must be noted that Mesh 3 and 4 have significantly longer simulation times in comparison to Mesh 1 and 2. Additionally, the simulated temperature results are in good correlation with the experimental results. Due to its computational advantages over Mesh 3 and 4 and its finer size compared to Mesh 1, Mesh 2 was selected for further simulations.

The behavior of turbulent flow localized around solid walls exhibits a low Reynolds number which differs significantly from high Reynolds free-stream flow far from solid walls due to variations in shear stresses. These shear stresses are low for most part of the fluid domain, except for the fluid layer near the solid walls. Hence, in conjugate heat transfer simulations, modelling these near wall regions accurately is very important as temperature changes over

fluid-wall (lubricant-tool in case of machining process) interface. To resolve this, one of the reliable methods is to create a fine mesh in CFD-domain. However, this will increase the computational cost enormously [157]. To counter this, wall functions are used in CFD-simulations. These wall functions represent simplified turbulence models that enable wall compensation without the need to resolve the near-wall region. Thus, near-wall regions serve as a fully developed turbulent boundary layer (prism layer) [158, 159]. Two variables that define the wall function are: u^+ (time averaged velocity parallel to wall) and y^+ (non-dimensional normal distance from wall). This dimensionless distance y^+ defines the height of first element adjacent to the wall and is shown diagrammatically in figure 5.4 [160].

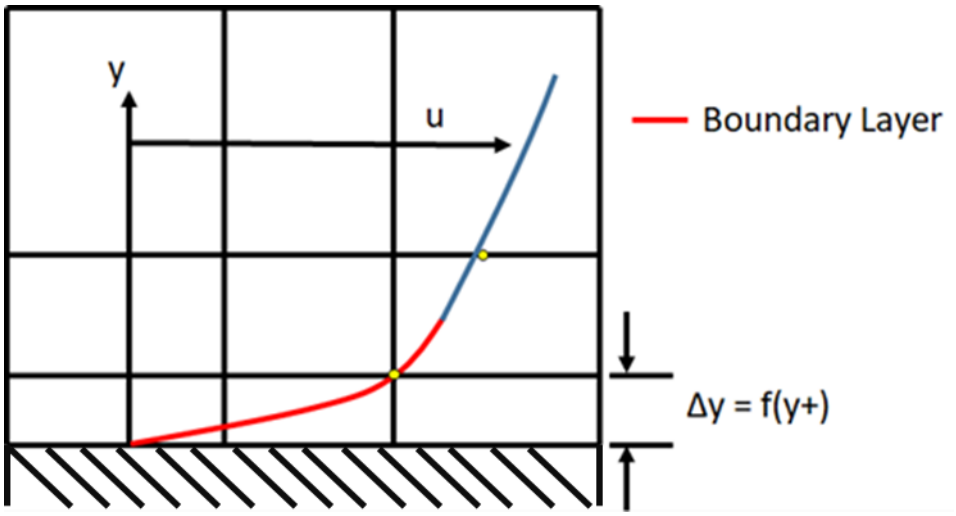

Figure 5-4: Definition of non-dimensional normal distance from wall y+ [160]

Flood lubrication simulations are based on conjugate heat transfer problems. Thus, their accuracy depends on the y^+ value of the first cell. For heat transfer problems, it is recommended to keep the y^+ value less than 2 to accurately predict the temperature values [161]. To keep the y^+ value less than 2, prism layer of 15µm was created on the tool surface.

5.2.1.3 Turbulence model analysis

Like mesh, turbulence model also has a huge impact on CFD-simulation results. Due to this reason, a turbulence model analysis was conducted to find the best suitable turbulence model for flood lubricated internal turning process. Two different turbulence models, realizable k-ε model and k-ω-SST model were analyzed. Table 5.5 shows the computational time taken by each turbulence model for 1.1s of internal turning process simulation along with the simulated temperatures.

Table 5-5: Comparison of realizable k-ε realizable and k-ω-SST turbulence model

Turbulence model	Y^+ value [-]	Simulation time [min]	Tool Temperature [°C]
Realizable k-ε model	1.62	255	471
k-ω-SST model	1.47	250	465
Measured Temperature result			514

Based on prism layer input from the meshing section, y^+ values were calculated on tool surface in simulations for both the turbulence models. The y^+ values for both the models were less than 2. It can be concluded that prism layer mesh and mesh parameters defined in the last section were suitable for simulations and they were further used for other internal turning process simulations. It can also be observed from table 5.5 that both turbulence models had approximately the same computational time and comparable temperature results to the experimentally measured values. Inspite of similar results, the k-ω-SST model was chosen over realizable k-ε model, because literature [162] confirms that the k-ω-SST model performs better for heat transfer problems.

5.2.1.4 First methodology: Flood lubrication in FEM-Software

In most of the FEM-software, lubrication effect is taken into account by defining the heat transfer coefficient value. This has been the base for first methodology. A schematic diagram of this methodology is shown below in figure 5.5.

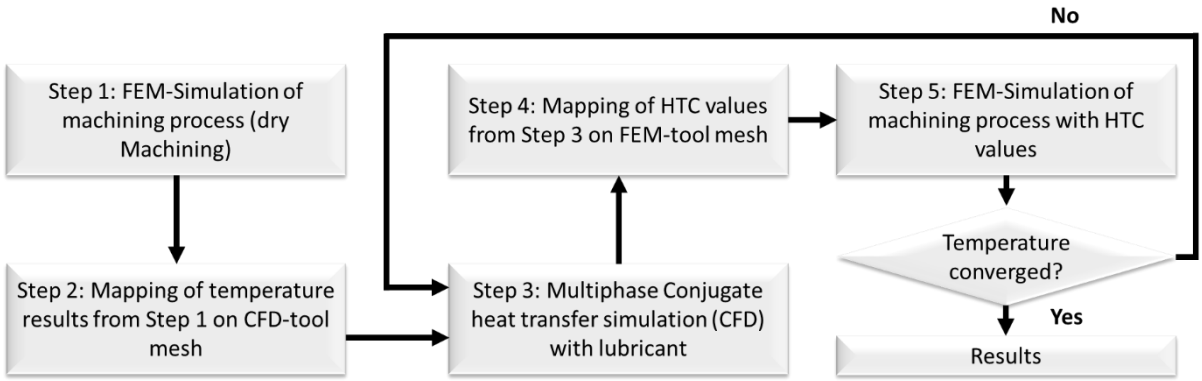

Figure 5-5: Flood lubrication in FEM-Software

In the first step, a dry FEM-internal turning process was started in the AdvantEdge software. Afterwards, the temperature results of these simulations were imported to CFD software (Star-CCM+) in CGNS file format. Surface mapping technique was used in Star-CCM+ to map the FEM-temperature values onto the CFD-tool mesh as an initial condition for simulations. This mapping was required because FEM-simulations used tetrahedral mesh whereas CFD-simulations were done with polyhedral mesh. Thus, temperature results from FEM-simulations cannot be directly used in CFD-simulations. Based on the accuracy of mapped temperature results, step 3 was conducted. Therefore, comparison of mapped temperature between FEM and CFD was required before progressing to step 3. The imported and mapped temperature results are compared in figure 5.6.

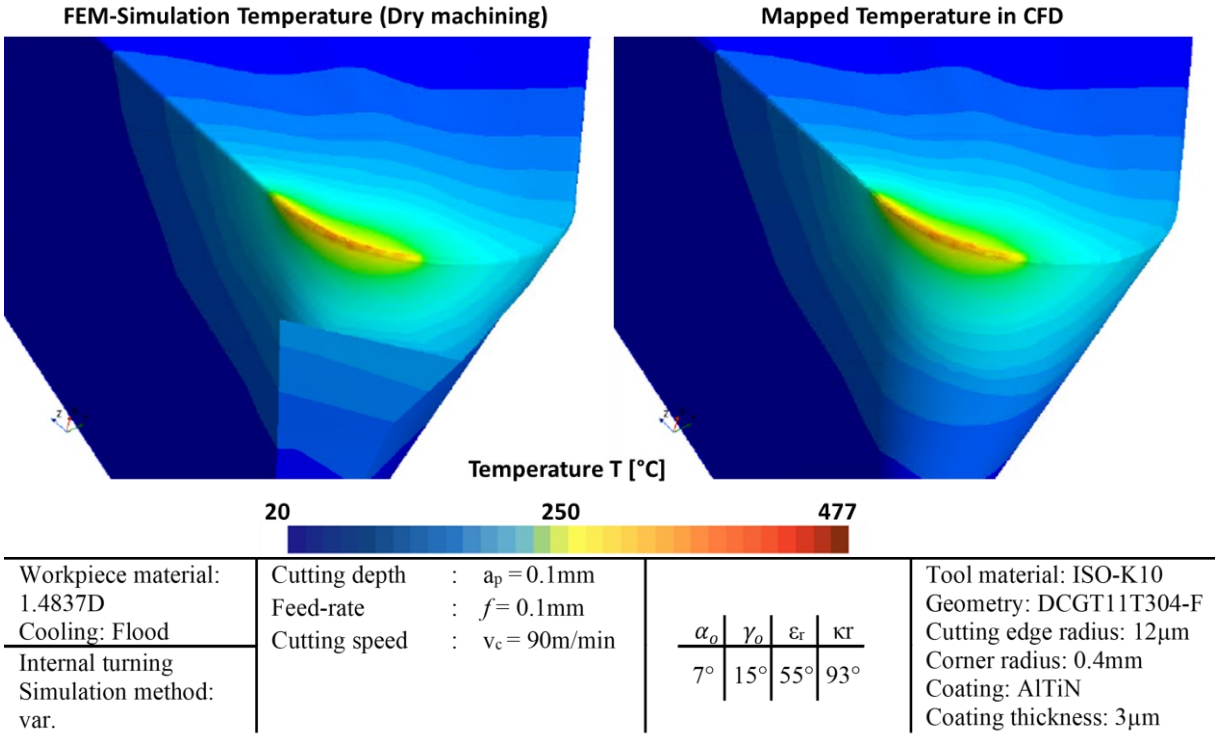

Figure 5-6: Comparison of FEM temperature (left) to CFD mapped temperature (right)

Figure 5.6 illustrates that mapped temperatures in CFD simulations are approximately equal to the simulated temperatures from FEM dry machining simulations. After this matching, in step 3, conjugate heat transfer analysis was conducted in the Star-CCM+ software. In step 4, heat transfer coefficient (HTC) values were extracted at every node on the tool surface in a tabular format. A part of the extracted data is shown in Table 5.6. From this table, it can be spotted that for same temperatures, different HTC values exist. This is because HTC is calculated by equation 5.1 in Star-CCM+.

$$h = \frac{q}{\Delta T} \quad 5.1$$

where, h is the heat transfer coefficient (HTC) in W/m²·K, q is the heat flux in W/m² and ΔT is the temperature difference between solid surface and adjacent fluid in kelvin.

Thus, for a same temperature difference (ΔT), different HTC values can exist due to the difference in heat flux value from one node to another. In Step 5 of this methodology, HTC values were taken as an input in AdvantEdge to simulate the effect of flood lubrication. However, AdvantEdge supports input format only as temperature vs HTC values, and not as temperature vs HTC values on every node. This methodology created ambiguity for the FEM-input data due to different HTC values at the same temperature. Hence, this methodology was discarded for flood lubrication process.

Table 5-6: Exported HTC values from CHT simulations

HTC (W/m². K)	Temperature [°C]	Nodal coordinates X [mm]	Nodal coordinates Y [mm]	Nodal coordinates Z [m]
-26324.5	339.86	7.19E-03	3.74	5.546
-26028.6	339.86	4.22E-02	3.533	5.412
-26282.9	339.87	2.30E-02	3.705	5.541
-26514.2	339.87	-1.30E-03	3.835	5.61
-26788.4	339.93	-3.20E-02	4.072	5.768
-25443.8	339.93	8.67E-02	3.156	5.167
-26018.4	339.95	3.74E-02	3.573	5.469
-28037.2	339.96	-1.70E-01	6.841	7.534

5.2.1.5 Second methodology: Flood lubrication in CFD-Software

The major difference between the two methodologies is that in the first, flood lubrication results are obtained through final FEM-simulations, whereas in the second, they are obtained through CFD-simulations. The schematic diagram of this methodology is shown below in figure 5.7. As mentioned, the flood lubricated internal turning process simulations were conducted in a CFD-software. However, it must be noted that the CFD-software (Star-CCM+) at the time of this

work was incapable of handling the plastic deformation of material for chip creation during machining simulations. To solve the flood lubricated internal turning process, only the heat source from FEM was taken to CFD. This means that only the thermal part of internal turning process was analyzed in this methodology and not the chip creation.

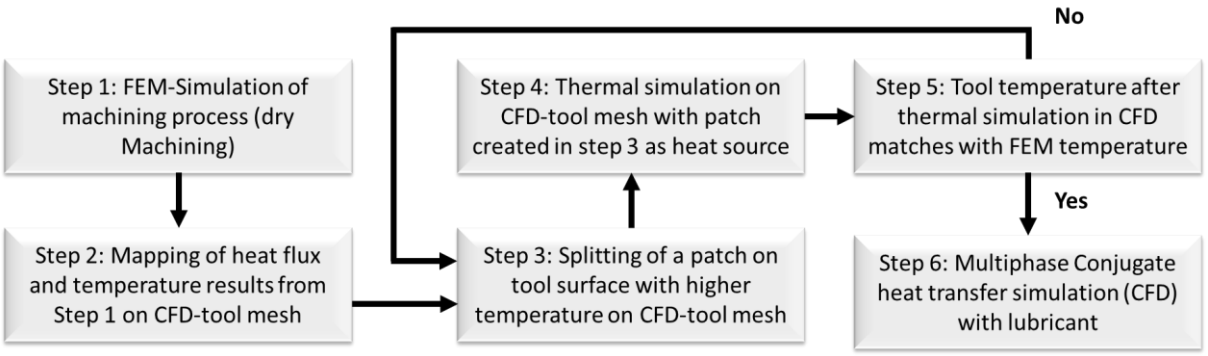

Figure 5-7: Flood lubrication in CFD-Software

As in the first methodology, the first step here was to calculate the tool temperature by conducting the dry internal turning process in the FEM software AdvantEdge. In the second step, heat flux and temperature results were exported via CGNS file interface. However, once the temperature results from AdvantEdge were closely observed, it was found that for each cutting parameter, the temperature development on tool was non-linear during the initial tool-workpiece engagement. In the first millisecond, the temperature increased rapidly and then acquired an equilibrium. The effect was observed due to different thermal conductivity of tool and workpiece. This behavior is shown as an example for the cutting parameters v_c =90m/min, f = 0.1mm and a_p =0.1mm in figure 5.8. Due to this non-linear behavior, heat flux and temperature results were taken from four points (T_1, T_2, T_3 and T_4) in form of four different CGNS files and results were mapped using the Star-CCM+ mapper on CFD volume mesh. The first three points were taken when there was a rapid increase in temperature during the first millisecond whereas the fourth point was noted at the highest temperature at end of simulation, as shown in figure 5.8.

After mapping the results in Star-CCM+ over tool volume mesh, the heat flux data was exported as CSV files for all the four points. These four CSV files were used as the input heat source for simulations in step 4 and later in step 6 for flood lubrication simulations.

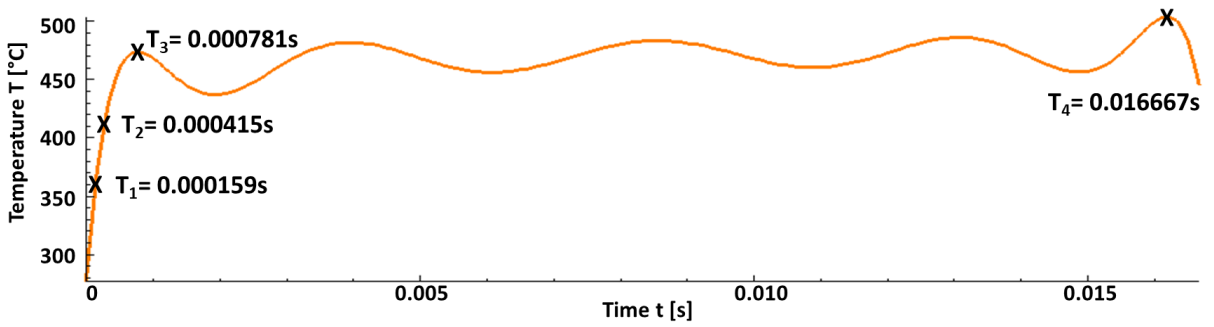

Workpiece material: 1.4837D Cooling: None Internal turning Simulation method: FEM	Cutting depth : a_p = 0.1mm Feed-rate : f = 0.1mm Cutting speed : v_c = 90m/min	α_o | γ_o | ε_r | κ_r 7° | 15° | 55° | 93°	Tool material: ISO-K10 Geometry: DCGT11T304-F Cutting edge radius: 12µm Corner radius: 0.4mm Coating: AlTiN Coating thickness: 3µm

Figure 5-8: FEM temperature results with four check points for CGNS file export

During machining, heat is generated due to plastic deformation of material in tool-chip contact area and this area acts as a heat source during machining. Thus, only this area was defined as heat source in CFD-simulations. To do this, a patch was created on tip of the tool surface, i.e., at tool-workpiece contact area and it was extracted from remainder of the tool surface. This patch was then used as an initial boundary condition to import the four CSV files from the last step in form of heat source in the next step. Created patch is illustrated as an example for v_c =90m/min, f = 0.1mm and a_p =0.1mm in Figure 5.9.

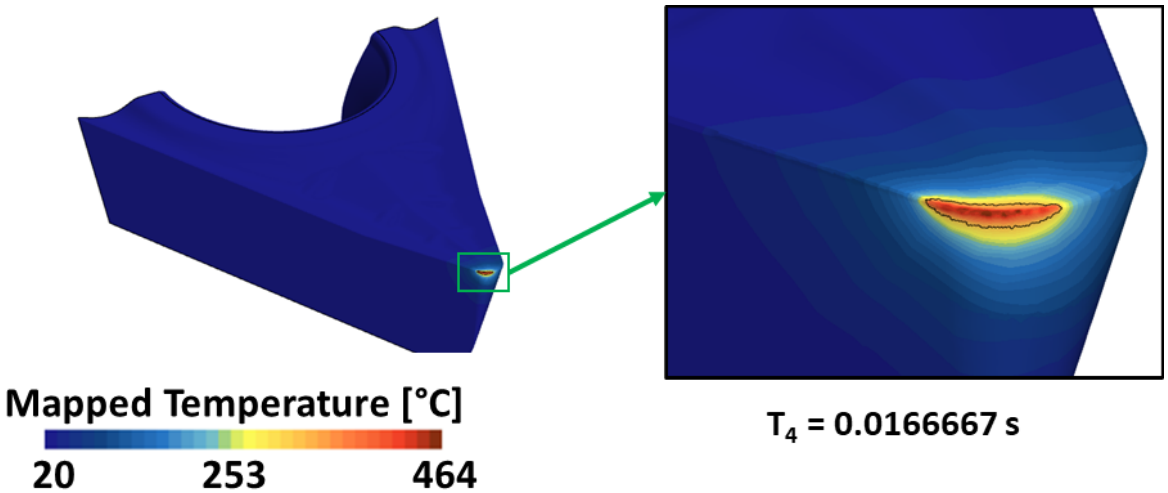

Workpiece material: 1.4837D Cooling: Flood Internal turning Simulation method: CFD	Cutting depth : a_p = 0.1mm Feed-rate : f = 0.1mm Cutting speed : v_c = 90m/min	α_o | γ_o | ε_r | κ_r 7° | 15° | 55° | 93°	Tool material: ISO-K10 Geometry: DCGT11T304-F Cutting edge radius: var. Corner radius: 0.4mm Coating: AlTiN Coating thickness: 3µm

Figure 5-9: Patch creating on tool tip surface at time T_4

After the creation of patch, all CSV files from step 2 were imported as the heat source. Using this heat source, a finite volume method (FVM) simulation was conducted without lubricant till Time=0.016667s (point T_4 from figure 5.8) for temperature calculations. These temperature results from FVM simulations were then compared with FEM results shown in figure 5.8. In case the tool temperature for these simulations did not match, the patch creation in step 3 was revised until the temperature matched. This was important to make sure that the heat source model in form of patch in CFD exactly replicates the thermal calculations from FEM internal turning process simulations.

In step 6, a multiphase conjugate heat transfer analysis with lubricant was conducted. Since chips act as a barrier for tool cooling during flood lubrication process, they were included in the simulations. As mentioned earlier, chip creation is not possible in these CFD-simulations, therefore, chip breakage was also not simulated. Due to this reason, a fixed shape of chip was implemented based on FEM-simulations and integrated in CFD-simulations here. Additionally, in the real world, there is a surface roughness on tool and workpiece where fluid can enter the effective zone during flood lubrication experiments. Whereas in CAD, the parts are smooth and hence an asperity contact was defined in simulations with chip at a fix distance of 30µm from the tool tip. Since there is no critical value of asperity contact distance at the tool-chip interface in literature, it was assumed to be 30µm for each simulation. A schematic diagram showing the asperity contact and chip is shown in figure 5.10.

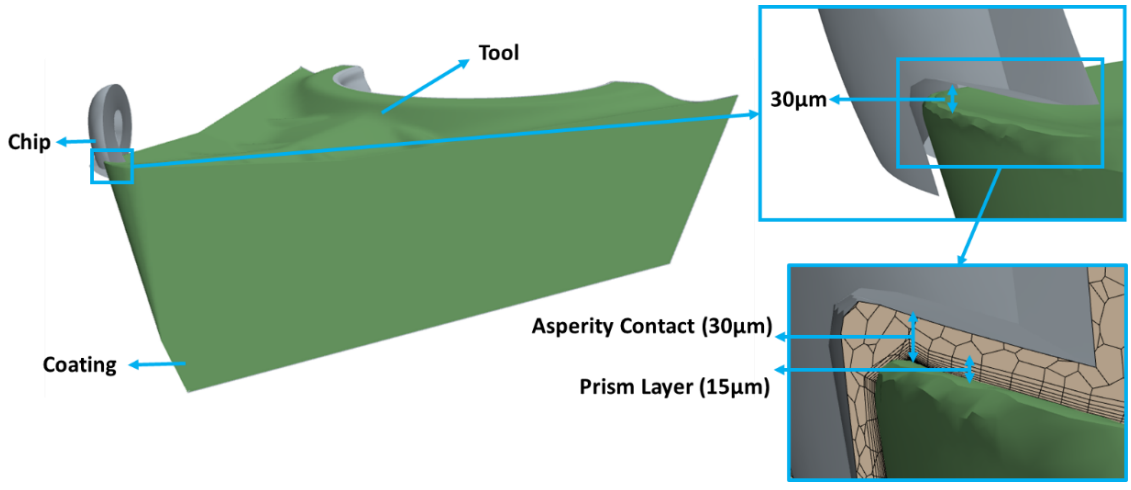

Figure 5-10: Asperity contact at tool-chip interface

After these definitions, initially a fluid flow simulation was started for 1s where the tool was rotated and lubricant was injected in the system through nozzles. This fluid simulation was conducted because in experiments, tool takes some time to make first contact with workpiece

for machining and in this time-period, system is continuously filled with the lubricant. Machining system for cutting parameter of v_c =90m/min, f = 0.1mm and a_p =0.1mm after one second of fluid flow simulation is illustrated in figure 5.11.

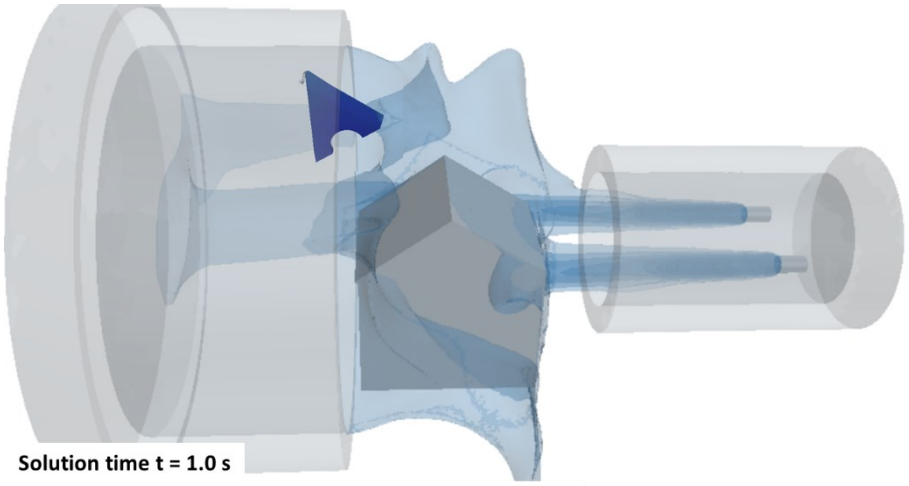

Workpiece material: 1.4837D Cooling: Flood	Cutting depth : a_p = 0.1mm Feed-rate : f = 0.1mm Cutting speed : v_c = 90m/min		Tool material: ISO-K10 Geometry: DCGT11T304-F Cutting edge radius: 12µm Corner radius: 0.4mm Coating: AlTiN Coating thickness: 3µm
Internal turning Simulation method: CFD		α_o | γ_o | ε_r | κ_r 7° | 15° | 55° | 93°	

Figure 5-11: Fluid flow simulation results after 1.0s for v_c =90m/min, f = 0.1mm and a_p =0.1mm

After fluid flow simulations, CHT analysis was performed by importing the four CGNS files from step 2 and multiphase conjugate heat transfer simulations were run for 0.1s with the mesh size and turbulence model explained in section 5.2.1.2 and 5.2.1.3 respectively. Temperature results on tool after 1.1s (1s fluid flow and 0.1s CHT analysis) of flood lubricated internal turning simulation for the cutting parameter v_c =90m/min, f = 0.1mm and a_p =0.1mm is shown in figure 5.12. In the figure, the whole setup is shown at the top and the tool temperature is plotted at the bottom. It can be observed that the maximum tool temperature reaches 465°C, which is around 40°C lower than the temperature that was observed in the dry internal turning process. This proves that this approach can model the cooling effect successfully.

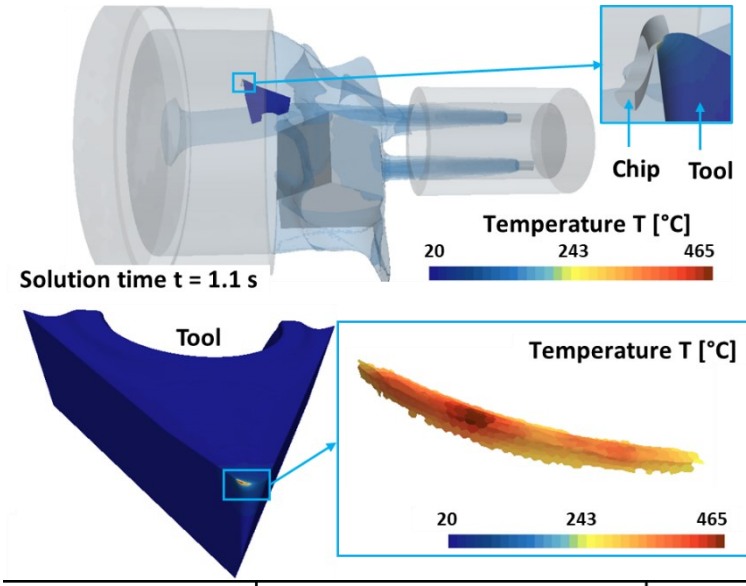

Workpiece material: 1.4837D Cooling: Flood	Cutting depth : $a_p = 0.1$mm Feed-rate : $f = 0.1$mm Cutting speed : $v_c = 90$m/min	α_o | γ_o | ε_r | κ_r 7° | 15° | 55° | 93°	Tool material: ISO-K10 Geometry: DCGT11T304-F Cutting edge radius: 12µm Corner radius: 0.4mm Coating: AlTiN Coating thickness: 3µm
Internal turning Simulation method: CFD			

Figure 5-12: Lubricated internal turning process simulation results

5.2.1.6 Comparison of simulation results with experiments

In this section, temperature results for flood lubricated internal turning process from experiments will be compared with the temperature results from simulations. This comparison was carried out to determine the accuracy of the second methodology with respect to experiments. Additionally, flood lubricated results were compared with dry internal turning results from chapter 4 and these results are plotted in figure 5.13.

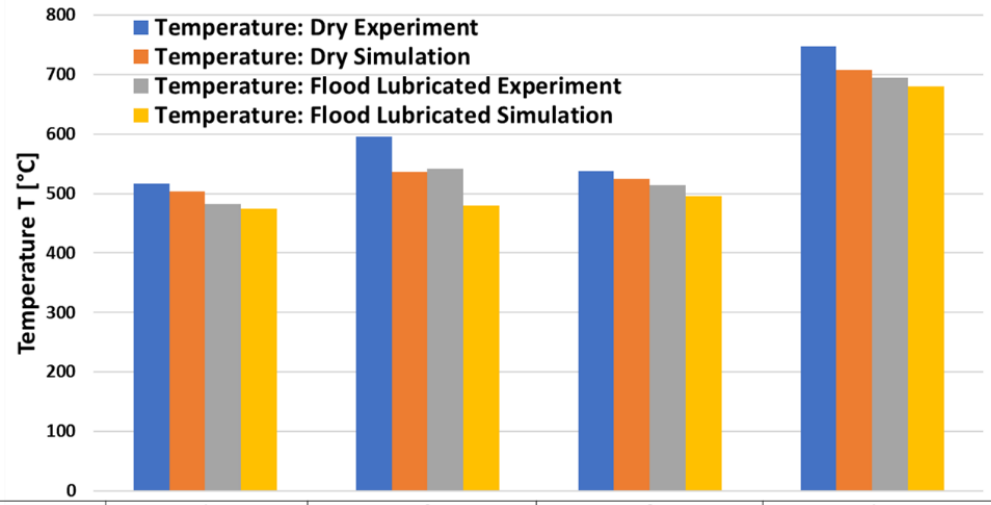

v_c (m/min)	90	90	90	170
f (mm)	0.1	0.25	0.1	0.1
a_p (mm)	0.1	0.1	0.3	0.3

Workpiece material: 1.4837D
Cooling: var.
Internal turning
Simulation method: CFD

Cutting depth : a_p = var.
Feed-rate : f = var.
Cutting speed : v_c = var.

α_o	γ_o	ε_r	κ_r
7°	15°	55°	93°

Tool material: ISO-K10
Geometry: DCGT11T304-F
Cutting edge radius: 12µm
Corner radius: 0.4mm
Coating: AlTiN
Coating thickness: 3µm

Figure 5-13: Temperature comparison for AlTiN coated inserts between experiments and simulations for dry and flood lubricated internal turning process

It can be observed from the above figure that temperature results of flood lubricated internal turning from simulations were in very good correlation with experimental results. For all the cutting parameters, simulation results underpredicted the experimental results. This could be based on the assumption of high asperity contact distance in simulation. Since the heat flux was defined as the heat source on the tool-tip surface in CFD-simulations, the simulated temperature from the tool-tip surface in flood lubricated internal turning process could not be compared with the experimental values. Instead, in flood lubricated simulations, the temperature results from a point slightly below the cutting edge radius, i.e., 2µm where heat source was defined, were compared with the experimental results.

From figure 5.13 it can be noticed that the presence of lubricant led to cooling effect by extracting heat from the tool. On comparing the temperature results between dry and flood lubricated internal turning process, a maximum temperature reduction of 7% was observed during the experiments whereas it was around 5.7% in simulations. These results imply that simulations can also model the cooling effect very well.

A successful comparison of temperature results for flood lubricated internal turning process proves that the methodology proposed can be used in future to simulate other machining processes. It can in turn help reduce experiments through application of digital tools. On the contrary, it must also be noted that certain assumptions like asperity contact distance and fixed chip were made during these simulations. Additionally, two different software were coupled to achieve this solution. Such an approach could be time-consuming and there are always possibilities of human error during patch creation or mapping of results from FEM-simulations to CFD-simulations. Therefore, an industrial solution is desired which can be implemented easily and can also reduce the possibility of human error during simulations. Hence, a new approach using a single software was developed.

5.2.2 Bidirectional FEM-CFD coupling using one software

Machining process simulations are computationally expensive due to a continuous remeshing in shear zone area for capturing the correct chip shape. This extensive remeshing for chip creation could not be achieved in the Star-CCM+ software and thus only the thermal part of flood-lubricated machining process was simulated. In an FEM-software where coupled FEM-CFD problem (like flood lubricated machining) can be solved, remeshing is required for both, structures (chip creation) and fluids (lubricant). Such complex remeshing problems either result in simulations that are very lengthy, or simulations that are unfeasible in most software. An alternative solution to this problem could be mesh-free methods for both, structure (tool-workpiece) and fluid (lubricant).

Since AdvantEdge does not offer mesh-free methods, LS-DYNA (a Multiphysics software) was used to evaluate these methods. However, before solving any complex flood lubricated simulations, these methods were implemented in dry machining process for low-nickel steel (1.4837D) material. Rana et al. applied SPH and MC-SPG methods to dry orthogonal machining and found a good agreement between simulated and experimentally measured force components. For SPH formulation, simulated forces had a difference of 10% and 12% with the measured forces for cutting and feed force respectively. Whereas for MC-SPG, the simulated forces deviated from the measured forces by 11% and 15% for cutting and feed force respectively. Additionally, it was observed that the simulated chip form was comparable to the experimental chip form. Temperatures were also simulated but they were not compared with experimental temperatures [163, 164].

These results from SPH and MC-SPG methods demonstrated that particle methods can simulate dry machining process. Thus, as the next step, particle methods were used to simulate flood lubricated machining process. To initially keep the problem statement simple, they were implemented in orthogonal turning process. Between the two particle methods, only SPH formulation could be used for fluid bodies and therefore it was used for the lubricant. On the other hand, both SPH and MC-SPG formulations could be used for structures. Since no coupling existed between SPH and MC-SPG formulations, SPH formulation was also used for the structural part (tool-workpiece). Hence an SPH-SPH coupling was used between the structure and fluid in LS-DYNA to solve the flood lubrication process.

5.2.2.1 Simulation setup

The simulation setup for flood lubricated orthogonal turning process is described. Uncoated tungsten carbide inserts ISO-K10 were used for orthogonal turning process. The process was simulated with flooding lubrication with a flow rate of 28 l/min. Cutting inserts had a clearance angle (α_o) of 7°, and rake angles (γ_o) of 15° and 0° with cutting edge radii r_β= 33µm and 24µm respectively. Tool height and width in simulation were defined as 1mm. The workpiece dimensions for simulations were defined as length=7mm, width=1mm and height=1mm. The tool and workpiece were modelled in the LS-PREPOST software and are shown in figure 5.14. All the simulations were conducted in high performance cluster (HPC) with 96 cores. A Node_to_Surface contact was used to define the contact between the workpiece, tool and lubricant and a coulomb friction model with a coefficient of friction value=0.5, provided by supplier, was used in simulations. These contact equations and friction model were defined in section 2.2.1.5. The cutting speed and feed-rate were defined for the tool and the workpiece was fixed in all the directions for translations and rotations, as shown in figure 5.14.

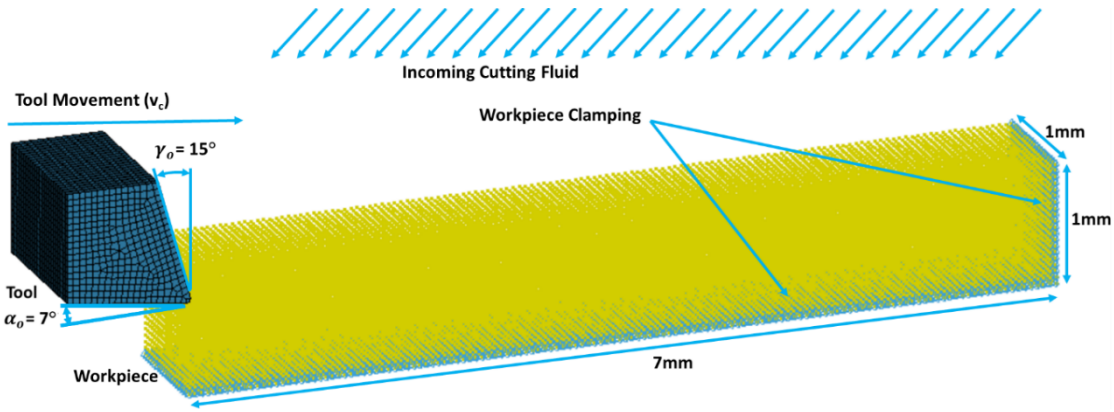

Figure 5-14: Simulation setup: Flood lubricated orthogonal turning simulations

5.2.2.2 Meshing and particle spacing

CAD-model of tool was initially meshed with solid elements in LS-PREPOST with a size of 0.05mm. However, for an SPH-SPH coupling to work efficiently in LS-DYNA software, the mesh was converted to SPH particles by placing an SPH particle at each node of the tool. For the workpiece, SPH particles were defined with a particle spacing of 0.02mm and for the lubricant, the particle spacing was defined as 0.1mm. Figure 5.15 shows the mesh and SPH particles of tool, workpiece and lubricant.

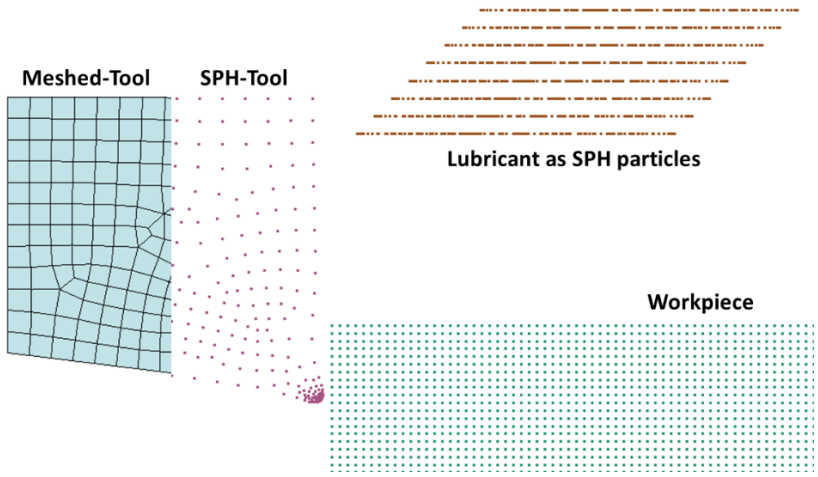

Figure 5-15: Mesh and SPH particles of tool, workpiece and lubricant

5.2.2.3 Material modelling

Thermo-mechanical simulations were carried out without considering the tool-wear. Thus, thermal and mechanical properties of the tool and workpiece were defined. The workpiece undergoes a plastic deformation under high strain-rate, strain and temperature during machining process. This plastic deformation affects flow stresses of material. During these simulations, the Johnson-Cook (JC) material model was used (section 2.2.1.4). This material model was chosen because the Power law material model (which was chosen for dry machining simulations in AdvantEdge) was not available in LS-DYNA. While using the JC-material model, an equation of state must be defined in the model and therefore, a linear polynomial equation of state (equation 2.17) was used in these simulations. Its C_1coefficient value was defined as 114 MPa, which is the bulk modulus of the 1.4837D material. The JC-material constants and thermo-mechanical properties were defined in earlier research work [163]. Since tool-wear was not simulated, tool was defined as a rigid material.

5.2.2.4 Simulation results of coupled SPH-SPH flood lubricated process

Coupled thermo-mechanical calculations with explicit time integration were carried out for 2.2ms. Particle approximation theory is important while performing SPH simulations (see section 2.2.1.2).

There are different particle approximation theories available for solids in LS-DYNA. However, for fluids, only default particle approximation theory is available. Since the theory could be defined only once, the default particle approximation theory was used for both, solids and fluids. For the first 0.2ms, only fluid was injected to make sure that the fluid was present in the cutting domain before the tool-workpiece contact. The reason for this is same as explained earlier in section 5.2.1.5. Afterwards, orthogonal turning process was simulated for 2ms with a continuous lubricant injection.

In total four different orthogonal turning simulations were conducted to capture the effect of tool rake angle, cutting speed and feed-rate on cutting forces and temperature. Additionally, dry orthogonal turning simulations were carried out with the same simulation setup to compare the results of flood lubricated and dry orthogonal turning simulations. Figure 5.16 presents the simulated force components for the cutting parameter v_c =100m/min, f = 0.25mm, b=1mm and tool angles α_o= 7°, γ_o= 15°. The increase in force components is visible in simulations after 0.2ms as until then only the lubricant was injected. It can be noticed that the dominant force is cutting force, followed by feed force. Since cutting edge of the tool is perpendicular to the working plane in orthogonal turning, the passive force becomes zero [153]. This was well observed in these flood lubricated orthogonal turning simulations and is depicted in this figure. Some fluctuations can be seen in this figure which could arise from friction model and particle spacing from SPH-workpiece.

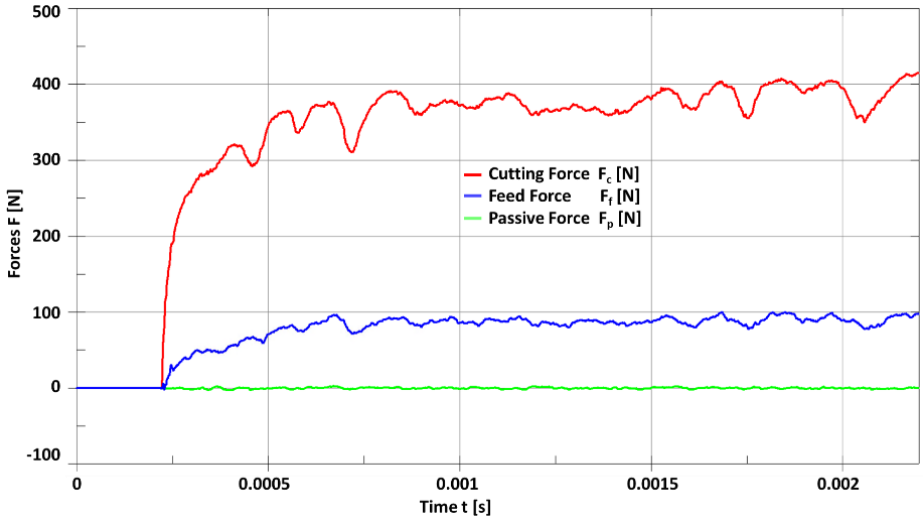

Workpiece material: 1.4837D Cooling: Flood	Feed-rate : f= 0.25mm Cutting speed : v_c= 100m/min Chip width : b= 1mm	α_o | γ_o 7° | 15°	Tool material: ISO-K10 Cutting edge radius: 33µm Coating: None
Orthogonal turning Simulation method: FEM & CFD			

Figure 5-16: Simulated forces from flood lubricated orthogonal turning process v_c =100m/min, f= 0.25mm and b=1mm

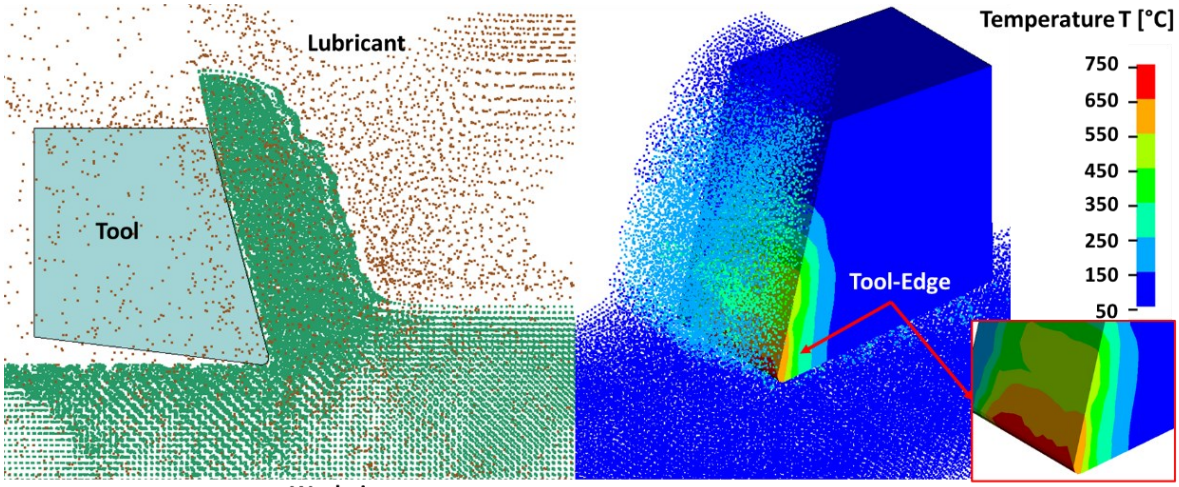

Workpiece material: 1.4837D Cooling: Flood	Feed-rate : f= 0.25mm Cutting speed : v_c= 100m/min Chip width : b= 1mm	α_o | γ_o 7° | 15°	Tool material: ISO-K10 Cutting edge radius: 33µm Coating: None
Orthogonal turning Simulation method: FEM & CFD			

Figure 5-17: Chip and temperature during flood lubricated orthogonal turning process

On the left side, Figure 5.17 shows chip creation during flood lubricated orthogonal turning process simulation and on the right side, it shows the tool temperature for the same cutting

parameter. From the temperature diagram, it can be observed that the highest tool temperature exists in the area slightly above the tool cutting edge.

It can also be seen in the same image that for this set of parameter, no chip curvature was observed during the orthogonal turning process simulation. The same issue was also noticed for all other cutting parameters too. This was due to the default particle approximation theory. To simulate chip bending in machining simulations, more advanced particle approximation theory should be used, for example particle renormalized approximation theory. However, it cannot be defined in these simulations as LS-DYNA currently allows only one particle approximation theory to be used in a simulation and fluids (lubricant) can be simulated only with default particle approximation theory. On the other hand, when renormalization particle approximation theory was used in dry orthogonal turning simulations, chip bending was observed and the results of default and renormalization particle approximation theory for cutting parameter v_c =100m/min, f = 0.25mm, b=1mm and tool angles α_o= 7°, γ_o= 15° are compared in figure 5.18.

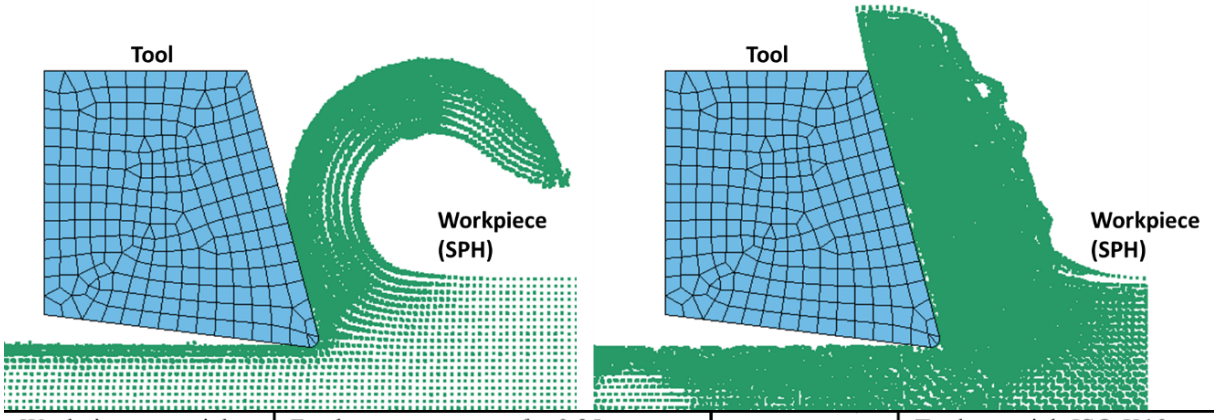

Figure 5-18: Chip comparison between default and renormalized particle approximation theory

5.2.2.5 Comparison of flood lubricated orthogonal turning simulations with dry simulations

Since temperature measurements during flood lubricated orthogonal turning process were not possible, experiments were not conducted. Due to this reason, flood lubricated simulations were compared to dry orthogonal turning simulations. This was done to determine the degree of correlation between flood lubricated simulations and dry simulations as per literature. Figure

5.19 compares the maximum temperature of dry (at top) with flood lubricated (at bottom) orthogonal turning simulations for all cutting parameters. It is evident in Figure 5.19 that the presence of lubricant reduces the tool temperature. It can also be observed that the tool with rake angle of 15° had lower temperature than the tool with rake angle of 0°. This effect was earlier observed for the same workpiece material in literature [164]. The effect of cutting speed was also well captured, i.e., with an increase in cutting speed, the temperature also increased. This behavior was also observed earlier in chapter 4 for both, experiments and simulations. With an increase in feed-rate and cutting speed, a rise in temperature was observed. However, the effect of cutting speed was dominant over feed-rate. From these results, it can be concluded that the SPH-SPH coupling for flood lubricated orthogonal turning simulations could capture thermal effects during machining. However, chip shape could influence these temperature results and this issue must be resolved in future work.

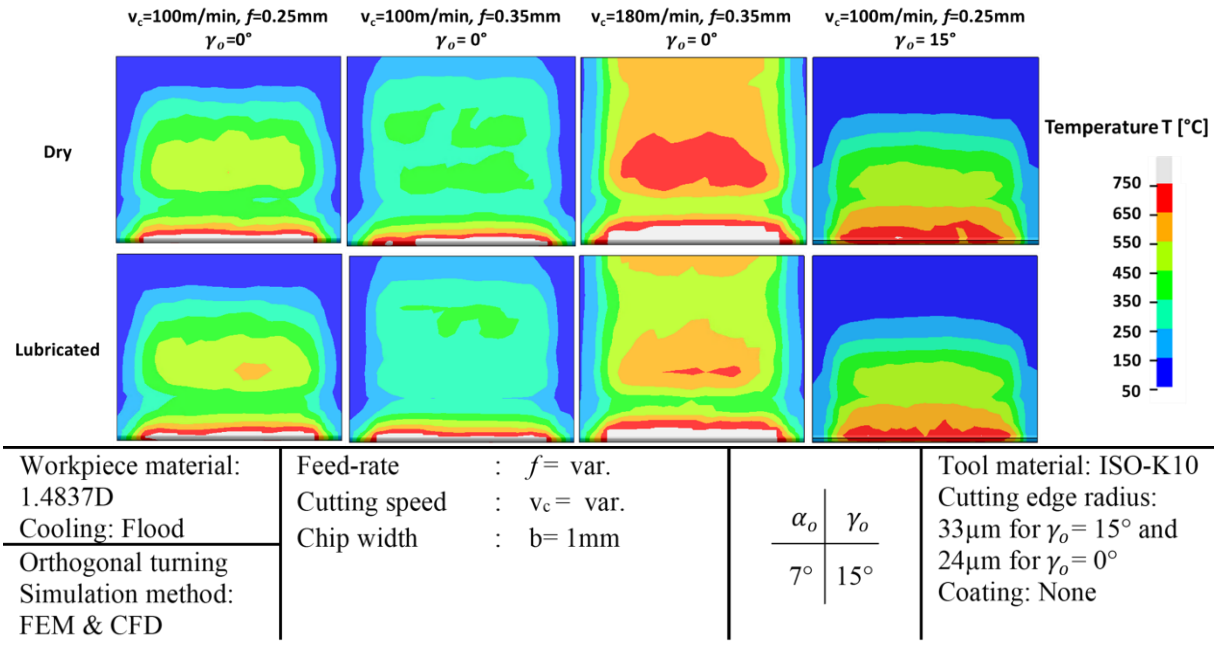

Workpiece material: 1.4837D Cooling: Flood	Feed-rate : f= var. Cutting speed : v_c= var. Chip width : b= 1mm	α_o | γ_o 7° | 15°	Tool material: ISO-K10 Cutting edge radius: 33µm for γ_o= 15° and 24µm for γ_o= 0° Coating: None
Orthogonal turning Simulation method: FEM & CFD			

Figure 5-19: Temperature comparison between flood lubricated and dry orthogonal turning simulations

Figure 5.20 lists all the cutting parameters, cutting forces and feed forces from dry and flood lubricated simulations. The comparison of both the force components depicts that flood lubricated simulation forces were marginally lower in comparison to dry orthogonal turning simulation forces. This reduction in forces is due to the cooling of workpiece in the presence of lubricant. A similar reduction of forces was observed in literature by other researchers during flood lubricated orthogonal turning process [165].

Based on the results from this approach (SPH-SPH coupling), it can be concluded that it is more suitable in an industrialized environment as there is no manual mapping of temperature results between the FEM and CFD-simulations as in first approach. Additionally, using a single software simplifies the coupling approach between fluid (lubricant) and solids (tool, workpiece and chip) as the user should understand one software rather than two different software, like in the first approach. However, there is a scope of improvement in these simulations with respect to chip bending.

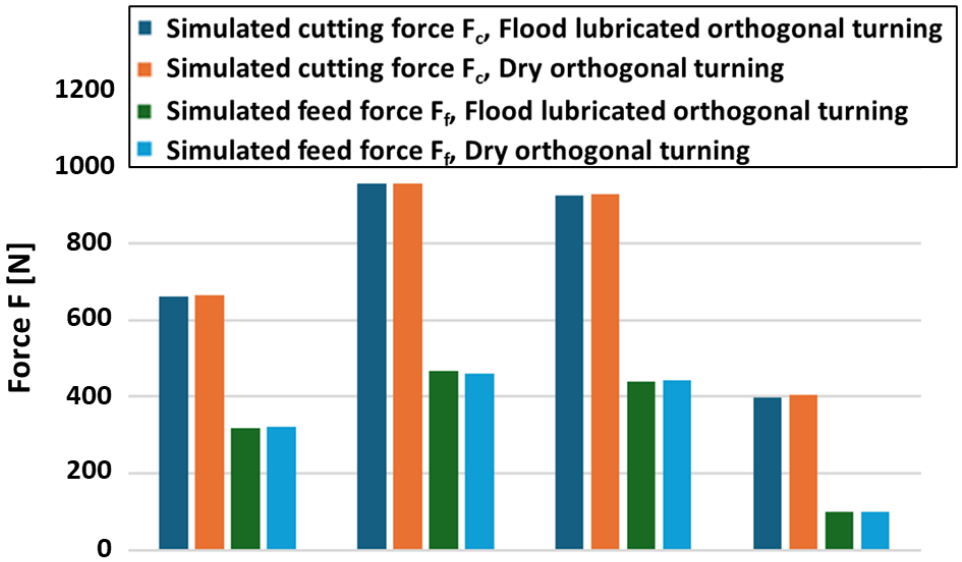

v_c (m/min)	100	100	180	100
f (mm)	0.25	0.35	0.35	0.25
γ_o [°]	0	0	0	15

Workpiece material: 1.4837D Cooling: var.	Feed-rate : f= var. Cutting speed : v_c = var. Chip width : b= 1mm		Tool material: ISO-K10 Coating: None
Orthogonal turning Simulation method: Flood: FEM & CFD Dry: FEM		α_o | γ_o 7° | 15°	

Figure 5-20: Comparison of dry and flood lubricated orthogonal turning simulations

5.3 Summary

A central question in this work was to find out the scope of digital tools in a production environment. To answer this question, it was necessary to figure out whether machining process with lubricants could be simulated. A lot of research on dry machining could be found but research on flood-lubricated simulations was missing. Hence, two new approaches were proposed and investigated.

In the first approach, a coupling between two software (AdvantEdge and Star-CCM+) was investigated and temperatures were validated for an internal turning process. There were three shortcomings in this methodology, namely asperity contact distance assumption, fixed chip shape and tedious coupling methodology in form of mapping and patch creation.

To resolve these three shortcomings, a second approach was proposed with SPH-SPH coupling between fluid and solids in a single software, LS-DYNA. This approach presents a two-way coupling between the FEM and CFD-solvers, reducing the manual work. However, since single particle approximation theory could be used in LS-DYNA, it produced unfavorable results, i.e., chip bending could not be simulated. Thus, this approach should also be improved in the future work.

From a digital strategy standpoint, the second approach has advantages over the first approach, because of the currently available two-way coupling in software. Additionally, it can reduce the number of tools required to build a digital process chain in process development.

6 Application of simulation tools in production

Turbine housings are an integral part of diesel and gasoline engines. In 2017, the number of turbine housings produced by Mercedes-Benz AG every year was well over 1 million parts and the number of variants of these housings were 13. Various turbine housing models for 4- and 6-cylinder diesel and gasoline engines are shown in figure 6.1.

Figure 6-1: Various turbine housing variants [17]

Thus, optimizing the turbine housing machining using digital tools will serve one of the goals, i.e., application of simulation tools in production. Additionally, due to different variants and large number of turbine housing produced every year, any optimization can lead to measurable results in company's balance sheet.

6.1 Turbine housing: Inner contour turning process

As mentioned in section 2.3.1, 1.4837D casted steel is used in the production of turbochargers at Mercedes-Benz AG. One of the major requirements of producing these turbochargers is high precision machining processes. However, downsizing of motors has led to increasingly complex component geometries that cannot always be directly machined via a milling or

drilling process. These complex geometries may require special machining process like inner contour turning process. Multi-spindle transfer center is used in machining of casted turbine housing. The housing is mounted firmly in clamping device as shown in figure 6.2 (A).

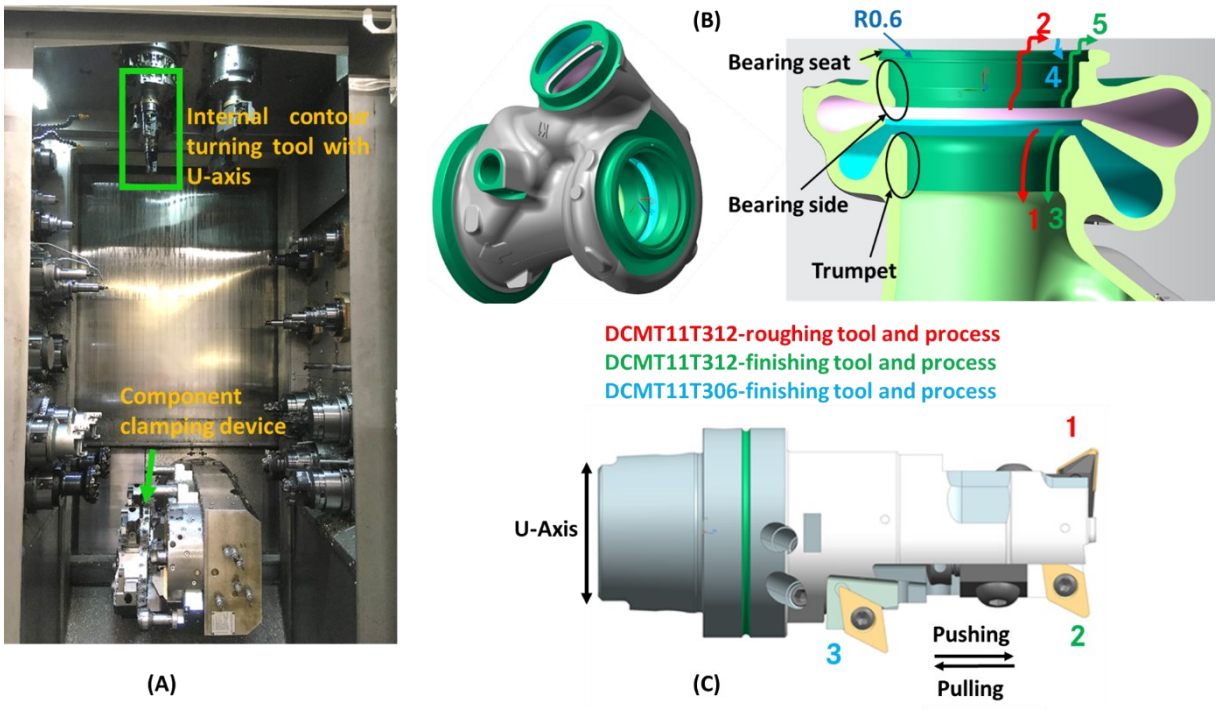

Figure 6-2: (A) Turbine housing machining in a multi-spindle transfer center, (B) Full and Cross-sectional CAD model of Turbine housing and (C) Inner contour turning tool

There were ten different tools inside this machining center and each of them was used for different machining process. Each of this tool was present twice, thus two turbine housing could be machined simultaneously inside the transfer center. Inner contour turning tool was present on the top side of machining center and is highlighted in figure 6.2 (A). Inner contour turning process accounted for more than 25% of the total machining time of turbine housing. One of the major reasons for this was high quality requirements with respect to shape accuracy, dimensional deviation and surface quality. Inner contour turning process is conducted in five steps that are mentioned below:

1. Roughing of the trumpet (pushing)
2. Roughing of the bearing side (pulling)
3. Finishing of the trumpet (pushing)
4. Finishing of the bearing seat (pushing)
5. Finishing of the bearing side (pulling)

These five machining steps are shown in the cross-sectional view of turbine housing in figure 6.2 (B). When the inner contour turning tool moves inside the turbine housing, the process is termed as pushing and when it moves out of the housing, it is termed as pulling.

The names of the above-mentioned machining steps come from the NC-program that is run in production line. The name trumpet is due to the geometric characteristic of this area. The trumpet area initially had a constant diameter of 42.23 mm and widened continuously over a radius of 3 mm to an inner diameter of 48.23 mm. Next to trumpet is the bearing side which consists of various diameters, while the bearing seat has a diameter of 58.025 mm. Since one of the prerequisites of turbine housing manufacturing was machining precision, an averaged surface roughness Rz of 12.5µm was required on the bearing seat diameter, on its flat surface and in the trumpet area. While in the remaining bearing side area, an averaged surface roughness of Rz =25 µm and Rz =50 µm was required.

To machine such a complex geometry, an equally complex tool was used in production which is shown in figure 6.2 (C). This tool consists of three cutting inserts, (1) a roughing cutting insert (red color) with the corner radius= 1.2mm, (2) a finishing cutting insert (green color) with the corner radius of 1.2mm and (3) an additional finishing cutting insert (blue color) with the corner radius= 0.6mm. This additional cutting insert was used to finish the bearing seat area to create a radius of r= 0.6mm radius, shown in blue color in figure 6.2 (B). The colored arrows in figure 6.2 (B) mark the tool path of three cutting inserts. The red arrow marks the path of roughing cutting insert, the green arrow shows the movement of finishing insert and the blue arrow stands for the motion of additional finishing cutting insert.

Pulling and pushing machining directions, mentioned earlier in 5 steps of inner contour turning, are visualized in figure 6.2 (C). All the three cutting inserts were standard inserts: DCMT11T312 (α_o=7°, γ_o= 15°and ε_r= 55°) for roughing and finishing, and DCMT11T306 (α_o=7°, γ_o= 15°and ε_r= 55°) was used as the additional finishing insert. However, to avoid collisions, roughing insert had a tool cutting edge angle κ_r =94° during pushing and κ_r =31° while pulling. Both finishing inserts had κ_r =98° during pushing and κ_r =27° while pulling. The roughing insert was made of ISO-K10 substrate material and coated with Ti(C,N) +Al_2O_3 coating with a thickness of 16µm. The cutting edge radius of roughing insert was r_β=60µm. Both finishing inserts were made of substrate ISO-S20 with cutting edge radius of r_β=30µm and had a TiAlN coating of 3µm.

To travel the complex inner contour path of turbine housing and generate different internal diameters, a special tooltronic tool control was used. The tooltronic was placed between the spindle and the three cutting insert tool holder. Along with the traditional X, Y and Z axis, an additional U-axis was given in this tool. By moving the tool along this U-axis, various inner contour diameters could be generated.

This tool was optimized to solve the issue of high cost of inner contour turning process. This high cost is due to the scrap rate of turbine housing. A Pareto analysis for defect was performed and it revealed that scrap rate accounts for 11.91% of the total turbine housing manufacturing defects and among these defects, 1.83% were due to the inner contour turbine housing process. It must be mentioned that before inner contour turning process, seven out of ten machining processes were already completed. Thus, a scrapped turbine housing during inner contour turning process also accounts the tool cost of earlier seven processes, making this process economically critical. Tolerance errors were the major defects in machining of bearing seat diameter and trumpet diameter. Additionally, when wear on the three cutting inserts were compared, it was found that the roughing tool insert had notable wear marks, whereas the two finishing inserts had a normal wear, figure 6.3. Consequently, the life of entire tool in production was primarily dependent on the life of roughing insert.

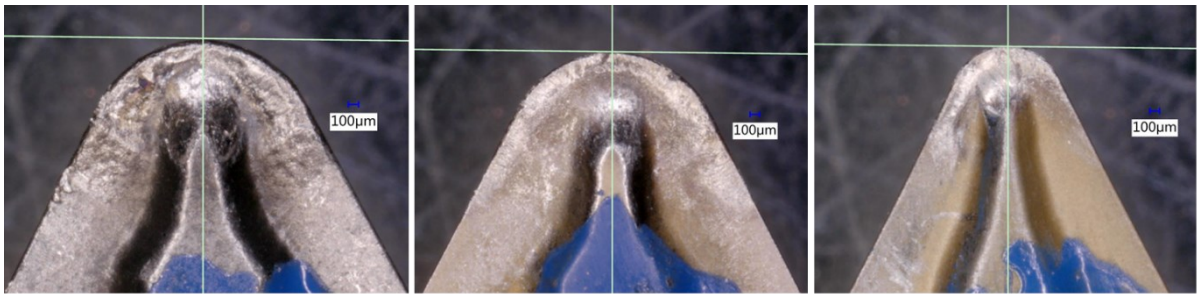

Figure 6-3: Tool wear on inner contour turning inserts: roughing insert (left), finishing insert (middle) & additional finishing insert (right)

Due to the mentioned reasons, in sections 6.2 and 6.4 mechanistic and FEM-numerical modelling techniques were used to increase the tool life of roughing insert and ultimately reduce the scrap rate. With mechanistic modelling, major goal was to achieve the uniform load on tool by optimizing the cutting process parameters. Since inner contour turning process does not have any stability problem (chatter), dynamic behavior of the tool was not analyzed. Additionally,

the knowledge gained earlier in chapter 4 via dry FEM simulations has been implemented on roughing tool insert to increase the tool life by optimizing the roughing insert coating.

6.2 Mechanistic simulation and optimization of inner contour turning process

The mechanistic simulations were run in the MACHPro software. The following inputs are required to do simulations in this software:

- CAD model of workpiece
- NC-program in CLS file format
- Force model

6.2.1 CAD modelling of the geometry for mechanistic simulations

For mechanistic simulations in MACHpro, a CAD model of turbine housing in STL format was required as one of the inputs for simulations. For turbine housing (workpiece) CAD construction, production designs were used, where machining operations were documented along with corresponding stock allowances. Based on the stock allowances, the raw and finished parts for inner contour turning process were created in Siemens NX. Figure 6.4 shows this for the inner contour turning process. The blue line shows the final contour after the inner contour turning process. By adding stack allowance for the process, the new red line was created, thus building the desired part before the inner contour turning process. In the end, the generated CAD model was exported from NX to be used for simulations. CAD model of the tool was created directly inside the MACHpro software and its creation will be discussed later in section 6.2.4.

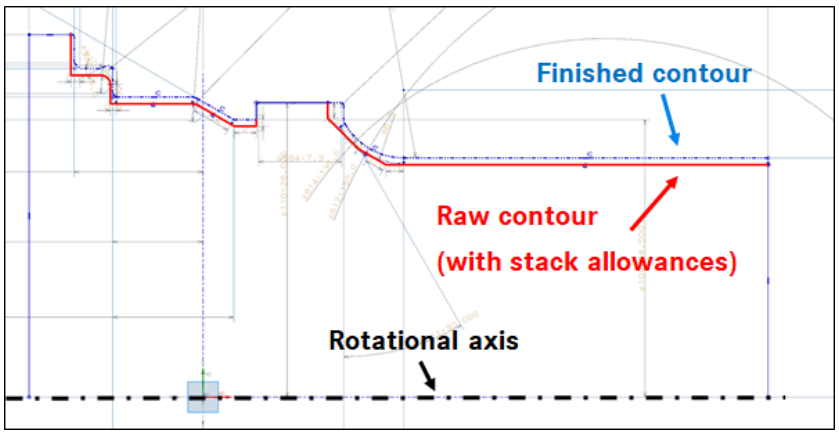

Figure 6-4: Stack allowance creation in contour of finished part

6.2.2 Inner contour NC-Program

NC-program run in the production line contains typical G-codes along with various syntaxes in an SPF file format. However, only CLS file format is readable in the MACHpro software and therefore, SPF file from production line was converted to CLS file format in CAM (Computer aided manufacturing) environment of Siemens NX. Since the tooltronic actuation provides a movement to tool along the U-axis, it makes the mapping of whole inner contour turning process in Siemens NX very complex. Therefore, an assumption was made for mechanistic simulations, i.e., turbine housing was not rigidly clamped, rather it rotated around its center axis and the three cutting inserts traversed the inner contour of turbine housing. The relative movement between the tool and workpiece was kept constant, regardless of the rotation of workpiece (in simulations) or tool (in reality).

Since inner contour turning process was fundamentally an internal turning process, the “Finish Bore ID” operation was used to generate the roughing and finishing operation in CAM, see figure 6.5. Using the first “roughing of the trumpet (pushing)” process as an example, the procedure for creating individual CAM operations is described below. Same procedure was followed for the remaining four processes. By using the “cut regions” button (shown in figure 6.5), two trim points (TP) were defined for each process, shown as TP1 and TP2. These points are nothing but the start and end points of the finished contour.

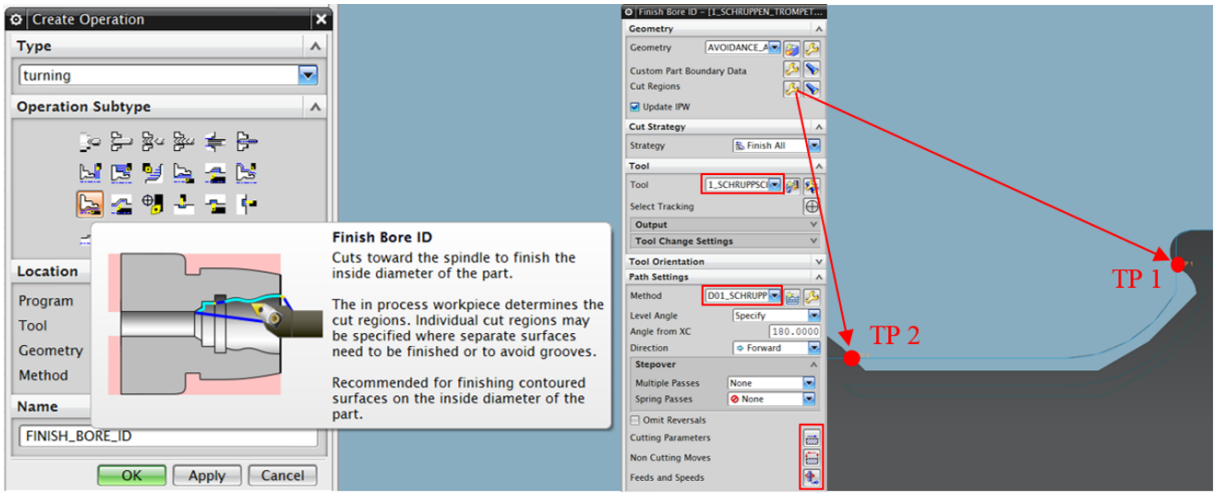

Figure 6-5: Creation of CAM operation for roughing of the trumpet (pushing) process

After the definition of trim points, tools were selected and cutting parameters, feed and spindle speeds were defined. In case of “roughing of the trumpet” process, the cutting speed was

110m/min and the feed rate was 0.46mm/rev. Figure 6.6 shows the tool path and stock allowances of the individual CAM operation for each process.

Light brown color depicts the finished part of turbine housing, green color region visualizes the additional material that had to be removed by the respective manufacturing step of inner contour turning process and light blue color represents the material that has already been removed by a completed manufacturing step. The fifth step, finishing operation on bearing side, could not be completed as a CAM operation in Siemens NX in one go and thus was divided into two steps, 5.1 and 5.2. This happened because in the fourth manufacturing step, the inside diameter and face of bearing seat were machined by the additional finishing insert (3rd insert) of the inner contour tool. Hence, no material was left to be machined in this area during the fifth manufacturing step. This was detected by the CAM software and in the first suboperation, the CAM operation of finishing process on the bearing side was carried out only up to the face of the bearing seat. In the second suboperation, the outer face and chamfer were machined.

After building CAM operations for all the five manufacturing steps in CAM environment, NC-programs were exported as CLS files and were used later in MACHpro simulations.

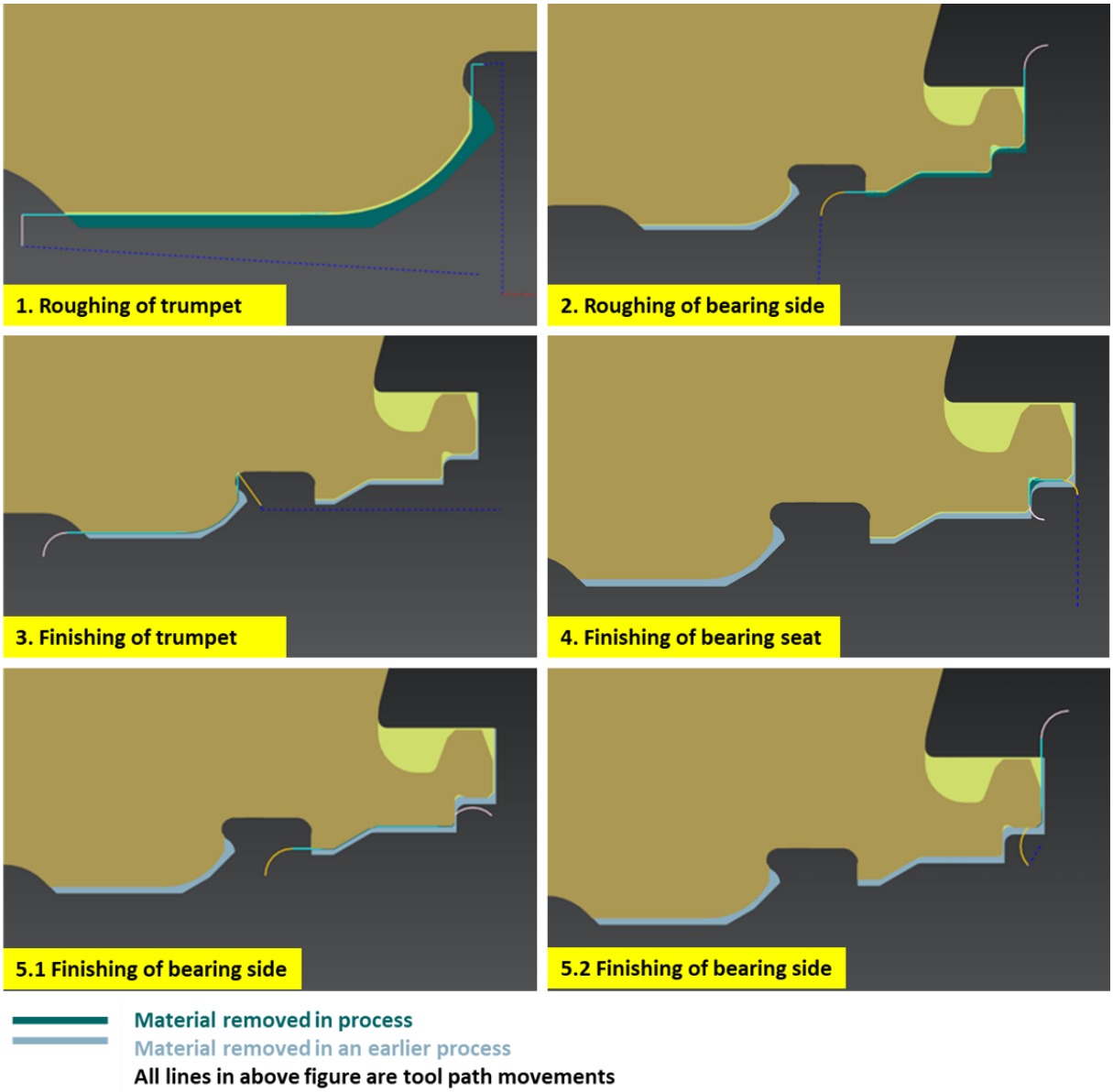

Figure 6-6: Tool paths and stock allowances in machining operations

6.2.3 Force model/ Material model for mechanistic simulations

The next input for MACHpro simulations is force-model, also called as material model for mechanistic simulations. This force model is based on the orthogonal-to-oblique (O-to-O) transformation explained in section 2.2.3.2. MACHpro has a material library where force models of various materials are available. However, the turbine housing material used for research is a patented material from Mercedes-Benz AG and thus not available in the MACHpro material library. Due to this reason, a force model for the turbine housing material (1.4837D) was created. The standard procedure to generate a force model is to perform multiple orthogonal

turning experiments and measure the process tangential and feed force. Additionally, chips are collected to measure their weight and length, and by using this information, the chip thickness is calculated with equation 2.51. Based on this calculated information and experimentally measured forces, a force model can be built using equations 2.52-2.57.

However, due to the good agreement achieved between experimentally measured forces and simulated forces (in chapter 4), the force model for MACHpro was created completely with FEM-simulations. This means that for the first time, during optimization of turbine housing machining process, a complete digital chain between FEM and mechanistic simulations was used. The required orthogonal turning FEM simulations for force model were conducted with lagrange formulation in AdvantEdge. One of the major reasons for choosing the lagrange formulation was easy model setup possibility in AdvantEdge. Additionally, in mechanistic-FEM simulation coupling approach, forces generated in FEM-machining simulations were used as an input in the force model.

Since in machining, micro-geometry of cutting insert plays an important role in force calculations, the micro-geometry of roughing and finishing inserts was measured with Alicona Infinite Focus G5, and the measured value of each insert is shown in figure 6.7. The measured cutting edge radius $r_ß$ was integrated on CAD model of cutting insert for FEM-orthogonal machining simulations to create the force model. The cutting parameters for force model were defined based on the real machining process parameters. For inner contour turning, roughing process was conducted at a cutting speed of 110m/min, and both the finishing operations with a cutting speed of 140m/min. The feed rate varied between 0.1 mm/rev to a maximum of 0.46 mm/rev in each case. Based on measurements of the cutting edge radius and the mentioned cutting parameters, a simulation plan for the force model was created and is shown in table 6.1.

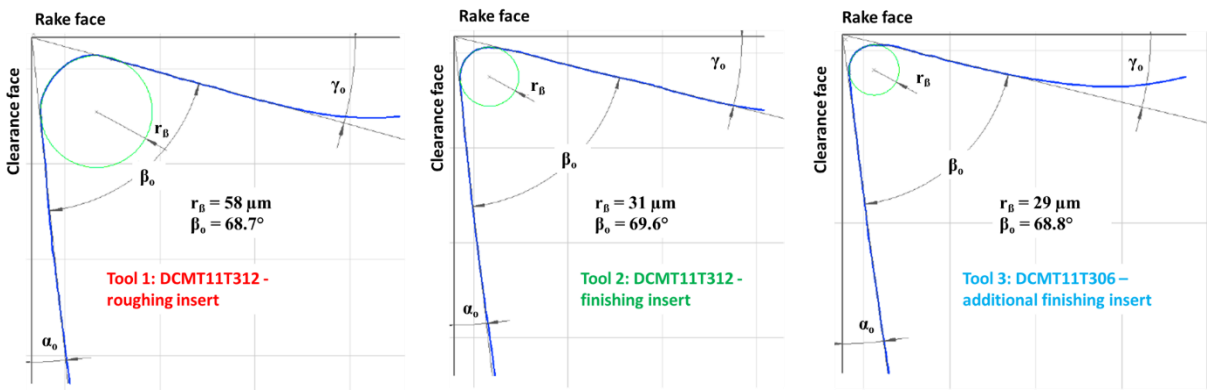

Figure 6-7: Measurement of tool micro-geometry, roughing insert (left), finishing insert (middle) and additional finishing insert (right)

Table 6-1: Simulation plan for orthogonal turning simulations to create force model

	Rake angle γ_o [°]	Cutting edge radius $r_ß$ [µm]	Cutting speed v_c [m/min]	Feed f [mm]
Roughing tool	15	60	110	0.075 0.1 0.125 0.15 0.175 0.2 0.225 0.25 0.35 0.5
Finishing tool	15	30	140	0.075 0.1 0.125 0.15 0.175 0.2 0.225 0.25 0.35 0.5

6.2.3.1 FEM-Simulation setup and results of orthogonal turning process to create force model for mechanistic simulations

For orthogonal turning simulations, a CAD model of tool and workpiece was prepared in the AdvantEdge software. The uncoated tool was made of ISO-K10 hardmetal with a rake angle γ_o= 15°, a clearance angle α_o= 7° and cutting edge radii $r_ß$= 30µm and 60µm for finishing and roughing tool respectively. The workpiece dimensions were defined as length = 10mm, height = 2mm and width = 1mm. The workpiece was fixed in all the three directions and the tool was provided a cutting speed and feed as per Table 6.1. The tool-workpiece setup is shown below in figure 6.8. The material model and mesh parameters for the simulations were same as mentioned earlier in chapter 4. A coulomb friction model was used in simulations and the coefficient of friction value between the uncoated tool and workpiece was defined as 0.5, which was provided by the supplier.

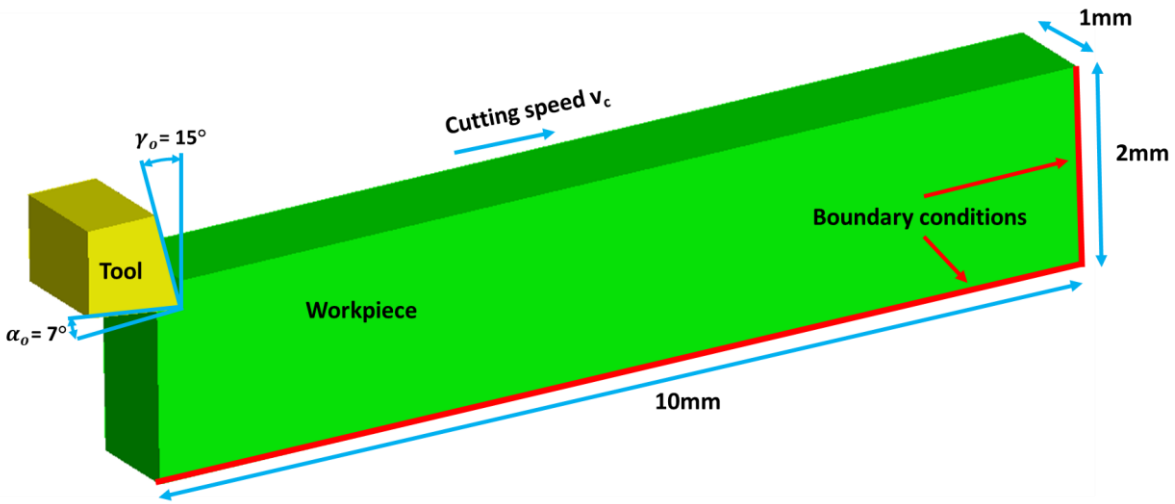

Figure 6-8: Orthogonal turning simulation setup

One of the major drawbacks of creating a force model with experiments is the measurement of chip thickness, because the process is time consuming and prone to human errors. This problem could be simplified via simulations. Figure 6.9 exemplifies the simulated chip thickness measurement for cutting speed v_c= 110m/min and feed rate f= 0.25mm. The chip thickness was measured by drawing a circle with the radius equivalent to chip thickness, as shown in figure 6.9. The chip thickness, tangential and feed force results from the simulation plan are presented in table 6.2. Based on these three results and equations from 2.49 to 2.57, other input parameters for force model were calculated and these results are mentioned in the same table.

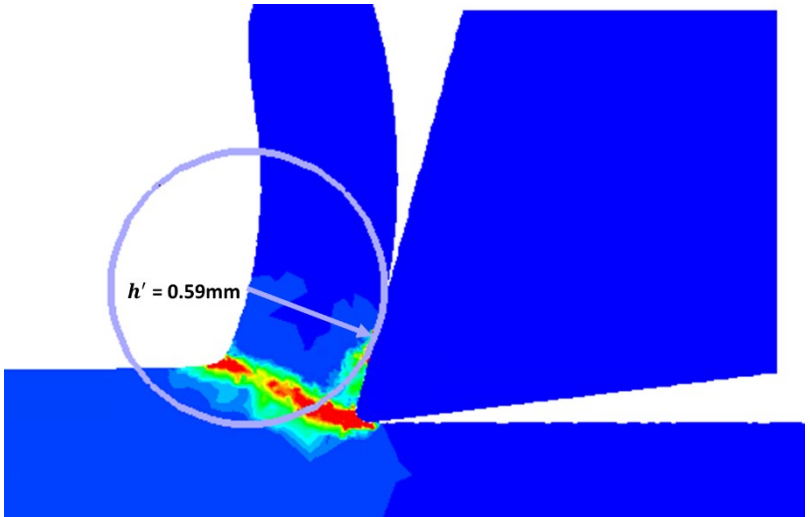

Workpiece material: 1.4837D Cooling: None	Feed-rate : f= 0.25mm Cutting speed : v_c= 110m/min Chip width : b= 1mm	α_o | γ_o 7° | 15°	Tool material: ISO-K10 Cutting edge radius: 60µm Coating: None
Orthogonal turning Simulation method: FEM			

Figure 6-9: Chip thickness results for v_c= 110m/min and f= 0.25mm for Lagrange formulation

Table 6-2: Force coefficients for material 1.4837D in roughing process

v_c [m/min]	f [mm]	F_{tc} [N]	F_{fc} [N]	h' [mm]	λ_{ch} [-]	ϕ [°]	ρ' [°]	τ_s [MPa]
110	0.075	216	118	0.182	0.4116	24.0	19.9	783.3
	0.100	266	128	0.243	0.4104	23.9	21.5	721.4
	0.125	319	140	0.309	0.4042	23.6	22.8	711.0
	0.150	371	147	0.365	0.4107	23.9	22.8	719.9
	0.175	418	153	0.426	0.4100	23.9	22.7	710.2
	0.200	455	145	0.467	0.4275	24.9	20.8	716.7
	0.225	507	149	0.534	0.4213	24.5	20.7	715.1
	0.250	556	157	0.590	0.4233	24.7	21.0	714.4
	0.350	759	178	0.829	0.4219	24.6	21.0	718.2
	0.500	1082	227	1.175	0.4253	24.8	21.8	734.1

A straight-line curve was obtained by plotting the simulated tangential and feed forces against various feed rates, figure 6.10. When the feed-rate is zero, the intercepts of two straight lines on Y-axis give the friction coefficient in tangential K_{te} and feed direction K_{fe}. Since there is no friction along the clearance face in orthogonal turning process, the friction coefficient in axial direction K_{ae} must be zero. It can be seen in table 6.2 that the friction angle ρ' roughly remained constant over the simulated feed-rate, and therefore its arithmetic mean value was chosen for simulations. On the other hand, it was noticed that the shear stress τ_s varied more over the feed-rate range. Hence, a second-degree polynomial trend line (figure 6.11) was used to describe shear stress as a function of feed rate. Similarly, for shear angle ϕ, results were plotted over the simulation plan feed-rate and a linear polynomial trend line was enough for shear angle.

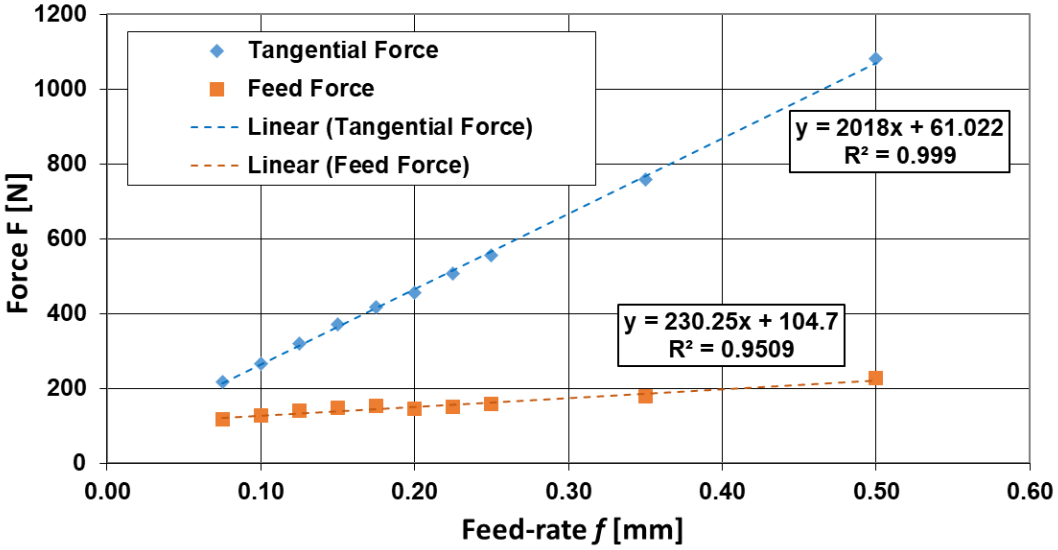

Workpiece material: 1.4837D Cooling: None	Feed-rate : f= var. Cutting speed : v_c= 110m/min Chip width : b= 1mm	α_o | γ_o 7° | 15°	Tool material: ISO-K10 Cutting edge radius: 60µm Coating: None
Orthogonal turning Simulation method: FEM			

Figure 6-10: Tangential and Feed forces over simulation plan feed-rate

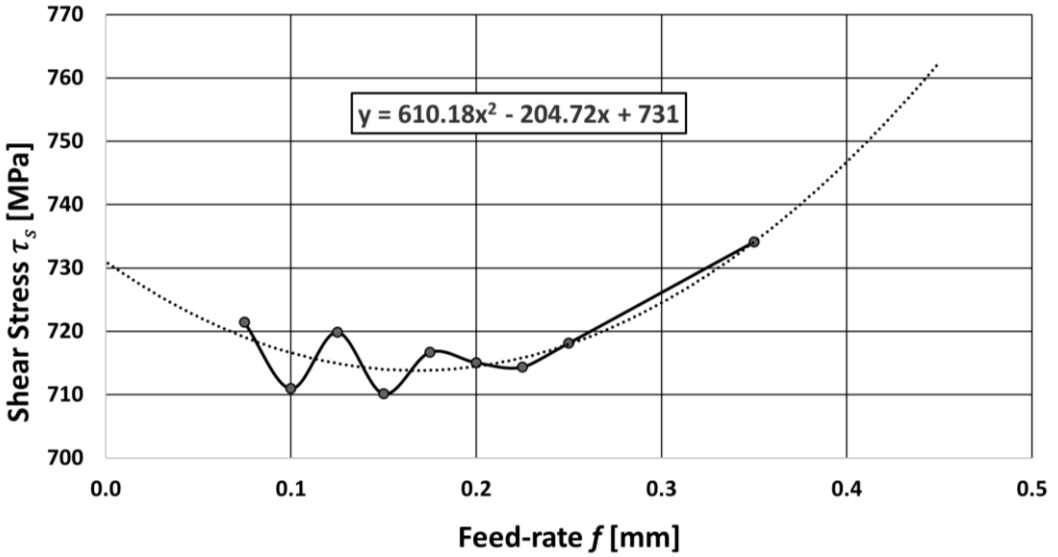

Workpiece material: 1.4837D Cooling: None	Feed-rate : f= var. Cutting speed : v_c= 110m/min Chip width : b= 1mm	α_o | γ_o 7° | 15°	Tool material: ISO-K10 Cutting edge radius: 60µm Coating: None
Orthogonal turning Simulation method: FEM			

Figure 6-11: Shear stress curve over simulation plan feed-rate

Based on table 6.2, figure 6.10 and 6.11, force coefficient for roughing process were determined as following:

$K_{te} = 61.02\ \mathrm{N/mm}$

$K_{fe} = 104.7\ \mathrm{N/mm}$

$K_{ae} = 0\ \mathrm{N/mm}$

$\rho' = 21.5°$

$$\tau_s = 610.18 * f^2 * \left(\frac{MPa}{mm^2}\right) - 204.72 * f * \left(\frac{MPa}{mm}\right) + 731\ (MPa) \quad 6.1$$

$$\phi = 2.5394 * f * \left(\frac{^\circ}{mm}\right) + 23.732\ (°) \quad 6.2$$

where, *f* represents the feed rate.

Similarly, force coefficients for the finishing process were calculated. However, for finishing operations, only shear stress required a second order polynomial trend line. Both, shear angle and friction angle, were approximately constant over the feed-rate range and thus their average value was used in simulations. Force coefficients for the finishing process are written below:

$K_{te} = 51.35\ \mathrm{N/mm}$

$K_{fe} = 59.7\ \mathrm{N/mm}$

$K_{ae} = 0\ \mathrm{N/mm}$

$\rho' = 21.2°$

$\phi = 23.5°$

$$\tau_s = -439.53 * f^2 * \left(\frac{MPa}{mm^2}\right) + 298.33 * f * \left(\frac{MPa}{mm}\right) + 636.51\ (MPa) \quad 6.3$$

6.2.4 Modelling of inner contour turning process

After preparing the three inputs defined earlier in sub-sections 6.2.1 to 6.2.3, a virtual CNC machine had to be defined considering the real performance limit of spindle. After defining a CNC machine in the software, the raw CAD model of turbine housing was imported in STL format. It must be noted that the software requires an axis-symmetrical CAD body for turning operations. Thus, not only the inner contour of turbine housing was axis-symmetrical in simulations, but also the outer contour. After this, the force model calculated for both, roughing and finishing process, in the last section was defined in the software. Only one force model could be used for the simulation project. Therefore, two projects, one for roughing and other for finishing process, had to be used for simulation of inner contour turning process. After the definition of force model, the NC-programs in form of CLS files were imported and indexable D-type inserts were defined for finishing and roughing turning process. It must be noted here

that these cutting inserts did not have a cutting edge radius. Their effect was thus integrated through force model. Before starting the simulation in MACHpro, the "engagement maps" were generated. These engagements maps are basically the sampling rate of result outputs from simulation. This means that small sampling rates increase the resolution of simulation in distance or time domain but at the cost of higher computational time and storage requirement for output result file. In the turning process, lower limit for sampling rate that could be defined was 1mm and this rate was used in the inner contour turning process simulation.

Lastly, parameters that need to be calculated (as output) were defined in the simulation. The following parameters were calculated for inner contour turning process: feed force, cutting force and passive force with respect to cutting edge of tool, torque, energy consumption and chip load.

6.2.5 Mechanistic simulation results of inner contour turning process

As inner contour turning process did not have any stability problems, the tool load was investigated by calculating the process forces, passive F_p, cutting F_c and feed forces F_f, with respect to cutting edge coordinate system. The three force components in cutting edge coordinate system for the inner contour turning process are shown below in figure 6.12. During simulations, it was found that the cutting force is the largest force component in terms of magnitude of force. Hence, the focus for tool load optimization in process was on cutting force.

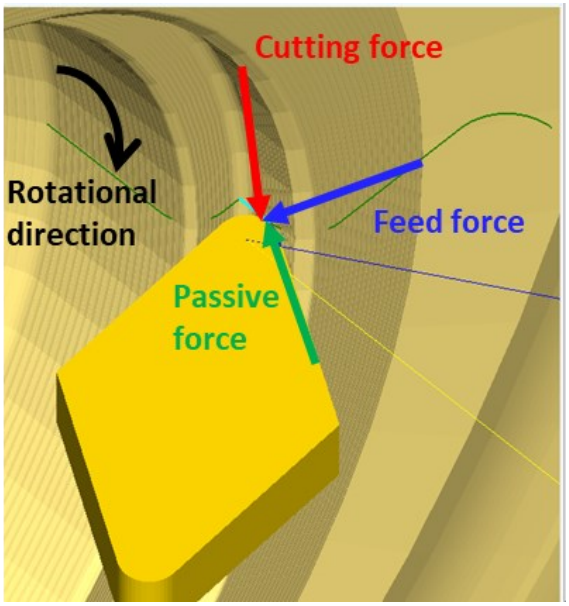

Figure 6-12: Force components in inner contour turning

Figure 6.13 shows the simulated cutting and feed force results of inner contour turning process and it can be observed that there were six critical force peaks (marked) in the process. The first position represented the tallest force peak F_c =925N, and it occurred at the beginning of the roughing of trumpet. This force peak was due to an unfavorable stock allowance situation, which was caused by the lack of flexibility of preceding milling process that removes material from this area. Likewise, second peak force position, too, had an unfavorable stock allowance situation.

Like in trumpet roughing, there were two force peaks in roughing on the bearing side. At position three, the increase in force was due to the transition radius. Due to a transition from facing to longitudinal turning at the fourth point, there was an increase in cross-section area at the bearing seat which caused the force to peak.

Fifth and sixth force peaks occurred during the finishing operations. However, their magnitude was lower as compared to roughing process due to a major material removal in the latter. At the fifth position, a radius was created which increased the cross-section area to be machined, ultimately causing a force peak. Similar to position three (shown in figure 6.13), at position six, an increase in the cross-section area resulted in a force peak. These forces peaks contributed to the major wear on the three cutting inserts. Since the magnitude of force peaks 1 and 4 is highest among all the force peaks, roughing cutting insert wore out faster than the other two inserts. Force optimization of these six force peaks was conducted by reducing the targeted feed-rate at these points. Results of optimization are discussed in the next sub-section.

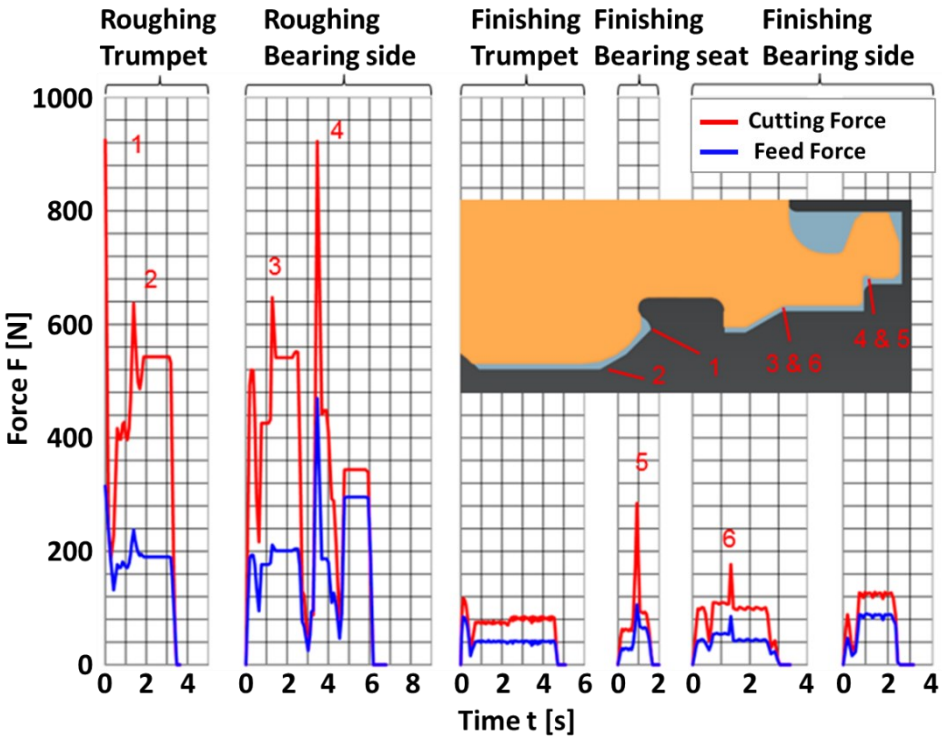

Workpiece material: 1.4837D	Process: Inner contour turning	Cooling: None Simulation method: Mechanistic

Figure 6-13: Simulated cutting and feed force curves for inner contour turning

6.2.6 Optimization of inner contour turning process based on mechanistic simulations

Optimization was carried out based on the six force peaks obtained from simulation results in the previous section. Since the first force peak (roughing in the trumpet area) had the maximum force magnitude, it was used as a guide to set the upper limit for force in cutting direction. After various manual optimization loops by reducing the feed-rate in region of force peaks, those peaks were reduced to the set limit of 560 N for cutting force. This limit was set as any further reduction in cutting force led to a significant increase in the cycle time. Figure 6.14 shows the optimized cutting forces after feed-rate reductions along the inner contour turning process.

These reduced feed-rate values from simulations were incorporated in NC-program and figure 6.15 shows an excerpt of optimized NC-program for two roughing processes. This optimized NC-program was then tested in production and consequently, the tool life improved by 46%. Due to feed-reductions, the cycle time increased but that was compensated as fewer tool replacements were required.

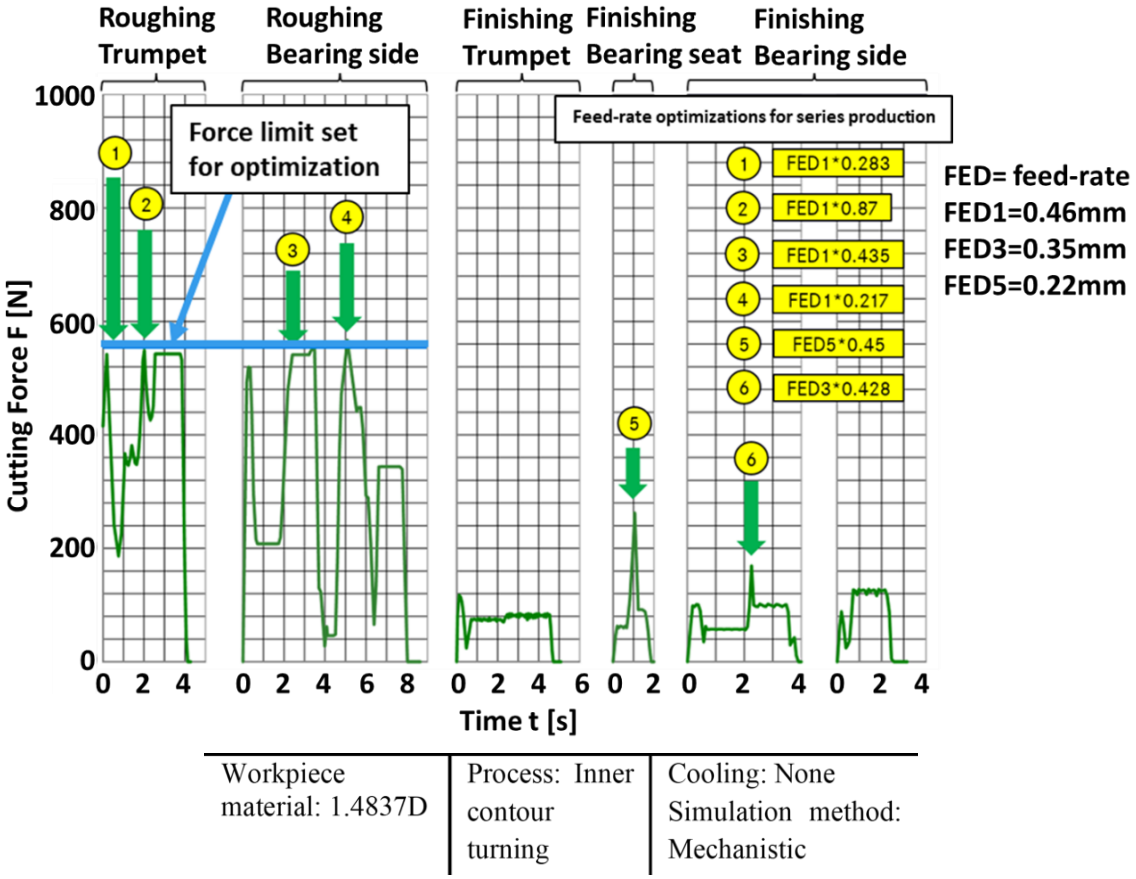

Figure 6-14: Optimized cutting force with feed optimizations for inner contour turning

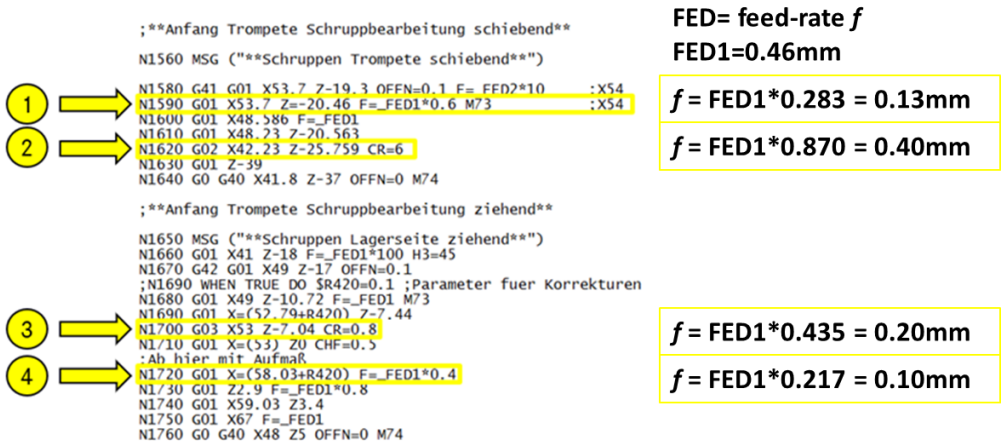

Figure 6-15: Implementation of feed-rate reduction in NC-program for roughing process

6.3 Conclusion of mechanistic simulation results

Results of complex inner contour turning process simulation were presented and optimized. In FEM with chip remeshing, the process is usually simulated for a few milliseconds. Due to its long cycle time, therefore, inner contour turning process simulation cannot be conducted with

FEM. In such scenarios, mechanistic simulations present a realistic approach to optimize the machining process in production.

Additionally, a novel coupling approach between FEM and mechanistic simulations in the form of force model was presented in this section. Since FEM simulations were used to create the force model, the number of experiments required to create it could be reduced. Another advantage of mechanistic simulations was that 2D orthogonal turning simulations could be used to model the 3D-machining process. Later, by using these mechanistic simulations, the feed-rate at six positions were optimized in an NC-program of inner contour turning process, which increased the tool life by 46%.

6.4 Further optimization of inner contour turning process using FEM-simulations

Even after the NC-program optimization in section 6.2.6, the inner contour roughing insert had a high wear and thus it was further analyzed. The analysis results are presented in section 6.4.2.

6.4.1 FEM-simulation setup of inner contour roughing insert

In this section, cutting inserts from the inner contour turning process were further optimized in pursuit of increasing the tool life. Since roughing insert had a higher wear in comparison to the other two inserts, optimization was conducted only for this tool. Additionally, it was observed that the coating was coming off roughing insert during the inner contour turning in production. Due to this reason, the better performing coating and coating thickness from chapter 4 were modelled on the roughing insert and the simulations were conducted. A total of two cutting inserts from the geometry DCMT11T312 were simulated: roughing cutting insert with 16µm Ti(C,N)+ Al_2O_3 coating and the same cutting insert with 4µm AlTiN coating. Due to difference in coating thicknesses, the two tools had a different cutting edge radius. For cutting insert with Ti(C,N)+ Al_2O_3 coating, the cutting edge radius was r_β =56µm, whereas for AlTiN coating it was r_β =44µm. These FEM-simulations were conducted with the same setup as defined in chapter 4, therefore no additional mesh sensitivity analysis was required and meshing in simulation was defined in accordance with section 4.5.2.

In inner contour roughing process, the feed-rate was as high as 0.46mm in comparison to the maximum feed-rate of 0.25mm in chapter 4. Due to this reason, the range of cutting parameters was redefined as following: feed-rate $f = 0.2 - 0.5mm$, cutting speed $v_c = 90 - 140\frac{m}{min}$,

depth of cut $a_p = 0.15 - 0.35mm$. However, a similar full factorial design with the center point as earlier was created and the DoE cube plot for two inserts is shown below in figure 6.16.

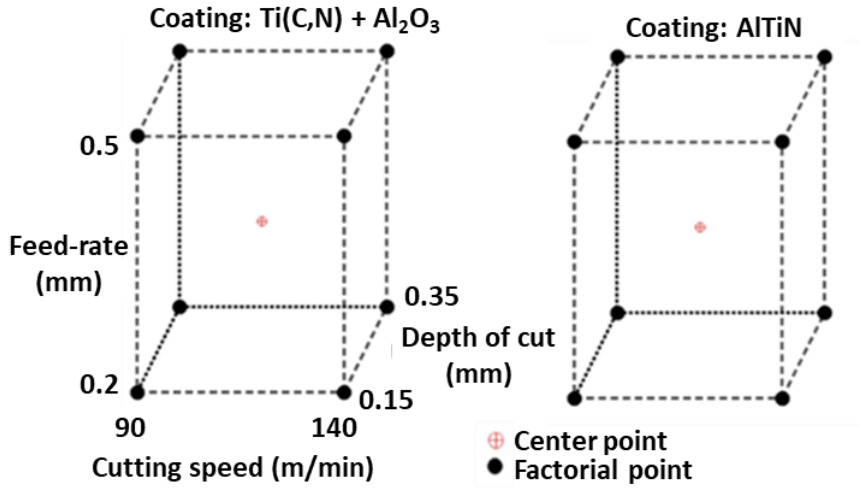

Workpiece material: 1.4837D Cooling: None	Cutting depth : a_p = var. Feed-rate : f = var. Cutting speed : v_c = var.	α_o	γ_o	ε_r	κ_r	Tool material: ISO-K10 Geometry: DCMT11T312-F Corner radius: 1.2 mm Coating: var.
Longitudinal turning Simulation method: FEM		7°	15°	55°	93°	

Figure 6-16: Cube plot diagram for Ti(C,N)+ Al_2O_3 and AlTiN coating

6.4.2 FEM-Simulation results of inner contour roughing insert of different coatings and cutting edge radii

The simulation results of two tools for Ti(C,N)+ Al_2O_3 and AlTiN coating are compared with each other. Figure 6.17 compares the temperature results between the two tools for four cutting parameters. It can be noticed that for both the tools, an increase in cutting parameter (depth of cut or feed-rate) leads to an increase in temperature. However, while comparing the two cutting inserts, AlTiN coated cutting inserts had lower tool temperatures. Due to the thermal conductivity of AlTiN coating, heat dissipation was faster with these cutting inserts, leading to a low temperature in simulations. Additionally, AlTiN coated inserts had a smaller cutting edge radius as compared to the other coating inserts.

Machining forces were also simulated for both the cutting inserts and cutting force was the dominant force among the three force components. For the cutting parameter v_c =90m/min, f =0.5mm and a_p =0.35mm, the cutting forces are compared in figure 6.18. It can be noticed that the AlTiN coated insert had lower cutting forces in comparison to the other insert. One of the

reasons for this difference in cutting forces is the small cutting edge radius of AlTiN coated insert as compared with Ti(C,N)+Al_2O_3 coated tool.

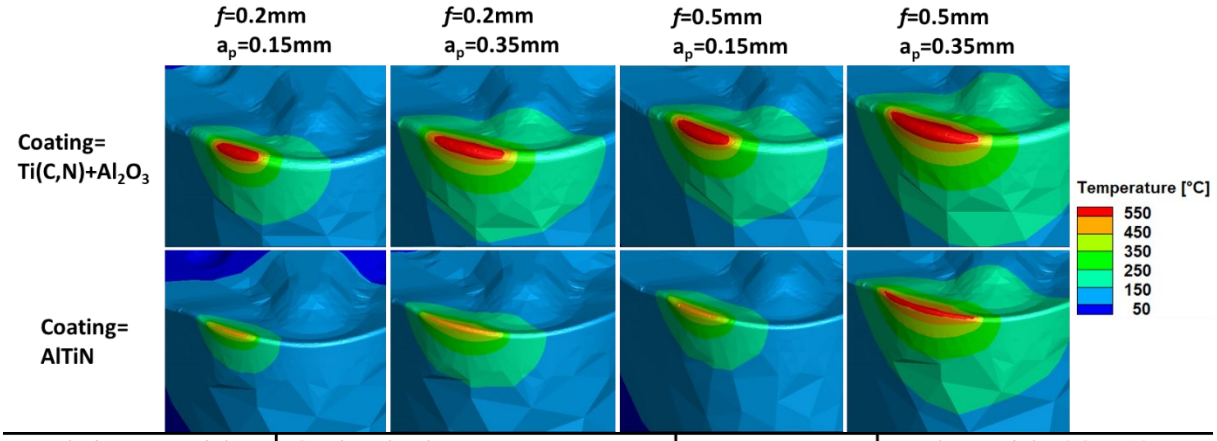

Workpiece material: 1.4837D Cooling: None	Cutting depth : a_p = var. Feed-rate : f = var. Cutting speed : v_c = 90m/min	α_o | γ_o | ε_r | κ_r 7° | 15° | 55° | 93°	Tool material: ISO-K10 Geometry: DCMT11T312-F Cutting edge radius: var. Corner radius: 1.2 mm Coating: var.
Longitudinal turning Simulation method: FEM			

Figure 6-17: Temperature comparison between Ti(C,N)+Al_2O_3 and AlTiN coated inserts

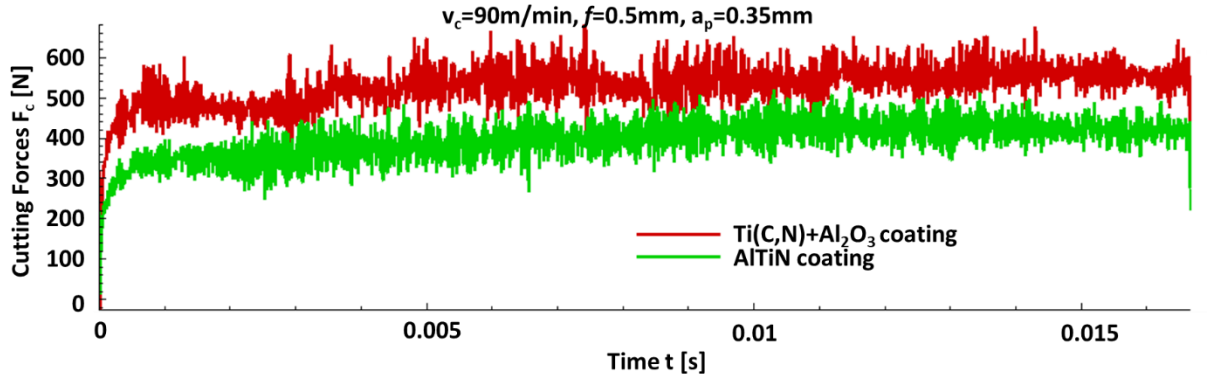

Workpiece material: 1.4837D Cooling: None	Cutting depth : a_p = 0.35mm Feed-rate : f = 0.5mm Cutting speed : v_c = 90m/min	α_o | γ_o | ε_r | κ_r 7° | 15° | 55° | 93°	Tool material: ISO-K10 Geometry: DCMT11T312-F Cutting edge radius: var. Corner radius: 1.2 mm Coating: var.
Longitudinal turning Simulation model: FEM			

Figure 6-18: Force comparison between Ti(C,N)+Al_2O_3 and AlTiN coated inserts for v_c= 90m/min, f =0.5mm and a_p =0.35mm

Lastly, main effect plots for cutting force and temperature were created and are shown in figure 6.19 and figure 6.20 respectively. The effect of cutting parameters on force and temperature results was analogous to the observations in DoE 1 and DoE 2. For each DoE input parameter, AlTiN coated inserts had lower forces and temperatures than Ti(C,N)+Al_2O_3 coated inserts.

Based on these results, it can be concluded that the new coating performed better than the older one. This better performance of AlTiN coating is due to its high toughness, stable hardness and ability to form a protective Al_2O_3 layer at an elevated temperature [7].

Since simulation results were matched for earlier tools in both design of experiments, no experiments were conducted for these two tools in order to reduce the number of experiments in production.

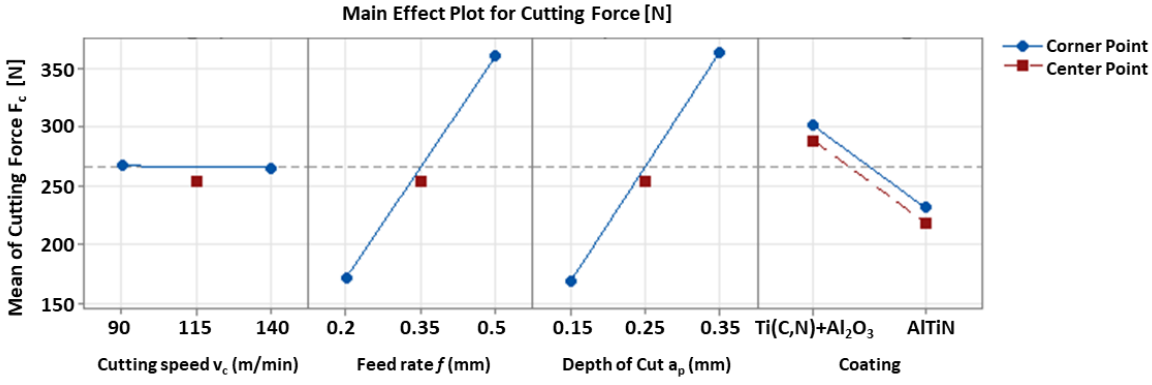

Workpiece material: 1.4837D Cooling: None	Cutting depth : a_p = var. Feed-rate : f = var. Cutting speed : v_c = var.	α_o	γ_o	ε_r	κ_r	Tool material: ISO-K10 Geometry: DCMT11T312-F Cutting edge radius: var. Corner radius: 1.2 mm Coating: var.
Longitudinal turning Simulation model: FEM		7°	15°	55°	93°	

Figure 6-19: Influence of DoE parameters on simulated forces for two inserts

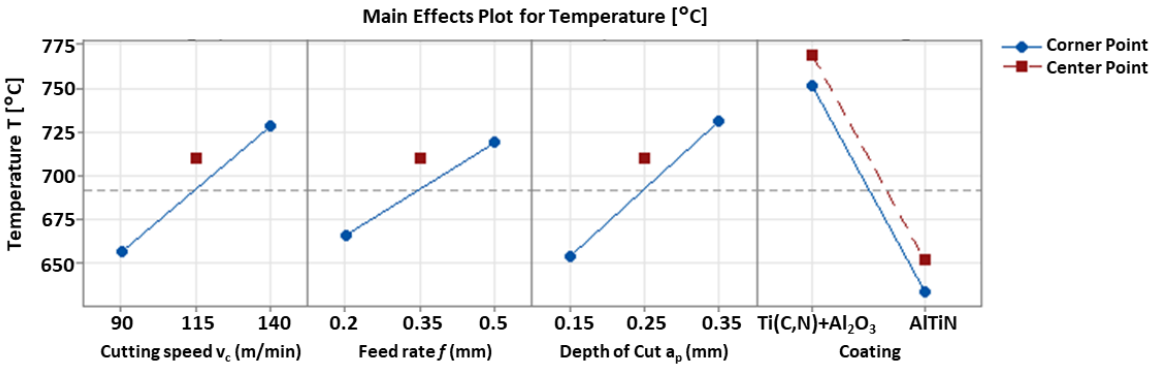

Workpiece material: 1.4837D Cooling: None	Cutting depth : a_p = var. Feed-rate : f = var. Cutting speed : v_c = var.	α_o	γ_o	ε_r	κ_r	Tool material: ISO-K10 Geometry: DCMT11T312-F Cutting edge radius: var. Corner radius: 1.2 mm Coating: var.
Longitudinal turning Simulation model: FEM		7°	15°	55°	93°	

Figure 6-20: Influence of DoE parameters on simulated temperature for two inserts

6.5 Summary: Impact of simulation results on mass production

After simulation results from section 6.4, a batch of tools with 4µm AlTiN coating thickness as roughing insert for inner contour turning process was procured. The new tool was tested, and the tool-life increased by more than 74% after NC-program optimization. Thus, the two simulation methods (Mechanistic + FEM) increased the tool-life by an overall amount of 154%. This benefit from tool optimization along with other benefits is shown in figure 6.21.

As mentioned in section 6.1, inner contour turning process accounted for a high percentage of scrap rate in the turbine housing production. Tool-life optimization not only saved the tool cost (around 17%) but also reduced the scrap rate massively, leading to savings of approximately 65% in the form of scrap costs. Ultimately, the machine downtime and tool preparation time were reduced by 51% because of longer tool life. In the end, it can be concluded that robust and validated simulation models can be implemented in production, which in turn leads to cost savings.

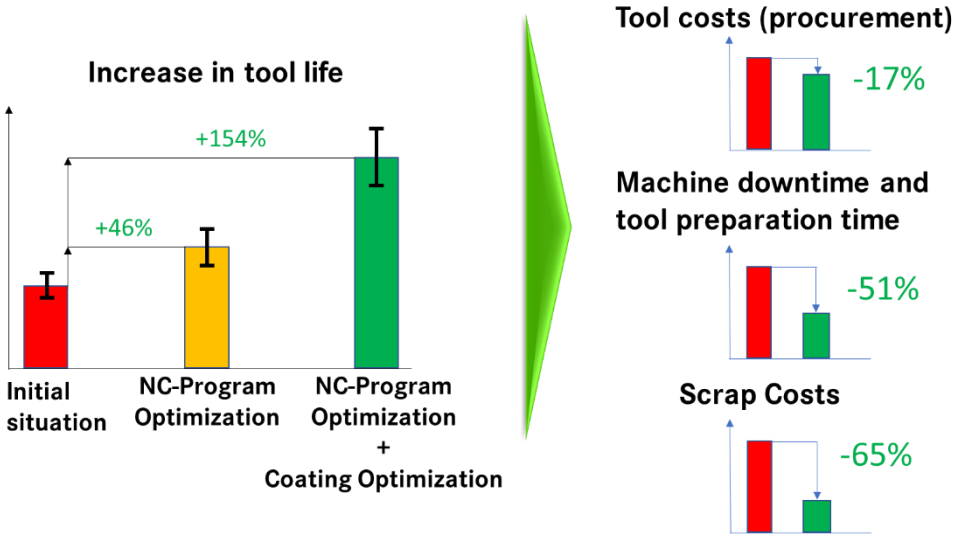

Figure 6-21: Benefits from tool optimization of roughing insert in Inner contour turning process of turbine housing

7 Comparative analysis of simulation methods

The methodology applied herein examined the extent and success of implementing different simulation tools in machining process optimization. The inner contour turning process from turbine housing made of the novel material 1.4837D was selected for this purpose. Major challenges of the 1.4837D material were high tools costs, high cycle time during machining and low tool-life for various processes. Additionally, inner contour turning process constituted high scrap rate in turbine housing production. Therefore, the process was digitally mapped, analyzed and optimized.

A digital strategy was presented at micro and macro level to optimize the most common machining parameters mentioned in figure 3.2. In the presented digital strategy, depending on the end goal of optimization, a modelling technique was chosen, for example: dry turning process was optimized using FEM, flood lubricated turning process was optimized with the CFD method and NC-program optimization was conducted by mechanistic methodology.

To reduce the number of experiments and bring digitalization to the production level, two new approaches were developed to couple the FEM and CFD methods for flood lubricated turning process. Additionally, a new approach was presented to couple the digital force model from FEM with the mechanistic simulation method. A schematic diagram of these approaches coupling different simulation methods is shown in figure 7.1.

Between the two approaches developed for the flood lubricated turning process, bi-directional (two-way) FEM-CFD coupling using single software provided better results than the uni-directional (one-way) coupling in the first approach. This could be explained by the fact that a chip formation is not possible in the first approach (fixed chip shape was assumed in this approach) and there is a probability of losing information during the mapping of results from FEM to CFD software. Additionally, the second approach is cost-conscious as only one software license had to be procured here.

After numerous validations of FEM results with the experimental results in chapter 4, it was concluded during FEM simulations, thermal and mechanical loads on the tool could be simulated very well. Based on this, a novel approach was presented to couple the FEM simulations with mechanistic simulations in chapter 6. The cutting forces from the FEM orthogonal turning simulations were used as a force model inside the mechanistic simulations. The optimized results from the mechanistic simulations using force model from FEM-

simulations were tested positive in production. This validation proved that this approach can be used in future to reduce the number of experiments and implement digitalization at both micro and macro level.

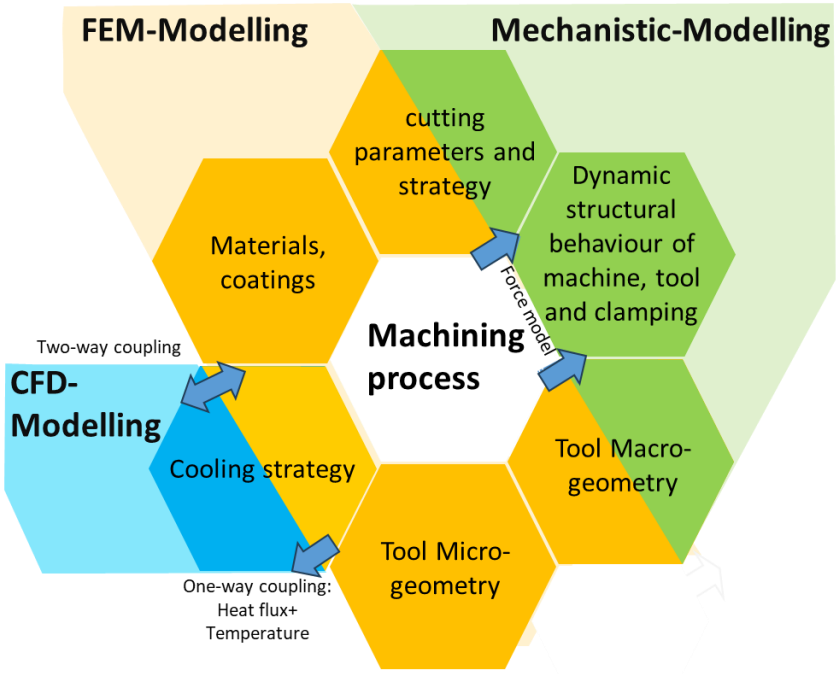

Figure 7-1: Schematic diagram of three approaches highlighting coupling of different simulation methods

Table 7.1 provides a comprehensive comparison of different tools used in this thesis. However, the choice of selecting a software depends on the problem statement.

Table 7-1: Comparison of different simulation tools for machining process simulations

Software / Criteria	AdvantEdge	LS-DYNA	Star-CCM+	MachPro
Modelling technique	Numerical modelling: FEM	Numerical modelling: FEM + CFD	Numerical modelling: CFD	Mechanistic modelling
Usage	Machining process analysis	General purpose software	General purpose CFD software	Machining process analysis
Cutting force prediction	Yes	Yes	No	Yes
Chip formation modelling	Yes	Yes	No	No
Thermal analysis	Yes	Yes	Yes	Yes
Tool-path analysis	Tool-engegement based	Tool-engegement based	Not possible	NC-program optimization
Bi-directional coupling	Not possible	Possible	Possible (with Abaqus software)	Possible (with software CutPro)

8 Conclusion and future work

8.1 Conclusion

FEM simulations were conducted for two different coatings, coating thicknesses and edge radii based on design of experiments. In the simulation analysis, force components and chips were the output variables in longitudinal turning simulations and temperature was the output variable in internal turning process. Each simulation was validated with experiments. In addition to forces and chips, surface roughness was also measured in the longitudinal turning experiments because it was a critical output parameter in the inner contour turning process. These experiments were conducted on casted cylindrical blanks of the 1.4837D material to save the cost of workpiece. Two DoEs were created for this optimization. In the first DoE, two different coatings were analyzed, and the better performing coating was used in second DoE for two different coating thicknesses and cutting edge radii. In both the DoEs, comparison of simulated and measured results depicted that the force components in simulations were underpredicted for most of the cutting parameters. Simulated forces had an average relative error of around 10% with respect to experiments. Simulated chips were also compared with experimental chips and a good comparison was found between them. Temperature in the internal turning process was measured with the help of a 2-color pyrometer. Temperatures for different cutting parameters in design of experiments were in the range of 500-900°C. Simulated temperature deviated from measured results by approximately 4%. AlTiN coating performed better than TiSiN coated inserts in first DoE. Since, both coatings were not able to meet the tool-life criteria for the desired number of parts. Thus, the second DoE was created using AlTiN coating. From the DoE results, it was concluded that AlTiN coating with 44µm cutting edge radius and 4µm coating thickness performed better than other cutting inserts. This was validated by flank wear curve measured on a cutting parameter, similar to the mass production parameters.

Two novel simulation approaches were developed and defined in this thesis work for flood lubricated machining process. In the first approach, a unidirectional coupling was defined for internal turning process between FEM and CFD software. The effect of cutting parameters on temperature was studied here. Flood lubricated simulations were conducted in the CFD software and the simulated temperatures showed a deviation of approximately 4% when compared to the measured results. To overcome shortcomings from the first approach, a new approach was defined, where flood lubricated orthogonal turning process was simulated with

SPH-SPH coupling in a single software. Flood lubricated orthogonal turning simulations were conducted to analyze the effect of cutting parameters on temperature and these simulations were compared to dry orthogonal turning simulations. The comparison of temperature results between dry and flood lubricated simulations depicted that the effect of cutting parameters was in accordance with literature and lubricated simulations had lower temperature than dry orthogonal turning simulations.

To scale the simulations to turbine housing mass production level, mechanistic modelling technique was used. Since NC-program of inner contour turning process had various cutting speeds, feed-rates and depth of cuts, the FEM-simulation method would have been computationally very expensive. To digitally optimize the NC-program in realistic simulation time, mechanistic simulation technique was used. Instead of experiments, FEM simulations were used to digitally procure the force coefficients that are required in force model as an input for mechanistic simulations. At the end of simulation, a total of six force peaks were found over the simulated NC-program. In the end, several simulations were conducted to optimize these force peaks by reducing the feed-rate and keeping the cycle time in check. There was a small increase in cycle time after feed-rate reductions, but that was compensated by fewer tool replacements after NC-program optimization. Overall, mechanistic simulations increased the tool life by 46%. Last optimization on inner contour turning process at mass production level was conducted using FEM-simulations by optimizing the coating of roughing insert. This optimization was done by replacing the old cutting insert coating with the best performing coating and coating thickness from first DoE and second DoE respectively. On comparing the old cutting insert (DCMT11T312 with 16µm Ti(C,N)+Al_2O_3 coating) with the new cutting insert (DCMT11T312 with 4µm AlTiN coating), it was found that both, mechanical and thermal loads, were reduced on the new coating. After implementing the new cutting insert in mass production, tool-life increased by over 74%. This increase was observed after the NC-program optimizations. Thus, there was an overall increase of 154% in tool-life through NC-program and coating optimization.

Overall, it can be concluded that there was good agreement between simulations and experiments, and simulation results can be scaled to mass production level. Thus, in future, simulations can help in reducing the number of inserts that are tested today in mass production which can save material, tool, and machine costs. But, to gain maximum benefit through digital strategy proposed in this work, it should not be limited to mass production. The strategy could

also be used in early stages of product development where the information on process, material and machine is limited. In such a scenario, simulations can be used to gain more insights in process and can help in reducing product development times.

8.2 Future work

Dry machining (FEM) simulations in this work presented good results in comparison to experiments, but they can be further optimized in future by using better friction models. Both the approaches for flood lubricated machining simulations had their respective shortcomings. In the first approach (unidirectional coupling), the asperity contact distance should be studied further in detail. Additionally, discrete element method (DEM) could be used to create chips in flood lubricated simulations. This will overcome the deficit of using the fixed chip shape in current flood lubricated simulations. Though using DEM could increase the accuracy of simulations, it could also increase the simulation time drastically. In the second approach (bidirectional coupling), SPH-MC-SPG (lubricant-tool/workpiece) coupling can solve the issue of chip bending without increasing the simulation time drastically. Rana et al. [164] showed that chip bending could be very well simulated with MC-SPG and the chip shape in simulations was in good agreement with the experimentally created chip. With the current particle approximation theory, fluids can be well modelled with SPH formulation, making this approach a plausible solution for flood lubricated simulations in future. Tool wear was not simulated during this thesis work as it was out of scope for this work. But tool wear simulations may directly help process developers in tool selection and hence it should be researched further. MC-SPG formulation could also be a possible solution to the tool wear problem.

To make a bigger impact through simulations or to create a digital process chain, coupling methodology between different software must be defined. This methodology can be achieved if the simulation data results from one process are used as an input in the next process. An alternative to this methodology could be the usage of limited number of software along the manufacturing process chain. Further research and use-cases are required in future to select any of the two above-mentioned approaches.

9 References

[1] GROHE, Heinz and Gerald RUSS, 2010. *Otto- und Dieselmotoren*. 15. Würzburg: Vogel. ISBN: 978-3-8343-3186-1.

[2] MAYER, Michael and Günter KRÄMER, 2011. *Abgasturbolader*. 6. München: Süddeutscher. Vol. 103. ISBN: 9783862360260.

[3] KAISER, Timotheus, Siegfried BOTSCH and Karl-L WEISSKOPF, 2013. Wirtschaftliches Stahlgießen für die Produktion von Turbinengehäusen: Entwicklung Werkstoff und Einführung in den Serienprozess bei der Daimler AG. *Giesserei*, 10, pp. 36-45.

[4] DEUTSCHES INSTITUT FÜR NORMUNG e.V., 2003. *ISO 8580:2003-09, Fertigungsverfahren – Begriffe, Einteilung*. Berlin: Beuth, 00.09.2003.

[5] DEUTSCHES INSTITUT FÜR NORMUNG e.V., 2003. *ISO 8589-0:2003-09, Fertigungsverfahren Spanen – Teil 0: Allgemeines – Einordnung, Unterteilung, Begriffe*. Berlin: Beuth, 00.09.2003.

[6] DEUTSCHES INSTITUT FÜR NORMUNG e.V., 2003. *ISO 8589-1:2003-09, Fertigungsverfahren Spanen – Teil 1: Drehen – Einordnung, Unterteilung, Begriffe*. Berlin: Beuth, 00.09.2003.

[7] KLOCKE, Fritz, 2011. *Manufacturing Processes 1 – Cutting*. 1. Heidelberg: Springer Berlin. ISBN: 9783642119781.

[8] DEUTSCHES INSTITUT FÜR NORMUNG e.V., 1985. *ISO 6581:1985-10, Begriffe der Zerspantechnik: Bezugssysteme und Winkel am Schneidteil des Werkzeugs*. Berlin: Beuth, 01.10.1985.

[9] TOENSHOFF, Hans Kurt and Berend DENKENA, 2013. *Basics of Cutting and Abrasive Processes*. 1. Heidelberg: Springer Berlin. ISBN: 9783642332562.

[10] ALTINTAS, Yusuf, 2012. *Manufacturing Automation: Metal Cutting Mechanics, Machine Tool Vibrations, and CNC Design*, 2. Cambridge: Cambridge University Press. ISBN: 9781107001480.

[11] DEUTSCHES INSTITUT FÜR NORMUNG e.V., 1982. *ISO 6584:1982-10, Begriffe der Zerspantechnik; Kräfte, Energie, Arbeit, Leistungen*, Berlin: Beuth, 01.10.1982.

[12] KRONENBERG, Max, 1954. *Grundzüge der Zerspanungslehre. Theorie und Praxis der Zerspanung für Bau und Betrieb von Werkzeugmaschinen*, Springer Berlin, Heidelberg. ISBN: 978-3-642-49037-8.

[13] DA SILVA, Marcio Bacci and James WALLBANK, 1999. Cutting temperature: prediction and measurement methods—a review, *Journal of Materials Processing Technology*, Vol. 88, pp. 195-202. ISSN: 0924-0136.

[14] KÜSTERS, Karl Josef, 1956. *Temperaturen im Schneidkeil spanender Werkzeuge.* [Dissertation], Aachen: Technische Hochschule Aachen.

[15] ARRAZOLA, Pedro-J., Patxi ARISTIMUNO, Daniel SOLER, and Tom CHILDS, 2015. Metal cutting experiments and modelling for improved determination of chip/tool contact temperature by infrared thermography, *CIRP Annals*, Vol. 64, pp. 57-60. ISSN: 0007-8506.

[16] THAKARE, Amol, Anders NORDGREN, 2015. Experimental Study and Modeling of Steady State Temperature Distributions in Coated Cemented Carbide Tools in Turning, *Procedia CIRP*, Vol. 31, pp. 234-239. ISSN: 2212-8271.

[17] HABERMEIER, Julius, 2017. *Technologische Untersuchungen der Bearbeitung nickelreduzierter Stahlgusslegierungen für Turbinengehäuse.* [Dissertation], Technische Universität Dortmund, Essen: Vulkan Verlag. ISBN: 978-3-8027-8796-6.

[18] MÜLLER, Bernhard and Ulrich RENZ, 2003. Time resolved temperature measurements in manufacturing, *Measurement*, Vol. 34, pp. 363-370. ISSN: 0263-2241.

[19] KOMANDURI, Ranga and Lionel RAFF, 2001. A review on the molecular dynamics simulation of machining at the atomic scale. Vol. 215, 12, pp. 1639-1672.

[20] TAYLOR, Federick Winslow, 1907. On the Art of Cutting Metals. 1119, New York: American Society of Mechanical Engineers, Transaction of the ASME, Vol. 28, pp. 31-248.

[21] VAN LUTTERVELT, C. A., Thomas H.C. CHILDS, I. S. JAWAHIR, Fritz KLOCKE, Patri K. VENUVINOD, Yusuf ALTINTAS, E. J.A. ARMAREGO, David Alan DORNFELD, Igor GRABEC, Jürgen LEOPOLD, Bo LINDSTRÖM, Don A. Lucca, Toshiyuki OBİKAWA, SHIRAKASHI and Hisayoshi SATO, 1998. Present Situation and Future Trends in Modelling of Machining Operations Progress Report of the CIRP Working Group 'Modelling of Machining Operations'. 2, Elsevier, *CIRP Annals*, Vol. 47, pp. 587-626. ISSN: 0007-8506.

[22] SURMANN, Tobias, 2017. *Simulation der Dynamik von Dreh- und Fräsprozessen*, Essen: Vulkan. ISBN: 9783802787942.

[23] SOEHNER, Jörg, 2003. *Beitrag zur Simulation zerspanungstechnologischer Vorgänge mit Hilfe der Finite-Element-Methode.* [Dissertation]. Karlsruhe: Universität Karlsruhe (TH).

[24] KIENZLE, Otto, 1952. Die Bestimmung von Kräften und Leistungen an spanenden Werkzeugen und Werkzeugmaschinen. 11, VDI-Z, Vol. 94.

[25] VICTOR, Hans, 1976. Zerspankraftprognose. 98, *Industrie-Anzeiger*, Vol. 102, pp. 1825-1830. ISSN: 0019-9036.

[26] KRONENBERG, Max, 1963. *Grundzüge der Zerspanungslehre - Theorie und Praxis der Zerspanung für Bau und Betrieb von Werkzeugmaschinen Zweiter Band*

Mehrschneidige Zerspanung (Stirnfräsen, Bohren). 2. Heidelberg: Springer Berlin. ISBN: 978-3642928628.

[27] ZABEL, Andreas, 2010. *Prozesssimulation in der Zerspanung: Modellierung von Dreh- und Fräsprozessen.* [Habilitation]. Essen: Vulkan-Verlag. ISBN: 9783802787522.

[28] CLAUSEN, Marc, 2005. *Zerspankraftprognose und -simulation für Dreh- und Fräsprozesse.* [Dissertation]. IFW, Leibniz Universität Hannover. Hannover: PZH, Produktionstechn. Zentrum GmbH. ISBN: 3936888809.

[29] MERCHANT, M. Eugene, 1944. Basic Mechanics of the Metal-Cutting Process. 3, ASME, September 1944, *Journal of Applied Mechanics*, Vol. 11, pp. A168-A175. ISSN: 0021-8936.

[30] MERCHANT, M. Eugene, 1945. Mechanics of the Metal Cutting Process. I. Orthogonal Cutting and a Type 2 Chip. 5, AIP Publishing, *Journal of Applied Physics*, Vol. 16, pp. 267–275. ISSN: 0021-8979.

[31] OXLEY, Professor L.B., 1962. Shear angle solutions in orthogonal machining. 3, Pergamon Press, *International Journal of Machine Tool Design Research*, Vol. 2, pp. 219-229. ISSN: 0020-7357.

[32] DAVIM, João Paulo, 2008. *Machining - Fundamentals and Recent Advances.* 1. London: Springer. ISBN: 9781848002128.

[33] MARKOPOULOS, Angelos P., 2013. *Finite Element Method in Machining Processes.* 1. London: Springer. ISBN: 9781447143291.

[34] MACKERLE, Jaroslav, 2003. Finite element analysis and simulation of machining: an addendum: A bibliography (1996–2002). 1, Elsevier, *International Journal of Machine Tools and Manufacture*, Vol. 43, pp. 103-114. ISSN: 0890-6955.

[35] MACKERLE, Jaroslav, 1998. Finite-element analysis and simulation of machining: a bibliography (1976–1996). 1-3, Elsevier, *Journal of Materials Processing Technology*, Vol. 86, pp. 17-44. ISSN: 0924-0136.

[36] MADHAVAN, Vis, 2015. Simulation in Machining. [book auth.] Andrew Y. C. Nee. *Handbook of Manufacturing.* London: Springer, pp. 1155-1183.

[37] HORA, Pavel, 2015. Finite Elemente Methode (FEM) Prozess-Simulation in der Blechumformung. [book auth.] Klaus SIEGERT. *Blechumformung.* Berlin, Heidelberg: Springer, pp. 257–307.

[38] LSTC, 2006. *LS-DYNA Theory Manual.* Livermore: Livermore Software Technology Corporation. ISBN: 0977854000.

[39] LAKSHMANA RAO, Chebolu, Vijayabaskar NARAYANAMURTHY, and K. R. Y. SIMHA, 2016. *Applied Impact Mechanics.* Chichester: Wiley. ISBN: 9781119241805.

[40] GINGOLD, Robert and MONAGHAN, Joseph, 1977. Smoothed particle hydrodynamics: theory and application to non-spherical stars. 3, Oxford University Press, *Monthly Notices of the Royal Astronomical Society*, Vol. 181, pp. 375–389. ISSN: 0035-8711.

[41] Lucy, L.B., 1977. A numerical approach to the testing of the fission hypothesis. *Astronomical Journal*, Vol. 82, pp. 1013-1024.

[42] LIU, Moubin and Gui Rong LIU, 2010. Smoothed Particle Hydrodynamics (SPH): an Overview and Recent Developments. Springer, *Archives of Computational Methods in Engineering*, Vol. 17, pp. 25-76. ISSN: 1134-3060.

[43] LIU, Gui Rong and Moubin LIU, 2003. *Smoothed Particle Hydrodynamics.* New Jersey: World Scientific. ISBN: 9789812384560.

[44] MONAGHAN, Joseph, 1992. Smoothed Particle Hydrodynamics. *Annual Review of Astronomy and Astrophysics*, Vol. 30, pp. 543-574.

[45] WU, C. T., Y. GUO and W. HU, 2014. An Introduction to the LS-DYNA® Smoothed Particle Galerkin Method for Severe Deformation and Failure Analyses in Solids. Livermore: s.n., *13th International LS-DYNA Users Conference*.

[46] LSTC, 2014. *Smoothed Particle Galerkin Formulation for Simulating Physical Behaviors in Solids Mechanics.* Erfinder: Cheng-Tang WU. United States, Patentschrift US20150112653A1.

[47] WU, Cheng-Tang, Youcai WU, Dandan LYU, Xiaofei PAN and Wei HU, 2019. The momentum-consistent smoothed particle Galerkin (MC-SPG) method for simulating the extreme thread forming in the flow drill screw-driving process. Springer, *Computational Particle Mechanics*, Vol. 7, pp. 177–191. ISSN: 2196-4378.

[48] PAN, X., C.T WU, W. HU, and Y.C WU, 2018. Smoothed Particle Galerkin Method with a Momentum-Consistent Smoothing Algorithm for Coupled Thermal-Structural Analysis. Livermore Software Technology Corporation, *15th International LS-DYNA® Users Conference*.

[49] TAY, A.O., M.G STEVENSON and G. DE VAHL DAVIS, 1974. Using the Finite Element Method to Determine Temperature Distributions in Orthogonal Machining. 1, Sage Journals, *Proceedings of the Institution of Mechanical Engineers*, Vol. 188, pp. 627-638.

[50] CARROLL III, John T. and John S. STRENKOWSKI, 1988. Finite element models of orthogonal cutting with application to single point diamond turning. 12, Elsevier, *International Journal of Mechanical Sciences*, Vol. 30, pp. 899-920. ISSN: 0020-7403.

[51] STRENKOWSKI, John and Kyoung-Jin MOON, 1990. Finite Element Prediction of Chip Geometry and Tool/Workpiece Temperature Distributions in Orthogonal Metal Cutting. 4, ASME, *Journal of Engineering for Industry*, Vol. 112, pp. 313-318. ISSN: 0022-0817.

[52] CHILDS, Thomas H.C. and Katsuhiro MAEKAWA, 1990. Computer-aided simulation and experimental studies of chip flow and tool wear in the turning of low alloy steels by cemented carbide tools. 2, Elsevier, *Wear*, Vol. 139, pp. 235-250. ISSN: 0043-1648.

[53] MARUSICH, T. D. and M. ORTIZ, 1995. Modelling and simulation of high-speed machining. 21, Wiley, *International Journal for Numerical Methods in Engineering*, Vol. 38, pp. 3675-3694. ISSN: 0029-5981.

[54] CERETTI, Elisabetta, Peter FALLBÖHMER, Weitsu WU and Taylan ALTAN, 1996. Application of 2D FEM to chip formation in orthogonal cutting. 1-2, Elsevier, *Journal of Materials Processing Technology*, Vol. 59, pp. 169-180. ISSN: 0924-0136.

[55] CERETTI, Elisabetta, Marco LUCCHI and Taylan ALTAN, 1999. FEM simulation of orthogonal cutting: serrated chip formation. 1-3, Elsevier, *Journal of Materials Processing Technology*, Vol. 95, pp. 17-26. ISSN: 0924-0136.

[56] ÖZEL, Tuğrul and Taylan ALTAN, 2000. Determination of workpiece flow stress and friction at the chip–tool contact for high-speed cutting. 1, Elsevier, *International Journal of Machine Tools & Manufacture*, Vol. 40, pp. 133-152. ISSN: 0890-6955.

[57] ÖZEL, Tuğrul and Taylan ALTAN, 2000. Process simulation using finite element method — prediction of cutting forces, tool stresses and temperatures in high-speed flat end milling. 5, Elsevier, *International Journal of Machine Tools and Manufacture*, Vol. 40, pp. 713-738. ISSN: 0890-6955.

[58] KLOCKE, Fritz, Hans-Willi RAEDT and Stefan HOPPE, 2001. 2D-FEM Simulation of the orthogonal high speed cutting process. 3, Taylor & Francis, *Machining Science and Technology*, Vol. 5, pp. 323-340. ISSN: 1091-0344.

[59] EL-MAGD, Essam and Christoph TREPPMANN, 2000. Mechanical behaviour of AA7075, Ck45N and TiAl6V4 at high strain rates, *Materials week*, Vol. 9.

[60] ÖZEL, Tuğrul, 2006. The influence of friction models on finite element simulations of machining. 5, Elsevier, *International Journal of Machine Tools and Manufacture*, Vol. 46, pp. 518-530. ISSN: 0890-6955.

[61] GRZESIK, Wit, Marian BARTOSZUK and Piotr NIESŁONY, 2005. Finite element modelling of temperature distribution in the cutting zone in turning processes with differently coated tools. Elsevier, *Journal of Materials Processing Technology*, Vols. 164-165, pp. 1204-1211. ISSN: 0924-0136.

[62] KUMAR, Sateesh, Saroj Kumar PATEL and Anshuman DAS, 2018. Experimental and numerical investigations on the temperature distribution in PVD AlTiN coated and uncoated Al2O3/TiCN mixed ceramic cutting tools in hard turning of AISI 52100 steel. 1, *IOP Conference Series: Materials Science and Engineering*, Vol. 338. ISSN: 1757-899X.

[63] KUMAR, Khirod, Manne HAREESH, P. Vamsi KRISHNA and S. Sambhu PRASAD, 2020. FEM Modeling of Coated Tools to Study the Influence of Coating Thickness.

Springer, *Advances in Applied Mechanical Engineering*, pp. 899–911. ISBN: 978-981-15-1200-1.

[64] OLOVSSON, Lars, Larsgunnar NILSSON and Kjell SIMONSSON, 1999. An ALE formulation for the solution of two-dimensional metal cutting problems. 4-5, Elsevier, *Computers & Structures*, Vol. 72, pp. 497-507. ISSN: 0045-7949.

[65] MOVAHHEDY, M. R., M.S. GADALA and Y. ALTINTAS, 2000. Simulation of chip formation in orthogonal metal cutting process: an ALE finite element approach. 1, *Machining Science and Technology*, Taylor & Francis, Vol. 4. ISSN: 1091-0344.

[66] MOVAHHEDY, M. R., Y. ALTINTAS and M.S. GADALA, 2002. Numerical Analysis of Metal Cutting With Chamfered and Blunt Tools. 2, ASME Journals, *Journal of Manufacturing Science and Engineering*, Vol. 124. ISSN: 1087-1357.

[67] MADHAVAN, Vis and Amir ADIBI-SEDEH, 2005. Understanding of finite element analysis results under the framework of Oxley's machining model. 3, Taylor & Francis, *Machining Science and Technology*, Vol. 9, pp. 345-368. ISSN: 1091-0344.

[68] NASR, Mohamed, Mohamed A.A. ELBESTAWI and Eugene NG, 2008. A modified time-efficient FE approach for predicting machining-induced residual stresses. 4, Elsevier, *Finite Elements in Analysis and Design*, Vol. 44, pp. 149-161. ISSN: 0168-874X.

[69] ARRAZOLA, Pedro J. and Tugrul ÖZEL, 2010. Investigations on the effects of friction modeling in finite element simulation of machining, *International Journal of Mechanical Sciences*, Vol. 52, pp. 31-42. ISSN: 1879-2162.

[70] KRAJINOVIĆ, Ivan, Werner DAVES, Michael TKADLETZ, Tamara TEPPERNEGG, Thomas KLÜNSNER, Nina SCHALK, Christian MITTERER, Christian TRITREMMEL, Werner ECKER and Christoph CZETTL, 2016. Finite element study of the influence of hard coatings on hard metal tool loading during milling, *Surface and Coatings Technology*, Vol. 304, pp. 134-141. ISSN: 0257-8972.

[71] LIMIDO, J., C. ESPINOSA, M. SALAUN and J. L. LACOME, 2006. A new approach of high speed cutting modelling: SPH method, *Journal de Physique IV (Proceedings)*, Vol. 134, pp. 1195–1200. ISSN: 1764-7177.

[72] LIMIDO, Jérôme, Christine ESPINOSA, Michel SALAUN and Jean Luc LACOME, 2007. SPH method applied to high speed cutting modelling, *International Journal of Mechanical Sciences*, Vol. 49, pp. 898-908. ISSN: 0020-7403.

[73] OLLEAK, Alaa and Hassan A. EL-HOFY, 2015. SPH Modelling of Cutting Forces while Turning of Ti6Al4V Alloy, 10th European LS-DYNA Conference, Würzburg: DYNAmore GmbH.

[74] OLLEAK, Alaa, Mohamed NASR and Hassan A EL-HOFY, 2015. The Influence of Johnson-Cook Parameters on SPH Modelling of Orthogonal Cutting of AISI 316L, Wurzburg: DYNAmore GmbH.

[75] HEISEL, Uwe, Wiliam ZALOGA, Dmitrii KRIVORUCHKO, Michael STORCHAK and Liubov GOLOBORODKO, 2013. Modelling of orthogonal cutting processes with the method of smoothed particle hydrodynamics, *Production Engineering*, Vol. 7, pp. 639–645. ISSN: 1863-7353.

[76] LAMPROPOULOS, Adam, Angelos MARKOPOULOS and Dimitrios MANOLAKOS, 2019. Modeling of Ti6Al4V Alloy Orthogonal Cutting with Smooth Particle Hydrodynamics: A Parametric Analysis on Formulation and Particle Density, *Metals*, Vol. 9, p. 388. ISSN: 2075-4701.

[77] BOLDYREV, I. S., 2019. SPG Simulation of Free Orthogonal Cutting for Cutting Forces Prediction, *Proceedings of the 4th International Conference on Industrial Engineering*, pp. 1695–1700. ISBN: 978-3-319-95629-9.

[78] HUANG, Li, Youcai Wu, Garret HUFF, Shiyao HUANG, Andrey ILINICH, Amanda FREIS and George LUCKEY, 2018. Simulation of Self-Piercing Rivet Insertion Using Smoothed Particle Galerkin Method, 15th International LS-DYNA® Users Conference, Detroit.

[79] WU, C. T., Tinh Quoc BUI, Youcai WU, Tzui-Liang LUO and Morris WANG, 2017. Numerical and experimental validation of a particle Galerkin method for metal grinding simulation, *Computational Mechanics*, Vol. 61, pp. 365–383. ISSN: 1432-0924.

[80] WU, Youcai, C. T. WU and Wei HU, 2018. Parametric and Convergence Studies of the Smoothed Particle Galerkin (SPG) Method in Semi-brittle and Ductile Material Failure Analyses, 15th International LS-DYNA Users Conference, Detroit.

[81] CASELLAS, Daniel, P. JONSÉN, Giselle Ramírez SANDOVAL, Andreas SVANBERG, Ricardo Hernandez ROSSI, Stefan MARTH, Mats OLDENBURG and Hans-Åke HÄGGBLAD, 2019. A novel method for modelling of cold cutting of microstructurally tailored hot formed components, *7th CHS2 Conference: Hot Sheet Metal Forming of High-Performance Steel*, Luleå (Sweden).

[82] LIU, Yang, Yihao ZHENG, Annie Dian-Ru LI, Yao LIU and Luis E. SAVASTANO, 2019. Cutting of blood clots – Experiment and smooth particle Galerkin modelling, *CIRP Annals*, Vol. 68, pp. 97-100. ISSN: 0007-8506.

[83] PAN, Xiaofei, C. T. WU, Wei HU, and Youcai WU, 2019. A momentum-consistent stabilization algorithm for Lagrangian particle methods in the thermo-mechanical friction drilling analysis, *Computational Mechanics*, Vol. 64, pp. 625–644. ISSN: 1432-0924.

[84] NIESŁONY, Piotr, Wit GRZESIK, R. CHUDY and W. HABRAT, 2015. Meshing strategies in FEM simulation of the machining process, *Archives of Civil and Mechanical Engineering*, Vol. 15, pp. 62-70. ISSN: 1644-9665.

[85] AMBATI, Ravindra, and Huang YUAN, 2010. FEM mesh-dependence in cutting process simulations, *The International Journal of Advanced Manufacturing Technology*, Vol. 53, pp. 313–323. ISSN: 1433-3015.

[86] JASPERS, S. P. F. C., and Johan Hubertus DAUTZENBERG, 2002. Material behaviour in metal cutting: strains, strain rates and temperatures in chip formation, *Journal of Materials Processing Technology*, Vol. 121, pp. 123-135. ISSN: 0924-0136.

[87] Third Wave Systems, 2020. *AdvantEdge User's Manual.*

[88] LSTC, 2020. *LS-DYNA Keyword User´s Manual, Vol. II.*

[89] JOHNSON, Gordon R., and William H. COOK, 1983. A Constitutive model and data for metals subjected to large strains, high strain rates and high temperatures, *Proceedings of the Seventh International Symposium on Ballistics*, pp. 541-547.

[90] JOHNSON, Gordon R., and William H. COOK, 1985. Fracture characteristics of three metals subjected to various strains, strain rates, temperatures and pressures, *Engineering Fracture Mechanics*, Vol. 21, pp. 31-48. ISSN: 0013-7944.

[91] PERVAIZ, Salman, Saqib ANWAR, Sathish KANNAN and Ali ALMARFADI, 2018. Exploring the influence of constitutive models and associated parameters for the orthogonal machining of Ti6Al4V, *IOP Conference Series: Materials Science and Engineering*, Vol. 338. ISSN: 1757-899X.

[92] TAYLOR, L. M. and D. P. FLANAGAN, 1987. *PRONTO 2D: A Two-Dimensional Transient Solid Dynamics Program,* Sandia National Laboratories.

[93] LSTC, 2020. *LS-DYNA Keywords User´s Manual*, Vol. 1.

[94] ZOREV, N. N., 1963. Interrelationship between shear processes occurring along tool face and on shear plane in metal cutting, *Proceedings of the International Research in Production Engineering Conference*, New York: ASME, pp. 42-49.

[95] USUI, Eji, Katsuhiro MAEKAWA, and Takahiro SHIRAKASHI, 1981. Simulation analysis of built-up edge formation in machining low carbon steels, *Bulletin of the Japan Society of Precision Engineering*, Vol. 15, pp. 237-242. ISSN: 0582-4206.

[96] IWATA, K., K. OSAKADA, and Y. TERASAKA, 1984. Process Modeling of Orthogonal Cutting by the Rigid-Plastic Finite Element Method, *Journal of Engineering Materials and Technology*, Vol. 106, pp. 132-138. ISSN: 1528-8889.

[97] SEKHON, G. S. and J. L. CHENOT, 1993. Numerical simulation of continuous chip formation during non-steady orthogonal cutting, *Engineering Computations*, Vol. 10, pp. 31-48. ISSN: 0264-4401.

[98] YANG, Xiaoping and C. Richard LIU, 2002. A new stress-based model of friction behavior in machining and its significant impact on residual stresses computed by finite element method, *International Journal of Mechanical Sciences*, Vol. 44, pp. 703-723. ISSN: 0020-7403.

[99] MALAKIZADI, Amir, Keyvan HOSSEINKHANI, Emilia MARIANO, E. NG, Antonio DEL PRETE, and Lars NYBORG, 2016. Influence of friction models on FE

simulation results of orthogonal cutting process, *The International Journal of Advanced Manufacturing Technology*, Vol. 88, pp. 3217–3232. ISSN: 1433-3015.

[100] PARK, K. C. and Carlos FELIPPA, 1983. [ed.] T. BELYTSCHKO and T. J. R. HUGHES. Partitioned Analysis of Coupled Systems, *Computational Methods for Transient Analysis*, Vol. 1, pp. 157-219. ISBN: 978-0444864796.

[101] LEMONDS, Jeffery and Alan NEEDLEMAN, 1986. Finite element analyses of shear localization in rate and temperature dependent solids, *Mechanics of Materials*, Vol. 5, pp. 339-361. ISSN: 0167-6636.

[102] KLOEPPEL, Thomas, 2020. New Implementation of a Weakly Thermal-Mechanical Coupling Scheme in LS-DYNA, *16th International LS-DYNA® Users Conference*, Stuttgart: DYNAmore GmbH.

[103] KUS, Abdil, Yahya ISIK, M. CAKIR, Salih COŞKUN, and Kadir ÖZDEMIR, 2015. Thermocouple and Infrared Sensor-Based Measurement of Temperature Distribution in Metal Cutting, *Sensors*, Vol. 15, pp. 1274–1291. ISSN: 1424-8220.

[104] KUMAR, Ramanuj, Amlana PANDA, Ashok Kumar SAHOO, and SINGHAL, Deepak, 2021. Analysis of Heat Transfer Coefficient in Turning Process, *Proceedings of International Conference on Thermofluids*, pp. 655-663. ISBN: 978-981-15-7830-4.

[105] BRITO, Rogério Fernandes, Solidônio Rodrigues CARVALHO, and S. M.M. LIMA E SILVA, 2015. Experimental investigation of thermal aspects in a cutting tool using COMSOL and inverse problem, *Applied Thermal Engineering*, Vol. 86, pp. 60-68. ISSN: 1359-4311.

[106] NG, Eugene, David Keith ASPINWALL, D. BRAZIL, and John M. MONAGHAN, 1999. Modelling of temperature and forces when orthogonally machining hardened steel, *International Journal of Machine Tools and Manufacture*, Vol. 39, pp. 885-903. ISSN: 0890-6955.

[107] NAZMA SULTANA, Mst, Nikhil RANJAN DHAR, and Prianka BINTE ZAMAN, 2019. A review on different cooling/lubrication techniques in metal cutting, *American Journal of Mechanics and Applications*, Vol. 7, pp. 71-87. ISSN: 2376-6115.

[108] VERSTEEG, H. K. and W. MALALASEKER, 2007. *An Introduction to Computational Fluid Dynamics: The Finite Volume Method*, Pearson Education. ISBN: 978-0131274983.

[109] MOUKALLED, F., L. MANGANI, and M. DARWISH, 2016. *The Finite Volume Method in Computational Fluid Dynamics - An Advanced Introduction with OpenFOAM® and Matlab*, Cham: Springer. ISBN: 978-3-319-16873-9.

[110] ARIS, Rutherford, 1989. *Vectors, Tensors and the Basic Equations of Fluid Mechanics*, New York: Dover Publication Inc. ISBN: 9780486661100.

[111] TENNEKES, Henk and John L. LUMLE, 2018. *A First Course in Turbulence*, The MIT Press. ISBN: 9780262536301.

[112] SPALART, Philippe R., 2000. Strategies for turbulence modelling and simulations, *International Journal of Heat and Fluid Flow*, Vol. 21, pp. 252-263. ISSN: 0142-727X.

[113] SHIH, Tsan-Hsing, William W. LIOU, Aamir SHABBIR, Zhigang YANG, and Jiang ZHU, 1995. A new k-ϵ eddy viscosity model for high Reynolds number turbulent flows, *Computers & Fluids*, Vol. 24, pp. 227–238. ISSN: 0045-7930.

[114] WILCOX, David C., 1998. Reassessment of the scale-determining equation for advanced turbulence models, *AIAA Journal*, Vol. 26, pp. 1299–1310. ISSN: 1533-385X.

[115] MENTER, Florian, 1994. Two-equation eddy-viscosity turbulence models for engineering applications, *AIAA Journal*, Vol. 32, pp. 1598–1605. ISSN: 1533-385X.

[116] PERELMAN, T. L., 1961. On conjugated problems of heat transfer, *International Journal of Heat and Mass Transfer*, Vol. 3, pp. 293-303. ISSN: 0017-9310.

[117] Siemens, 2020. *Simcenter STAR-CCM+ Documentation.*

[118] PERVAIZ, Salman, Ibrahim DEIAB, Essam WAHBA, Amir RASHID, and Cornel Mihai NICOLESCU, 2015. A novel numerical modeling approach to determine the temperature distribution in the cutting tool using conjugate heat transfer (CHT) analysis, *The International Journal of Advanced Manufacturing Technology*, Vol. 80, pp. 1039-1047. ISSN: 0268-3768.

[119] PERVAIZ, Salman, Ibrahim DEIAB, Essam WAHBA, Amir RASHID, and Mihai NICOLESCU, 2018. A numerical and experimental study to investigate convective heat transfer and associated cutting temperature distribution in single point turning, *The International Journal of Advanced Manufacturing Technology*, Vol. 94, pp. 897-910. ISSN: 0268-3768.

[120] HELMIG, Thorsten, Bingxiao PENG, Claas EHRENPREIS, Thorsten AUGSPURGER, Yona FREKERS, Reinhold KNEER, and Thomas BERGS, 2019. A Coupling Approach Combining CFD and FEM Methods to Predict Cutting Fluid Effects on the Tool Temperature in Cutting Processes, *Journal of Manufacturing Science and Engineering*, Vol. 141. ISSN: 1087-1357.

[121] LIU, Hui, Thorsten HELMIG, Thorsten AUGSPURGER, Nhat NGUYEN, Reinhold KNEER, and Thomas BERGS, 2021. Modeling the cooling effect of the cutting fluid in machining using a coupled Fe-Cfd Simulation, *MM Science Journal*, Vol. 2021, pp. 4576-4583. ISSN: 1803-1269.

[122] SPIEGEL, Martin, Thomas REDEL, Y. Jonathan ZHANG, Tobias STRUFFERT, Joachim HORNEGGER, and Robert GROSSMAN, 2011. Tetrahedral vs. polyhedral mesh size evaluation on flow velocity and wall shear stress for cerebral hemodynamic simulation, *Computer Methods in Biomechanics and Biomedical Engineering*, Vol. 14, pp. 9–22. ISSN: 1476-8259.

[123] SOSNOWSKI, Marcin, Jaroslaw KRZYWANSKI, and Renata GNATOWSKA, 2017. Polyhedral meshing as an innovative approach to computational domain discretization

of a cyclone in a fluidized bed CLC unit, *E3S Web of Conferences*, Vol. 14, p. 01027. ISSN: 2267-1242.

[124] SU, Junwei, Zhaolin GU, Chungang CHEN, and Xiao Yun XU, 2015. A two-layer mesh method for discrete element simulation of gas-particle systems with arbitrarily polyhedral mesh, *International Journal for Numerical Methods in Engineering*, Vol. 103, pp. 759-780. ISSN: 0029-5981.

[125] BRECHER, Christian, 2011. *Integrative Produktionstechnik für Hochlohnländer*, Springer Berlin, Heidelberg. ISBN: 978-3-642-20693-1.

[126] ALTINTAS, Yusuf, 2000. Modeling Approaches and Software for Predicting the Performance of Milling Operations at MAL-UBC, *Machining Science and Technology*, Vol. 4, pp. 445-478. ISSN: 1532-2483.

[127] HEISEL, Uwe, Fritz KLOCKE, Eckart UHLMANN, and Günter SPUR, 2014. *Handbuch Spanen*, München: Carl Hanser Verlag. ISBN: 978-3-446-42826-3.

[128] ARMAREGO, Edwin J. A. and Robert H. BROWN, 1969. *The Machining of Metals*, Prentice Hall, p. 305. Vol. 14. ISBN: 9780135422090.

[129] BUDAK, Erhan, Yusuf ALTINTAS, and E. J. A. ARMAREGO, 1996. Prediction of Milling Force Coefficients From Orthogonal Cutting Data, *Journal of Manufacturing Science and Engineering*, Vol. 118, pp. 216-224. ISSN: 1087-1357.

[130] Manufacturing Automation Laboratories Inc., 2013. *CUTPRO: Fundamentals of Machining – Start to Finish Guide.*

[131] BÜRGEL, Ralf, Hans Jürgen MAIER, and Thomas NIENDORF, 2011**.** *Handbuch Hochtemperatur-Werkstofftechnik*, 4th edition, Vieweg+Teubner Verlag Wiesbaden. ISBN: 978-3-8348-9907-1.

[132] KAISER, Timotheus, 2014. *Entwicklung eines Nickel-reduzierten Austenits als Werkstoff im thermisch hoch beanspruchten Abgasturbolader.* [Dissertation], TU Clausthal, Clausthal-Zellerfeld: Universitätsbibliothek Clausthal. ISBN: 978-394-391-798-7.

[133] GROHE, Heinz and Gerald RUSS, 2015. *Otto- und Dieselmotoren: Arbeitsweise, Aufbau und Berechnung von Zweitakt- und Viertakt-Verbrennungsmotoren*, Vogel Buchverlag, Würzburg. Vol. 16. ISBN: 978-3-8343-3351-3.

[134] SCHARF, Johannes, Taner GÖCMEZ, Michael WITTLER, Stefan PISCHINGER, Richard AYMANNS, and Christoph STEFFENS, 2009. Integration von Aufladesystem- und Motorentwicklung, *MTZ - Motortechnische Zeitschrift*, Vol. 70, pp. 908–915. ISSN: 0024-8525.

[135] DEUTSCHES INSTITUT FÜR NORMUNG e.V., 2003. *ISO 10295:2003-01, Hitzebeständiger Stahlguss*, Berlin: Beuth, 00.01.2003.

[136] HESTERBERG, Stefan, 2006. *Trockenbearbeitung nichtrostender Stähle - Prozessgestaltung für das Drehen und Bohren mit Wendeschneidplatten.*

[Dissertation], Technische Universität Dortmund, Essen: Vulkan Verlag. ISBN: 978-3-8027-8735-5.

[137] HORNBOGEN, Erhard, Hans WARLIMONT, 2006. *Metalle: Struktur und Eigenschaften der Metalle und Legierungen*, 5th edition, Springer Berlin, Heidelberg. ISBN: 978-3540340102.

[138] CORDES, Susanne Eva, 2012. *Tribomechanik beschichteter Zerspanwerkzeuge.* [Dissertation], Wissenschaftsverlag des Instituts für Industriekommunikation und Fachmedien an der RWTH Aachen, Aachen: Apprimus Verlag. ISBN: 978-3-86359-122-9.

[139] DEUTSCHES INSTITUT FÜR NORMUNG e.V., 2014. *ISO 513:2014-05, Klassifizierung und Anwendung von harten Schneidstoffen für die Metallzerspanung mit geometrisch bestimmten Schneiden - Bezeichnung der Hauptgruppen und Anwendungsgruppen*, Berlin: Beuth, 00.05.2014.

[140] RUPPI, Sakari, 2001. Advances in chemically vapor deposited wear resistant coatings, *Journal de Physique IV*, Vol. 11, pp. 847-859.

[141] PALDEY, Sohini and Seetharama C. DEEVI, 2003. Single layer and multilayer wear resistant coatings of (Ti,Al)N: a review, *Materials Science and Engineering: A*, Vol. 342, pp. 58-79. ISSN: 0921-5093.

[142] RUPPI, Sakari and Rachid M'SAOUBI, 2009. Wear and thermal behaviour of CVD α-Al2O3 and MTCVD Ti(C,N) coatings during machining, *CIRP Annals*, Vol. 58, pp. 57-60. ISSN: 0007-8506.

[143] GRZESIK, Wit, 1999. Experimental investigation of the cutting temperature when turning with coated indexable inserts, *International Journal of Machine Tools and Manufacture*, Vol. 39, pp. 355-369. ISSN: 0890-6955.

[144] HAUERT, Roland and Jörg PATSCHEIDER, 2000. From Alloying to Nanocomposites—Improved Performance of Hard Coatings, *Advanced Engineering Materials*, Vol. 2, pp. 247-259. ISSN: 1438-1656.

[145] ZOCH, Hans-Werner and Günter SPUR, 2015. *Handbuch Wärmebehandeln und Beschichten*, Carl Hanser Verlag, München. ISBN: 978-3-446-42779-2.

[146] Boost, H.-P., A. Popp and H. Engström, 2015. *Herausforderungen bei der Hochleistungs-Drehbearbeitung von Stahl und Guss annehmen*, Nürtingen: VDI-Fachtagung Stahl- und Gusszerspanung.

[147] KONÉ, Fousseny, Christophe CZARNOTA, Badis HADDAG, and Mohammed NOUARI, 2011. Finite element modelling of the thermo-mechanical behavior of coatings under extreme contact loading in dry machining, *Surface and Coatings Technology*, Vol. 205, pp. 3559-3566. ISSN: 0257-8972.

[148] SARGADE, Vikas G., Soumya GANGOPADHYAY, Soumitra PAUL, and Ajit K. CHATTOPADHYAY, 2011. Effect of Coating Thickness on the Characteristics and Dry Machining Performance of TiN Film Deposited on Cemented Carbide Inserts

Using CFUBMS, *Materials and Manufacturing Processes*, Vol. 26, pp. 1028-1033. ISSN: 1042-6914.

[149] KUMAR, Ch Sateesh and Saroj Kumar PATEL, 2017. Experimental and numerical investigations on the effect of varying AlTiN coating thickness on hard machining performance of Al2O3-TiCN mixed ceramic inserts, *Surface and Coatings Technology*, Vol. 309, pp. 266-281. ISSN: 0257-8972.

[150] KUMAR, Ch Sateesh and Saroj Kumar PATEL, 2018. Investigations on the effect of thickness and structure of AlCr and AlTi based nitride coatings during hard machining process, *Journal of Manufacturing Processes*, Vol. 31, pp. 336-347. ISSN: 1526-6125.

[151] Werkzeug Technik, 2019. *Werkzeug Technik: Technologie, System, Logistik*, Bolougne: Societe Francaise d'editions techniques. ISSN: 0997-6981.

[152] Kistler Instrumente GmbH, 2003. Betriebsanleitung, Quarzkristall, 3-Komponenten-Werkzeughalter-Dynamometer Typ 9121.

[153] PAUCKSCH, Eberhard, Sven HOLSTEN, Marco LINß, and Franz TIKAL, 2008. *Cutting Technology, S94*, Vieweg & Teubner, Vol. 12. ISBN: 978-3-8348-0279-8.

[154] How Minitab handles center points in a 2-level factorial design - Minitab, [05.09.2024]. [Online]. Available at: https://support.minitab.com/en-us/minitab/help-and-how-to/statistical-modeling/doe/supporting-topics/factorial-and-screening-designs/how-minitab-handles-center-points-in-a-2-level-factorial-design/

[155] JIN, Xiaoliang and Yusuf ALTINTAS, 2012. Prediction of micro-milling forces with finite element method, *Journal of Materials Processing Technology*, Vol. 212, pp. 542-552. ISSN: 0924-0136.

[156] ZHUANG, Kejia, Jinqiang GAO, Tao YE, and Xing DAI, 2022. Effect of cutting edge radius on cutting force and surface roughness in machining of Ti-6Al-4V, *Procedia CIRP*, Vol. 108, pp. 571-576. ISSN: 2212-8271.

[157] JASAK, Hrvoje, 1996. *Error Analysis and Estimation for the Finite Volume Method With Applications to Fluid Flows.* [Dissertation], London: Department of Mechanical Engineering, Imperial College of Science, Technology and Medicine.

[158] LAUNDER, Brian E. and Dudley Brian SPALDING, 1974. The numerical computation of turbulent flows, *Computer Methods in Applied Mechanics and Engineering*, Vol. 3, pp. 269-289. ISSN: 0045-7825.

[159] GOSMAN, A. D. and F. J. K. IDERIAH, 1983. *TEACH-2E, a General Computer Program for Two-dimensional, Turbulent, Recirculating Flows*, Department of Mechanical Engineering, Imperial College.

[160] TAHERKHANI, Ali Reza, 2015. *Computational fluid dynamics based optimisation of emergency response vehicles.* [Dissertation], Leeds: School of Mechanical Engineering, University of Leeds.

[161] SPRING, Sebastian, Diane LAUFFER, Bernhard WEIGAND, and Matthias HASE, 2010. Experimental and Numerical Investigation of Impingement Cooling in a Combustor Liner Heat Shield, *Journal of Turbomachinery*, Vol. 132. ISSN: 528-8900.

[162] WANG, Peng, Yu LI, Zhengping ZOU, and Songhe SONG, 2013. Influence of turbulence model parameter settings on conjugate heat transfer simulation, *Heat and Mass Transfer*, Vol. 50, pp. 521-532. ISSN: 0947-7411.

[163] RANA, Pulkit, Waldemar ZIELASKO, Thomas SCHUSTER, and Wolfgang HINTZE, 2019. Orthogonal Turning Simulations for Casted Steel Alloy Using Mesh Free Methods, *Production at the Leading Edge of Technology*, Springer Vieweg, Berlin, Heidelberg, pp. 337-346. ISBN: 978-3-662-60416-8.

[164] RANA, Pulkit, Wolfgang HINTZE, Thomas SCHALL, and Wilfrid POLLEY, 2023. Implementation of MC-SPG Particle Method in the Simulation of Orthogonal Turning Process, *Production at the Leading Edge of Technology* (WGP 2022), Springer, Cham, pp. 355-365. ISBN: 978-3-031-18317-1.

[165] UHLMANN, Eckart, Enrico BARTH, Tobias SEIFARTH, Maximilian HÖCHEL, Jörg KUHNERT and Almut EISENTRÄGER, 2021. Simulation of metal cutting with cutting fluid using the Finite-Pointset-Method, *Procedia CIRP*, Vol. 101, pp. 98-101. ISSN: 2212-8271.

A Appendix

Table A 1: Experimental machines

Machine	**Gildemeister CTX310**	**Heller MC12**
Illustration		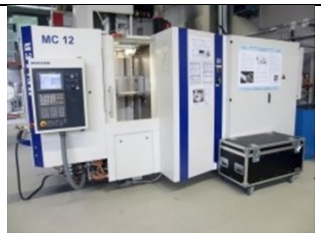
Type	2-axis Universal Lathe Machine	4-axis (Transl. 3, Rot. 1) Horizontal Machine
Control Unit	Heidenhain: CNC Pilot 4290	Siemens: FANUC 18iMB
Speed (n) in min^{-1}	20-6000	45-12000
Power (P) in kW	12	26
Torque (M_d) in Nm	153 (1250 Max.)	1800 Max.
Travel X/Z in mm	213/450	560/510

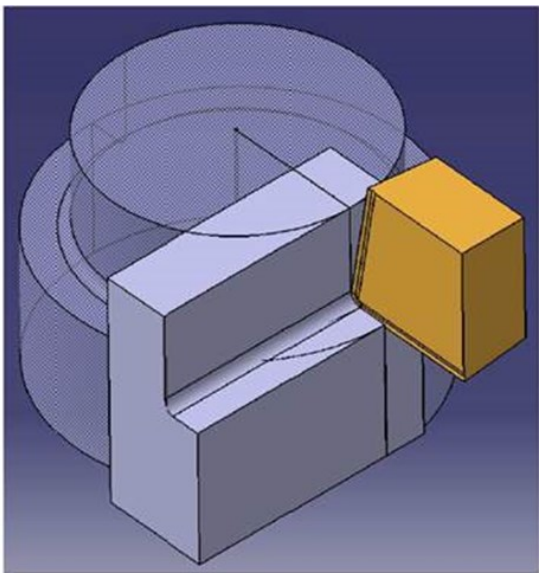

Figure A 1: Process kinematics comparison between longitudinal and linear longitudinal turning process

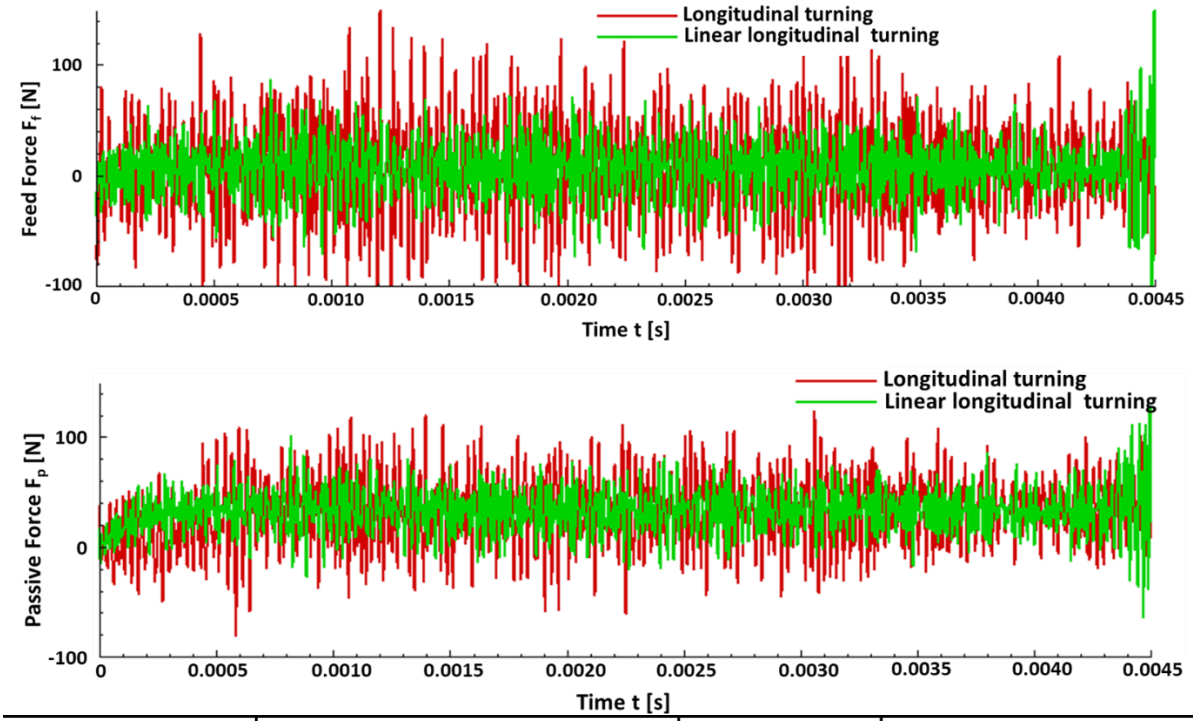

Workpiece material: 1.4837D Cooling: None	Cutting depth : $a_p = 0.3$mm Feed-rate : $f = 0.25$mm Cutting speed : $v_c = 90$m/min		α_o	γ_o	ε_r	κ_r	Tool material: ISO-K10 Geometry: DCGT11T304-F Cutting edge radius: 12µm Corner radius: 0.4mm Coating: AlTiN Coating thickness: 3µm
Longitudinal turning Simulation method: FEM			7°	15°	55°	93°	

Figure A 2: Comparison of feed and passive forces during longitudinal turning and linear longitudinal turning

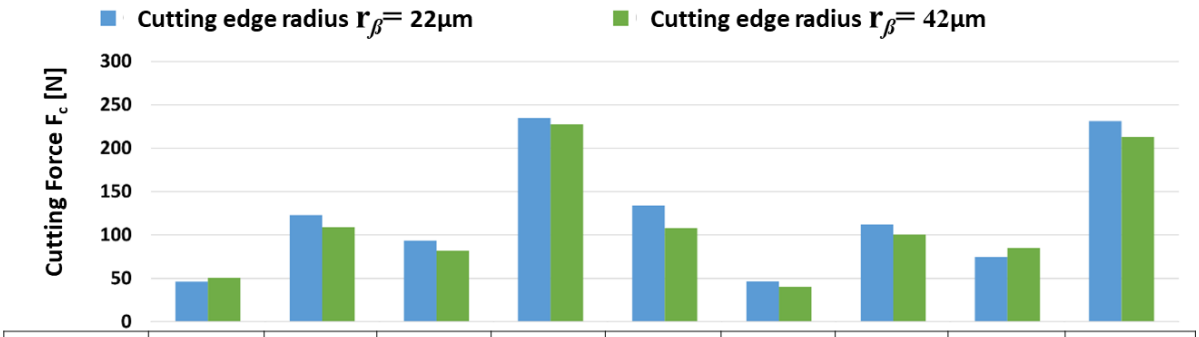

v_c (m/min)	90	90	90	90	130	170	170	170	170
f (mm)	0.1	0.1	0.25	0.25	0.175	0.1	0.1	0.25	0.25
a_p (mm)	0.1	0.3	0.1	0.3	0.2	0.1	0.3	0.1	0.3

Workpiece material: 1.4837D Cooling: None		α_o	γ_o	ε_r	κ_r	Tool material: ISO-K10 Geometry: DCGT11T304-F Cutting edge radius: var. Corner radius: 0.4mm Coating: AlTiN Coating thickness: 2µm
Longitudinal turning		7°	15°	55°	93°	

Figure A 3: Comparison of measured feed and passive forces for cutting edge radius of 22µm and 42µm

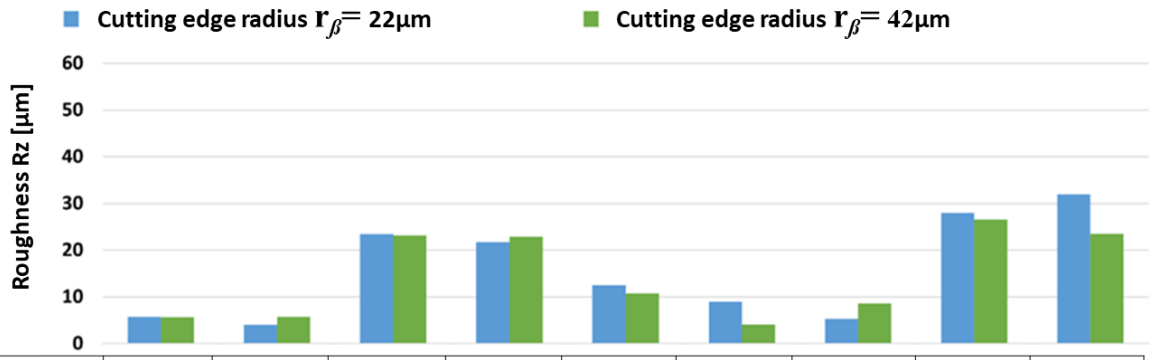

v_c (m/min)	90	90	90	90	130	170	170	170	170
f (mm)	0.1	0.1	0.25	0.25	0.175	0.1	0.1	0.25	0.25
a_p (mm)	0.1	0.3	0.1	0.3	0.2	0.1	0.3	0.1	0.3

Workpiece material: 1.4837D
Cooling: None
Longitudinal turning

α_o	γ_o	ε_r	κ_r
7°	15°	55°	93°

Tool material: ISO-K10
Geometry: DCGT11T304-F
Cutting edge radius: var.
Corner radius: 0.4mm
Coating: AlTiN
Coating thickness: 2µm

Figure A 4: Comparison of measured averaged surface roughness for cutting edge radius of 22µm and 42µm

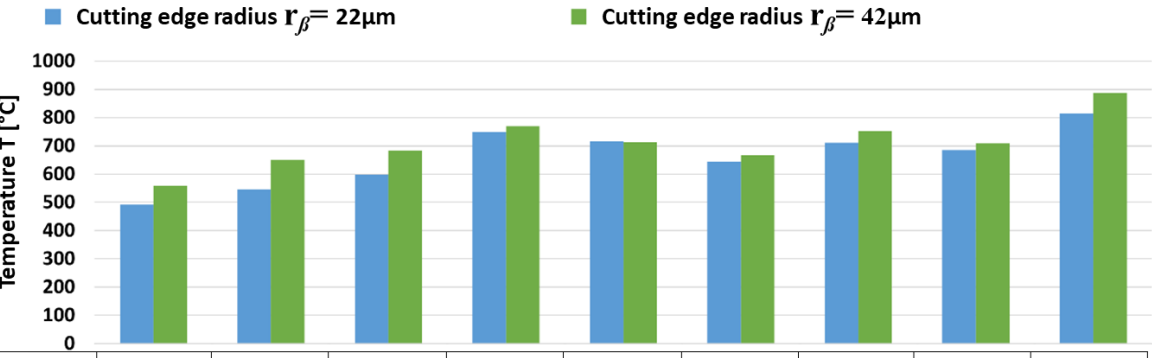

v_c (m/min)	90	90	90	90	130	170	170	170	170
f (mm)	0.1	0.1	0.25	0.25	0.175	0.1	0.1	0.25	0.25
a_p (mm)	0.1	0.3	0.1	0.3	0.2	0.1	0.3	0.1	0.3

Workpiece material: 1.4837D
Cooling: None
Internal turning

α_o	γ_o	ε_r	κ_r
7°	15°	55°	93°

Tool material: ISO-K10
Geometry: DCGT11T304-F
Cutting edge radius: var.
Corner radius: 0.4mm
Coating: AlTiN
Coating thickness: 2µm

Figure A 5: Comparison of measured temperature for cutting edge radius of 22µm and 42µm

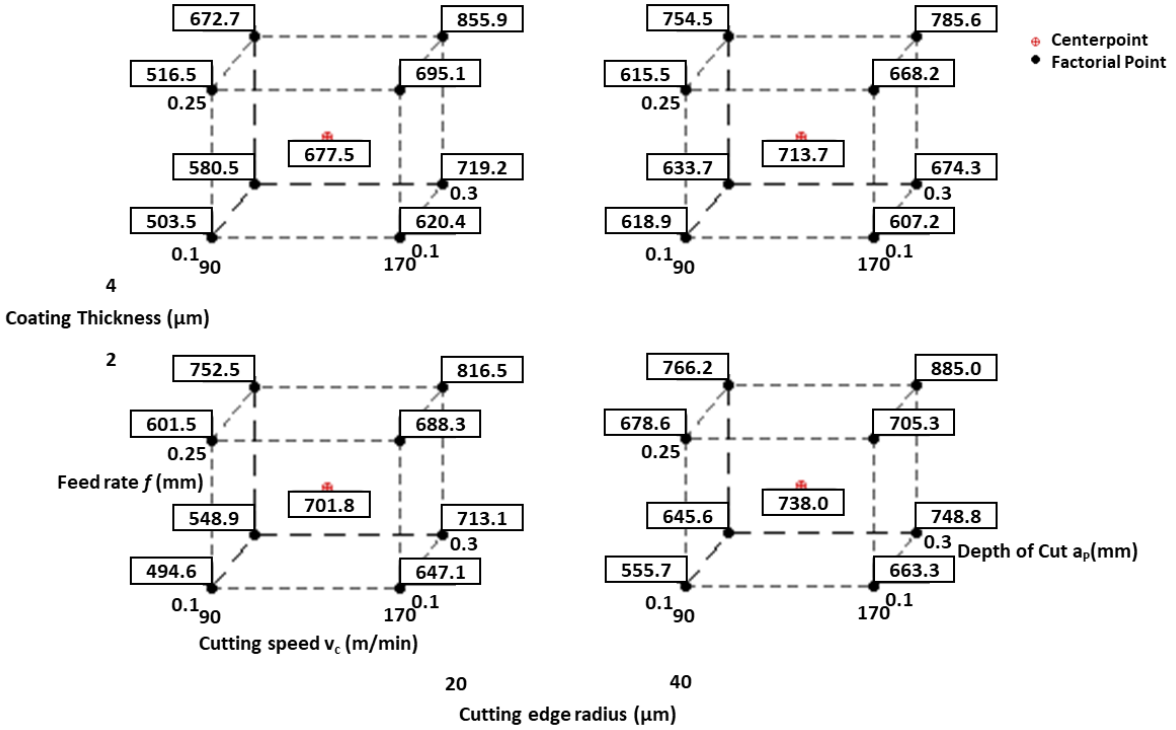

Workpiece material: 1.4837D Cooling: None Internal turning	α_o / 7°	γ_o / 15°	ε_r / 55°	κ_r / 93°	Tool material: ISO-K10 Geometry: DCGT11T304-F Cutting edge radius: var. Corner radius: 0.4mm Coating: AlTiN Coating thickness: var.

Figure A 6: Measured temperature results for each parameter set in second DoE

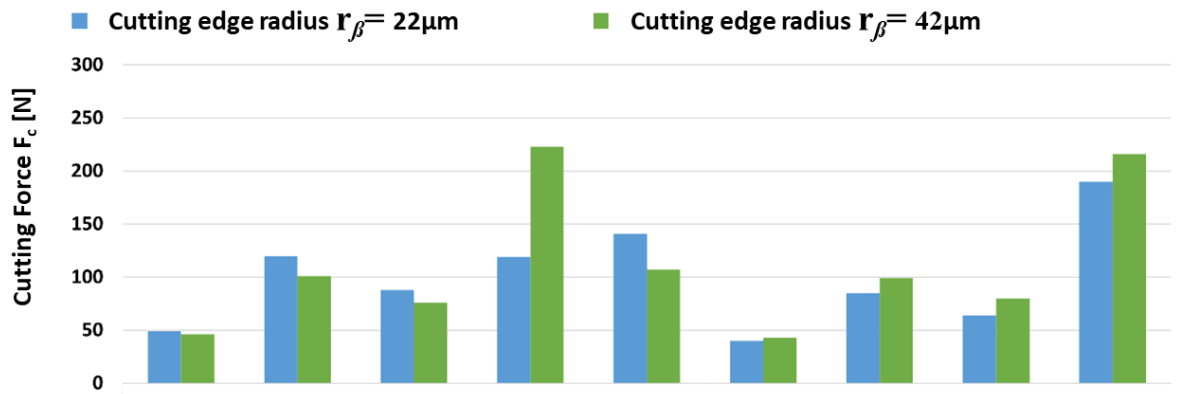

v_c (m/min)	90	90	90	90	130	170	170	170	170
f (mm)	0.1	0.1	0.25	0.25	0.175	0.1	0.1	0.25	0.25
a_p (mm)	0.1	0.3	0.1	0.3	0.2	0.1	0.3	0.1	0.3

Workpiece material: 1.4837D Cooling: None Longitudinal turning Simulation method: FEM	α_o / 7°	γ_o / 15°	ε_r / 55°	κ_r / 93°	Tool material: ISO-K10 Geometry: DCGT11T304-F Cutting edge radius: var. Corner radius: 0.4mm Coating: AlTiN Coating thickness: 2µm

Figure A 7: Comparison of simulated cutting forces for cutting edge radius of 22µm and 42µm

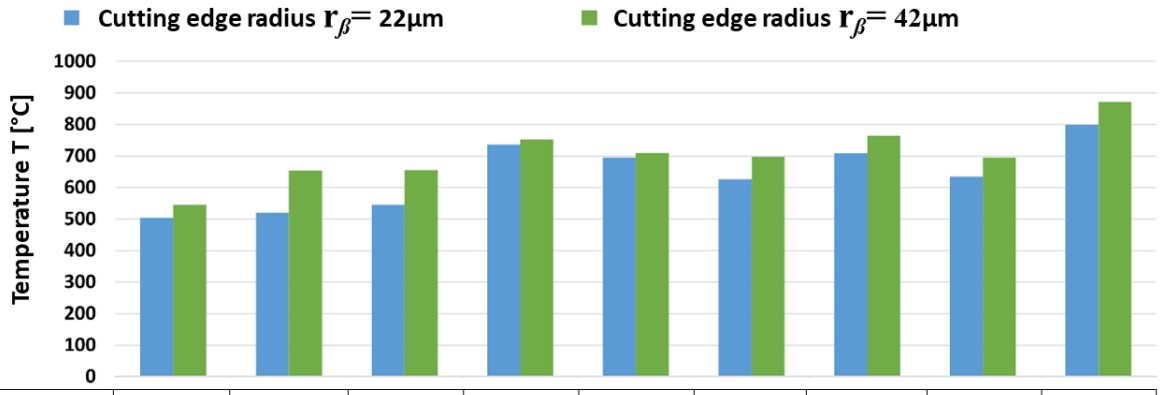

v_c (m/min)	90	90	90	90	130	170	170	170	170
f (mm)	0.1	0.1	0.25	0.25	0.175	0.1	0.1	0.25	0.25
a_p (mm)	0.1	0.3	0.1	0.3	0.2	0.1	0.3	0.1	0.3

Workpiece material: 1.4837D Cooling: None	α_o	γ_o	ε_r	κ_r	Tool material: ISO-K10 Geometry: DCGT11T304-F Cutting edge radius: var. Corner radius: 0.4mm Coating: AlTiN Coating thickness: 2µm
Internal turning Simulation method: FEM	7°	15°	55°	93°	

Figure A 8: Comparison of simulated temperature for cutting edge radius of 22µm and 42µm

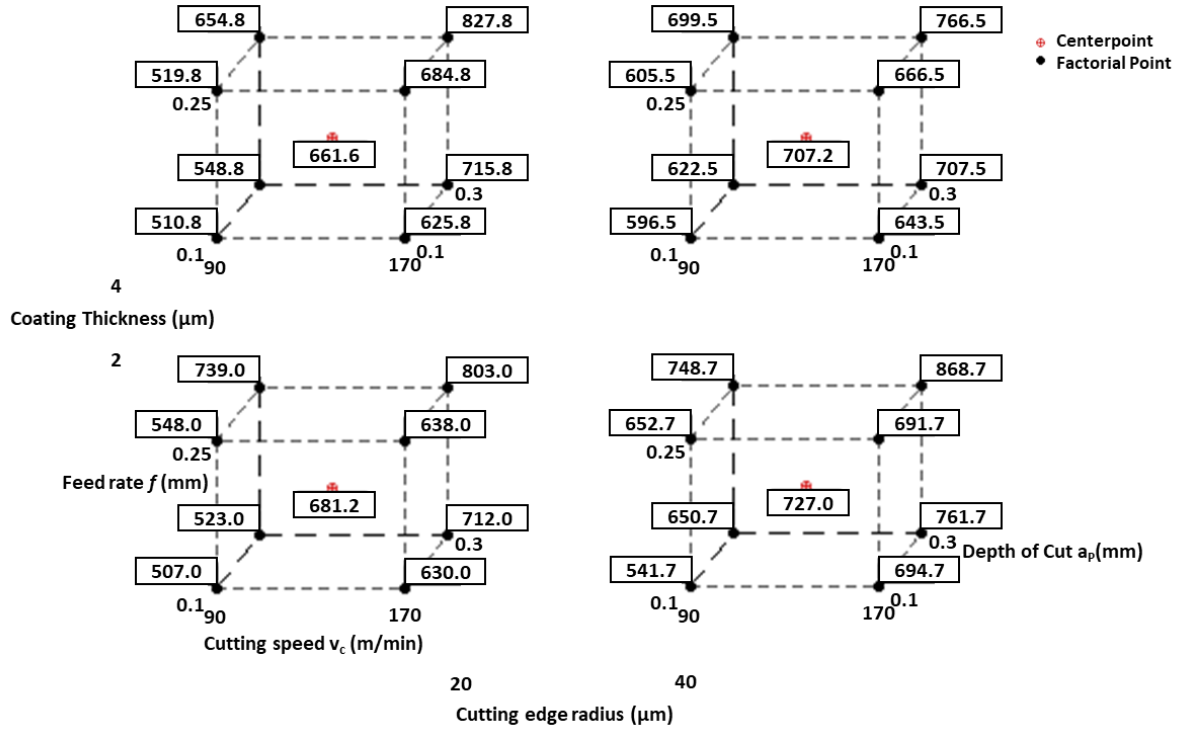

Workpiece material: 1.4837D Cooling: None	α_o	γ_o	ε_r	κ_r	Tool material: ISO-K10 Geometry: DCGT11T304-F Cutting edge radius: var. Corner radius: 0.4mm Coating: AlTiN Coating thickness: var.
Internal turning Simulation method: FEM	7°	15°	55°	93°	

Figure A 9: Results for the temperatures for each parameter set in second DoE from simulations

Schriftenreihe

Band 1

Koch, Jens Bodo: Unterstützung der schiffbaulichen Projektierung durch Repräsentation von Erfahrungswissen, 2004.

Band 2

Meyer, Sven: Flexible Gruppenarbeit in der Auftragsfertigung, 2004.

Band 3

Joswig, Dirk: Untersuchungen zum Zerspanverhalten weicher Elastomerwerkstoffe, 2005.

Band 4

Kerse, Nils: Unterstützung der schiffbaulichen Produktentstehung durch Einsatz von Virtual Reality (VR)-Technologien, 2007.

Band 5

Kurzewitz, Mathias: Kompetenzentwicklung als Element erfolgreicher Strategieumsetzung – dargestellt am Beispiel des Schiffbaus, 2007.

Band 6

Davids, Niko: Workflow-Management in Produktentwicklungsprojekten der Investitionsgüterindustrie, 2008.

Band 7

Möller, Carsten: Untersuchungen zum Drehen von gesinterten WC-Co-Hartmetallwalzringen, 2009.

Band 8

Gotsch, Falko: Untersuchungen zum Zerspanverhalten von Elastomerschäumen mit dem Ziel einer wirtschaftlichen Fertigung von Feder-Dämpfer-Bauteilen, 2009.

Band 9

Neumann, Lutz: Risikomanagement bei der Gestaltung von Unternehmenskooperationen – untersucht am Beispiel der Investitionsgüterindustrie, 2009.

Band 10

Sellmer, Dirk: Untersuchungen zur Verbesserung des Arbeitsergebnisses beim Vollbohren unter besonderer Berücksichtigung der Prozesskräfte und der Spanbildung, 2010.

Band 11

Eggers, Daniel: Entwicklung von Dienstleistungsportfolios bei Investitionsgüterherstellern – dargestellt am Beispiel der maritimen Industrie, 2009.

Band 12

Kindler, Jörg: Werkstückqualität und Standzeitoptimierung von Zerspanwerkzeugen bei der Umrissbearbeitung von kohlenstofffaserverstärkten Kunststoffen, 2010.

Band 13

Frömming, Hanno: Zerspanung von WC-Co-Hartmetall im unterbrochenen Schnitt, 2011.

Band 14

Schweitzer, Thomas: Nutzungsgradsteigerung verketteter Produktionslinien, 2011.

Band 15

Wagner, Lars Arne: Szenariobasierte Planung und Steuerung mit Simulation im Schiffbau, 2011.

Band 16

Schäfer, Christoph: Einsatzmodell zur systematischen Nutzung von Virtueller Realität in der Unikatproduktion, 2012.

Band 17

Hartmann, Dirk: Delamination an Bauteilkanten beim Umrissfräsen kohlenstofffaserverstärkter Kunststoffe, 2012.

Band 18

Kuyumcu, Arif: Modellierung der Termintreue in der Produktion, 2013.

Band 19

Czumanski, Thomas: Handlungsorientierte Analyse der Arbeitsproduktivität in der Serienproduktion, 2013.

Band 20

Schütte, Christoph: Bohren und Hobeln von kohlenstofffaserverstärkten Kunststoffen unter besonderer Berücksichtigung der Schneide-Faser-Lage, 2014.

Band 21

Wandt, Robert: Modellgestützte Fertigungssteuerung in der Unikatfertigung am Beispiel des Schiffbaus, 2014.

Band 22

Eichenseer, Christiane: Beschichtung, thermomechanische Charakterisierung und Spannungsanalyse von Schneidkeramik, 2014.

Band 23

Heinig, Martin: Nutzung von Virtuellen Technologien für die Montageplanung von Unikaten, 2015.

Band 24

Körkel, Gregor K.: Zerspanbarkeitsbewertung von Faserverbundkunststoffen bei der Fräsbearbeitung dünnwandiger Bauteile in der Großserie, 2015.

Band 25

Ramirez Martinez, Juan A.: Flexible Automated Assembly Systems for Large CFRP-Structures using Geometrical and Force Information, 2015.

Band 26

Dose, Frank: Methode zur wissensbasierten Prozessentwicklung - Ein Ansatz für die Berücksichtigung sich wandelnder Teilsysteme beim Bohren von Schichtverbunden, 2015.

Band 27

Trzyna, Daniel: Modellierung und Steuerung von Eilaufträgen in der Produktion, 2015.

Band 28

Griefahn, Dominik M.: Geometrieprüfung innerer Strukturen von Faserverbund-Sandwichbauteilen, 2015.

Band 29

Borrmann, Christof: Adaptive Montageprozesse für CFK-Großstrukturen mittels Offline-Programmierung von Industrierobotern, 2016.

Band 30

Klingelhöller, Christian: Trennschleifen von CFK-Schalenbauteilen mit räumlich gekrümmten Konturen, 2016.

Band 31

Titov, Fedor: Technologiegestützte Angebotserstellung für den Umbau komplexer Investitionsgüter, 2016.

Band 32

Tietze, Florian: Analyse und Verbesserung der Arbeitsproduktivität in der Unikatproduktion, 2017.

Band 33

Geis, Tobias: Bearbeitungsstrategien zur Zerspanung von Faser-Verbund-Honeycomb-Sandwich, 2017.

Band 34

Koppold, Nico: Kapazitätsplanung und -steuerung in der Instandhaltungsproduktion von Investitionsgütern, 2017.

Band 35

Halata, Philipp S.: Augmented-Reality-gestützte Informationsbereitstellung für die Unikatproduktion, 2018.

Band 36

Brügmann, Felix: Bauteilqualität und Werkzeugverschleiß beim Fräsen von CFK-Gelege unter räumlichen Eingriffsbedingungen, 2018.

Band 37

Benter, Martin: Analyse von Bewegungsabläufen mit 3D-Kameras, 2018.

Band 38

Koch, Christoph: Wertstromanalyse und -design für Auftragsfertiger, 2018.

Band 39

Cordes, Marcel: Modellierung von Bahngenauigkeit und dynamischer Stabilität beim robotergeführten Fräsen, 2019.

Band 40

Piontek, Andreas: Modellierung der Termintreue im Auftragsdurchlauf, 2020.

Band 41

Grabner, Constantin: Methodengestütztes Produktivitätsmanagement. Entwicklung eines datenbasierten Vorgehens, 2020.

Band 42

Glöckner, Robert: Entwicklung eines Gesamtmodells der Arbeitsproduktivität und der logistischen Zielgrößen, 2020.

Band 43

Schröder, Henrik: Kompetenzentwicklung in der Montage mit Hilfe virtueller Technologien, 2020.

Band 44

Engehausen, Friederike: Modellierung und Auslegung der Reihenfolgebildung mit Rüstfamilien, 2021.

Band 45

Sikorra, Jan Niklas: Frühzeitige Aufwands- und Termineinschätzung der schiffbaulichen Unikatproduktion, 2021.

Band 46

Haux, Moritz A.: Modellierung von Unsicherheiten in der Planung der Unikatproduktion, 2021.

Band 47

von Wenserski, Robert: Helixfräsen und Bohren von laseradditiv gefertigten Bauteilen aus Titan für Luftfahrtanwendungen, 2021.

Band 48

Meluzov, Nikolaj: Informationsmanagement für ein digitales Instandhaltungsassistenzsystem, 2022.

Band 49

Rost, Jan Robert: Digitale Assistenzsysteme für kollaboratives Arbeiten in der Unikatproduktion, 2023.

Band 50

Steenwerth, Philipp: Analyse und Optimierung von Suchvorgängen in der industriellen Produktion, 2023.

Band 51

Brosche, Justus: Nutzung von Motion-Capture-Technologien zur individuellen Ergonomieanalyse in der Produktion, 2023.

Band 52

Mehnen, Jan: Modellgestützte Berechnung der thermischen Belastung bei der Zerspanung von unidirektionalem CFK, 2023.

Band 53

Mundt, Christopher: Modellbasierte Auftragsannahme und -terminierung, 2024.

Band 54

Winter, Michael: Logistische Modellierung von Chargenarbeitssystemen, 2024.

Band 55

Elzalabany, Ahmed: A Digital Assistance System for Maritime Commissioning Processes, 2024.

Band 56

Breitzke, André: Modellbasierte Identifikation und Korrektur umgebungstemperatur-abhängiger thermoelastischer Verlagerungen dreiachsiger Portalfräsmaschinen, 2024.

Band 57

Köttner, Lars Stephan: Zerspankraftmodellierung und Prozessgrenzen der Umrissbearbeitung von FKV-Bauteilen mit scheibenförmigen Werkzeugen, 2025.

Band 58

Rana, Pulkit: Efficient optimization of turning processes for powertrain components using multi model-based simulation, 2025.